Establishment of Numerical Analysis Method and Orbit Demonstration of Membrane Structure Deployment Behavior using Self-extending Booms under Microgravity Environment

著者	Pala Alperen AhmedAlperen Ahmed Pala
学位授与機関	Tohoku University
URL	http://hdl.handle.net/10097/00137520

博士学位論文
Doctoral Thesis

論文題目

Thesis Title

Establishment of Numerical Analysis Method and Orbit Demonstration of Membrane Structure Deployment Behavior using Self-extending Booms under Microgravity Environment

東北大学大学院工学研究科

Graduate School of Engineering,

TOHOKU UNIVERSITY

専攻/Department: Aerospace Engineering

氏名/Name: Alperen Ahmed PALA

TOHOKU UNIVERSITY

Graduate School of Engineering

Establishment of Numerical Analysis Method and Orbit Demonstration of Membrane Structure Deployment Behavior using Self-extending Booms under Microgravity Environment

（微小重力環境における薄膜構造物の伸展ブームによる展開挙動の数値解析手法構築と軌道上実証）

A dissertation submitted for the degree of Doctor of Philosophy (Engineering)

Department of Aerospace Engineering

by

Alperen Ahmed PALA

July 8，2022

Establishment of Numerical Analysis Method and Orbit Demonstration of Membrane Structure Deployment Behavior using Self-extending Booms under Microgravity Environment

Alperen Ahmed PALA

Abstract

Since the launch of the first artificial Earth satellite Sputnik 1 in 1957, mankind has been launching various objects into space. Many of these objects, including once useful satellites and no longer useful 2nd stage rocket parts, start orbiting around Earth for long periods of time, whether intentionally or as a byproduct. In addition, many of the useful objects remain in orbit even after they lose their functionality and turn into debris. Although space is vast, useful space is not as vast as humans hope. Decades of space missions have accumulated extreme amounts of space debris in the limited useful orbits around Earth, occupying valuable orbit space, and potentially hindering the launch of future missions. In recent years many organizations have taken notice of the growing space debris issue. Especially, with the inclusion of the eventual Kessler Syndrome into considerations, the cascading effect caused by a single collision of debris in space can turn into a catastrophic destruction of the whole orbit. This imminent danger is ever nearing with every mission turned into debris with no considerations of de-orbiting.

Many international bodies including the National Aeronautics and Space Administration (NASA), the European Space Agency (ESA), the Inter-Agency Space Debris Coordination Committee (IADC) and Japan Aerospace Exploration Agency (JAXA) are actively raising awareness on this issue and are contributing to the reduction of the space debris in two main ways: Active debris removal, and implementation of debris mitigation strategies. There are many proposed methods of active debris removal. But all these options are incredibly costly with no monetary return on the establishment that is running these missions. The incentive for such practice is very low for the private industry. Most of these missions are proposed by government bodies that have the budget and funding regardless of the monetary return. Therefore, the removal of currently existing debris is beyond the scope of most private industries. Conversely, given the internationally accepted rules on debris mitigation, new missions are responsible to follow the guidelines for the elimination of their debris. For this purpose, much research is conducted for the de-orbiting of mission turned debris, both by private industry and governments around the world.

With planning ahead, many different strategies can be utilized to de-orbit a satellite after its mission comes to an end. Many of these options are passive and do not require further operation of the satellite to accomplish the de-orbiting. Additionally, they can be set up to be initiated in the case of unexpected and irreparable satellite system malfunction or shutdown. One example of a method used for such devices is thorough the use of membrane structures as a drag sail against the atmospheric resistance to slow down the debris and gradually induce its re-entry back to Earth. With the use of membrane structures, the effective drag area acting on the satellite can be increased by many folds, which will then decrease the ballistic coefficient of the satellite body and shorten the orbit time. With such a simple idea, many different devices with similar capabilities can be developed, however it is both costly and time consuming to test in a real space mission to prove their usefulness. In order to overcome these hurdles, researchers have turned to simulative methods as a first step to confirm the integrity of a given de-orbiting device and its mechanics. Using numerical methods to estimate and simulate the dynamics of an action pre-mission is very valuable and have been used in the aerospace industry for decades. However, having an accurate simulation platform, numerical method, mathematical theory, and corresponding parameters are essential to ensure the usefulness of simulation. In comparison there is a lack of real mission data to compare to for the deployment and de-orbiting behavior for membrane structure used in space missions.

A de-orbiting device consisting of self-extending convex tapes and a thin membrane element is used for the partial de-orbiting of the artificial shooting star generating micro-satellite ALE-1 as part of its pre-mission orbital maneuver from 500 km orbital altitude to sub 400 km orbital altitude where the risk of hitting the International Space Station (ISS) with the shooting star generating particles becomes zero. Data on the deployment and post-deployment dynamics of the membrane, and the de-orbiting behavior of the satellite is gathered to be used in conjunction with the proposed simulation platform in order to ensure the fidelity and reliability of the established platform. In chapter 1 of this dissertation, the space debris issue, the mitigation strategies, different methods of de-orbiting are discussed as an extensive literature review. Following this, the equipment ad mission used in this research are introduced along with the goals of this research.

In chapter 2 of this dissertation, a review of the numerical analysis methods used for the membrane deployment behavior throughout the years are discussed. As a start, the fundamentals of nonlinear finite element methods are introduced. Following this, the wrinkle/slack theory used in the simulation of membrane structures is

introduced with the various different variations used over the years. Building on these foundations, the stiffness reduction model introduced by Miyazaki in 2005 and its use together with the energy-momentum method is explored. Following this a similar model used for the extension behavior of self-extending convex tapes is introduced, and the initial results of both models and their fusion is presented.

In chapter 3 of this dissertation, the de-orbiting mechanism used for this research in ALE-1 is discussed. However, this mechanism is inherently designed for the end-of-life disposal of satellite. If used alone, it is designed to completely de-orbit the satellite. In order to increase the main mission orbit time after desired altitude is reached, a separability function is designed and added to this mechanism. Furthermore, in order not to risk the satellite life through lack of power generation and lack of operability during this orbital maneuver, an extendibility function is designed and added to the mechanism as well. On top of that, in order to elucidate the little-known dynamics of membrane structure deployment dynamics, convex tape properties, as well as de-orbiting behavior of satellites using drag sails; a subsystem of observational tools are designed and implemented into the mission of ALE-1 using this rare opportunity. All of these systems and their functions are tested on ground to space qualify for in-space use and their functionality is ascertained. Chapter 2 of this dissertation discusses the mission design, system design, mechanical design, and the preliminary requirements and criteria for this orbital maneuver mission. Furthermore, the observational sub-systems designed and used for this mission, as well as their capabilities are explored, and the results of ground verification and evaluation of all the systems used for this research to qualify for in-space use are presented. ALE-1 and the Separable De-Orbit Mechanism (SDOM) it carries are launched into orbit in January 2019. The SDOM mission is initiated, and its boom is initiated to be extended to bring the sail deployment mechanism away from the satellite. After extension of the boom, the system before extension and the system after extension are compared through an analysis using Fourier transform on the tumbling data attitude data of the satellite before and after extension. The similar profile for each case proved the laterally rigid nature of the boom as far as the satellite operation is concerned. Following this, the sail is deployed, and the deployment is recorded into a video including distance data with a time-of-flight laser range finder. This deployment is compared to ground experiment results. Additionally, quantitative analysis is conducted to calculate the deployment rate in space. These analyses showed the sail moving out of its deployment plane which was unexpected result. Furthermore, the torsional vibration of the boom induced by the sail deployment is analyzed to quantify torsional rigidity of the boom. Shortly after deployment, the sail breaks in two corners and turns from a drag sail into a drag-flag. The de-orbiting rate of ALE-1 is analyzed in this condition and an effective drag area is calculated for the drag-flag state of ALE-1 using real mission two-line elements (TLE) of 19 months passed since it's the sail deployment. This value is then used to estimate the future de-orbiting of ALE-1 and the projected initiation of the separation action for the SDOM.

In chapter 4 of this dissertation, the simulation platform established in chapter 2 is updated in conjunction with the in-orbit flight results presented in chapter 3. The model parameters that are most impactful on the deployment behavior are identified and adjusted to match real flight data in order to establish a more realistic simulation platform. The effects of various parameters implemented are discussed and the simulation results when they are varied are presented.

In conclusion this research achieved the following: 1) the implementation of a simulation platform for self-deploying membranes used for de-orbiting satellites, 2) the design and ground verification of a separable de-orbit mechanism for micro-satellites, the in-orbit verification of the aforementioned mechanism, acquisition of World's first recorded data from a vertical angle showing the deployment behavior of a membrane structure in space, 3) the adjustment of the simulation environment for the deployment behavior of membrane structures in conjunction with the acquired in-orbit flight data to reflect reality. These achievements are contributing to the general expansion of space industry, as well as the depth of understanding of research in the field. Chapter 5 of this dissertation is discussing these contributions in a more detailed manner.

Table of Contents

List of Figures

List of Tables

1. Introduction

For millennia humans have tried to utilize whatever miniscule information they can gather from around them to their advantage. One source of such information has always been space. Be it looking at the sky to predict tomorrow’s weather or looking at the stars to find their way back home, humans have always seen value in space. In recent years, this value has increased by thousands of folds with the development of space technologies starting from the 1960s. With each passing decade, space technologies, and in conjunction the space itself have become increasingly available to the public. Today all of us, carry around some sort of device that communicates with a space entity, let it be through GPS or cellular communication, or even simple TV broadcast; they can all be achieved through strategic placement of satellites.

1.1. Space Debris Issue

Space missions are inherently extremely expensive. Although in recent years, they have been getting cheaper and cheaper by many orders of magnitude, space industry is still one of the most expensive if not the most expensive industry on earth. But technological advancements have enabled privately owned companies to design and start their own space missions, after a long reign of exclusively governmental missions due to high budget estimations. In recent years even startup companies can design, build, and send their spacecrafts into orbit. For most space applications, it is important to design the orbit very carefully, to gain maximum efficiency from the mission.

Orbits of Earth are classified into 4 categories, with respect to the altitude:

- High Earth Orbit (HEO)
- Geosynchronous Orbit (GEO)
- Medium Earth Orbit (MEO)
- Low Earth Orbit (LEO)

From these four, Geo and LEO are especially important for various reasons. GEO is an orbit that has a specific altitude which is 42164 km from earths center. At this height, the orbiting body has the same period as 1 sidereal day. Therefore, the spacecraft stays always at the same point when observed from earth. This brings many advantages with it, such as ease of ground station establishment and communication. However, as this is only true for this one specific height, it makes this orbit extremely valuable and a finite resource.

Similarly, LEO is the general term used for a band of altitudes ranging from 160 km to 2000 km above the sea level. This region is extremely useful for a several reasons as well. First, it requires the least amount of energy to put a spacecraft into orbit in this region compared to other regions. Second, LEO provides widest range of communication features. Third, the hardware requirements for a spacecraft at LEO is much less severe than other regions, etc. These are all because LEO is closest to Earth. However, it comes with a disadvantage, which is it is also the narrowest region of all. That means the amount of spacecraft that can orbit in this region at once is the least. Therefore, LEO also is an extremely valuable and finite resource as an orbit.

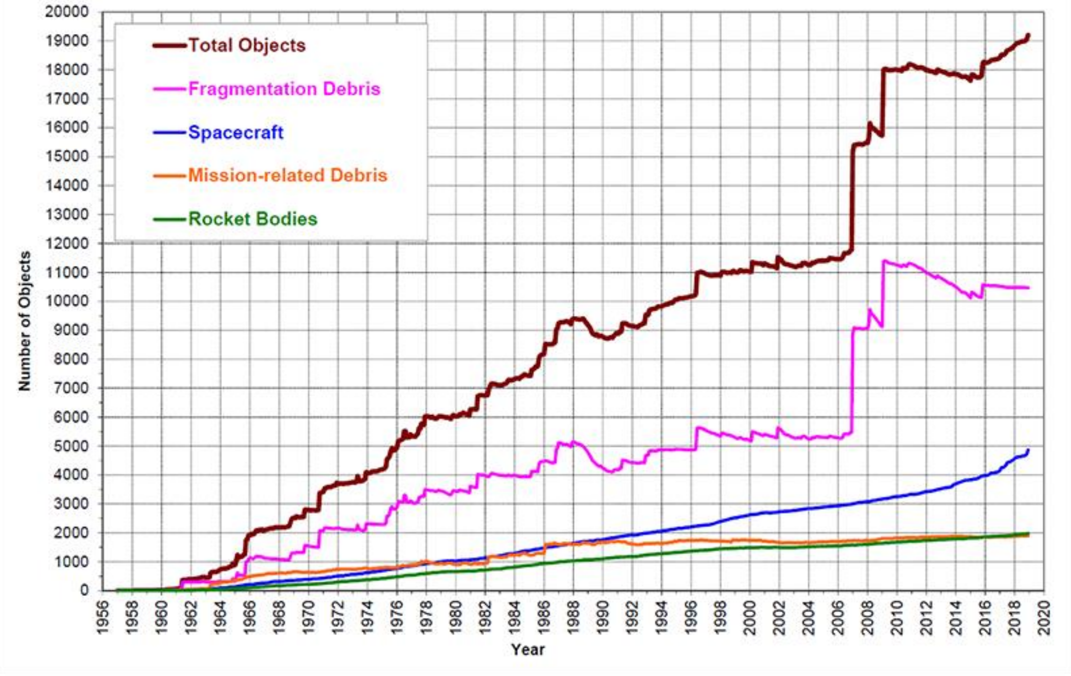

Fig. 1.1: Monthly number of objects in low earth orbit by object type up to November 2020. (©NASA)

It is undesired to occupy these orbits with dead satellites, instead of possible missions. Yet decades of accumulated missions, have built up many space debris occupying these valuable orbits, and making it harder to place new missions with each passing day.[1] Not only that, but also the space debris issue can grow exponentially at any moment with the start of a single chain of collisions.[2,3] Figure 1.1 (data courtesy of National Aeronautics and Space Administration, NASA) shows the number of objects in Earth orbit by object type. The upwards spike in the graph around 2007 is due to anti-satellite missile tests. And the spike around 2009 is due to an on-orbit collision of two spacecrafts. The danger of such events is the possibility of collision cascading, a chain reaction of collisions that keep exponentially increasing the number of debris, within a small amount of time, to the point where future space missions are not possible anymore.[4] Figure 1.2 is a representation of the earth and the amount of spacecraft around it.

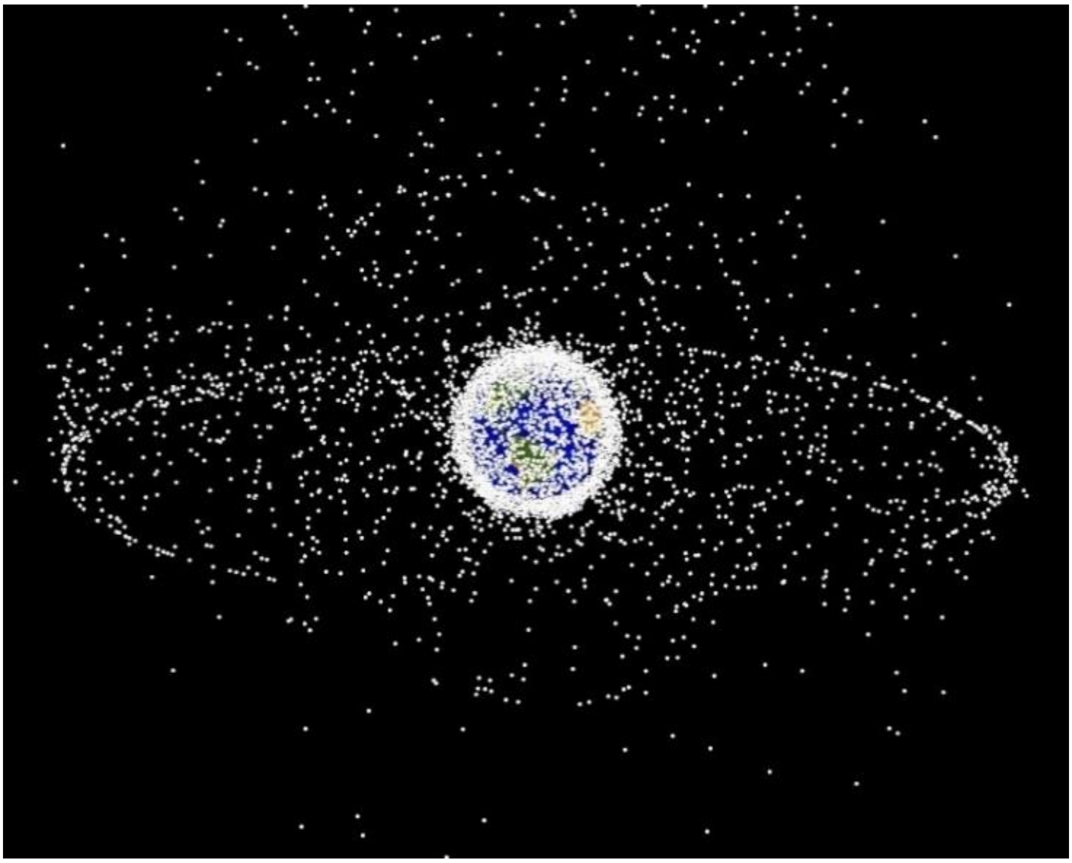

Figure 1.2. Representation of earth and the orbiting bodies around it. (Objects not to scale, ©NASA)

The Inter-Agency Space Debris Coordination Committee (IADC) defines space debris in the IADC Space Debris Mitigation Guidelines as follows: Space debris are all man-made objects including fragments and elements thereof, in Earth orbit or re-entering the atmosphere, that are non-functional.[5] This definition not only includes decommissioned satellites, but also fragmentation related elements left in orbit from the second stages of rockets, elements generated by a few rare explosions of mission bodies in space etc. We can categorize space debris into three as shown in the following Table 1.1. Any debris larger than 10 cm, will cause total destruction of the hit object with a hyper velocity collision. Fortunately, objects larger than 10 cm can be tracked and possibly avoided eat least for the case of critical missions such as the International Space Station (ISS) with humans on board. Any debris smaller than 10 cm will damage the hit object with a real possibility of total destruction. Additionally, objects smaller than 10 cm are not trackable in most cases. Any debris smaller than 1 cm will cause damage to the hit object. As an example, Figure 1.3 shows the damage caused by a small sphere of aluminum, hitting a block of aluminum of 18 cm thickness at a velocity of 6.8 km/s. Such an impact will cause a crater that is about 8 cm deep and 18 cm wide, and even a spallation at the other side of the block. Even at small sizes of debris, the damage is extremely catastrophic for any functioning satellite due to high velocity and high energy thereof.

Table 1.1: Different categories of space debris with respect to size.

Size	Remark	Collision Risk
> 10 cm	Can be tracked	Total destruction
1-10 cm	May be tracked if large enough	Extreme damage or total destruction
< 1 cm	Cannot be tracked	Damage

Fig. 1.3: Damage caused by a small sphere of aluminum to a block of 18 cm thick aluminum at hyper velocity. (©ESA)

1.2. Debris Mitigation Strategies

There are two main strategies to mitigate space debris. First option is the actively capturing and removal of existing space debris.[6] There are various projects that aim to achieve this and Fig 1.4 show one example from the e.Deorbit project of European Space Agency (ESA). [7] However, these are usually extremely costly with little to no monetary return of investment. [8,9] Many governments are encouraging these kinds of active debris removal research and missions with governmental funding as these kinds of missions are near to impossible to find private funding for. Second option is the prevention of further space debris. [10] With this strategy, it is essential that any new missions are equipped with the capability of disposing the satellite or spacecraft after the mission is finished within a set amount of time. This disposal can either be the movement of the satellite to a graveyard orbit, which is occupied with dead satellites and at which altitude collision becomes irrelevant, or it can be the de-orbiting of the satellite back to earth and consequently the destruction of it through burnout at re-entry. Table 1.2 shows the NASA standards for debris assessment for various orbits.

Table 1.2: NASA Standards for Debris Assessment Methods for LEO, MEO and GEO summarized. [11]

Orbit	Debris Assessment Methods
LEO	• Direct retrieval within 10 years • Re-entry within 25 years • Re-orbiting to a highly elliptic orbit
MEO	Re-orbiting to an elliptic graveyard orbit
GEO	Re-orbiting to a graveyard orbit above GEO

The end-of-life disposal of satellites through de-orbiting is essential for sustainable space usage. If the critical point is crossed, a passive option such as this, will not be viable anymore, but until then, it is a cheaper, and more expectable option for newer missions. This can be achieved through various methods.

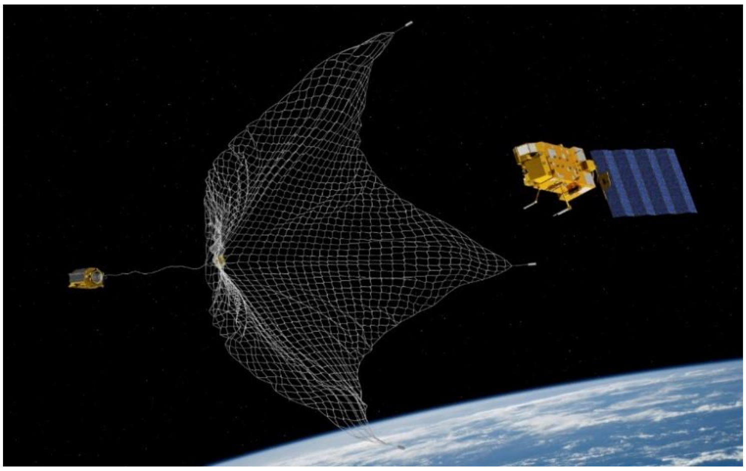

Figure 1.4. Artists rendering of active capture and disposal of space debris within the scope of e.Deorbit mission of ESA. (©ESA)

1.2.1. Active De-Orbiting

First method is active de-orbiting of the spacecraft with complete control. This is usually achieved using thrusters, and active de-orbiting methods usually take less time for complete de-orbiting.[12,13] However, there are some disadvantages. Active systems require higher power and mass budget out of the spacecraft mission. Not only this, but the spacecraft usually needs to still have complete operability for a fully controlled de-orbiting. As the generated thrust on the system is high, a wrong direction may cause longer orbit life, instead of shorter, and therefore full controllability is important. This makes active systems harder to use as a measure if the spacecraft is damaged and inoperable anymore, whereas passive systems are usually enabled with a simple sequence and continue the de-orbiting process until the system burns up in the upper atmosphere at re-entry. An example of a thruster developed for active de-orbiting of micro- and nano-satellites is the IFM Nano Thruster developed by ESA shown in Fig. 1.5. [14]

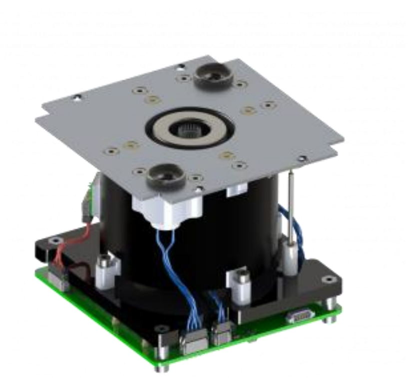

Fig. 1.5: IFM Nano Thruster Module developed by ESA as a Commercial off-the-shelf (COTS) unit. (© ESA)

1.2.2. Inflatable Balloons

One example of a passive de-orbiting method is the use of an inflatable balloon.[15] The idea is very simple. At the end of the mission life, when it is time for disposal, a balloon is inflated from any side of the spacecraft. This effectively decreases the ballistic co-efficient of the system by increasing the drag area. Consequently, the system decelerates faster, and therefore the orbit of the system decays faster. Advantages of inflatables include, small storage volumes and less mass when compared to the surface area they provide for drag. Disadvantages include the inevitable use of some kind of gas source. This can be a compressed gas released from a pressurized tank, or gas producing chemical reactants. In both cases, many extra precautions are needed to be taken to ensure regular missions safety due to inclusion of potentially hazardous items for the post-mission disposal of the satellite. Especially when it comes to chemical reactants, choosing safe compounds become essential due to not only potential in-orbit hazards, but possible pollution that may be caused to the atmosphere at re-entry and burnout. Considering the uncontrollability of the re-entry site, especially in the case of re-entry to a foreign soil, the issue can escalate into an international crisis quite quickly similar to the 1979 COSMOS 954 incident, which is the reason for many international law in satellite accidents. [16] This issue can be avoided more easily for compressed gas as most widely used gas is nitrogen which make up most of the atmosphere and is safe. One notable example for inflatable de-orbiting device is the Gossamer Orbit Lowering Device (GOLD) proposed by Global Aerospace Corporation shown in Fig. 1.6. [17]

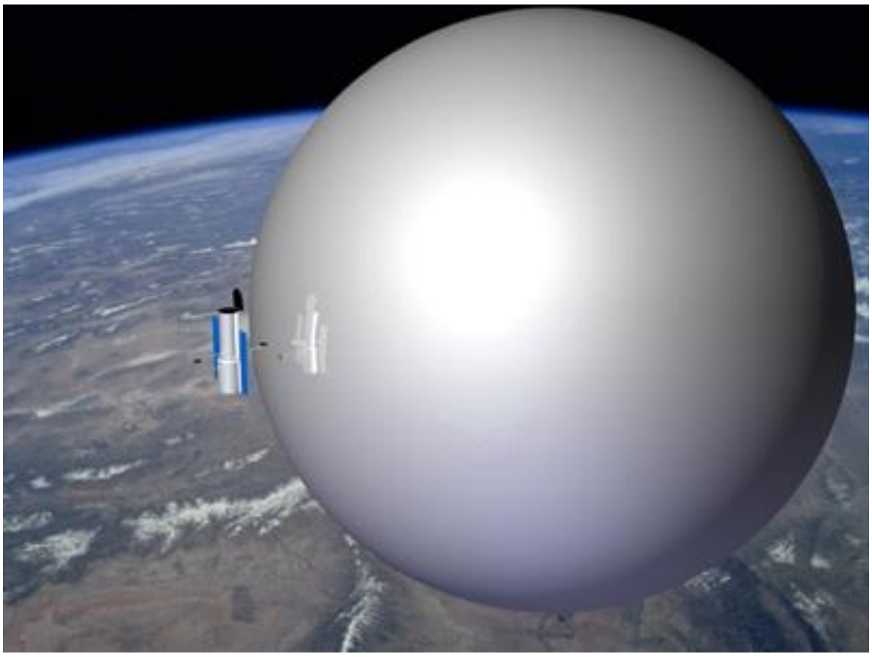

Fig. 1.6: Rendering of Gossamer Orbit Lowering Device (GOLD) initiating the de-orbiting of a spacecraft. (©AIAA)

1.2.3. Electromagnetic Tethers

Another example for a passive de-orbiter system would be the use of electromagnetic tethers. [18,19] For this, a long conductive tether is deployed from the satellite. While orbiting around Earth, current is induced in this tether through electron emission at the end. When the direction of this current and the magnetic field of Earth follow the right-hand rule, the induced Lorentz force is on the opposite direction of cruise direction. Consequently, the orbiting velocity decreases due to deceleration caused by the induced Lorentz force and the satellite gradually de-orbits. Figure 1.7 shows this working principle for Kounotori Integrated Tether Experiments (KITE) that was mounted on H-II Transfer Vehicle (HTV) of Japan Aerospace Exploration Agency (JAXA). [20]

Electromagnetic tethers are very popular in recent years due many advantages they have over other systems. [21] These advantages include lesser mass requirements, fast de-orbiting times. However, there are some risks with them as well. Biggest risk is the fact that the tethers are incredibly thin and long. The chance of severing a tether is not negligible, and in the event of a severed tether, space debris will have been increased instead of decreased. Additionally, very long tethers inherently bring with them very long satellite systems, increasing the chance for collision, or failure. However, bearing risks mean the opportunity for improvement, and electromagnetic tethers have been a thriving topic of research in space debris mitigation and satellite de-orbiting for years. Many projects were proposed using electromagnetic tethers including ProSEDs by NASA Marshall Space Flight Center [22], EDOARD by University “La

Sapienza" [23] and maybe the most successful to this day, Terminator Tape by Tethers Unlimited [24]. Terminator Tape has demonstrated its function in space and therefore has space heritage, as well as different sizes for different target satellites.[25] Figure 1.8 shows the Terminator Tape for Nano-satellite use. Although electromagnetic tethers are mostly used for passive de-orbiting, some work has been proposed for active debris removal utilizing electromagnetic tethers as well. [26]

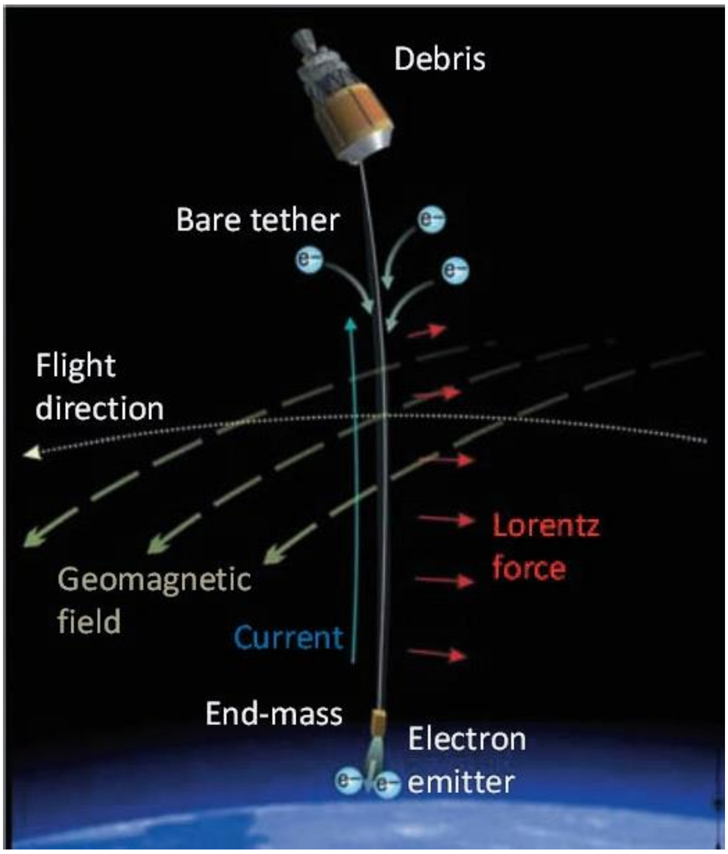

Fig. 1.7: The working principle of the electrodynamic tether system used in Kounotori Integrated Tether Experiment (KITE) launched with the 6th H-II Trasfer Vehicle (HTV-6) of JAXA. (©JAXA)

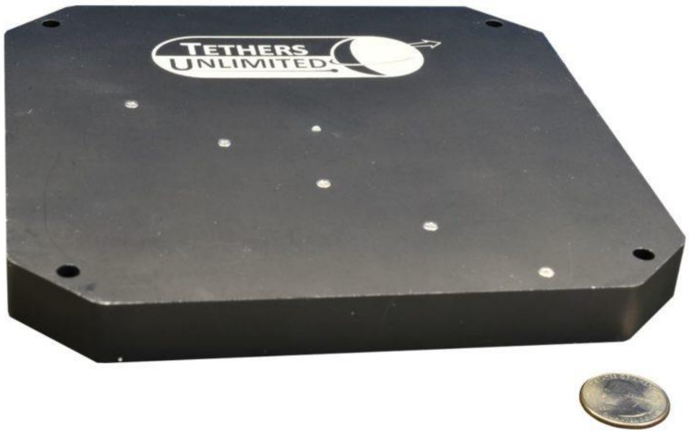

Fig. 1.8: The Terminator Tape developed by Tethers Unlimited for de-orbiting of Nano-satellites from Low Earth Orbit. (© Tethers Unlimited, Inc.)

1.2.4. Drag Sails

The most common method of passive de-orbiting would be the use of drag sails. Drag sails, similar to solar sails, are gossamer structures, that are usually stored in very small packages, but provide a large surface area when deployed to increase the ballistic coefficient of the system. Usually, the sail consists of deployable boom elements to provide shape, rigidity and support; and space ready thin film elements that are curtained between the boom elements to provide the intended increase in drag area.

For a nearly convex satellite that is in orbit, the effective drag area can be estimated as ¼ of the effective total surface area of the satellite.[27] For a system that assumes a stable attitude relative to the velocity vector in orbit, the effective drag area will be the cross-sectional area with regards to the velocity vector. This means that for systems that deploy a drag sail and tumble, the increased effective drag area is actually only ¼ of the area increase, which will be around ½ of the area of the sail considering the sail has 2 sides. However, if the attitude of the space craft is stabilized in a manner that allows for maximum cross-sectional area for the sail in the velocity vector direction, then the effective drag area will be maximized.

Stabilization can be achieved in two different ways. An active attitude control can be implemented to ensure the drag sail is always facing the same direction as the velocity vector. This will ensure maximum effective drag area, but continuous active attitude control can be costly in terms of power budget of the satellite. Another way can be a passive stabilization of the attitude. In order to achieve such stabilization, the environmental disturbance torques that are usually considered are aerodynamic torque, magnetic torque, gravity gradient torque, and solar radiation torque. Below 500 km altitude, the dominant torque is usually aerodynamic torque.[28] However, if there is a mass element at a distance from the satellite, then the gravity gradient effect can be dominant depending on the initial attitude. Solar radiation torque and magnetic torque are usually dominant at higher regions. If the aerodynamic torque is ensured to be dominant, the system can be induced into weather-cock stability. Weathercock stability is a directional stability in flying objects, induced by a restoring force profile of aerodynamic torques that occur when the center of pressure of the system is behind the center of mass of the system with respect to the direction of the flight.[29] This is easily achievable for airplanes and rockets with fins. Satellites can also be designed while considering a passive directional stability which can increase effectiveness of de-orbiting through a drag sail.

Drag sails are used to decelerate the system for de-orbiting, whereas solar sails are used for propulsion of systems mostly in deep space through the use of solar flux and the conversion

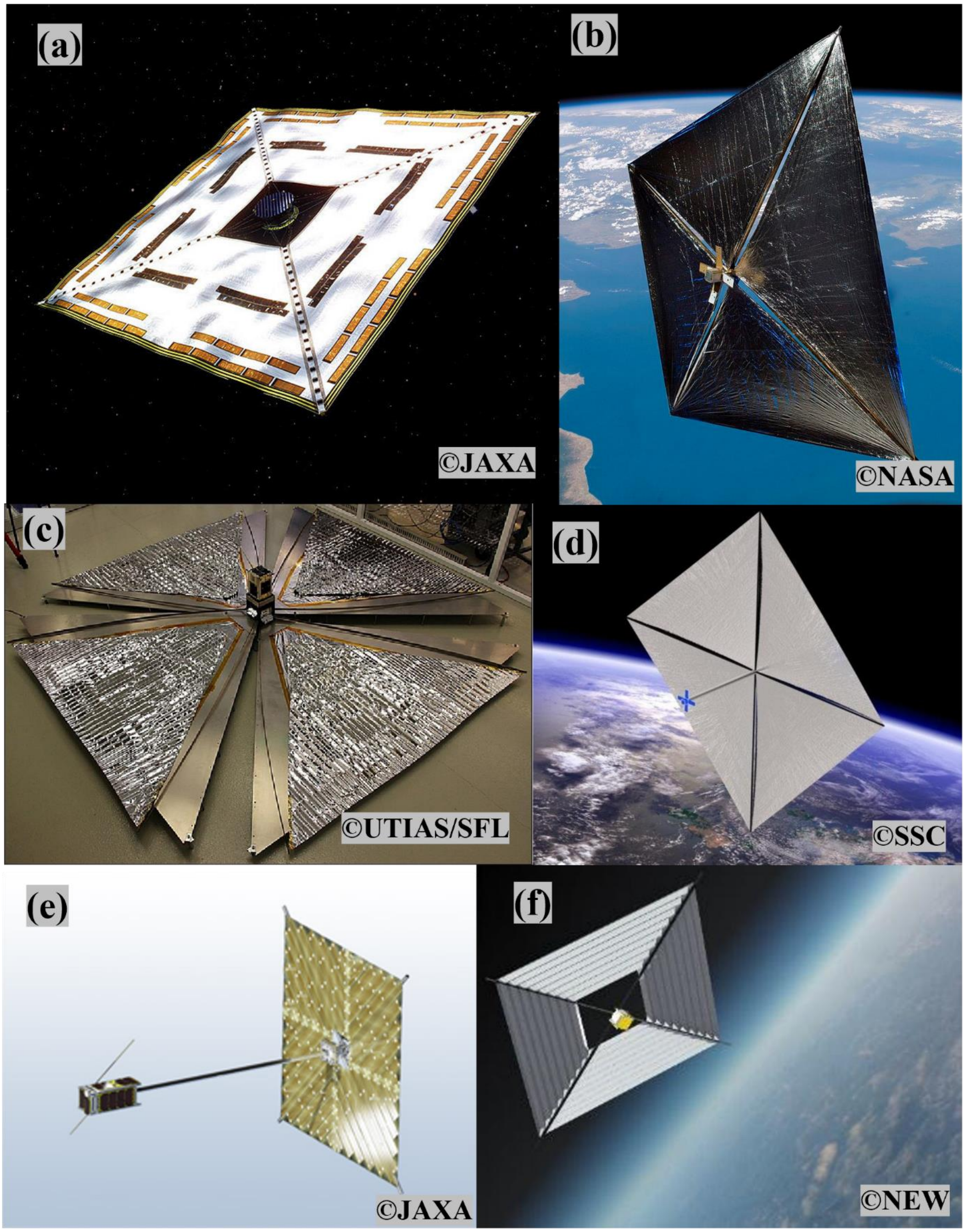

Figure 1.9: Notable drag sail and solar sail missions with in-orbit demonstration: (a) Interplanetary Kite-craft Accelerated by Radiation Of the Sun by JAXA (©JAXA), (b) NanoSail-D2 by NASA (©NASA), (c) Canadian Advanced Nanospace eXperiment-7 by University of Toronto Institute for Aerospace Studies/Space Flight Laboratory (©UTIAS/SFL), (d) InflateSail by Surrey Space Center (©SSC), (e) OrigamiSAT-1 by Tokyo Institute of Technology (©JAXA), (f) FreeDOM by Tohoku University and Nakashimada Engineering Works. (©NEW)

of the momentum of light photons into physical thrust. [30,31] This can be either for deceleration, or acceleration, or simply navigation of the system depending on the situation and intention.[32]

Notable examples of solar sail and drag sail demonstration missions include, Interplanetary Kite-craft Accelerated by Radiation Of the Sun (IKAROS) by JAXA [33,34], NanoSail-D2 by NASA [35,36], Canadian Advanced Nanospace eXperiment-7 (CanX-7) by University of Toronto Institute for Aerospace Studies/Space Flight Laboratory (UTIAS-SFL) [37,38], InflateSail by Surrey Space Center (SSC) [39,40], ORganizatIon of research Group on Advanced deployable Membrane structures for Innovative space science project by Tokyo Institute of Technology [41,42], FreeDOM by Tohoku University and Nakashimada Engineering Works [43,44] as shown in Fig. 1.9.

1.3. De-Orbit Mechanism (DOM)

Nakashimada Engineering Works and Tohoku University have been collaborating in research and development of a de-orbit mechanism called De-Orbit Mechanism (DOM) for the end of mission disposal of small-, micro- and nano-satellies through the use of the aforementioned drag sails. This mechanism has various sizes for various different applications and is used in several past space missions including the FreeDOM mission, which was only to demonstrate this module and to gain space heritage. Table 1.3 summarizes different variations of DOM and Table 1.4 summarizes the past missions including various DOMs.

Table 1.3: Various sizes of DOMs that are available for quotation or in development.

	DOM500	**DOM1500**	**DOM2500**	**DOM1000 (Estimation)**	**DOM4500 (Estimation)**
Sail size [mm]	500 x 500	1500 x 1500	2500 x 2500	1000 x 1000	4500 x 4500
Center hole of sail [mm]	100 x 100	500 x 500	500 x 500	100 x 100	500 x 500
Mass [g]	250	1000	1600	350	2500
Range of operating temperature [℃]	-20 to +70				

Table 1.4: Various past missions including a DOM.

Launch Year	**Satellite**	**DOM series**	**Carrier**	**Initial Orbit Altitude [km]**
2012	CubeSat RAIKO [45,46]	DOM500	H-2B	~400
2014	RISING-2 [47,48]	DOM2500	H-2A	~600
2016	FreeDOM [43,44]	DOM1500	H-2B	~400
2017	Flying Laptop [49,50]	DOM2500	Soyuz	~700
2018	RISESAT [51,52]	DOM2500	Epsilon	~500
2018	ALE-1 [53,54]	DOM2500	Epsilon	~500

1.4. ALE-1

Microsatellites have always been a good platform for the demonstrations of new space technology due to their rapid mission development time, and relatively low mission costs. ALE-1 is one such micro-satellite developed by Astro Live Experiences (ALE) Co. Ltd. and Tohoku University. The main mission of ALE-1 is the demonstration of artificial generation of visual of shooting stars. [55,56] This is achieved through the release of small metallic pellets from the satellite in-orbit in a way that would re-enter the atmosphere and burnout. As a result, these pellets would emit light and visually appear similar to a shooting star observed from Earth. Figure 1.10: shows the mechanics of the shooting star generation. The pellets are released opposite to the velocity vector of the satellite, resulting in less speed of the pellets, which then cause them to sink into a lower orbit. During this descent, at around 80 km above ground, the pellets get hot enough to shine and they continue to emit light until about 60 km above the ground where they completely burn out. Although the primary objective of ALE-1 is for entertainment purposes, it is also possible to study the mechanics of real shooting stars and the properties of upper atmosphere, as well as the opportunity it provides for secondary missions.

ALE-1 was planned to launch with the Epsilon 4 rocket of JAXA under the Innovative Satellite Technology Demonstration-1 program.[57-58] Epsilon 4 had the small satellite RAPid Innovative payload demonstration Satellite 1 (RAPIS-1) developed by Axelspace as its main payload, which tests many field including a HAN-based green propellant for future space mission. [59] Epsilon 4 carried many other satellites and modules as secondary payload including micro-satellites RISESAT and MicroDragon, cubesats OrigamiSat-1, Next generation X Unique Satellite (NEXUS) by Nihon University and Aoba VELOX-IV. [60,61,62] Other equipment used for new technology demonstration within the scope of Innovative Satellite Technology Demonstration-1 program include a Space Particle Monitor (SPM), a Deep Learning Attitude Sensor (DLAS), a Thin Membrane Solar Array Paddle (TMSAP) and a Miniature Spaceborne GNSS Receiver (Fireant). [63, 64] Unfortunately for ALE-1, this meant that the orbital altitude chosen for the mission is decided by the requirements of the primary payload RAPIS-1 and was around 500 km above the sea level.

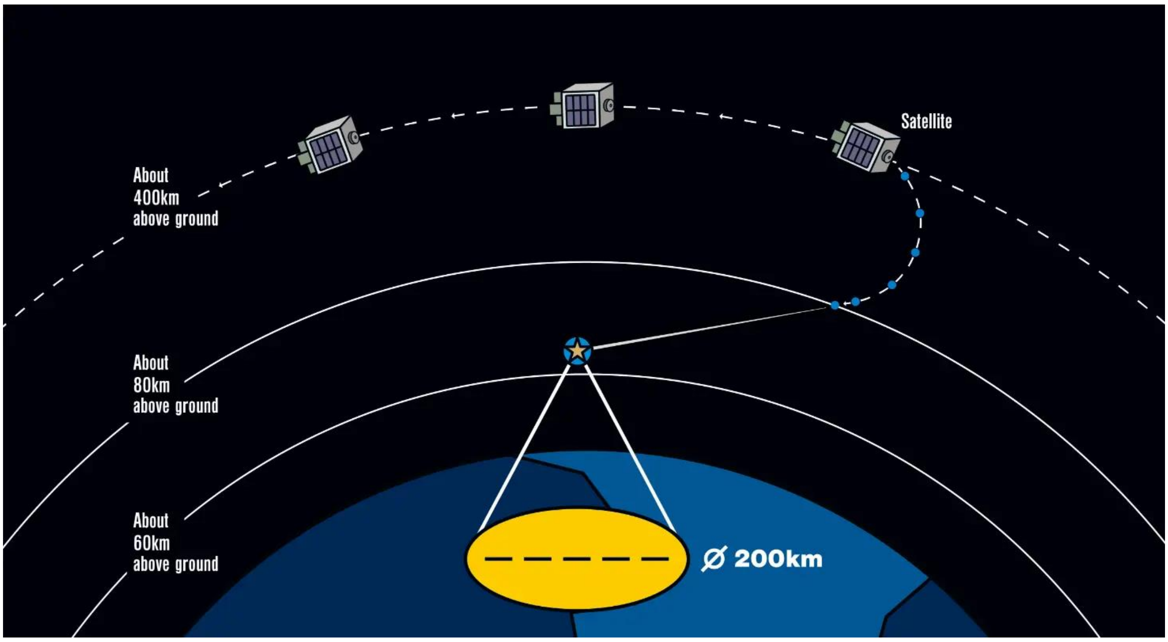

Fig. 1.10: Principles of artificial shooting star generation used in ALE-1.

This is an issue for ALE-1 because the International Space Station (ISS) is located at around 400 km of altitude. Since ALE-1 is shooting pellets towards earth, anything below it is a potential target. Although the risk of hitting another object is in the order of magnitude of 10e-6 or lower, considering more multiple trials mean additional risk for each pellet. ISS has manned missions throughout the year and any risk value, no matter how low, is too high when human lives are in the equation. Therefore, it was a necessity to lower the orbit of ALE-1 to below 400 km before the start of its main mission to get around this risk. Additionally, many precautions were taken to ensure that the shooting direction for ALE-1 is in fact true to the intended direction. [65,66]

For this orbital maneuver of ALE-1 from 500 km to 400 km of height, the passive de-orbiter DOM was chosen to be utilized, even though active thruster systems are usually more suited for this kind of orbital maneuvers in terms of mission time. The main reason for this was the severe safety review requirements to rideshare on Epsilon 4. However, as the DOM was designed to be deployed at the end of a satellite's life for disposal purposes, its design was not very suitable for a pre-mission for ALE-1. In order to comply with ALE-1's requirements, design upgrades were necessary on DOM. Figure 1.11 shows flight configuration of ALE-1.

Figure 1.11: Flight configuration of world's first artificial shooting star generating satellite ALE-1.

1.5. Simulative Approach

In general, for aerospace applications, new ideas and designs are extremely costly to demonstrate. This is due to high costs and low availability of spaceflights. Additionally, testing new ideas and designs on ground does not always guarantee that the same setup will behave similarly in space where there is little to no atmosphere and micro to no gravity. With various techniques, these differences can be recreated on ground, however having all the differences at once is as costly and as difficult as the spaceflight itself. For years researchers have been borrowing the help of computers to simulate the behavior of such systems designed for space using numerical analysis methods. These analysis methods are vastly useful especially on structural and thermal analysis of space systems. Most space missions include redundancy to ensure mission success however, there are many make-or-break elements in every space mission. Especially for structural and thermal integrity of the mission, rigorous testing is applied. But these ground testing methods are also extremely costly. It is usually cheaper and faster to conduct simulative analysis on the system before testing to decrease time and monetary cost of the testing phase.

Simulative analysis is not only limited to the aforementioned areas but can also be useful in determining whether a devised concept or mechanism will be successful or not. A good example can be the orbital trajectory simulations to have an idea of what the mission orbit will be beforehand. Similar to this, if one can establish a realistic simulation platform, one can analyze the orbit decay of a post mission disposal of a satellite or fairing. This not only useful as a first impression of the mission, but also if proven realistic, such platforms can be used to analyze future missions' success as well. Up to this point, there are limited real data on the de-orbiting bodies, and the de-orbiting mechanics. Therefore, there are limited platforms that realistically reflect the space conditions with high confidence. Achieving this requires not only rigorous work on the establishment of such numerical analysis platforms but also their proof using real mission data. To the knowledge of the author, this has not been achieved to a high confidence level up to this point.

1.6. Aim of this Research

As discussed, up to this point, there is a great need for effective de-orbiting devices for the future remediation of the growing space debris problem. An excellent candidate for such a function is the utilization of deployable gossamer structures as drag sails. However, another functionality of these drag sails is the potential of orbital maneuvers they can induce. This was always disregarded in favor of other faster orbital transfer mechanisms. This research was conducted to demonstrate the usefulness of drag sails not only as complete de-orbiting tools, but also for orbital altitude change maneuvers. Additionally, the establishment of a numerical analysis platform to accurately simulate the space behavior of drag sails. The scope of this research includes:

- Design and development of a system that can achieve an orbital altitude change using a gossamer structure-based drag sail
- Design and development of a system that can observe the said drag sail system
- Demonstration of the said systems on ground to prove their functionality
- Demonstration of said systems in orbit to prove their functionality in space
- Collection and analysis of in-orbit data on:
    - The de-orbiting behavior of a satellite using a drag-sail
    - The deployment behavior of gossamer structures in space

- Establishment of an accurate simulation environment for said deployment behavior
- Fine-tuning the simulation environment using space data to prove its accuracy and use for future mission prediction

With the achievement of above goals, this research aims to shine more light on the little known space behavior of gossamer structures. Regardless of the method of de-orbiting, gossamer structures pay a great role in them, and the sustainable future of space missions depend on finding a successful solution to the space debris issue.

1.7. Overview of this Dissertation

This dissertation consist of five chapters as follows:

In chapter 1, a general introduction for the growing space debris issue and possible solutions for it are given along with a summary of existing missions contributing to these solutions. In addition, the platform of micro-satellite ALE-1 and De-Orbit Mechanism DOM which enable this research are introduced. A clear aim for this research is defined, and an overview of the whole dissertation is given.

In chapter 2, details of a ground simulation environment developed during this research are explained. The numerical model used is explained in detail and a simulation platform for sail deployment is presented, and a model of DOM2500 is implemented within the platform ready to be simulated.

In chapter 3, the module developed for this research, Separable De-Orbit Mechanism (SDOM) is introduced. Starting with an explanation on the design requirements for this module for the success of ALE-1, a clear mission plan for the SDOM is defined. Afterwards, the system design and mechanical design of SDOM and its subsequent mechanisms are explained. The observation sub-systems developed for this research are introduced. A time of flight camera system is used for the observation of the sail, and a serial camera is used for the confirmation of SDOM operational phases. Details of these systems are thoroughly explained. The ground tests and evaluations of each functionality of SDOM are explored. The results of these tests are presented along with discussion at points of failure, and how they were overcome. Additionally, the in orbit results of SDOM mission are discussed. Starting with a brief mission history of ALE-1 and SDOM since their launch up to today, each event that occurred is thoroughly discussed and analyzed. This chapter is concluded with current status of SDOM and ALE-1 and a future projection for the remainder of their mission.

In chapter 4 environment and model parameters are explored while comparing the simulative results to ground experiment results and in-orbit deployment results. Various parameters are finetuned using acquired space data to improve the reliability of the established simulation platform. Finally, this chapter is concluded with a listing of possible future work in conjunction with this research.

Chapter 5 concludes this dissertation with a general summary and discussion on this research, its implications, benefits, and findings.

2. Numerical Analysis Methods for Membrane Deployment Behavior

In this chapter the establishment of the simulation platform used in this research is explored and the mathematical model used for the numerical analysis is explained.

2.1. Review of Nonlinear Finite Element Methods

2.1.1. Finite Element Method

In this section the finite element method for structural analysis based on the finite displacement theory is described.

In finite element method for structural analysis the object of interest is divided into finite elements and the degrees of freedom in each element are interpolated and approximated by nodal degrees of freedom to obtain a finite number of degrees of freedom. Following this, the principle of virtual work is formulated in the weak form of integral form to obtain a finite number of equilibrium equations. In more detail, an elastic body is divided into finite elements and the degrees of freedom of any point P in each element are interpolated and approximated by the degrees of freedom of each node n constituting one element. The virtual displacement of each point P can be interpolated and approximated by the virtual displacements of its constituent nodes and the principle of virtual work is integrated over the entire region of interest to obtain an equation in which the on unknown nodal displacements are the virtual displacements. Using this equation, an equilibrium equation is derived. In order to describe the deformation of an object, it is necessary to express the positions of all arbitrary points in the object before and after deformation in terms of coordination variables.

To achieve this, a three dimensional coordinate system $\sum$ to describe the three dimensional position vector X of any arbitrary point P in the object before deformation, a map φ to describe the correspondence from the three dimensional position vector X of each arbitrary point P before deformation to the three dimensional position vector x after deformation, and an approximation method for describing a continuum with infinite degrees of freedom from the obtained finite degrees of freedom are required. The finite element method is introduced to solve the second and third conditions described. In this analysis, the position vectors of the finite number of points in the object are formulated as unknowns.

2.1.2. Embedded Coordinate System

In the finite element method, an embedded coordinate system is introduced to represent the position of any arbitrary point in an element in three dimensional physical space for various descriptions in the element. A coordinate system Q with base vectors (ξ^1 ,ξ^2 ,ξ^3) is embedded in the object. Let **X**,**x** be the position vectors of an arbitrary point in the object before and after deformation as viewed in the absolute coordinate system R_I. In this case:

$$\xi \equiv \begin{bmatrix} \xi^1 \\ \xi^2 \\ \xi^3 \end{bmatrix} \tag{2.1}$$

That is, **X**,**x** can be regarded as a function of ξ.

An advantage of the embedded coordinate system is that the range of integration after weak formalization can be simplified. In the rectangular region shown in Figure 2.1 the range of integration is complex, but if the embedded coordinate system $G - \xi^1 - \xi^2$ is used, the range of integration can be expressed simpler as shown in Figure 2.1.

$$(\xi^1, \xi^2) | -1 \leq \xi^1 \leq 1,\ -1 \leq \xi^2 \leq 1 \tag{2.2}$$

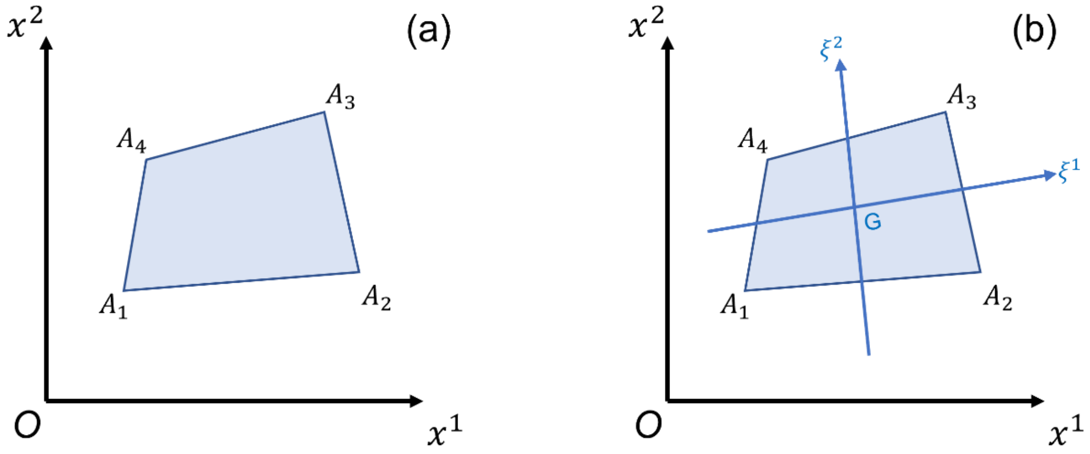

Figure 2.1: (a) Integral domain in the absolute coordinate system and (b) Integral domain in the embedded coordinate system.

In other words the integral domain becomes a square centered at the origin.

2.1.3. Equilibrium Equation

In a micro-parallelepiped with widths dξ^1, dξ^2 and dξ^2 in the respective directions of ξ^1, ξ^2 and ξ^3, the forces acting from a point (ξ_o^1, ξ_o^2, ξ_o^3) within the body can be expressed as in Fig. 2.2. From these, the balance of forces can be expressed by the following equation.

$$\left(\boldsymbol{t}^{\mathrm{i}} + \frac{\partial \boldsymbol{t}^{\mathrm{i}}}{\partial \xi^{\mathrm{i}}} d\xi^{\mathrm{i}}\right) \mathrm{d}s_{\mathrm{i}} - \boldsymbol{t}^{\mathrm{id}} s_{\mathrm{i}} + \phi \boldsymbol{f} dv = \mathbf{0} \tag{2.3}$$

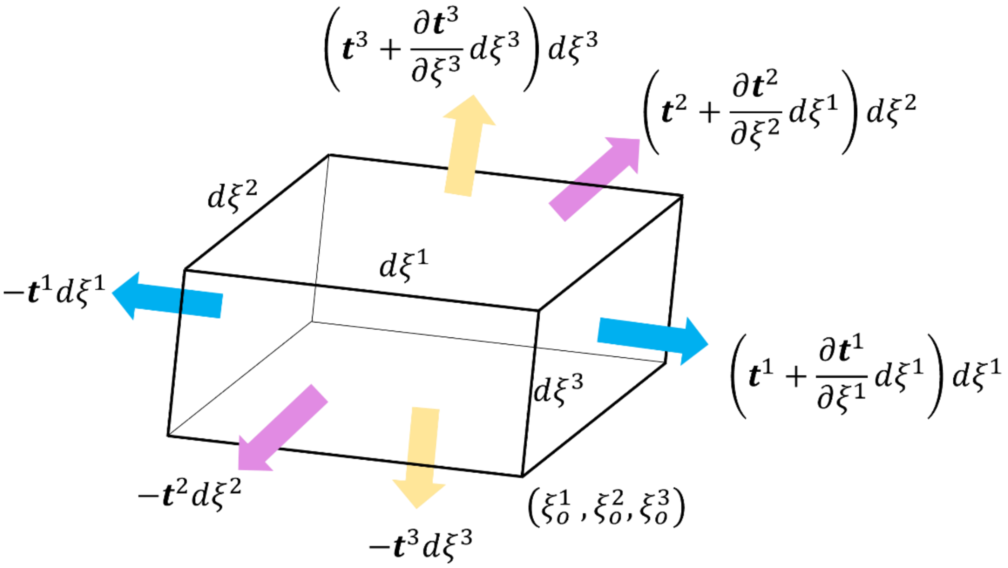

Fig. 2.2: Micro-parallelepiped and the forces acting on it.

The relation between Cauchy stress $\boldsymbol{t}^n$ and the Cauchy stress tensor $\boldsymbol{T}$ is given by the following equation.

$$\boldsymbol{t}^{\mathrm{n}} = \boldsymbol{T}\boldsymbol{n} \tag{2.4}$$

From Eq. 2.4, because the normal vector $\mathbf{n}^i(\xi_o^1, \xi_o^2, \xi_o^3)$ of each surface is independent of (ξ^1, ξ^2, ξ^3) the following Eq. 2.5 can be obtained.

$$\frac{\partial \zeta^2 \boldsymbol{t}^{\mathrm{i}}}{\partial \xi^{\mathrm{i}}} = \frac{\partial \boldsymbol{T}}{\partial \xi^{\mathrm{i}}} \boldsymbol{n}^{\mathrm{i}} \tag{2.5}$$

From this, the force balance equation can be expressed as,

$$\frac{\partial \boldsymbol{T}}{\partial \xi^i} \cdot \boldsymbol{n}^i d\xi^i ds_i + \phi \boldsymbol{f} d\boldsymbol{v} = \mathbf{0} \tag{2.6}$$

Substituting the following Eq. 2.7 into Eq. 2.6,

$$n^{\boldsymbol{i}} \boldsymbol{ds}_{\mathbf{i}} d\boldsymbol{\xi}^{\mathbf{1}} = \boldsymbol{g}^{\boldsymbol{i}} dv \tag{2.7}$$

and from the definition of ∇ as,

$$\nabla \equiv \mathbf{i}^i \frac{\partial}{\partial x^i} \tag{2.8}$$

The final force balance equation can be obtained as the following Eq. 2.9

$$(\nabla \cdot \boldsymbol{T} + \rho \boldsymbol{f}) dv \tag{2.9}$$

Since Cauchy's stress tensor $\boldsymbol{T}$ is a symmetric tensor, the following equilibrium equation can be obtained from the force balance equation.

$$\nabla \cdot \boldsymbol{T} + \rho \boldsymbol{f} = \boldsymbol{0} \tag{2.10}$$

2.1.4. Principle of Virtual Work

The inner product of Eq. 2.10 and the virtual displacement $\delta\mathbf{x}$, represents the virtual work of the deformation of the body, and is expressed as the following Eq. 2.11.

$$\int_{\beta} (\nabla \cdot \boldsymbol{T} + \rho \boldsymbol{f}) \cdot \delta \boldsymbol{x} dv = \boldsymbol{0} \tag{2.11}$$

By applying the second Piola-Kirchhoff stress tensor and the Green-Lagrange strain tensor to this relation, the virtual work principle can be transformed into Equation 2.12.

$$\int_{E_0} S^{ij} \delta E_{ij} dV = \int_{\beta_0} \rho_0 \boldsymbol{f} \cdot \delta \boldsymbol{x} dV + \int_{\partial \upbeta_0^{\sigma}} \boldsymbol{t}^n \cdot \delta \boldsymbol{x} dS \tag{2.12}$$

Here a reference vector $\mathbf{z}$ is defined as,

$$\delta E_{ij} = \frac{\partial E_{ij}}{\partial \boldsymbol{z}} \delta z \tag{2.13}$$

$$\delta x = \frac{\partial x}{\partial z} \delta z \tag{2.14}$$

Substituting Eqs. 2.13 and 2.14 into 2.12 it is obtained that,

$$\left[\int_{E_0} S^{ij} \frac{\partial E_{ij}}{\partial \boldsymbol{z}} dV - \int_{\beta_0} \rho_0 \boldsymbol{f} \frac{\partial \boldsymbol{x}}{\partial \boldsymbol{z}} dV - \int_{\partial \beta_0^{\sigma}} \boldsymbol{t}^n \frac{\partial \boldsymbol{x}}{\partial \boldsymbol{z}} dS\right] \cdot \delta \boldsymbol{z} = \boldsymbol{0} \tag{2.15}$$

Since $\delta\mathbf{z}$ can take any value,

$$\begin{aligned} \boldsymbol{f}_{\boldsymbol{z}} &= \left[\int_{E_0} S^{ij} \frac{\partial E_{ij}}{\partial \boldsymbol{z}} dV - \int_{\beta_0} \rho_0 \boldsymbol{f} \cdot \frac{\partial \boldsymbol{x}}{\partial \boldsymbol{z}} dV - \int_{\partial \beta_0^{\sigma}} \boldsymbol{t}^n \cdot \frac{\partial \boldsymbol{x}}{\partial \boldsymbol{z}} dS \right]^{\boldsymbol{T}} \\ &= \int_{E_0} S^{ij} \left(\frac{\partial E_{ij}}{\partial \boldsymbol{z}}\right)^T dV - \int_{\beta_0} \rho_0 \left(\frac{\partial \boldsymbol{x}}{\partial \boldsymbol{z}}\right)^{\boldsymbol{T}} \cdot \boldsymbol{f} dV - \int_{\partial \beta_0^{\sigma}} \left(\frac{\partial \boldsymbol{x}}{\partial \boldsymbol{z}}\right)^T \cdot \boldsymbol{t}^n dS = \boldsymbol{0} \end{aligned} \tag{2.16}$$

Equation 2.16 is a discretized equilibrium equation and to solve it the Jacobian $\boldsymbol{J}$ differentiated by $\mathbf{z}$ (i.e. the tangential stiffness matrix) needs to be solved, and $\mathbf{z}$ must be updated as follows,

$$\boldsymbol{z} - \boldsymbol{J}^{-1} \boldsymbol{f}_{\boldsymbol{z}} \rightarrow \boldsymbol{z} \tag{2.17}$$

2.1.5. Equivalent Nodal Force

In the presence of strain energy π the equivalent nodal force due to deformation can be expressed as,

$$\int_{E_0} S^{ij} \left(\frac{\partial E_{ij}}{\partial \boldsymbol{z}}\right)^T dV = \left(\frac{\partial \pi}{\partial \boldsymbol{z}}\right)^T \tag{2.18}$$

From this, the equation to be solved by the finite element method becomes,

$$\boldsymbol{f}_{\boldsymbol{z}} = \left(\frac{\partial \pi}{\partial \boldsymbol{z}}\right)^T - \int_{\beta_0} \rho_0 \left(\frac{\partial \boldsymbol{x}}{\partial \boldsymbol{z}}\right)^T \boldsymbol{f} dV - \int_{\partial \beta_0^\sigma} \left(\frac{\partial \boldsymbol{x}}{\partial \boldsymbol{z}}\right)^T \boldsymbol{t}^n dS = \boldsymbol{0} \tag{2.19}$$

2.2. Wrinkle/Slack Theory

This chapter presents the analytical theory that describes the deformation of Gossamer space structures and then explains the wrinkle/slack model that occurs on the membrane surface.

2.2.1. Mathematical Model

Let us consider the membrane surface in the plane stress model. Let the membrane surface under no stress be $\beta^0 \subset \mathbb{R}^3$, and let the current membrane surface be $\beta \subset \mathbb{R}^3$. Let S^0,S be the intermediate surfaces of the membrane surface for each state β^0,β. Let $\mathbf{X} \in S^0$, $\mathbf{x} \in S$ be the position vector in the embedded coordinate system (ξ^1,ξ^2). Here, the covariant basis vector at β^0 is given as

$$\boldsymbol{G}_\alpha := \frac{\partial \boldsymbol{X}}{\partial \xi^\alpha} \tag{2.20}$$

Furthermore, the unit vector $\boldsymbol{G}_3$ along the direction ξ^3 is defined as

$$\boldsymbol{G}_3 := \frac{\boldsymbol{G}_1 \times \boldsymbol{G}_2}{|\boldsymbol{G}_1 \times \boldsymbol{G}_2|} \tag{2.21}$$

The weighted tensor for the covariant component is defined as,

$$G_{\mathrm{ij}} := \boldsymbol{G}_i \cdot \boldsymbol{G}_j \tag{2.22}$$

Then, the weighted tensor for the contravariant component becomes,

$$G^{ij} = \left[G_{ij}\right]^{-1} \tag{2.23}$$

Thus, the contravariant basis vector becomes,

$$\boldsymbol{G}^i = G^{ij} \boldsymbol{G}_j \tag{2.24}$$

Similarly, the covariant vector $\boldsymbol{g}_i$ and the metric tensor G_{ij} for the covariant components are defined as follows,

$$\boldsymbol{g}_\alpha := \frac{\partial \boldsymbol{x}}{\partial \xi^\alpha} \quad \text{where} \quad \alpha = 1,2 \tag{2.25}$$

$$\boldsymbol{g}_3 := \frac{\boldsymbol{g}_1 \times \boldsymbol{g}_2}{|\boldsymbol{g}_1 \times \boldsymbol{g}_2|} \tag{2.26}$$

$$G_{ij} := \boldsymbol{g}_i \cdot \boldsymbol{g}_j \tag{2.27}$$

Following this, the deformation gradient tensor $\boldsymbol{F}$ and the Green-Lagrange strain tensor $\underline{\mathbf{E}}$ are defined as follows,

$$\boldsymbol{F} := \boldsymbol{g_i} \otimes \boldsymbol{G}^{\mathrm{i}} \tag{2.28}$$

$$\underline{\boldsymbol{E}} := \frac{1}{2}(\boldsymbol{F}^T\boldsymbol{F} - \boldsymbol{I}) = E_{\alpha\beta}\boldsymbol{G}^\alpha \otimes \boldsymbol{G}^\beta \tag{2.29}$$

$$\text{where} \quad E_{\alpha\beta} := \frac{1}{2}\left(g_{\alpha\beta} - G_{\alpha\beta}\right)$$

$\boldsymbol{I}$ is the unit vector and the relation between the Green-Lagrange stress tensor $\underline{\boldsymbol{E}}$ and the second Piola-Kirchoff stress tensor $\underline{\boldsymbol{S}}$ is,

$$\underline{\boldsymbol{S}} := \underline{\boldsymbol{CE}} \tag{2.30}$$

Here $\underline{\boldsymbol{C}}$ is the elastic tensor given as,

$$\underline{\boldsymbol{C}} = C^{\alpha\beta\zeta\eta}\boldsymbol{G}_\alpha \otimes \boldsymbol{G}_\beta \otimes \boldsymbol{G}_\zeta \otimes \boldsymbol{G}_\eta \tag{2.31}$$

When a wrinkle/slack occurs at a point within the membrane, the membrane usually deforms in the out-of-plane direction. Conventional planar stress models are based on in-plane strain and cannot account for out-of-plane strain. Therefore, it is necessary to modify the stress field to account for out-of-plane strain. Hereinafter, the variables in this modified stress field will be denoted with a ~.

2.2.2. Wrinkle/Slack Component Coordinate System

Let the unit vector and the modified unit vector in the wrinkle direction be $\boldsymbol{w}, \widetilde{\boldsymbol{w}}$ respectively. Then, $\boldsymbol{w_0}$ is

$$\boldsymbol{w}_o = w_\alpha \boldsymbol{G}^\alpha \tag{2.32}$$

$$\text{where} \quad (w_1, w_2) = (w\cos\theta, w\sin\theta)$$

Here θ is the angle in the wrinkle direction. The vector $\boldsymbol{n}_o$ which is independent of $\boldsymbol{w}_o$ will then become,

$$\boldsymbol{n}_o := n_\alpha \boldsymbol{G}^\alpha \tag{2.33}$$

$$\text{where,} \quad (n_1, n_2) = (-n\sin\theta\,, n\cos\theta)$$

After deformation, $\boldsymbol{w}_o$ is assumed to be $\boldsymbol{w}$ and the following equation holds.

$$\boldsymbol{w}_o = \boldsymbol{F}^T\boldsymbol{w} = \widetilde{\boldsymbol{F}}^T\widetilde{\boldsymbol{w}} \tag{2.34}$$

Similarly, the following relation will hold for $\boldsymbol{n}$ and $\widetilde{\boldsymbol{n}}$.

$$\boldsymbol{n}_o = \boldsymbol{F}^T\boldsymbol{n} = \widetilde{\boldsymbol{F}}^T\widetilde{\boldsymbol{n}} \tag{2.35}$$

Next, the stress-free state($\boldsymbol{w}_o$,$\boldsymbol{n}_o$), and the current state($\boldsymbol{w}$,$\boldsymbol{n}$) are derived in the wrinkle/slack component coordinate system. The stress component vector $\boldsymbol{S}$, the strain component vector $\boldsymbol{E}$, and the elasticity matrix $\boldsymbol{C}$ are represented in the vector representation as follows,

$$S := \begin{bmatrix} S^{11} \\ S^{22} \\ S^{12} \end{bmatrix}, E := \begin{bmatrix} E^{11} \\ E^{22} \\ 2E^{12} \end{bmatrix}, C := \begin{bmatrix} C^{1111} & C^{1122} & C^{1112} \\ C^{2211} & C^{2222} & C^{2212} \\ C^{1211} & C^{1222} & C^{1212} \end{bmatrix} \tag{2.36}$$

Here the following constitutive relation holds.

$$\boldsymbol{S} = \boldsymbol{CE} \tag{2.37}$$

If the the stress vector σ and the strain vector ϵ in the absolute coordinate system are $\sigma = (\sigma^{11}, \sigma^{22}, \sigma^{12})^T$ and $\epsilon = (\epsilon^{11}, \epsilon^{22}, \epsilon^{12})^T$, the stress and strain vectors modified to the wrinkle component coordinate system become,

$$\sigma = \boldsymbol{R}_\sigma^T\boldsymbol{S}, \quad \tilde{\sigma} = \boldsymbol{R}_\sigma^T\tilde{\boldsymbol{S}}, \quad \epsilon = \boldsymbol{R}_\epsilon^T\boldsymbol{E}, \quad \tilde{\epsilon} = \boldsymbol{R}_\epsilon^T\widetilde{\boldsymbol{E}} \tag{2.38}$$

$\boldsymbol{R}_\sigma(\theta)$, $\boldsymbol{R}_\epsilon(\theta)$ are transformation matrices given below,

$$\boldsymbol{R}_\sigma(\theta) = [\boldsymbol{U}^1\ \boldsymbol{U}^2\ \boldsymbol{U}^3] := \begin{bmatrix} cos^2\theta & sin^2\theta & -\sin\theta\cos\theta \\ sin^2\theta & cos^2\theta & \sin\theta\cos\theta \\ 2\sin\theta\cos\theta & -2\sin\theta\cos\theta & cos^2\theta - sin^2\theta \end{bmatrix} \tag{2.39}$$

$$\boldsymbol{R}_\epsilon(\theta) = [\boldsymbol{U}_1\ \boldsymbol{U}_2\ \boldsymbol{U}_3] := \begin{bmatrix} cos^2\theta & sin^2\theta & -2\sin\theta\cos\theta \\ sin^2\theta & cos^2\theta & 2\sin\theta\cos\theta \\ \sin\theta\cos\theta & -\sin\theta\cos\theta & cos^2\theta - sin^2\theta \end{bmatrix} \tag{2.40}$$

$\boldsymbol{U}^i$ and $\boldsymbol{U}_i$ are conjugate and

$$\boldsymbol{U}_i \cdot \boldsymbol{U}^j = \delta_i^j \tag{2.41}$$

$$\boldsymbol{U_i} \times \boldsymbol{U_j} = \boldsymbol{U^k}, \qquad \boldsymbol{U^i} \times \boldsymbol{U^j} = \boldsymbol{U_k}$$

where, $(i,j,k) = (1,2,3),(2,3,1),(3,1,2)$

Under uniaxial stress conditions, the following relation holds with the modified second Piola-Kirchiff stress as $\underset{\sim}{\tilde{S}}$,

$$\boldsymbol{w_o} \cdot \underset{\sim}{\tilde{\boldsymbol{S}}}\boldsymbol{w_o} = \boldsymbol{0}, \ \boldsymbol{n_0} \cdot \underset{\sim}{\tilde{\boldsymbol{S}}}\boldsymbol{w_o} = \boldsymbol{0} \tag{2.42}$$

From this, the following equation will also hold,

$$\tilde{\sigma}^{11} = \boldsymbol{U}^1 \cdot \tilde{\boldsymbol{S}} = 0, \ \tilde{\sigma}^{12} = \boldsymbol{U}^3 \cdot \tilde{\boldsymbol{S}} = 0 \tag{2.43}$$

Hence, it can be concluded that the normal and shear stresses in the direction of the generated wrinkle are zero.

2.2.3. Conventional Wrinkle/Slack Theory

In previous research, there have been many proposed analytical models for membrane wrinkling most of which are based on tension field theory.[67] In this theory, the in-plane bending stiffness is assumed to be zero, and when a compressive stress acts in-plane, it is completely released through out-of-plane wrinkling. In this case, the stress field of the membrane can form a uniaxial tensile stress field where the principal stress in one direction is positive and the other direction is zero. When considering isotropic elastic membranes, the out-of-plane deformation caused by wrinkling can be modeled by replacing it with in-plane contraction (Fig. 2.3). Assuming the in-plane contraction occurs in a direction perpendicular to the tension field, the deformation will not generate energy. If modeled in this way, the wrinkling phenomenon of membrane can be simplified to a planar problem without buckling analysis.

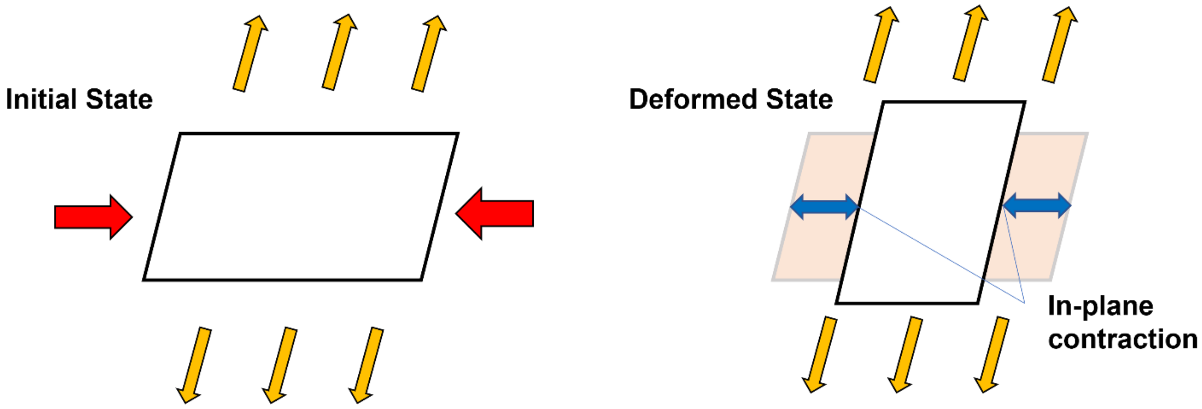

Fig. 2.3: Representation of out-of-plane deformation in tension field theory.

Stein and Hedgepath, proposed to calculate the stress field and the wrinkled region with a variable Poisson’s ratio so the minor principle stress term vanishes.[68] Ding and Yang implemented this theory into the finite element method.[69]

Pipkin took a step further to model the wrinkling of membrane structures as an energy minimization problem for an elastic body that has zero bending stiffness.[70] When modeled with a relaxed energy density proposed by himself, assuming the quasiconvexity of the strain energy function, instead of a strain energy density. By doing so, compressive stresses do not appear in the solution. Roddeman *et al.* [71] introduced a model which considers the virtual stretching of a membrane in the conventional plane stress model until the magnitude of the minor principal stress becomes zero. This virtual stretching is assumed to be the actual deformation and the direction of extension is assumed to coincide with the direction of zero principal stress. As such, the deformation gradient tensor can be modified as follows,

$$\widetilde{\boldsymbol{F}} = (\boldsymbol{I} + \beta \boldsymbol{w} \otimes \boldsymbol{w})\boldsymbol{F} \tag{2.44}$$

Where β is virtual elongation. Following this, the stress-strain vector is modified as below,

$$\widetilde{\boldsymbol{E}} = \boldsymbol{E} + \mu \boldsymbol{U}^{\boldsymbol{1}}, \tag{2.45}$$

$$\tilde{\boldsymbol{S}} = \boldsymbol{C}\boldsymbol{E} \tag{2.46}$$

where, $\mu = \beta(2 + \beta)\omega^2/2$ indicates the amount of wrinkles.

Substituting this relation into Eq. 2.43 will yield,

$$\mu = -\frac{\boldsymbol{U}^1 \cdot \boldsymbol{S}}{\boldsymbol{U}^1 \cdot \boldsymbol{C}\boldsymbol{U}^1} \tag{2.47}$$

$$(\boldsymbol{U}^1 \cdot \boldsymbol{C}\boldsymbol{U}^1)(\boldsymbol{U}^3 \cdot \boldsymbol{S}) - (\boldsymbol{U}^1 \cdot \boldsymbol{C}\boldsymbol{U}^3)(\boldsymbol{U}^1 \cdot \boldsymbol{S}) = 0 \tag{2.48}$$

From Eq. 2.48, the angle θ in the wrinkle direction can be obtained. Furthermore, by simplifying the wrinkle condition equation, the strain energy density π can be modified as follows,

$$\tilde{\pi} = \frac{1}{2}\widetilde{\boldsymbol{E}} \cdot \boldsymbol{C}\widetilde{\boldsymbol{E}} = \frac{1}{2}\boldsymbol{E} \cdot \widetilde{\boldsymbol{C}}\boldsymbol{E} \tag{2.49}$$

$$\text{where,} \quad \widetilde{\boldsymbol{C}} = \boldsymbol{B}^T\boldsymbol{C}\boldsymbol{B} = \boldsymbol{C} - \frac{1}{\boldsymbol{U}^1 \cdot \boldsymbol{C}\widetilde{\boldsymbol{U}}}(\boldsymbol{C}\boldsymbol{U}^1) \otimes (\boldsymbol{C}\boldsymbol{U}^1) \tag{2.50}$$

By doing so, Roddeman *et al*, proposed a modification from the plane stress model to the wrinkle model.

Building on the relaxed energy function model, Epstein and Fornicito extended it to anisotropic membrane through saturated elasticity.[72] In general deformation after wrinkling satisfies the following conditions,

$$f := S^{11}S^{22} - S^{12}S^{21} = 0 \tag{2.51}$$

This relation is interpreted as the saturation condition and a differential equation for the deformation after wrinkling is derived from the first-order partial differential equation as follows,

$$\frac{dE_{ij}}{ds} = \frac{\partial f}{\partial S^{ij}}, \ \frac{dS^{ij}}{ds} = 0 \quad \text{where,} \quad \forall i, j \tag{2.52}$$

Here, s is the arc length after wrinkling. Solving this differential equation yields the following,

$$\boldsymbol{E} = \widetilde{\boldsymbol{E}} + s\boldsymbol{J}\widetilde{\boldsymbol{S}} \quad \text{where} \quad \boldsymbol{J} = \begin{bmatrix} 0 & 1 & 0 \\ 1 & 0 & 0 \\ 0 & 0 & -2 \end{bmatrix} \tag{2.53}$$

Furthermore, under uniaxial stress the modified stress can be given as,

$$\widetilde{\boldsymbol{S}} = \lambda \boldsymbol{U}_2 \tag{2.54}$$

Substituting Eq. 2.54 and $\boldsymbol{JU_2} = \boldsymbol{U^1}$ into Eq. 2.53 yields,

$$\boldsymbol{E} = \widetilde{\boldsymbol{E}} + \lambda s \boldsymbol{U^1} \tag{2.55}$$

Under the condition $\mu = -\lambda s$ the Roddeman model and the Epstein model can be regarded as equivalent.

Kang and Im proposed a model that modifies the conventional uniaxial tensile model by modifying the normal and shear strain in the direction of the wrinkle generation so that the normal and shear stresses in the same direction disappear.[73] The modified constitutive relation in the wrinkle component coordinate system is as follows,

$$\tilde{\epsilon} = \Lambda \tilde{\delta} \quad \text{where} \quad \Lambda = \boldsymbol{R}_{\epsilon}^{T} \boldsymbol{D} \boldsymbol{R}_{\epsilon} \tag{2.56}$$

In order to eliminate the stress elements $\tilde{\delta}^{11}$ and $\tilde{\delta}^{12}$, the strain elements $\tilde{\epsilon}^{11}$ and $\epsilon\delta^{12}$ are modified and the wrinkles are calculated.

$$\tilde{\epsilon} = \begin{bmatrix} \tilde{\epsilon}_{11} \\ \epsilon_{22} \\ 2\epsilon_{12} \end{bmatrix}, \quad \tilde{\sigma} = \begin{bmatrix} 0 \\ \tilde{\sigma}_{22} \\ 0 \end{bmatrix} \tag{2.57}$$

Substituting the Eq 2.57 into the Eq. 2.56, the following is obtained,

$$\tilde{\sigma}^{22} = \frac{\epsilon_{22}}{\boldsymbol{i}_2 \cdot \Lambda \boldsymbol{i}_2} = \frac{\epsilon_{22}}{\boldsymbol{U}_2 \cdot \boldsymbol{D} \boldsymbol{U}_2} \quad \text{where} \quad \boldsymbol{i}_2 = (0,\ 1,\ 0)^T \tag{2.58}$$

Here, the modified strain energy density becomes,

$$\tilde{\pi} = \frac{1}{2}\tilde{\sigma} \cdot \tilde{\epsilon} = \frac{1}{2}\tilde{\sigma}^{22}\epsilon_{22} \tag{2.59}$$

From Eq. 2.58, the modified elasticity matrix can also be obtained.

$$\widetilde{\boldsymbol{C}} = \frac{1}{\boldsymbol{U}_2 \cdot \boldsymbol{D} \boldsymbol{U}_2} \boldsymbol{U}_2 \otimes \boldsymbol{U}_2 \tag{2.60}$$

The wrinkle models proposed so far are characterized by the elimination of stress in the direction of wrinkling. Iwasa et al, [74] pointed out that a small amount of compressive stress exists in the wrinkle region by comparing the membrane model with the shell model. From this they concluded that the conventional tension field theory is only applicable to very thin membranes, and a small compressive stiffness should be taken into consideration. If a wrinkle occurs in a certain direction, the buckling load in the direction normal to the wrinkle increases due to the curvature caused by the out-of-plane deformation of the membrane. This results in a very small compressive stiffness in the direction normal to the wrinkle. Miyazaki proposed a membrane model that takes this into account and includes the compressive stiffness of the membrane to describe the deformation through the wrinkling.[75] In his model, the stress along the wrinkle is not zero, but very small.

2.2.4. Virtual Deformation Model

The virtual deformation model (VDM) is a model proposed by Roddeman that considers virtual shear deformation in addition to virtual elongation. The modified deformation gradient tensor is as follows

$$\widetilde{\boldsymbol{F}} \equiv \boldsymbol{F}_w \boldsymbol{F} \quad \text{where} \quad \boldsymbol{F}_w = \boldsymbol{I} + \beta_1 \boldsymbol{w} \otimes \boldsymbol{w} + \beta_2 \boldsymbol{n} \otimes \boldsymbol{w} \tag{2.61}$$

β_2 represents the virtual shear deformation. In this case, the modified strain vector is as follows

$$\widetilde{\boldsymbol{E}} = \boldsymbol{E} + \mu_1 \boldsymbol{U}^{\boldsymbol{1}} + \mu_{\boldsymbol{3}} \boldsymbol{U}^{\boldsymbol{3}} \tag{2.62}$$

Under uniaxial tensile conditions, the modified elasticity matrix is as follows

$$\widetilde{\boldsymbol{C}} = \boldsymbol{B}^T \boldsymbol{C} \boldsymbol{B} = \frac{\boldsymbol{1}}{\boldsymbol{U}_{\boldsymbol{2}} \cdot \boldsymbol{D} \boldsymbol{U}_{\boldsymbol{2}}} \boldsymbol{U}_{\boldsymbol{2}} \otimes \boldsymbol{U}_{\boldsymbol{2}} \quad \text{where} \quad \boldsymbol{D} = \boldsymbol{C}^{-1} \tag{2.63}$$

This result is consistent with the Kang model. Therefore, the Kang model is equivalent to the VDM except for the wrinkle angle θ. Furthermore, the VDM has the advantage of being able to determine the wrinkle angle under any conditions. In determining the wrinkle angle, the modified strain energy density $\tilde{\pi} = E - C\tilde{E}/2$ is minimized. Here, the condition for minimizing $\tilde{\pi}$ is that

$$(\boldsymbol{U_2} \cdot \boldsymbol{DU_2})(\boldsymbol{U_3} \cdot \boldsymbol{E}) - (\boldsymbol{U_3} \cdot \boldsymbol{DU_2})(\boldsymbol{U_2} \cdot \boldsymbol{E}) = 0 \tag{2.64}$$

From the above equation, $\mathbf{U}_3 = -\partial \mathbf{U}_2/\partial\theta$ is derived, which can be transformed into the following equation using the covariant and contravariant vector properties.

$$\boldsymbol{E} \cdot [\boldsymbol{U}^1 \times (\boldsymbol{D}\boldsymbol{U}_2)] = 0 \tag{2.65}$$

The above equation is consistent with Roddeman's model. Thus, the models proposed by Roddeman, Kang, and Epstein are equivalent under minimum energy conditions. Furthermore, the VDM can be used at non-minimum energy, allowing the wrinkle angle to be defined arbitrarily.

2.2.5. Conversion to Cartesian Coordinate System

Although the derivation has been performed in the embedded coordinate system, in general, the constitutive side is derived in the absolute coordinate system. Therefore, it is necessary to rewrite the constitutive side using the basis vectors $\boldsymbol{N}_i$ and $\boldsymbol{N}^i$ in absolute coordinates. For the stress element $S_o^{\alpha\beta}$ in the embedded coordinate system,

$$S^{\alpha\beta}\boldsymbol{G}_\alpha \otimes \boldsymbol{G}_\beta = S_0^{\xi\eta}\boldsymbol{N}_\xi \otimes \boldsymbol{N}_\eta \tag{2.66}$$

A vector can also be expressed as follows.

$$\boldsymbol{S} = \boldsymbol{P^T S_o} \tag{2.67}$$

where $\boldsymbol{S}_o$ is the stress vector in the embedded coordinate system and $\boldsymbol{P}$ is the following transformation matrix,

$$P = \begin{bmatrix} (T_1^1)^2 & (T_1^2)^2 & T_1^1 T_1^2 \\ (T_2^1)^2 & (T_2^1)^2 & T_2^1 T_2^2 \\ 2T_1^1 T_2^1 & 2T_1^2 T_2^2 & T_1^1 T_2^2 + T_2^1 T_1^2 \end{bmatrix} \qquad \text{where} \qquad T_\alpha^\xi := \boldsymbol{G}^\xi \cdot \boldsymbol{N}_\alpha \tag{2.68}$$

Similarly, the transformation for $\boldsymbol{E}$, $\boldsymbol{C}$, and $\boldsymbol{D}$ yields,

$$\boldsymbol{E} = \boldsymbol{P}^{-1}\boldsymbol{E}_o, \quad \boldsymbol{C} = \boldsymbol{P}^T\boldsymbol{C}_o\boldsymbol{P}, \quad \boldsymbol{D} = \boldsymbol{P}^{-1}\boldsymbol{D}_o\boldsymbol{P}^{-T} \tag{2.69}$$

For the wrinkle direction **w**,

$$\boldsymbol{w} = w_\alpha \boldsymbol{G}^\alpha = q_\xi \boldsymbol{N}^\xi \qquad \text{where} \qquad q_\alpha = T_\alpha^\xi w_\xi \tag{2.70}$$

At ($\cos\theta_o$,$\sin\theta_o$), when transformed as (q_1,q_2), $\boldsymbol{U}^i$,$\boldsymbol{U}_i$ is transformed as follows,

$$\boldsymbol{U}_o^i = \boldsymbol{P}\boldsymbol{U}^i, \ \ \boldsymbol{U}_{oi} = \boldsymbol{P}^{-T}\boldsymbol{U}_i \tag{2.71}$$

2.2.6. Application to Isotropic Membranes

For an isotropic film, the elasticity matrix and compliance matrix in absolute coordinates can be expressed as follows,

$$\boldsymbol{C}_o = \tfrac{E}{1-\nu^2}\begin{bmatrix} 1 & \nu & 0 \\ \nu & 1 & 0 \\ 0 & 0 & \tfrac{(1-\nu)}{2} \end{bmatrix}, \ \boldsymbol{D}_o = \tfrac{1}{E}\begin{bmatrix} 1 & -\nu & 0 \\ -\nu & 1 & 0 \\ 0 & 0 & 2(1+\nu) \end{bmatrix} \tag{2.72}$$

where E is Young's modulus and ν is Poisson's ratio. From Eqs. 2.69, 2.71, and 2.72, the following equations can be derived for any wrinkle angle.

$$\boldsymbol{U}^3 \cdot \boldsymbol{C}\boldsymbol{U}^1 = 0, \qquad \boldsymbol{U}^3 \cdot \boldsymbol{C}\boldsymbol{U}^2 = 0, \ \ \boldsymbol{U}_3 \cdot \boldsymbol{C}\boldsymbol{U}_1 = 0, \ \ \boldsymbol{U}_3 \cdot \boldsymbol{C}\boldsymbol{U}_2 = 0,$$

$$\boldsymbol{U}^1 \cdot \boldsymbol{C}\boldsymbol{U}^1 = \boldsymbol{U}^2 \cdot \boldsymbol{C}\boldsymbol{U}^2 = \frac{E}{1-\nu^2}, \qquad \boldsymbol{U}_1 \cdot \boldsymbol{C}\boldsymbol{U}_1 = \boldsymbol{U}_2 \cdot \boldsymbol{C}\boldsymbol{U}_2 = \frac{1}{E},$$

$$(\boldsymbol{C}_o\boldsymbol{U}_o^1) \times \boldsymbol{U}_{o2} = \tfrac{E}{1-\nu^2}\boldsymbol{U}_o^3, \ \ \boldsymbol{U}_1 \times (\boldsymbol{D}_o\boldsymbol{U}_{o2}) = \tfrac{1}{E}\boldsymbol{U}_{o3} \tag{2.73}$$

The wrinkle direction coincides with the principal stress or strain direction. If the principal stress direction is θ_p, the following relationship holds since $\theta_o = \theta_p$.

$$\tfrac{S_o^{22}-S_o^{11}}{2}\sin 2\theta_p + S_o^{12}\cos 2\theta_p = 0,$$

$$\tfrac{E_o^{22}-E_o^{11}}{2}\sin 2\theta_p + E_o^{12}\cos 2\theta_p = 0, \tag{2.74}$$

From Eqs. 2.73 and 2.74, the modified elasticity matrix $\widetilde{\boldsymbol{C}}_0$ is,

$$\widetilde{\boldsymbol{C}}_0 = \tfrac{E}{4}\begin{bmatrix} 4s^2 & 0 & -2sc \\ 0 & 4c^2 & -2sc \\ -2sc & -2sc & 1 \end{bmatrix} \ \ \text{where} \ \ c = \cos\theta_p, \ s = \sin\theta_p \tag{2.75}$$

2.2.7. Summary of Wrinkle Theory

From the above discussion, it is clear that the wrinkle model has various properties and physical interpretations. In short, by applying the wrinkle model, the modified stress, modified strain, and modified strain energy density can be expressed as follows.

$$\widetilde{\boldsymbol{E}} = \frac{\boldsymbol{U}_2 \cdot \boldsymbol{E}}{\boldsymbol{U}_2 \cdot \boldsymbol{C}\boldsymbol{U}_2} \boldsymbol{D}\boldsymbol{U}_2 \tag{2.76}$$

$$\tilde{\boldsymbol{S}} = \frac{\boldsymbol{U}_2 \cdot \boldsymbol{E}}{\boldsymbol{U}_2 \cdot \boldsymbol{C}\boldsymbol{U}_2} \boldsymbol{U}_2 \tag{2.77}$$

$$\widetilde{\boldsymbol{C}} = \frac{1}{\boldsymbol{U}_2 \cdot \boldsymbol{C}\boldsymbol{U}_2} \boldsymbol{U}_2 \otimes \boldsymbol{U}_2 \tag{2.78}$$

$$\tilde{\pi} = \frac{(\boldsymbol{U}_2 \cdot \boldsymbol{E})^2}{2\boldsymbol{U}_2 \cdot \boldsymbol{D}\boldsymbol{U}_2} \tag{2.79}$$

where $\boldsymbol{U}_2$ is the uniaxial stress direction in the modified stress field. The wrinkle angle can be derived from the following two equations.

$$\boldsymbol{E} \cdot [\boldsymbol{U}^{\boldsymbol{1}} \times (\boldsymbol{D}\boldsymbol{U}_2)] = \boldsymbol{0}$$

$$\boldsymbol{S} \cdot [(\boldsymbol{C}\boldsymbol{U}^{\boldsymbol{1}}) \times \boldsymbol{U}_{\boldsymbol{2}}] = \boldsymbol{0} \tag{2.80}$$

2.2.8. Criteria for Wrinkles

Kang and Im et al. established three criteria for wrinkling in terms of stress, strain, and stress-strain.[76] First, the criteria in the stress-strain criterion are shown below.

(a) $\tau^1 \geq 0$, taut

(b) $\gamma_2 \leq 0$, slack

(c) Otherwise, wrinkled

τ^1 and γ_2 are the minimum principal stress and maximum principal strain, respectively. Lu et al. also expressed this criterion more succinctly.[77]

$$(a) \quad \begin{cases} S^{11}G_{11} + S^{22}G_{22} + 2S^{12}G_{12} \geq 0 \\ \qquad S^{11}S^{22} - S^{12}S^{12} \geq 0 \end{cases} \qquad \text{taut}$$

$$(b) \quad \begin{cases} E_{11}G^{11} + E_{22}G^{22} + 2E_{12}G^{12} < 0 \\ \qquad E_{11}E_{22} - E_{12}E_{12} \geq 0 \end{cases} \qquad \text{slack}$$

(c) Otherwise wrinkled

In general, wrinkles are assumed to occur when an in-plane compressive load is applied to a membrane in a taut, wrinkle-free state. In addition, a film surface is considered to be slack when a compressive load is applied in the other direction (Figure 2.4). By this definition, it is very rare for a stretched thin film to momentarily slack. Therefore, the stress field changes gradually from a taut state to a wrinkled state and then to a slack state. In order to describe the process of such a change in the stress field, the wrinkle criterion should be described by the modified principal stress. When the modified principal stress is $\tilde{\tau}^2$, the wrinkle criterion is expressed as follows.

(a) $\tau^1 \geq 0$ taut

(b) $\tau^1 < 0 \rightarrow \begin{cases}(b-1)\tilde{\tau}^2 > 0 \\ (b-1)\tilde{\tau}^2 \leq 0\end{cases}$ wrinkled, slack

The criterion based on modified stress is superior in that it can be applied to membrane models with small compressive stiffness.

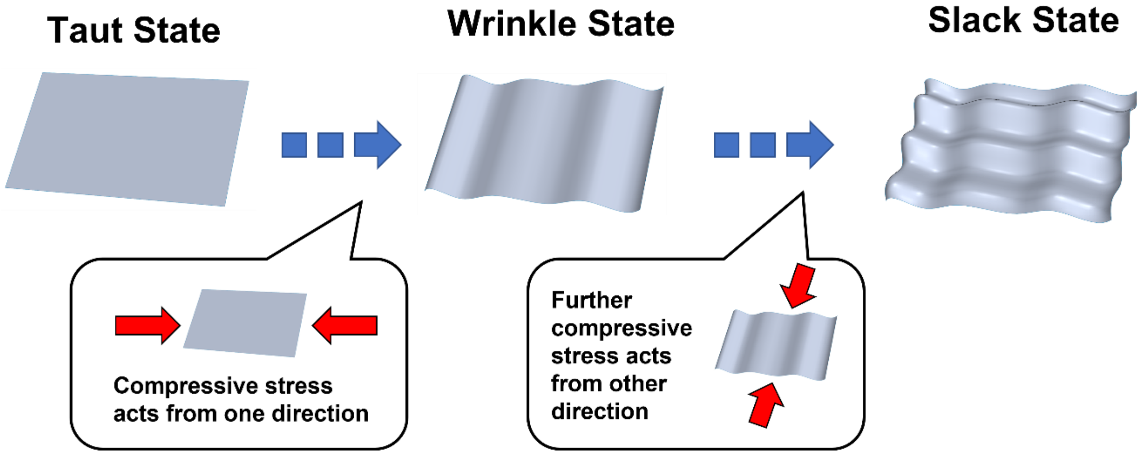

Fig 2.4: State Transitions in Membranes.

2.2.9. Stiffness Reduction Model

Miyazaki proposed a stiffness reduction model (SRM) for isotropic thin films [78]. The minor principal strain γ_1 and the major principal stress τ_2 can be derived from the following eigenvalue problem.

$$\underline{\boldsymbol{E}}\boldsymbol{t} = \gamma \boldsymbol{t} \tag{2.81}$$

The eigenvalue ***t*** can be expressed by a covariant basis vector as,

$$\boldsymbol{t} = t^{\xi}\boldsymbol{G}_{\xi} \tag{2.82}$$

At this point, rewriting the eigenvalue problem in terms of the strain tensor and the weighing tensor, we obtain,

$$[G^{\xi\alpha}E_{\alpha\beta}][t^{\beta}] = \gamma[t^{\xi}] \tag{2.83}$$

The principal strains obtained from the above equations are obtained as eigenvalues, as follows,

$$\gamma_1 = \frac{A-B}{2}, \gamma_2 = \frac{A+B}{2} \tag{2.84}$$

where, $$\begin{gathered} A = E_{11}G^{11} + E_{22}G^{22} + 2E_{12}G^{12}, \;\; B = \sqrt{A^2 - 4DH} \\ D = E_{11}E_{22} - E_{12}E_{12}, \;\;\; H = G^{11}G^{22} - G^{12}G^{12} \end{gathered} \tag{2.85}$$

The principal stresses can also be derived as follows,

$$\tau^1 = \frac{P-Q}{2}, \;\; \tau^2 = \frac{P+Q}{2} \tag{2.86}$$

where,

$$\begin{gathered} P = S^{11}G_{11} + S^{22}G_{22} + 2S^{12}G_{12}, \;\; Q = \sqrt{P^2 - 4SG} \\ S = S^{11}S^{22} - S^{12}S^{12}, \;\;\; G = G_{11}G_{22} - G_{12}G_{12} \end{gathered} \qquad 2.87)$$

In general, the principal stress direction and the principal strain direction coincide in an isotropic film. Therefore, the following equation holds for τ^{α} and γ_{β} using the elastic matrix Γ.

$$\tau = \Gamma\gamma \;\text{ where, }\; \tau = \begin{bmatrix} \tau^1 \\ \tau^2 \end{bmatrix} \;\;\; \gamma = \begin{bmatrix} \gamma^1 \\ \gamma^2 \end{bmatrix} \tag{2.88}$$

$$\Gamma = \frac{E}{1-\nu^2}\begin{bmatrix} 1 & \nu \\ \nu & 1 \end{bmatrix} \tag{2.89}$$

If the thin film is taut at a certain point on the absolute coordinate system, the elastic matrix coincides with Γ. Let $\tilde{\Gamma_t}$ be Γ at this point. Next, when wrinkles occur in an isotropic film, the following two conditions are imposed.

*C*1 : When wrinkles occur in the direction of negative principal stress in the absolute coordinate system: Young's modulus and Poisson's ratio are not considered

*C*2 : When wrinkles occur: Young's modulus and Poisson's ratio are taken to be very small values ε

Based on these conditions, the elasticity matrix can be written as follows.

$$\widetilde{\boldsymbol{\Gamma}_w} = \frac{E}{1-\varepsilon_1\nu^2}\begin{bmatrix} \varepsilon_1 & \varepsilon_1\nu \\ \varepsilon_1\nu & 1 \end{bmatrix} \tag{2.90}$$

When slack occurs in the membrane, the following conditions exist.

*C*3 : When slack occurs, in the absolute coordinate system: Young's modulus and Poisson's ratio in the direction of major principal strain are not considered or a very small value of ε_2 is considered

Similar to the wrinkle condition, the elastic matrix is as follows

$$\widetilde{\boldsymbol{\Gamma}_s} = \frac{E}{1-\varepsilon_1\varepsilon_2\nu^2}\begin{bmatrix} \varepsilon_1 & \varepsilon_1\varepsilon_2\nu \\ \varepsilon_1\varepsilon_2\nu & \varepsilon_2 \end{bmatrix} \tag{2.91}$$

The values of ε_1 and ε_2 are the same when the taut membrane relaxes instantaneously, but they are different when the wrinkled membrane relaxes. In addition, the wrinkled membrane has some compressive stiffness in the direction of the maximum principal stress. From the above, it is necessary to modify the elastic matrix and principal stresses of the membrane according to the wrinkling and slackening of the membrane. The modified elastic matrix $\widetilde{\boldsymbol{\Gamma}}$ and the modified principal stress $\tilde{\tau}$ are defined as follows

$$\tilde{\tau} = \widetilde{\boldsymbol{\Gamma}}\gamma,\ \ \tilde{\tau} = \begin{bmatrix} \tilde{\tau}^1 \\ \tilde{\tau}^2 \end{bmatrix} \tag{2.92}$$

From Equations 2.89 to 2.91, the elasticity matrix $\widetilde{\boldsymbol{\Gamma}}$ can be summarized as follows,

$$\widetilde{\boldsymbol{\Gamma}} = \frac{E}{1-a_1a_2\nu^2}\begin{bmatrix} a_1 & a_1a_2\nu \\ a_1a_2\nu & a_2 \end{bmatrix} \tag{2.93}$$

Here, a_1 and a_2 are parameters that represent the wrinkle and slack states.

(a) Taut : $(a_1, a_2) = (1, 1)$

(b) Wrinkle: $(a_1, a_2) = (\varepsilon_1, 1)$

(c) Slack : $(a_1, a_2) = (\varepsilon_1, \varepsilon_2)$

Parameters f_1 and f_2 are defined as follows,

$$f_1 := \gamma_1 + \nu\gamma_2$$

$$f_2 := \gamma_2 + \varepsilon_1\nu\gamma_1 \tag{2.94}$$

When these parameters are introduced, the wrinkle criterion can be expressed as follows,

(a) $f_1 \geq 0$ Taut state $(a_1,a_2) = (1,1)$

(b) $f_1 < 0, f_2 > 0$ Wrinkle state $(a_1,a_2) = (\varepsilon_1,1)$

(c) $f_2 \leq 0$ Slack state $(a_1,a_2) = (\varepsilon_1,\varepsilon_2)$

This expression is advantageous in finite element analysis because it allows us to derive and determine the deformations γ_1 and γ_2 from the nodal positions of the elements. Furthermore, the modified strain energy $\widetilde{\Pi}$ is given by,

$$\tilde{\Pi} = \int_{\beta^0} \tilde{\pi}\, d\Omega = \int_{\beta^0} \frac{1}{2}\gamma \cdot \tilde{\tau}\, d\Omega = \int_{\beta^0} \frac{1}{2}\gamma \cdot \tilde{\boldsymbol{\Gamma}}\, d\Omega \qquad (2.95)$$

dΩ represents the microvolume on β^0. The equivalent nodal force of the membrane can be derived from a variant of $\tilde{\Pi}$ from which the tangential stiffness matrix can be derived. Conversely, for models other than SRM, if the membrane is determined to be completely slackened during the iterative calculation process, such as the Newton method, the calculation becomes invalid.

Additionally, for a very thin membrane the introduced small compression stiffness allows for the alleviation of spring back modeling between folded elements. Folded membrane has an equilibrium state with least energy at a semi-folded state due to plastic deformation at the fold lines. Figure 2.5 represents this state. When folded down further, the membrane will exert expanding force, and when pulled outwards for a flatter configuration, the membrane will exert a contracting force. In order to model this, a rotational spring back force can be utilized between each fold. However, this will ultimately increase the computational cost with the addition of spring elements. For a very thin membrane, this effect can be replicated with the inclusion of a small compressive stiffness and therefore through the adjustment of the compression stiffness ratio.

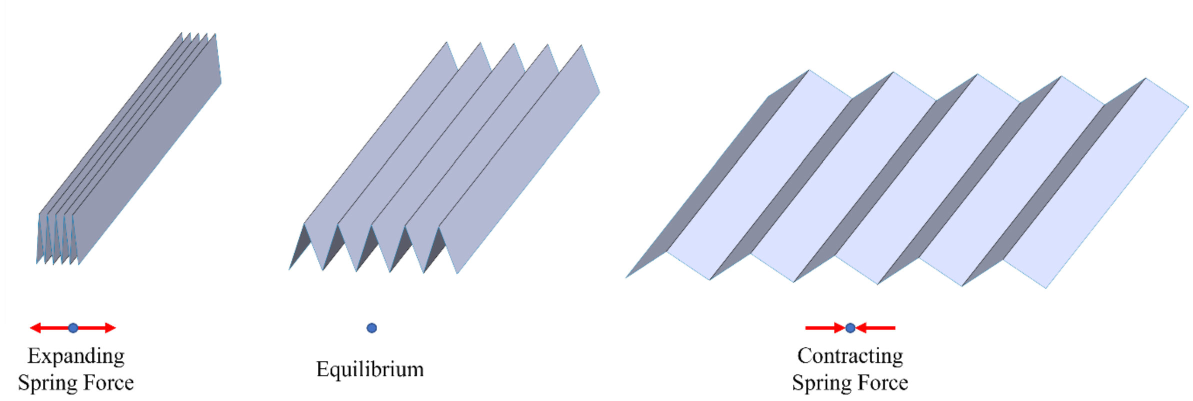

Figure 2.5: Representation of the contracted, expanded and the equilibrium states for the folded membrane.

2.3. Application to Nonlinear Finite Elements

Numerical analysis of membranes with wrinkles has low convergence because the equations of motion are nonlinear, and the stiffness locally varies between large values and zero during the iterative calculation process. Therefore, they are prone to numerical instability. In numerical analysis, these problems must be solved in order to obtain appropriate solutions. In nonlinear dynamic behavior, the energy and momentum principles are good criteria for numerical stability. Currently, the Energy-Momentum Method (EMM) is a time integration law based on this criterion, which discretizes the virtual work principle to derive an equation of motion different from D'Alembert's Lagrangian equation. The EMM method was established in the 1990s, and its effectiveness and accuracy have been extensively verified. Miyazaki implemented EMM on a wrinkled membrane and demonstrated its effectiveness [75,78].

2.3.1. The Three Principles

In general, the equation of motion using the finite element method is solved by substituting the Lagrangian into the Lagrangian equation. The Lagrangian satisfies the following three principles.

1. The time rate of change of the mechanical energy is equal to the work rate due to non-conservative external forces.

2. The rate of change of momentum over time is equal to the sum of the external forces.

3. The rate of change of angular momentum with time is equal to the sum of the moments of the external forces.

Satisfying the above means that the instantaneous time rate of change is satisfied and does not guarantee that the following incremental relationship holds.

1. The increment of the mechanical energy is equal to the work due to the non-conservative external force.

2. The increment of momentum is equal to the sum of the force products due to external forces.

3. The increment of angular momentum is equal to the sum of the angular force products of the moments of the external forces.

The failure of this condition causes fluctuations in the mechanical energy in the dynamics calculations of flexible nonlinear structures such as membranes, even in conservative systems. This causes divergence during the calculation.

2.3.2. Energy Momentum Method (EMM)

The energy-momentum method discretizes the Lagrangian equations so that the incremental relationship among the above three principles hold. The important point is that the time integration law is specified in the process of deriving the equations of motion. First, the theory of EMM is described. Consider a flexible manifold **Ω**. From Fig. 2.5, the position vectors of the nodes and the basis vector $\boldsymbol{e}_k$ in the local coordinate system within the object can be interpolated by the nodal variables as follows,

$$\boldsymbol{x} = N_m x^m + N_p Y^k \boldsymbol{e}_k^p,\ \ \boldsymbol{e}_k = N_p \boldsymbol{e}_k^p \mathbf{x} \tag{2.96}$$

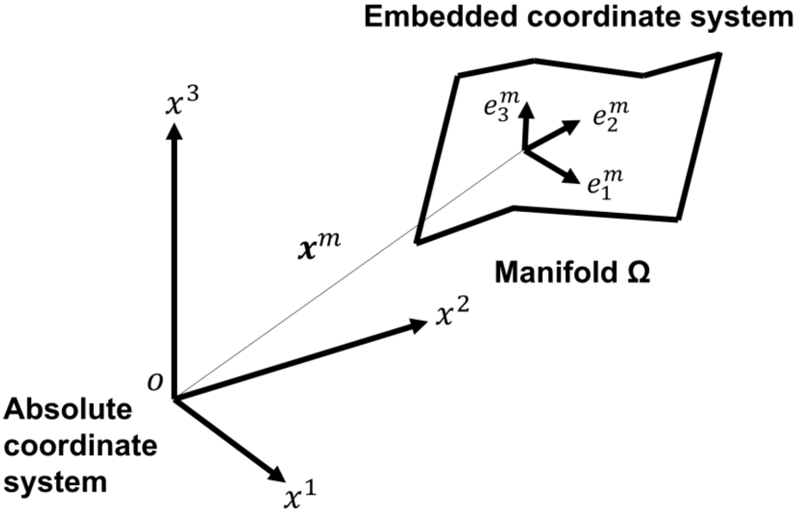

Fig. 2.6: Flexible and Diverse System.

Let N_m be the interpolation function for node m in the object and Y^k be the coordinates in the local coordinate system. The angular velocity of node p in the local coordinate system, ω^p, is determined from the basis matrix $\boldsymbol{R}^p$ of the local coordinate system and its time derivative $\dot{\boldsymbol{R}}^{\boldsymbol{p}}$ by,

$$\dot{\boldsymbol{R}}^{\boldsymbol{p}} = \boldsymbol{R}^p \widehat{\omega^p} \tag{2.97}$$

Note that ω^p is an antisymmetric matrix including the outer product. The velocity $\dot{x}$ and angular velocity ω are interpolated in the same way and can be written as follows,

$$\dot{x} = N_m \dot{\boldsymbol{x}}^{\boldsymbol{m}}\ ,\ \omega = N_p \omega^{\boldsymbol{p}} \tag{2.98}$$

At this point, the kinetic energy is,

$$T = \frac{1}{2} M_{mn} \dot{\boldsymbol{x}}^m \cdot \dot{\boldsymbol{x}}^n + \frac{1}{2} \omega^{\boldsymbol{p}} \cdot \boldsymbol{J}_{\boldsymbol{pq}} \omega^{\boldsymbol{p}} \tag{2.99}$$

where, $M_{mn} = \int_\Omega \rho N_m N_n d\Omega$ and $\boldsymbol{J}_{\boldsymbol{pq}} = \int_{\boldsymbol{\Omega}} \left(Y^{\boldsymbol{k}} Y^{\boldsymbol{k}} \boldsymbol{I} - Y_i Y_j \boldsymbol{i}_i \otimes \boldsymbol{i}_i\right) N_p N_q d\Omega$

If the internal energy is U^{in} , then the total energy Π is the sum of the kinetic energy and the internal energy as follows,

$$\Pi = \frac{1}{2} M_{mn} \dot{\boldsymbol{x}}^m \cdot \dot{\boldsymbol{x}}^n + \frac{1}{2} \omega^{\boldsymbol{p}} \cdot \boldsymbol{J}_{\boldsymbol{pq}} \omega^{\boldsymbol{p}} + U^{in}\left(\boldsymbol{x}^m, \boldsymbol{e}_k^p\right) \tag{2.100}$$

Additionally, the total momentum $\boldsymbol{P}$ and the total angular momentum $\boldsymbol{L}$ are ,

$$\boldsymbol{P} = M_{mn}\dot{\boldsymbol{x}}^{n}, \;\; \boldsymbol{L} = \boldsymbol{x}^{m} \times M_{mn}\dot{\boldsymbol{x}}^{n} + \boldsymbol{R}^{p}\boldsymbol{J}_{pq}\omega^{q} \tag{2.101}$$

Now, let θ^{p} be the virtual displacement vector corresponding to the moment of force at node p. The following relation holds for the variants of the orthonormal basis matrix R^{p}.

$$\Delta\boldsymbol{R}^{p} = \widehat{\Delta\theta^{p}}\,\overline{\boldsymbol{R}^{p}} \tag{2.102}$$

Then, the following time integration rule is assumed.

$$\overline{\dot{\boldsymbol{x}}^{m}} = \frac{\Delta\boldsymbol{x}^{m}}{\Delta t} \tag{2.103}$$

$$\overline{\dot{\omega}^{p}} = (\overline{\boldsymbol{R}^{\boldsymbol{p}}})^{\mathrm{T}}\frac{\Delta\theta^{p}}{\Delta t} \tag{2.104}$$

The time derivatives of the total energy, momentum, and angular momentum are then,

$$\Delta\Pi = \widetilde{\boldsymbol{f}_{m}^{x}} \cdot \Delta\boldsymbol{x}^{m} + \widetilde{\boldsymbol{f}_{p}^{\theta}} \cdot \Delta\boldsymbol{\theta}^{\boldsymbol{p}} \tag{2.105}$$

$$\frac{\Delta\boldsymbol{P}}{\Delta t} = \widetilde{\boldsymbol{f}_{m}^{x}} \tag{2.106}$$

$$\frac{\Delta\boldsymbol{L}}{\Delta t} = \overline{\boldsymbol{x}^{m}} \times \widetilde{\boldsymbol{f}_{m}^{x}} + \widetilde{\boldsymbol{f}_{p}^{\theta}} \tag{2.107}$$

Here $\overline{\boldsymbol{x}}^{\boldsymbol{m}}$ refers to the average of the position vectors of the current and next steps, $\tilde{\boldsymbol{f}}_{\boldsymbol{m}}^{\boldsymbol{x}}$ is the modified internal force vector acting on node m, and $\tilde{\boldsymbol{f}}_{\boldsymbol{p}}^{\theta}$ is the moment vector of the force acting on node p in the absolute coordinate system, as follows,

$$\tilde{\boldsymbol{f}}_{\boldsymbol{m}}^{\boldsymbol{x}} = M_{mn}\frac{\Delta\dot{\boldsymbol{x}}^{\boldsymbol{n}}}{\Delta t} + \left(\frac{\partial\widetilde{U^{\mathrm{in}}}}{\partial\boldsymbol{x}^{\boldsymbol{m}}}\right)^{\mathrm{T}} \tag{2.108}$$

$$\tilde{\boldsymbol{f}}_{\boldsymbol{p}}^{\theta} = \frac{\Delta}{\Delta t}\left(\boldsymbol{R}_{p}\boldsymbol{J}_{p}q\omega^{\boldsymbol{q}}\right) + \overline{\boldsymbol{e}_{k}^{\boldsymbol{p}}} \times \left(\frac{\partial\widetilde{U^{\mathrm{in}}}}{\partial\boldsymbol{e}_{k}^{\boldsymbol{P}}}\right)^{\mathrm{T}} \tag{2.109}$$

Here the tilde symbol above the variable indicates the discrete derivative that satisfies Eq. 2.110.

$$\Delta A(\boldsymbol{q}) = \left(\widetilde{\frac{\Delta A}{\Delta\boldsymbol{q}}}\right)\Delta\boldsymbol{q} \tag{2.110}$$

The following relation holds for the discrete derivative of the internal energy.

$$\sum_{m}\left(\frac{\partial\widetilde{U^{\mathrm{in}}}}{\partial\boldsymbol{x}^{m}}\right)^{\mathrm{T}} = 0 \tag{2.111}$$

$$\sum_m \left[\overline{\boldsymbol{x^m}} \times \left(\frac{\partial \widetilde{U^{in}}}{\partial \boldsymbol{x^m}} \right)^{\mathrm{T}} + \overline{\boldsymbol{e}_k^{\boldsymbol{p}}} \times \left(\frac{\partial \widetilde{U^{\mathrm{in}}}}{\partial \boldsymbol{e}_k^{\boldsymbol{p}}} \right)^{\mathrm{T}} \right] = \mathbf{0} \tag{2.112}$$

$\widetilde{\boldsymbol{F}_{\boldsymbol{m}}^{\boldsymbol{x}}}$ is defined as the modified external force vector and $\widetilde{\boldsymbol{F}_{\boldsymbol{p}}^{\theta}}$ as the modified external moment vector, and are approximated by the following equation,

$$\widetilde{\boldsymbol{F}_{\boldsymbol{m}}^{\boldsymbol{x}}} \approx \overline{\boldsymbol{F}_{\boldsymbol{m}}^{\boldsymbol{x}}}^{nc} - \left(\frac{\partial \widetilde{U^{\mathrm{ex}}}}{\partial \boldsymbol{x^m}} \right)^{\mathrm{T}} \tag{2.113}$$

$$\widetilde{\boldsymbol{F}_{\boldsymbol{p}}^{\theta}} \approx \overline{\boldsymbol{F}_{\boldsymbol{p}}^{\theta}}^{nc} - \overline{\boldsymbol{e}_k^{\boldsymbol{m}}} \times \left(\frac{\partial \widetilde{U^{\mathrm{ex}}}}{\partial \boldsymbol{e}_k^{\boldsymbol{m}}} \right)^{\mathrm{T}} \tag{2.114}$$

where $(\boldsymbol{F}_{\boldsymbol{m}}^{\boldsymbol{x}})^{nc}$ is the nonconservative external force vector, $(\boldsymbol{F}_{\boldsymbol{p}}^{\theta})^{nc}$ is the nonconservative moment vector, and U^{ex} is the potential energy due to the conserved external force. Thus, the incremental external work, ΔW, is,

$$\Delta W = \widetilde{\boldsymbol{F}_{\boldsymbol{m}}^{\boldsymbol{x}}} \cdot \Delta \boldsymbol{x^m} + \widetilde{\boldsymbol{F}_{\boldsymbol{p}}^{\theta}} \cdot \Delta \theta^{\boldsymbol{p}} \tag{2.115}$$

From the above, the variational relationship between the total energy $\mathbf{\Pi}$ and the external work W, the total momentum $\mathbf{P}$ and the external force vector $\widetilde{\boldsymbol{F}_{\boldsymbol{m}}^{\boldsymbol{x}}}$, and the total angular momentum $\mathbf{L}$ and the external moment vector $\widetilde{\boldsymbol{F}_{\boldsymbol{p}}^{\theta}}$ is as follows

$$\Delta \mathbf{\Pi} = \Delta W \tag{2.116}$$

$$\frac{\Delta \boldsymbol{P}}{\Delta t} = \widetilde{\boldsymbol{F}_{\boldsymbol{m}}^{\boldsymbol{x}}} \tag{2.117}$$

$$\frac{\Delta \boldsymbol{L}}{\Delta t} = \overline{\boldsymbol{x^m}} \times \widetilde{\boldsymbol{F}_{\boldsymbol{m}}^{\boldsymbol{x}}} + \widetilde{\boldsymbol{F}_{\boldsymbol{p}}^{\theta}} \tag{2.118}$$

In other words, total energy, momentum, and angular momentum are conserved for the object. This prevents energy divergence during iterations and maintains computational stability. Now, let us discuss the case where EMM is incorporated into a wrinkled membrane model. As mentioned earlier, ε_1 and ε_2 are $0 \leq \varepsilon_1 \leq 1$ and $0 \leq \varepsilon_2 \leq 1$, because the stiffness in the compressive direction is very small compared to the wrinkle criterion in Eq. 2.91. When the membrane is taut, the elastic matrix Γ_t is,

$$\Gamma = \Gamma_t \equiv \frac{E}{1-\nu^2} \begin{bmatrix} 1 & \nu \\ \nu & 1 \end{bmatrix} \tag{2.119}$$

In addition, the elasticity matrix Γ_w in the case of wrinkling is,

$$\Gamma = \Gamma_w \equiv \frac{E}{1-\epsilon_1 \nu^2} \begin{bmatrix} \epsilon_1 & \epsilon_1 \nu \\ \epsilon_1 \nu & 1 \end{bmatrix} \tag{2.120}$$

Similarly, the elasticity matrix Γ_s in the case of slackening is,

$$\Gamma = \Gamma_s \equiv \frac{E}{1-\epsilon_1\epsilon_2\nu^2}\begin{bmatrix} \epsilon_1 & \epsilon_1\epsilon_2\nu \\ \epsilon_1\epsilon_2\nu & \epsilon_2 \end{bmatrix} \tag{2.121}$$

Using these elastic matrices, the internal energy is derived.

$$U^{in} = \int_{\Omega} \frac{1}{2}\gamma \cdot \boldsymbol{\Gamma} \cdot \gamma d\Omega \tag{2.122}$$

The time integral law is,

$$\overline{\boldsymbol{x}^{\dot{m}}} = \frac{\Delta x^m}{\Delta t} \tag{2.123}$$

$$\overline{\omega^p} = \frac{\Delta \theta^{\boldsymbol{p}}}{\Delta t} \tag{2.124}$$

Let the nth time step be the current step and the n+1st time step be the next step and let half of the increment of the nodal position $\mathbf{x}_m$ from time t_n to t_{n+1} be $\boldsymbol{u}_h^m$ and half of $\Delta\theta^{\mathbf{p}}$ be the coordination variables. Then,

$$\boldsymbol{x}^m = \underline{\boldsymbol{x}^m} + \boldsymbol{2u}_h^m \tag{2.125}$$

$$\boldsymbol{R}^p = \underline{\boldsymbol{R}^p}\boldsymbol{T}^p \qquad \text{where,} \quad \boldsymbol{T}^p = \boldsymbol{I} + \frac{2}{1+|\beta_h^p|^2}\left[\widehat{\beta_h^p} + \widehat{\beta_h^p}^2\right] \tag{2.126}$$

From here, the discrete equations of motion and the equivalent nodal forces are derived.

2.4. Mathematical Model for Self-Extending Convex Tapes

In this section, a mathematical model for the extension of self-extending convex tapes is described.

2.4.1. Wrapping of the Convex Tapes around a Hub Element

In this model, a node element (without rotational degree of freedom) is prepared at the center, and a hub element is created to rotate around the node element. Furthermore, we consider a boom element that wraps around the hub element. The boom element extending from the hub element is assumed to extend in a fixed direction while contacting a guide roller element. The boom consisting of convex tapes is assumed to be wrapped around the hub element in a counterclockwise direction. Let h_s be half the thickness of the boom when stowed (i.e., the thickness of a single boom), α_w be the azimuth angle of the boom's hub attachment point relative to the node when stored, and ϕ be the angle of rotation relative to the node element when the hub element rotates. From here, the radius and position vector at the wrap-around angle θ can be obtained by assuming that the number of booms wrapped around the hub element is N as follows,

$$r = r(\theta) = r_h + 2Nh_s\theta + h_s \equiv a_r\theta + r_o \tag{2.127}$$

$$\boldsymbol{x} = r\boldsymbol{e}, \boldsymbol{e} \equiv \begin{bmatrix} \cos(\theta + \alpha_w + \phi) \\ \sin(\theta + \alpha_w + \phi) \end{bmatrix} \tag{2.128}$$

$$\text{where,} \quad a_r = 2Nh_s,\ r_o = r_h + h_s \tag{2.129}$$

Following this, the strain energy generated when the boom is stowed is derived. Let Q be the strain energy per unit length of the boom when it is completely wrapped around the hub. In general, when an axial force T_{end} acts on both ends of a convex tape and an equally distributed load p_{zo} acts on the surface, the strain energy per unit length stored when the tape is wound with curvature κ so that the arc points outwards can be written by Equation 2.130.[79]

$$p(\kappa) = \frac{1}{2}b\widetilde{D_x}\left(1 - \nu_x\nu_y\right)\kappa^2 + \frac{1}{2}b\widetilde{D_y}(\kappa_o + \nu_x\kappa)^2(1 - A_1) + \frac{bp_zo^2}{2E_xh}\frac{A_3 - 1}{\kappa^2}$$

$$-bp_zo\frac{A_3-1}{\kappa}\epsilon_{end} + \frac{1}{2}E_xbhA_3\epsilon^2 \tag{2.130}$$

$$\text{where,} \quad \begin{cases} D_x = \frac{E_xh^3}{12(1-\nu_x\nu_y)} & \widetilde{D_x} = D_x\left(1 - \frac{h^2\kappa_o^2}{12}\right) \\ D_y = \frac{E_yh^3}{12(1-\nu_x\nu_y)} & \widetilde{D_y} = D_y\left(1 - \frac{h^2\kappa_o^2}{12}\right) \end{cases}$$

$$\text{and} \quad \eta \equiv \sqrt[4]{\frac{E_xb^4h\kappa^2}{64\widetilde{D_y}}} = p_o\sqrt{|\kappa|},\ \ p_o = \sqrt[4]{q_0}\ , \quad q_o \equiv \frac{E_xb^4h}{64\widetilde{D_x}} \tag{2.131}$$

$$A_1 = \frac{\cosh 2\eta - \cos 2\eta}{\eta(\sinh 2\eta + \sin 2\eta)} \qquad A_3 = \frac{2\eta(\cosh 2\eta + \cos 2\eta)}{\sinh 2\eta + \sin 2\eta} \tag{2.132}$$

Neglecting the tension and surface distributed load generated during wrapping, the strain energy can be approximated by Equation 2.133.

$$p(\kappa) \approx p_{\text{free}} \equiv \frac{1}{2}b\widetilde{D_x}\left(1 - \nu_x\nu_y\right)\kappa^2 + \frac{1}{2}b\widetilde{D_y}(\kappa_o + \nu_x\kappa)^2(1 - A_1) \tag{2.133}$$

Here, the bending moment M_{free} generated by the boom is,

$$M_{\text{free}} = \frac{\partial p_{\text{free}}}{\partial \kappa} = b\widetilde{D_x}\left(1 - \nu_x\nu_y\right)\kappa + b\nu_x\widetilde{D_y}(\kappa_o + \nu_x\kappa)(1 - A_1) - \frac{1}{2}b\widetilde{D_y}(\kappa_o +$$

$$\nu_x\kappa)^2\frac{\partial A_1}{\partial \kappa} \tag{2.134}$$

$$\text{where,}\quad \begin{cases} \frac{\partial A_1}{\partial \kappa} = \frac{\partial \eta}{\partial \kappa}\frac{\partial A_1}{\partial \eta} = \frac{A_4 - A_1}{2\kappa} \\ A_4 = \frac{4\sinh 2\eta \sin 2\eta}{(\sinh 2\eta + \sin 2\eta)^2} \end{cases} \tag{2.135}$$

If M_{free} is differentiated by κ, then N_{free} becomes,

$$N_{\text{free}} \equiv \frac{\partial M_{\text{free}}}{\partial \kappa}$$

$$= b\widetilde{D_x}\left(1 - \nu_x\nu_y\right) + b\nu_x^2\widetilde{D_y}(1 - A_1) - 2b\nu_x\widetilde{D_y}\,(\kappa_o + \nu_x\kappa)\frac{\partial A_1}{\partial \kappa} - \frac{1}{2}b\widetilde{D_y}(\kappa_o + \nu_x\kappa)^2\frac{\partial^2 A_1}{\partial \kappa^2} \tag{2.136}$$

where,

$$\begin{aligned} \frac{\partial^2 A_1}{\partial \kappa^2} &= \frac{\partial}{\partial \kappa}\left(\frac{A_4 - A_1}{2\kappa}\right) \\ &= \frac{1}{2\kappa}\frac{\partial \eta}{\partial \kappa}\frac{\partial}{\partial \eta}(A_4 - A_1) - \frac{A_4 - A_1}{2\kappa^2} \\ &= \frac{1}{4\kappa^2}\frac{\partial}{\partial \eta}(A_4 - A_1) - \frac{A_4 - A_1}{2\kappa^2} \\ &= \frac{1}{4\kappa^2}\left[A_5 - (A_4 - A_1)\right] - \frac{A_4 - A_1}{\alpha\kappa^2} \\ &= \frac{A_5 - 3A_4 + 3A_1}{4\kappa^2} \end{aligned} \tag{2.137}$$

$$A_5 = \eta\frac{\partial A_4}{\partial \eta} = 4\eta\begin{bmatrix} \frac{2(\cosh 2\eta \sin 2\eta + \sinh 2\eta \cos 2\eta)}{(\sinh 2\eta + \sin 2\eta)^2} \\ -\frac{\cosh 2\eta + \cos 2\eta}{\sinh 2\eta + \sin 2\eta}A_4 \end{bmatrix} \tag{2.138}$$

2.4.2. Transition from Wrapped State to Extended State

This section describes the static shape deformation during the transition region (hereafter referred to as the ploy region) (Figure 2.6) when the boom, which is wrapped around the hub element and is almost in a circular arc, is extended and returns to its original cross-sectional C shape. The ploy region is assumed to be constant in length, and the strain energy is also assumed to be constant. Assuming the boom is in translational motion at the same speed as the rotational speed of the hub, the kinetic energy is also equivalent. After the boom has completed its extension, the ploy region is assumed to be resolved and the boom is in a fully deployed state. To account for the dynamics of this situation, it is necessary to formulate the total energy U_{pl} of the ploy region. Here, we refer to reference [80].

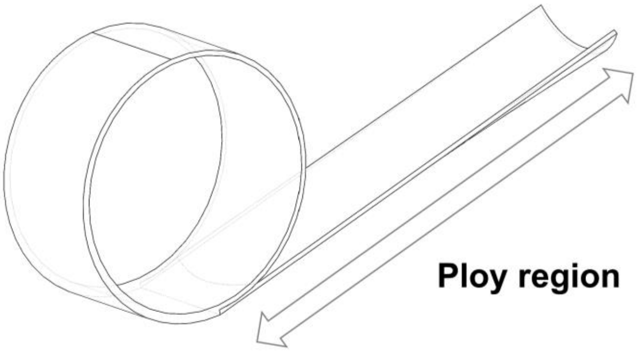

Fig. 2.7: Ploy region during deformation of convex tape.

Let L_{pl} be the length in the ploy region.

$$U_{pl} = C_U \frac{E_y}{1-\nu_x\nu_y} b^3 h^2 \kappa_o^2 \sqrt{h\kappa_o} \sqrt[4]{\frac{(1-\nu_x\nu_y)\nu_x}{\nu_y}} \tag{2.139}$$

$$L_{pl} = C_L b^2 \sqrt{\left(\frac{\kappa_o}{h}\right)} \tag{2.140}$$

$$C_U = \frac{1}{90\sqrt{70}}, \quad C_L = \frac{1}{\sqrt{70}} \frac{4}{\frac{\nu_x}{\nu_y}} \tag{2.141}$$

Adopting the characteristic values of the convex tape in Table 4.1, we obtain,

$$(C_U, C_L) = (1.32 \times 10^{-3}, 1.19 \times 10^{-1}) \tag{2.142}$$

Accordingly, U_{pl} and L_{pl} becomes,

$$U_{pl} = \frac{1}{90\sqrt{70}} \times \frac{E_y}{1-\nu_x\nu_y} b^3 h^2 \kappa_o^2 \sqrt{h\kappa_o} \sqrt[4]{\frac{(1-\nu_x\nu_y)\nu_x}{\nu_y}} \tag{2.143}$$

$$L_{pl} = \frac{1}{\sqrt{70}} \sqrt[4]{\frac{\nu_x}{\nu_y}} \times b^2 \sqrt{\left(\frac{\kappa_o}{h}\right)} \tag{2.144}$$

In this case, L_{pl} is assumed to be shorter than the tangential distance between the hub and the guide roller.

2.4.3. Winding Angle of Boom

The boom body is modeled by a beam element. The positions of both nodes are fully constrained to be in the form of a spiral curve during wrapping, each node is given a fixed radius r_i, the wrapping angle at node i is θ_i^s, and the length before deformation from the attachment point of the boom to the hub element to node i is L_i. Then,

$$\int_0^{\theta_i^s} \sqrt{(a_r\theta + r_o)^2 + a_r^2}\, d\theta = L_i \tag{2.145}$$

As $r_i \equiv a_r\theta_i + r_o$, L_i then becomes,

$$\frac{\theta_i}{2}\frac{(r_i+r_o)(r_i^2+r_o^2+a_r^2)}{r_i\sqrt{r_i^2+a_r^2}+r_o\sqrt{r_o^2+a_r^2}} + h_s \log\frac{r_i+\sqrt{r_i^2+a_r^2}}{r_o+\sqrt{r_o^2+a_r^2}} = L_i \tag{2.146}$$

Therefore, it is sufficient to iteratively find the value of θ_i^s that satisfies this equation. If Π_m can be derived, the strain energy Π_m of element m sandwiched between nodes i and i + 1can be expressed by the following equations.

$$\kappa = \frac{1}{\sqrt{r(\theta)^2+a_r^2}} \tag{2.147}$$

$$\Pi_m = \int_{\theta_i^2}^{\theta_{i+1}^s} p_{\text{free}}(\kappa)\sqrt{r(\theta)^2 + a_r^2}d\theta \tag{2.148}$$

From the above, the average strain energy π_m per unit length of the boom element is,

$$\pi_m = \frac{P_m}{L_{i+1}-L_i} = \frac{1}{L_{i+1}-L_i}\int_{\theta_i^2}^{\theta_{i+1}^s} p(\kappa)\sqrt{r(\theta)^2 + a_r^2}d\theta \tag{2.149}$$

2.4.4. Detachment Point of the Boom Element from the Hub Element

We describe a peeling point at which a boom element wrapped around a hub is released from the hub by extension. First, let θ_p be the angle of wrapping around the hub element at the detachment point, $\mathbf{z}_p$ be the position vector of the detachment point in the local coordinate system of the node, and $\mathbf{a}_p$ be the direction vector of the boom, then,

$$\boldsymbol{z}_p = r_p\boldsymbol{e}_p \tag{2.150}$$

$$\text{where,} \quad r_p \equiv a_{r\theta_p} + r_o, \quad \text{and} \quad z_p \equiv \begin{bmatrix} \cos(\theta_p + \alpha_w + \phi) \\ \sin(\theta_p + \alpha_w + \phi) \\ 0 \end{bmatrix} \tag{2.151}$$

$$\boldsymbol{a}_p = 2Nh_s\boldsymbol{e}_p + r_p\boldsymbol{t}_p \tag{2.152}$$

$$\text{where,} \quad \boldsymbol{t}_p \equiv \begin{bmatrix} -\sin(\theta_p + \alpha_w + \phi) \\ \cos(\theta_p + \alpha_w + \phi) \\ 0 \end{bmatrix} \tag{2.153}$$

To simplify the calculation, let $\mathbf{a}_p \approx r_p\mathbf{t}_p$. Assuming that $\mathbf{y}_g$ is the relative rotation vector of the center of the guide rail from the center of the hub and h_d is half the thickness of the boom at the end of its deployment, the position vector of the separation point where the boom meets the guide roller is,

$$\boldsymbol{z}_p = \boldsymbol{y}_h - (r_h + h_d)\boldsymbol{e}_p \tag{2.154}$$

$$\text{where,} \qquad \boldsymbol{y}_g = y_g \begin{bmatrix} \cos\alpha_y \\ \sin\alpha_y \\ 0 \end{bmatrix} \tag{2.155}$$

Here, $\mathbf{x}_h$ is the position vector of the hub in terms of the inertial coordinate system, R_n,R_h is the attitude matrix of the node and the hub, and $\tilde{\boldsymbol{e}}_{\boldsymbol{p}}$ is the unit vector in the direction of the detachment point in terms of the hub-fixed coordinate system. In this case,

$$\cos\left(\alpha_y - \phi - \theta_p - \alpha_w\right) = \frac{r_p + h_d + r_g}{y_g} \tag{2.156}$$

$$2Nh_s\theta_p + r_h + h_d + h_s + r_g = y_p \cos(\alpha_y - \theta_p - \alpha_w - \phi) \tag{2.157}$$

Equation 2.157 becomes a nonlinear equation for θ_p. From this, the wrap-around radius r_p at the peeling point becomes,

$$r_p = r_p(\phi) = a_{r\theta_p} + r_o = a_r\theta_{po} + r_o - \alpha_r w_p \phi \tag{2.158}$$

$$\equiv r_{po} - a_r w_p \phi \tag{2.159}$$

Also, let $L_p = L_p(\phi)$ be the length of the boom before deformation from the attachment point to the detachment point from the hub of the boom,

$$L_p(\phi) = \frac{\theta_p}{2} \frac{(r_p + r_o)(r_p^2 + r_o^2 + a_r^2)}{r_p\sqrt{r_p^2 + a_r^2} + r_o\sqrt{r_o^2 + a_r^2}} + h_s \log \frac{r_p + \sqrt{r_p^2 + a_r^2}}{r_o + \sqrt{r_o^2 + a_r^2}} \tag{2.160}$$

In addition, the distance $l_p = l_p(\phi)$ from the peeling point to the contact point of the guide roller is,

$$l_p(\phi) = \sqrt{\left|\boldsymbol{y}_g\right|^2 - \left[r_p(\phi) + h_s + h_d + r_g\right]^2} \tag{2.161}$$

Let ϕ_{max} be ϕ at the completion of extension, when $\theta_p = 0$, then,

$$\phi_{\max} = \frac{\theta_{po}}{w_p} = \alpha_y - \alpha_w \cos^{-1} \frac{r_h + h_s + h_d + r_g}{y_g} \tag{2.162}$$

The direction vector $\boldsymbol{e}_p^h(\phi)$ of the peeling point and the direction vector $t_p^h(\phi)$ of the boom as viewed from the hub are,

$$\boldsymbol{e}_p^h(\phi) = \begin{bmatrix} \cos(\theta_p + \alpha_w) \\ \sin\,(\theta_p + \alpha_w) \\ 0 \end{bmatrix} \begin{bmatrix} \cos(\alpha_{po} - w_p\phi) \\ \sin\,(\alpha_{po} - w_p\phi) \\ 0 \end{bmatrix} \tag{2.163}$$

$$t_p^h(\phi) = \begin{bmatrix} -\sin(\alpha_{po} - w_p\phi) \\ \cos(\alpha_{po} - w_p\phi) \\ 0 \end{bmatrix} \tag{2.164}$$

where, $$\alpha_{po} = \theta_{po} + \alpha_w \tag{2.165}$$

From here, the position vector $\mathbf{x}_p$ of the peeling point in the inertial coordinate system becomes,

$$\boldsymbol{x}_p = \boldsymbol{x}_h + r_p \boldsymbol{R}_h \boldsymbol{e}_p^h \tag{2.166}$$

2.4.5. Boom Wrapping and Peeling Model

In this section the equivalent nodal force vector and tangential stiffness matrix generated by the boom element wrapped around the hub are formulated. The following six cases are assumed as constraints on the boom. Let i and $i + 1$ be the root and tip sides of the boom, respectively for the nodes of the beam element, and let L_i, and L_{i+1} be the distances from the hub attachment point to each beam element node, and similarly, let L_p be the distance from the hub attachment point to the detachment point, then,

Case 0 : $L_p + l_p < L_i$

(Not constrained by either the hub element or the guide roller element)

Case 1 : $L_p < L_i \leq L_p + l_p$, $L_p + l_p \leq L_{i+1}$

(Contact with guide roller elements)

Case 2 : $L_i \leq L_p, L_p + l_p \leq L_{i+1}$

(Contacts with both guide rollers and hub elements)

Case 3 : $L_p < L_i < L_p + l_p, L_p < L_{i+1} < L_p + l_p$

(Present between the guide roller element and the hub element.)

Case 4 : $L_i \leq L_p$, $L_p < L_{i+1} < L_p + l_p$

(Not in contact with the guide roller element, but partially wrapped around the hub element)

Case 5 : $L_{i+1} \leq L_p$

(Completely wrapped around the hub element)

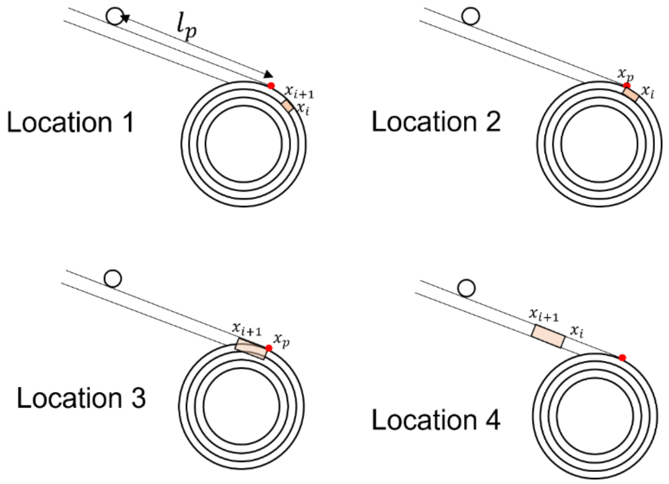

Fig. 2.8: Constraints on boom elements.

The equivalent nodal forces are different each time because of the different constraints to which the boom elements are subjected. These six situations described above can be represented by a combination of the following four locations. This is shown in Figure 4.2.

Location 1: In the wrapped condition, both ends are $(\mathbf{x}_i,\mathbf{x}_{i+1})$

Location 2 : In the wrapped condition, both ends are $(\mathbf{x}_i,\mathbf{x}_p)$

Location 3 : Free from wrapping, with both ends $(\mathbf{x}_p,\mathbf{x}_{i+1})$ in a straight line

Location 4 : In a straight line, both ends are $(\mathbf{x}_i,\mathbf{x}_{i+1})$

Let us consider a situation where there is a transition from case 4 to case 3 between time t and $t + \Delta t$. The transition from location 3 at time t to location 4 at time $t+\Delta t$ is not desirable in the formulation. Therefore, we define location 5 as follows.

At time t, $\mathbf{x}_i$ is at the peeling point $\mathbf{x}_p$, the velocity is equal to the Lagrangian velocity $\mathbf{v}_p$ at the peeling point, both ends are $(\mathbf{x}_{i+1},\mathbf{x}_i)$ in a linear state, and the length of the element changes.

2.4.6. Energy, Momentum and Angular Momentum of Boom Elements

The boom element is partially or fully wrapped around the hub, and after extension the boom is constrained against the guide rollers and straightened. In this section, we will discuss the wrapping and straightening of the boom element. The formulation of kinetic energy, strain energy, momentum, and angular momentum are also described.

In locations 1 and 2, consider a situation in which only the portion of element m whose wrap-around angle is from θ_s to θ_e is wrapped. The length L_w of this portion becomes,

$$L_w = f(\theta_e) - f(\theta_s) \tag{2.167}$$

$$f(\theta) \equiv \int_{\theta_s}^{\theta_e} \sqrt{r_\theta^2 + a_r^2} d\theta \tag{2.168}$$

$$= \frac{\theta}{2} \frac{(r_\theta + r_o)(r_\theta^2 + r_o^2 + a_r^2)}{r_\theta \sqrt{r_\theta^2 + a_r^2} + r_o \sqrt{r_o^2 + a_r^2}} + h_s \log \frac{r_\theta + \sqrt{r_\theta^2 + a_r^2}}{r_o + \sqrt{r_o^2 + a_r^2}} \tag{2.169}$$

Then, as the position vector $r_\theta = r(\theta)$ in the boom cross section with wrap-around angle θ,

$$\boldsymbol{x} = \boldsymbol{x}_h + \boldsymbol{R}_h \boldsymbol{T}_\theta (r_\theta \boldsymbol{i}_1 + \boldsymbol{y}) \tag{2.170}$$

Here, **y** is the local coordinate in the cross section and $\boldsymbol{T}_\theta$ is the rotation matrix around the z-axis of the hub element. In other word,

$$\boldsymbol{y} = \begin{bmatrix} y_1 \\ 0 \\ y_3 \end{bmatrix}, \quad \boldsymbol{T}_\theta = \begin{bmatrix} \cos(\alpha_w + \theta) & -\sin(\alpha_w + \theta) & 0 \\ \sin(\alpha_w + \theta) & \cos(\alpha_w + \theta) & 0 \\ 0 & 0 & 1 \end{bmatrix} \tag{2.171}$$

Therefore, the velocity becomes,

$$\dot{\boldsymbol{x}} = \dot{\boldsymbol{x}}_h \widehat{+ \Omega_h} \boldsymbol{R}_h \boldsymbol{T}_\theta (r_\theta \boldsymbol{i}_1 + \boldsymbol{y}) \tag{2.172}$$

From this, the kinetic energy of the wrapped part can be expressed as,

$$T_w = \int_{\theta_s}^{\theta_e} \sqrt{r_\theta^2 + a_r^2}\, d\theta \iint_A \rho \dot{\boldsymbol{x}}^{\mathrm{T}} \dot{\boldsymbol{x}}\, dA \tag{2.173}$$

$$\approx L_w \left(\frac{1}{2} \rho A \dot{\boldsymbol{x}}_h^{\mathrm{T}} \boldsymbol{x}_h + \frac{1}{2} \dot{\omega}_h^{\mathrm{T}} \boldsymbol{J}_o \omega_h \right) \tag{2.174}$$

where j_{11}, and j_{22} are the secondary moments of the section of the boom, and

$$j_o = \frac{1}{L_{i+1} - L_i} \times \rho \int_{\theta_i}^{\theta_{i+1}} \begin{bmatrix} c^2 j_{11} + s^2 j_{22} & sc(j_{11} - j_{22}) & 0 \\ sc(j_{11} - j_{22}) & c^2 j_{22} + s^2 j_{11} & 0 \\ 0 & 0 & j_{11} + j_{22} \end{bmatrix} \sqrt{r_\theta^2 + a_r^2} d\theta$$

$$+ \rho A \int_{\theta_i}^{\theta_{i+1}} \begin{bmatrix} s^2 & -sc & 0 \\ -sc & c^2 & 0 \\ 0 & 0 & 1 \end{bmatrix} \sqrt{r_\theta^2 + a_r^2} r_\theta^2 d\theta \tag{2.175}$$

Here, $c = \cos\alpha_w + \theta$ and $s = \sin\alpha_w + \theta$. The strain energy can then be approximated by the following equation,

$$V_w \approx L_w p_m \tag{2.176}$$

Rearranging the momentum and angular momentum yields,

$$\begin{cases} \boldsymbol{p}_w \equiv \rho A \boldsymbol{x}_h, \ \boldsymbol{h}_w \equiv \boldsymbol{J}_o \dot{\omega}_h, \quad \boldsymbol{H}_w \equiv \boldsymbol{R}_h \boldsymbol{h}_w \\ \boldsymbol{M}_w^{\alpha} \equiv L_w \boldsymbol{H}_w, \ \ t_w \equiv \frac{1}{2} \dot{\boldsymbol{x}}_h^{\mathrm{T}} \boldsymbol{p}_w + \frac{1}{2} \omega_h^{\mathrm{T}} \boldsymbol{h}_w \\ T_w = L_w t_w, \ \ V_w = L_w p_m, \quad \boldsymbol{P}_w = L_w \boldsymbol{p}_w \\ \boldsymbol{M}_w = L_w(\boldsymbol{H}_w + \boldsymbol{x}_h \times \boldsymbol{p}_w) = \boldsymbol{M}_w^{\alpha} + \boldsymbol{x}_h \times \boldsymbol{P}_w \end{cases} \tag{2.177}$$

Here, the energy increment is

$$\Delta H_w = \Delta(T_w + V_w) \tag{2.178}$$

$$= \overline{L_w}\left[\overline{\dot{\boldsymbol{x}}_h} \Delta \boldsymbol{p}_w + \omega_h^T \overline{\Delta} \boldsymbol{h}_w\right] + \Delta L_w(\overline{t_w} + p_m) \tag{2.179}$$

Using EMM,

$$\overline{\dot{\boldsymbol{x}}_h} = \frac{\Delta \boldsymbol{x}_h}{\Delta t}, \quad \boldsymbol{\Omega}_h = \frac{2}{\Delta \mathrm{t}} \alpha_h - \boldsymbol{S}_h \underline{\boldsymbol{\Omega}_h} \tag{2.180}$$

$$\overline{\omega} = R^{\mathrm{T}} \frac{\alpha}{\Delta \mathrm{t}} = \underline{R}^{\mathrm{T}} \frac{\alpha}{\Delta \mathrm{t}} = \overline{R^{\mathrm{T}}} \frac{\alpha}{\Delta \mathrm{t}} \tag{2.181}$$

$$\boldsymbol{R}_h = \boldsymbol{S}_h \underline{R_h}, \ \ \boldsymbol{S}_h = \boldsymbol{I} + \frac{4}{4 + |\alpha_h|^2} \widehat{\alpha_h} + \frac{2}{4 + |\alpha_h|^2} \widehat{\alpha_h}^2 \tag{2.182}$$

Therefore,

$$\overline{\dot{\boldsymbol{x}}_h} \Delta \boldsymbol{p}_w = \Delta \boldsymbol{x}_h^T \frac{\Delta \boldsymbol{p}_w}{\Delta t} \tag{2.183}$$

$$\overline{\omega_h^{\mathrm{T}}} \boldsymbol{h}_w = \alpha_h^{\mathrm{T}} \frac{\Delta \mathbf{H}_{\mathrm{w}}}{\Delta t} \tag{2.184}$$

From this, the energy increment becomes,

$$\begin{aligned} \Delta H_w &= \Delta \boldsymbol{x}_h^T \left(\overline{L_w} \frac{\Delta \boldsymbol{p}_w}{\Delta t}\right) + \alpha_h^{\mathrm{T}} \left(\overline{L_w} \frac{\Delta \boldsymbol{H}_w}{\Delta t}\right) + \Delta L_w(\overline{t_w} + p_m) \\ &= \Delta \boldsymbol{x}_h^T \frac{\Delta \boldsymbol{P}_w}{\Delta t} + \alpha_h^{\mathrm{T}} \left(\frac{\Delta \boldsymbol{M}_w^{\alpha}}{\Delta t} + \frac{\Delta \boldsymbol{x}_h}{\Delta t} \times \overline{\boldsymbol{P}_w}\right) - \alpha_h^T \left(\frac{\Delta \boldsymbol{x}_h}{\Delta \mathrm{t}} \times \overline{\boldsymbol{P}_w}\right) \\ &+ \Delta L_w \left(\overline{t_w} + p_m - \overline{\dot{\boldsymbol{x}}_h^T}\, \overline{\boldsymbol{p}_w} - \overline{\omega_h^{\mathrm{T}}}\, \overline{\boldsymbol{h}_w}\right) \end{aligned} \tag{2.185}$$

Here,

$$\frac{\Delta \boldsymbol{x}_h}{\Delta t} \times \overline{\boldsymbol{P}_w} = \frac{\Delta \boldsymbol{x}_h}{\Delta t} \times \left(\overline{L_w}\, \overline{\boldsymbol{p}_w} + \frac{\Delta L_w \Delta \boldsymbol{p}_w}{4}\right) = \frac{\Delta L_w}{4} \frac{\Delta \boldsymbol{x}_h}{\Delta t} \times \Delta \boldsymbol{p}_w = \frac{\Delta L_w}{\Delta t} \underline{\boldsymbol{p}_w} \times \psi_H \tag{2.185}$$

$$\overline{t_w} - \overline{\dot{\boldsymbol{x}}_h^{\mathrm{T}}}\, \overline{\boldsymbol{p}_w} - \overline{\omega_h^{\mathrm{T}}}\, \overline{\boldsymbol{h}_w} = -\frac{1}{2} \underline{\boldsymbol{p}_w^{\mathrm{T}}} \dot{\boldsymbol{x}}_h - \frac{1}{2} \underline{\boldsymbol{h}_w^{\mathrm{T}}} \omega_h \tag{2.187}$$

Finally,

$$\Delta H_w = \Delta x_h^T \frac{\Delta P_w}{\Delta t} + \alpha_h^T \left(\frac{\Delta M_w^{\alpha}}{\Delta \mathrm{t}} + \frac{\Delta L_w}{\Delta t} p_w \times \psi_h\right)$$

$$+\Delta L_w \left(p_m - \frac{1}{2}\underline{\boldsymbol{p}_w^{\mathrm{T}}}\dot{\boldsymbol{x}}_h - \frac{1}{2}\underline{\boldsymbol{h}_w^{\mathrm{T}}}\omega_h - \frac{\alpha_h^{\mathrm{T}}}{\Delta t}\underline{\boldsymbol{p}_w \times \psi_h} \right) \tag{2.188}$$

From the above, the equivalent nodal forces $\boldsymbol{f}_h^x, \boldsymbol{f}_h^\alpha, f_\phi$ can be written as,

$$\boldsymbol{f}_h^x = \frac{\Delta \boldsymbol{P}_w}{\Delta t} \tag{2.189}$$

$$\boldsymbol{f}_h^\alpha = \frac{\Delta \boldsymbol{M}_w^\alpha}{\Delta t} + \frac{\Delta L_w}{\Delta t}\underline{\boldsymbol{p}_w} \times \psi_h = \frac{\Delta \boldsymbol{M}_w^\alpha}{\Delta t} - \overline{\boldsymbol{x}_h} \times \boldsymbol{f}_h^x \tag{2.190}$$

$$f_w \equiv p_m - \frac{1}{2}\underline{\boldsymbol{p}_w^{\mathrm{T}}}\dot{\boldsymbol{x}}_h - \frac{1}{2}\underline{\boldsymbol{h}_w^{\mathrm{T}}}\omega_h \frac{2\beta_h^{\mathrm{T}}}{\Delta t}\,\underline{\boldsymbol{p}_w \times \psi_h}$$

$$f_\phi = \frac{\Delta L_w}{\Delta \phi} f_w \tag{2.191}$$

From these, the tangential stiffness matrix can be computed.

$$\boldsymbol{k}_{hh}^{xx} \equiv \frac{\partial f_h^x}{\partial \psi_h}, \quad \boldsymbol{k}_{h\phi}^{x\phi} \equiv \frac{\partial f_h^x}{\partial \varphi} \tag{2.192}$$

$$\boldsymbol{k}_{hh}^{\alpha x} \equiv \frac{\partial f_h^\alpha}{\partial \varphi_h}, \quad \boldsymbol{k}_{hh}^{\alpha\alpha} \equiv \frac{\partial f_h^\alpha}{\partial \beta_h}, \quad \boldsymbol{k}_{h\phi}^{\alpha\phi} \equiv \frac{\partial f_h^\alpha}{\partial \varphi} \tag{2.193}$$

$$\boldsymbol{k}_{\phi h}^{\phi\alpha} \equiv \frac{\partial f_\phi}{\partial \beta_h}, \quad \boldsymbol{k}_{\phi\phi}^{\phi\phi} \equiv \frac{\partial f_\phi}{\partial \varphi} \tag{2.194}$$

The difference between location 1 and location 2 is L_w, the length wrapped around the hub element; in the case of location 1, $L_w = L_2 - L_1$, and in location 2, $L_w = L_p - L_1$.

Following this, the formulation is different in location 3 and location 4 when the element m is linear. Using the local coordinate system, the subscript of node i is represented as 1 instead of i, and the subscript of node i+1 is 2. The strain energy of the straight section corresponds to the energy of the transition region, but the strain energy of the straight section does not change during extension. In the case of location 3, when the position of the detachment point is $\mathbf{x}_p$ and the velocity is $\mathbf{v}_p$, the following time integration rule is assumed.

$$\overline{\boldsymbol{v}_p} = \frac{\Delta x_p}{\Delta t} - \frac{\Delta L_p}{\Delta_t}\overline{\boldsymbol{t}_p} \tag{2.195}$$

where, $\quad \boldsymbol{t}_p = \boldsymbol{R}_p \boldsymbol{i}_3 \qquad (2.196)$

Also, considering the constraint condition, the posture of the peeling point and node 2 will be the same. For the angular velocity, if the posture and angular velocity immediately before node 2 is peeled off are determined, the angular velocity of the peeling point and that of node 2 will thereafter be the same if node 2 is constrained. Under these conditions, the formulation is given as,

$$\boldsymbol{j}_{ob} = \rho \begin{bmatrix} j_{11} & 0 & 0 \\ 0 & j_{22} & 0 \\ 0 & 0 & j_{11} + j_{22} \end{bmatrix}, \quad L_b \equiv L_2 - L_1$$

$$\boldsymbol{p}_2 \equiv \frac{\rho A}{6}\left(2\dot{\boldsymbol{x}}_2 + \boldsymbol{v}_p\right), \quad \boldsymbol{p}_p \equiv \frac{\rho A}{6}\left(\dot{\boldsymbol{x}}_2 + 2\boldsymbol{v}_p\right)$$

$$\boldsymbol{h}_p \equiv \boldsymbol{j}_{ob}\omega_p, \quad \boldsymbol{H}_p \equiv \boldsymbol{R}_p \boldsymbol{h}_p$$

$$\boldsymbol{P}_2 \equiv L_b p_2, \quad \boldsymbol{P}_p \equiv L_b p_p, \quad \boldsymbol{M}_p \equiv L_b \boldsymbol{H}_p$$

$$t_b = \frac{1}{2}\dot{\boldsymbol{x}}_2{}^T \boldsymbol{p}_2 + \frac{1}{2}\boldsymbol{v}_p^{\mathrm{T}} \boldsymbol{p}_p + \frac{1}{2}\omega_p^{\mathrm{T}} \boldsymbol{h}_p \tag{2.197}$$

The energy, momentum, and angular momentum are then given as

$$H_b = L_b t_b, \quad \boldsymbol{P}_b = \boldsymbol{P}_2 + \boldsymbol{P}_1 \tag{2.198}$$

$$\boldsymbol{M}_b = \boldsymbol{M}_p + x_2 \times \boldsymbol{P}_2 + x_p \times \boldsymbol{P}_p \tag{2.199}$$

The equivalent nodal forces and tangential stiffness matrix are calculated in the same way as in location 1 and location 2. On the other hand, in the case of location 4, where one end is not a peeling point but a nodal point, the situation is the same as that of a straight rigid bar. In other words,

$$\boldsymbol{j}_{ob} = \rho \begin{bmatrix} j_{11} & 0 & 0 \\ 0 & j_{22} & 0 \\ 0 & 0 & j_{11} + j_{22} \end{bmatrix}, \quad L_b = L_2 - L_1$$

$$\boldsymbol{p}_1 \equiv \frac{\rho A}{6}(2\dot{\boldsymbol{x}}_1 + \dot{\boldsymbol{v}}_2), \quad \boldsymbol{p}_2 \equiv \frac{\rho A}{6}(\dot{\boldsymbol{x}}_1 + 2\dot{\boldsymbol{v}}_2)$$

$$\boldsymbol{h}_1 \equiv \frac{1}{6}\boldsymbol{j}_{ob}(2\omega_1 + \omega_2), \quad \boldsymbol{h}_2 \equiv \frac{1}{6}\boldsymbol{j}_{ob}(\omega_1 + 2\omega_2)$$

$$\boldsymbol{H}_1 \equiv \boldsymbol{R}_1 \boldsymbol{h}_1, \quad \boldsymbol{H}_2 \equiv \boldsymbol{R}_2 \boldsymbol{h}_2$$

$$\boldsymbol{P}_1 \equiv L_b p_1, \quad \boldsymbol{P}_2 \equiv L_b p_2$$

$$\boldsymbol{M}_1 \equiv L_b \boldsymbol{H}_1, \quad \boldsymbol{M}_2 \equiv L_b \boldsymbol{H}_2$$

$$t_b = \frac{1}{2}\dot{\boldsymbol{x}}_1{}^T \boldsymbol{p}_1 + \frac{1}{2}\boldsymbol{v}_2^{\mathrm{T}} \boldsymbol{p}_2 + \frac{1}{2}\omega_1^{\mathrm{T}} \boldsymbol{h}_1 + \frac{1}{2}\omega_2^{\mathrm{T}} \boldsymbol{h}_2$$

$$H_b = L_b t_b, \quad \boldsymbol{P}_b = L_b(\boldsymbol{p}_1 + \boldsymbol{p}_2) = \boldsymbol{P}_1 + \boldsymbol{P}_2$$

$$\boldsymbol{M}_b = L_b(\boldsymbol{H}_1 + \boldsymbol{H}_2 + x_1 \times p_1 + x_2 \times p_2) = \boldsymbol{M}_1 + \boldsymbol{M}_2 + x_1 \times \boldsymbol{P}_1 + x_2 \times \boldsymbol{P}_2 \tag{2.200}$$

Here, the energy increment becomes,

$$\Delta H_b = \Delta \boldsymbol{x}_1^{\mathrm{T}} \boldsymbol{f}_1^x + \Delta \boldsymbol{x}_2^{\mathrm{T}} \boldsymbol{f}_2^x + \alpha_1^{\mathrm{T}} \boldsymbol{f}_1^\alpha + \alpha_2^{\mathrm{T}} \boldsymbol{f}_2^\alpha \tag{2.201}$$

Therefore, the equivalent nodal force/tangential stiffness matrix is,

$$\boldsymbol{f}_1^x = \frac{\Delta \boldsymbol{P}_1}{\Delta t}, \quad \boldsymbol{f}_2^x = \frac{\Delta \boldsymbol{P}_2}{\Delta t} \tag{2.202}$$

$$\boldsymbol{f}_1^\alpha = \frac{\Delta \boldsymbol{M}_1}{\Delta t}, \quad \boldsymbol{f}_2^\alpha = \frac{\Delta \boldsymbol{M}_2}{\Delta t} \tag{2.203}$$

$$\boldsymbol{k}^{xx} \equiv \begin{bmatrix} \frac{\partial \boldsymbol{f}_1^x}{\partial \psi_1} & \frac{\partial \boldsymbol{f}_1^x}{\partial \psi_2} \\ \frac{\partial \boldsymbol{f}_2^x}{\partial \psi_1} & \frac{\partial \boldsymbol{f}_2^x}{\partial \psi_2} \end{bmatrix}, \qquad \boldsymbol{k}^{\phi\phi} \equiv \begin{bmatrix} \frac{\partial \boldsymbol{f}_1^\alpha}{\partial \beta_1} & \frac{\partial \boldsymbol{f}_1^\alpha}{\partial \beta_2} \\ \frac{\partial \boldsymbol{f}_2^\alpha}{\partial \beta_1} & \frac{\partial \boldsymbol{f}_2^\alpha}{\partial \beta_2} \end{bmatrix} \tag{2.204}$$

Finally, consider the case of location 5 where one end is a nodal point and the length changes. The energy, momentum, and angular momentum are the same as in location 4, but since L_b changes, the energy increment must be modified. To summarize the conclusions below, Eq. 2.160 of location 4 can be used as the conditional equation without modification.

$$\boldsymbol{j}_{ob} = \rho \begin{bmatrix} j_{11} & 0 & 0 \\ 0 & j_{22} & 0 \\ 0 & 0 & j_{11} + j_{22} \end{bmatrix}, \qquad L_b = L_2 - L_1$$

$$\boldsymbol{p}_1 \equiv \frac{\rho A}{6}(2\dot{\boldsymbol{x}}_1 + \dot{\boldsymbol{v}}_2), \quad \boldsymbol{p}_2 \equiv \frac{\rho A}{6}(\dot{\boldsymbol{x}}_1 + 2\dot{\boldsymbol{v}}_2)$$

$$\boldsymbol{h}_1 \equiv \frac{1}{6}\boldsymbol{j}_{ob}(2\omega_1 + \omega_2), \qquad \boldsymbol{h}_2 \equiv \frac{1}{6}\boldsymbol{j}_{ob}(\omega_1 + 2\omega_2)$$

$$\boldsymbol{H}_1 \equiv \boldsymbol{R}_1 \boldsymbol{h}_1, \qquad \boldsymbol{H}_2 \equiv \boldsymbol{R}_2 \boldsymbol{h}_2$$

$$\boldsymbol{P}_1 \equiv L_b p_1, \quad \boldsymbol{P}_2 \equiv L_b p_2$$

$$\boldsymbol{M}_1 \equiv L_b \boldsymbol{H}_1, \qquad \boldsymbol{M}_2 \equiv L_b \boldsymbol{H}_2$$

$$t_b = \frac{1}{2}\dot{\boldsymbol{x}}_1{}^T \boldsymbol{p}_1 + \frac{1}{2}\boldsymbol{v}_2^{\mathrm{T}} \boldsymbol{p}_2 + \frac{1}{2}\omega_1^{\mathrm{T}} \boldsymbol{h}_1 + \frac{1}{2}\omega_2^{\mathrm{T}} \boldsymbol{h}_2$$

$$H_b = L_b t_b, \quad \boldsymbol{P}_b = L_b(\boldsymbol{p}_1 + \boldsymbol{p}_2) = \boldsymbol{P}_1 + \boldsymbol{P}_2$$

$$\boldsymbol{M}_b = L_b(\boldsymbol{H}_1 + \boldsymbol{H}_2 + x_1 \times p_1 + x_2 \times p_2) = \boldsymbol{M}_1 + \boldsymbol{M}_2 + x_1 \times \boldsymbol{P}_1 + x_2 \times \boldsymbol{P}_2$$

$$f_b = \frac{1}{2}\left(\underline{\boldsymbol{p}_1^{\mathrm{T}}} \dot{\boldsymbol{x}}_1 + \underline{\boldsymbol{p}_2^{\mathrm{T}}} \dot{\boldsymbol{x}}_2 + \underline{\boldsymbol{h}_1^{\mathrm{T}}} \dot{\omega}_1 + \underline{\boldsymbol{h}_2^{\mathrm{T}}} \dot{\omega}_2\right) - \frac{\beta_1^{\mathrm{T}} + \beta_2^{\mathrm{T}}}{4}\left(\underline{\boldsymbol{p}_1} \times \dot{\boldsymbol{x}}_1 + \underline{\boldsymbol{p}_2} \times \dot{\boldsymbol{x}}_2\right)$$

$$\Delta H_b = \Delta \boldsymbol{x}_1^T \boldsymbol{f}_1^x + \Delta \boldsymbol{x}_2^T \boldsymbol{f}_2^x + \alpha_1^T \boldsymbol{f}_2^\alpha + \alpha_2^T \boldsymbol{f}_2^\alpha + f_\phi \Delta \phi \tag{2.205}$$

Therefore, the equivalent nodal force and tangential stiffness matrix are,

$$\boldsymbol{f}_1^x = \frac{\Delta \boldsymbol{P}_1}{\Delta t}, \qquad \boldsymbol{f}_2^x = \frac{\Delta \boldsymbol{P}_2}{\Delta t} \tag{2.206}$$

$$\boldsymbol{f}_1^\alpha = \frac{\Delta \boldsymbol{M}_1}{\Delta t} + \frac{1}{8}\Delta L_b \left(\underline{\boldsymbol{p}_1} \times \dot{\boldsymbol{x}}_1 + \underline{\boldsymbol{p}_2} \times \dot{\boldsymbol{x}}_2\right) \tag{2.207}$$

$$\boldsymbol{f}_2^\alpha = \frac{\Delta \boldsymbol{M}_2}{\Delta t} + \frac{1}{8}\Delta L_b \left(\underline{\boldsymbol{p}_1} \times \dot{\boldsymbol{x}}_1 + \underline{\boldsymbol{p}_2} \times \dot{\boldsymbol{x}}_2\right) \tag{2.208}$$

$$f_\phi = \frac{\Delta L_b}{\Delta \phi} f_b \tag{2.209}$$

$$\boldsymbol{k}_{11}^{xx} \equiv \frac{\partial \boldsymbol{f}_1^x}{\partial \psi_1}, \quad \boldsymbol{k}_{12}^{xx} \equiv \frac{\partial \boldsymbol{f}_1^x}{\partial \psi_2}, \quad \boldsymbol{k}_{1\phi}^{x\phi} \equiv \frac{\partial \boldsymbol{f}_1^x}{\partial \varphi} \tag{2.210}$$

$$\boldsymbol{k}_{21}^{xx} \equiv \frac{\partial \boldsymbol{f}_2^x}{\partial \psi_1}, \quad \boldsymbol{k}_{22}^{xx} \equiv \frac{\partial \boldsymbol{f}_2^x}{\partial \psi_2}, \quad \boldsymbol{k}_{2\phi}^{x\phi} \equiv \frac{\partial \boldsymbol{f}_2^x}{\partial \varphi} \tag{2.211}$$

$$\boldsymbol{k}_{11}^{\alpha x} \equiv \frac{\partial \boldsymbol{f}_1^\alpha}{\partial \psi_1}, \quad \boldsymbol{k}_{12}^{\alpha x} \equiv \frac{\partial \boldsymbol{f}_1^\alpha}{\partial \psi_2}, \quad \boldsymbol{k}_{11}^{\alpha\alpha} \equiv \frac{\partial \boldsymbol{f}_1^\alpha}{\partial \beta_1}, \quad \boldsymbol{k}_{12}^{\alpha\alpha} \equiv \frac{\partial \boldsymbol{f}_1^\alpha}{\partial \beta_2}, \quad \boldsymbol{k}_{1\phi}^{\alpha\phi} \equiv \frac{\partial \boldsymbol{f}_1^\alpha}{\partial \varphi} \tag{2.212}$$

$$\boldsymbol{k}_{21}^{\alpha x} \equiv \frac{\partial \boldsymbol{f}_2^\alpha}{\partial \psi_1}, \quad \boldsymbol{k}_{22}^{\alpha x} \equiv \frac{\partial \boldsymbol{f}_2^\alpha}{\partial \psi_2}, \quad \boldsymbol{k}_{21}^{\alpha\alpha} \equiv \frac{\partial \boldsymbol{f}_2^\alpha}{\partial \beta_1}, \quad \boldsymbol{k}_{22}^{\alpha\alpha} \equiv \frac{\partial \boldsymbol{f}_2^\alpha}{\partial \beta_2}, \quad \boldsymbol{k}_{2\phi}^{\alpha\phi} \equiv \frac{\partial \boldsymbol{f}_2^\alpha}{\partial \varphi} \tag{2.213}$$

$$\boldsymbol{k}_{\phi 1}^{\phi x} \equiv \frac{\partial f_\phi}{\partial \psi_1}, \quad \boldsymbol{k}_{\phi 2}^{\phi x} \equiv \frac{\partial f_\phi}{\partial \psi_2}, \quad \boldsymbol{k}_{\phi 1}^{\phi\alpha} \equiv \frac{\partial f_\phi}{\partial \beta_1}, \quad \boldsymbol{k}_{\phi 2}^{\phi\alpha} \equiv \frac{\partial f_\phi}{\partial \beta_2}, \quad \boldsymbol{k}_{\phi\phi}^{\phi\phi} \equiv \frac{\partial f_\phi}{\partial \varphi} \tag{2.214}$$

2.4.7. State Transition of Boom Elements

Assuming no boom unwinding, there are five types of state transition patterns from time *t* to *t*+Δ*t*.

(Type 1)	Location 1	→ Location 1
(Type 2)	Location 1	→ Location 2 + Location 3
(Type 3)	Location 2 + Location 3	→ Location 2 + Location 3
(Type 4)	Location 2 + Location 5	→ Location 5
(Type 5)	Location 4	→ Location 4

The formulations of the equivalent nodal forces and the tangential stiffness matrix for each type are described below. First, for type 1, the formulations are the same as those in Section 2.4.1.7, Eqs. 2.189 to 2.194. Type 2 can be expressed as the sum of the wrap-around part of Eqs. 2.189 to 2.194 and the straight part of Eqs. 2.202 to 2.204. However, since node 2 passes through the peeling point, the Newton iteration must become,

$$\psi_2 = \frac{1}{2}\left(x_2 - \underline{x_p}\right), \quad \dot{x}_2 = \frac{4}{\Delta t}\psi_2 - \boldsymbol{v}_p \tag{2.215}$$

Type 3 can be formulated in the same way as type 2, except that node 2 does not pass through the peeling point. Type 4 can be described as the sum of location 2 for the wrapped part and location 5 for the straight part. Note that node 1 passes through the peeling point, so as before, note the following.

$$\psi_1 = \frac{1}{2}\left(x_1 - \underline{x_p}\right), \quad \dot{x_1} = \frac{4}{\Delta t}\psi_1 - \boldsymbol{v}_p \tag{2.216}$$

Finally, node 1 of this element is the same node as node 2 of the neighboring element on the root side of the hub element, therefore, type 5 can be expressed as the sum of the winding part of Eqs. 2.189 to 2.194 and the straight part of Eqs. 2.206 to 2.214.

2.4.8. Friction Model Between Guide Roller Element and Boom

The friction between the guide roller and the boom element is given as an external force with respect to the relative rotation angle ϕ of the hub, resulting in a decrease in the mechanical energy of the entire system. We assume that the vertical drag force N that the boom element receives from the guide rollers gives the bending moment M_p of the boom element at the point of detachment from the guide rollers, thus

$$N = \frac{M_p}{l_p} \tag{2.217}$$

From Eq. 2.134 the friction force can be approximated as,

$$M_p \approx M_{\text{free}}\left(\kappa_p\right), \quad \kappa_p = \frac{1}{r_p} \tag{2.218}$$

The frictional force can then be expressed as,

$$F = -\text{sign}(\phi)\mu N \tag{2.219}$$

The incremental work due to friction is then approximated by,

$$\Delta W \approx \Delta L_p F = -\text{sign}(\phi)\mu N \Delta L_p = -\text{sign}(\phi)\mu \frac{M_p}{l_p}\frac{\partial \widetilde{L_p}}{\partial \phi}\Delta\phi \approx -\text{sign}(\phi)\mu \frac{M_p}{l_p}\frac{\partial L_p}{\partial \phi}\Delta\phi \tag{2.220}$$

Thus, for the frictional force with the guide roller and the frictional torque with respect to ϕ can be approximated.

$$F_\phi = -\text{sign}(\phi)\frac{M_p}{l_p}\frac{\partial L_p}{\partial \phi} \tag{2.221}$$

2.4.9. Reverse Bending of the Convex Tapes

In the case of bending of the convex tapes in the outer direction, the strain energy generated will vary. In the pre-deformed state, the case where the inner part of the arc is bent so that it is on the outer surface when it is wound onto the cylinder is defined as a reverse bending. Forward bending is defined as bending the inner part of the arc to the inner surface. (Fig. 2.8) In general, the strain energy generated when bending a convex tape onto a plane can be expressed as

$$\pi = \frac{A_0}{2}\frac{1}{R}\left(\frac{1}{R} + \ \nu\kappa\right)(1 - A_0)$$

$$\text{where,} \quad A_0 = 2bD\left(1 - \frac{h^2}{12R^2}\right) \tag{2.222}$$

However,

$$A_1 = 2\left(\frac{2(\cosh\eta - \cos\eta)}{\eta(\sinh\eta + \sin\eta)}\right) \tag{2.223}$$

D is the radius of the arc in equation (4.5) and *R* is the radius of the arc of the convex tape before deformation.

From Eq. 2.222, the strain energy is greater in reverse bending. In other words, the strain energy generated in the boom is the sum of the strain energies calculated for each value of the inner and outer convex tapes from Eq. 2.133.

$$\Pi_{total} = \ \pi(\kappa_{in}) + \ \pi(\kappa_{out}) \tag{2.224}$$

From Equation 2.224, the strain energy generated in the entire boom is Π_{total}.

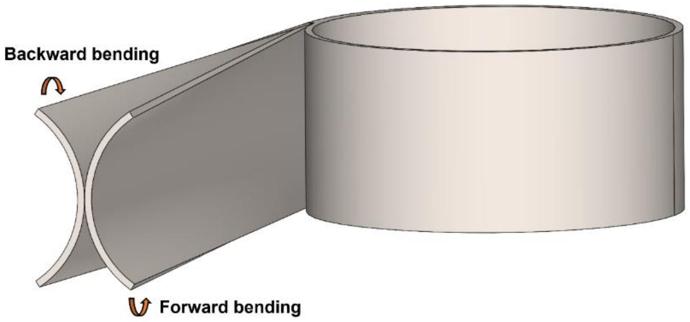

Fig. 2.9: Bending direction of convex tapes at stowage.

2.5. Implementation of Contact Restriction Model between the Hub and the Membrane Elements

Up to this point, element tangibility is not considered. Elements can cross through each other freely. This is not ideal for the deployment of a membrane. Usually for space missions, gossamer structures are advantageous due to their light and small storage capabilities before their deployments. This is also the case for DOM2500.

The membrane in DOM2500 is first folded from the square state down into a star shape. And then this state is placed around the central hub of DOM2500 and rotationally folded to fit within the housing. Figure 2.9 shows the membrane folded and inside DOM2500 in addition to the folding pattern visualized with the help of a paper model. The membrane is considered in 4 sections with the division lines at the diagonals. Each section is folded with mountains and valleys horizontal to their respective edge. The complete membrane is then folded down to a square hole with four lumps of membrane existing out of this hole in the diagonal direction starting from its corners as shown in Fig. 2.6 (e). This shape is then wrapped around a hub. Because the hub is considerably smaller than the inner hole, the shape is reduced further into a right-angled star shape first to achieve contact with the hub as shown in Fig. 2.6. (f). Then the membrane is simply wrapped around.

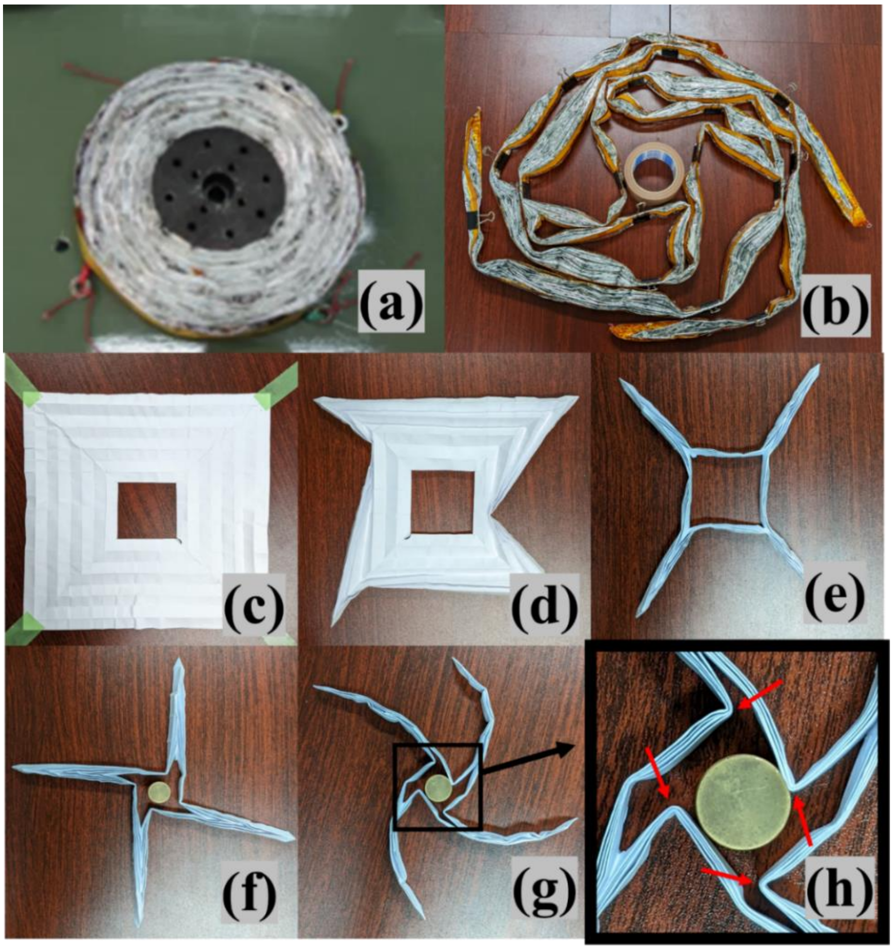

Figure 2.10: DOM2500 sail in folded configurations: (a) completely folded and wrapped around DOM2500 inner hub, (b) folded sail held down with clips, (c) paper model of the deployed sail, (d) paper model of the sail partially folded, (e) paper model of the sail folded down to star shape, (f) paper model of the folded sail in right-angled star shape, (g) paper model of the folded sail that with rotation around hub initiated and (h) a zoomed in view of (g).

Similarly folded membrane is modeled for analysis. However, the elements of the membrane are free to cross through each other and the hub during the simulation, whereas they will be physically obstructed to do so in the real case. Implementing this contact restriction between every element is computationally too demanding, however, implementing a restriction between the hub and the membrane is feasible. This will then facilitate the rotational unwrapping around the hub into the simulation.

In order to achieve this kind of restriction, a model is prepared which detects whether the nodes of a membrane element are within the hub element. There are four cases for this contact condition. Figure 2.10 show these cases. For case 1, no contact is detected therefore no changes are made. For case 2, both nodes of the membrane element are detected to be in the hub, and for cases 3 and 4 only one node of the element is detected to be in the hub. Afterwards, the nodal force $\boldsymbol{f_z}$ of the nodes detected to be within the hub are modified as follows:

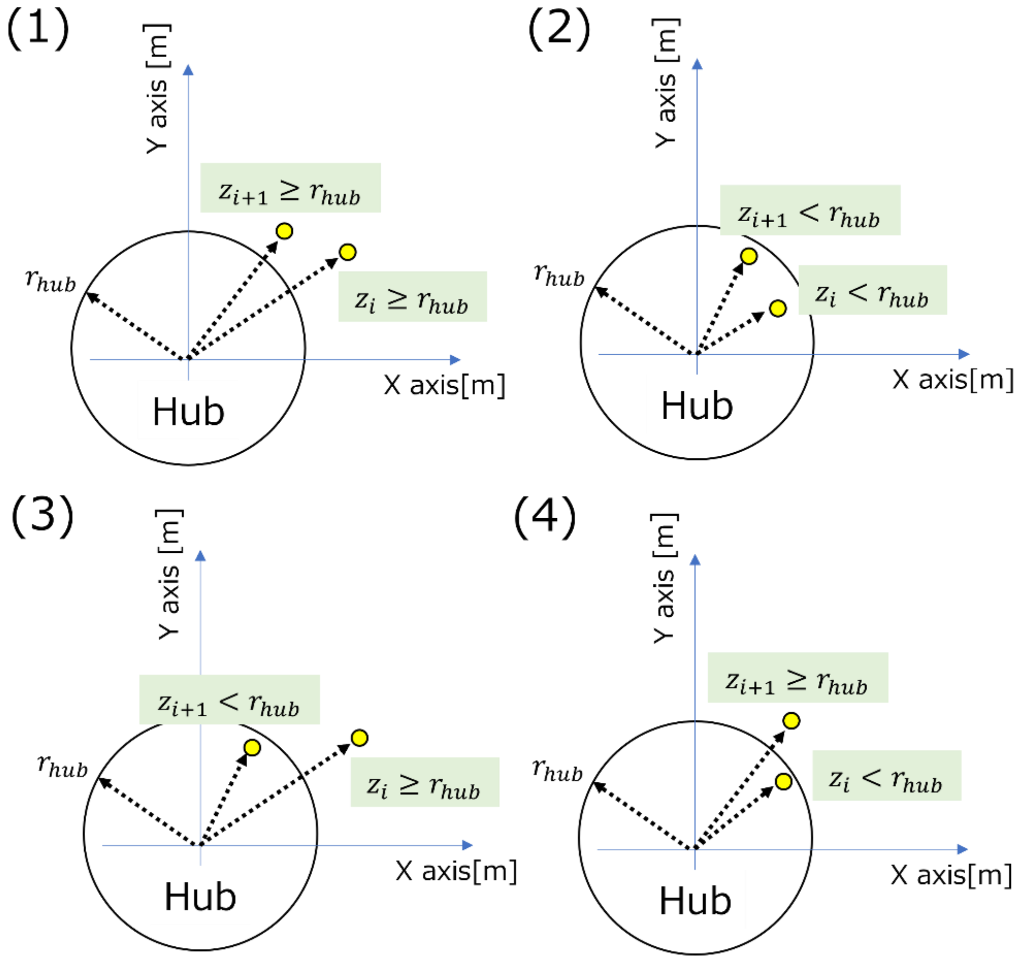

Figure 2.11: Four cases of contact detection between membrane element nodes and the hub model.

$$\boldsymbol{f_z}^{\boldsymbol{t+1}} = \boldsymbol{f_z}^{\boldsymbol{t}} + ku_b\boldsymbol{e} + \frac{\left\{kd\left(\frac{\boldsymbol{z_{i+1}}}{|\boldsymbol{z_{i+1}}|} - \frac{\boldsymbol{z_i}}{|\boldsymbol{z_i}|}\right)\boldsymbol{e}_{i+1}\right\}}{\Delta t} \tag{2.225}$$

The tangential stiffness matrix $\boldsymbol{K_{zz}}$ then becomes:

$$\boldsymbol{K_{zz}} = \frac{\partial \boldsymbol{f_z}}{\partial z}$$

$$= k\{(\boldsymbol{e_{i+1}} \times \boldsymbol{e_i}) + u_b \boldsymbol{K_G}\} + \left\{\frac{[kd(\boldsymbol{e_{i+1}} \times \boldsymbol{e_i})\boldsymbol{K_G}]}{\Delta t} + \mathbf{2} * (\boldsymbol{e_{i+1}} \times \boldsymbol{e_i})\right\} \quad (2.226)$$

where,

$$u_b = \left|\frac{\boldsymbol{z_{i+1}} + \boldsymbol{z_i}}{2}\right| - r_{hub} \quad (2.227)$$

$$\boldsymbol{K_G} = \frac{\left\{\begin{bmatrix} \mathbf{1} & \mathbf{1} \\ \mathbf{1} & \mathbf{1} \end{bmatrix} - (\boldsymbol{e_{i+1}} \times \boldsymbol{e_i})\right\}}{\left|\frac{\boldsymbol{e_i} + \boldsymbol{e_{i+1}}}{2}\right|} \quad (2.228)$$

$$\boldsymbol{e} = \frac{\frac{\boldsymbol{z_{i+1}} + \boldsymbol{z_i}}{\mathbf{2}}}{\left|\frac{\boldsymbol{z_{i+1}} + \boldsymbol{z_i}}{\mathbf{2}}\right|} \quad (2.229)$$

Here, k and d are defined as contact and damping coefficients respectively and are arbitrarily introduced as variables. They represent the spring constant and the damping ratio for a spring if the hub is considered to be an omni-directional spring element. u_b is the difference from the hub radius, $\boldsymbol{K_G}$ is the stress stiffness or otherwise known as geometrical stiffness, $\boldsymbol{e}$ is the unit direction vector and Δt is the integration time used in the iterative calculation.

2.6. Results of Simulation

2.6.1. Results of Membrane Simulation

The sail in DOM is a 2.5 meter by 2.5 meter sail with a hole in the middle. Its folding width is 2 cm, and differing from many other designs, it is a singular sail as opposed to 4 different sails each occupying a quadrant between two convex tapes extending in the diagonal direction. The sail is pulled by the Dyneema wire attached to the tip of the convex tapes. As a first step, the simulation will need a folded model of the sail as a starting point, a deployed model of the sail as an end point to converge to, and a pulling force from the corners simulating self-extending convex tape dynamics. The convex tapes themselves and the connecting Dyneema wire between the tip of the convex tapes and the corners of the sail are not included in the model at this stage. Instead, the force is directly applied to the nodes at the corners of the sail. Additionally, the sail folding width is 2 cm in the actual sail as stated before, but for the simulation a folding width of 10 cm with partial increase in mesh resolution is adopted. This is due to significant calculation times and unconverging calculation steps due to large element and node numbers. With a mesh the size of the real folding width of 2 cm, running a single simulation was projected to cost 2 months in real time. This duration was decreased to as short as 25 hours with the adopted 10 cm mesh size. After every parameter is tuned with a course mesh, the simulation can then be run for the long duration of weeks for a final result with a finer mesh size reflecting the reality better.

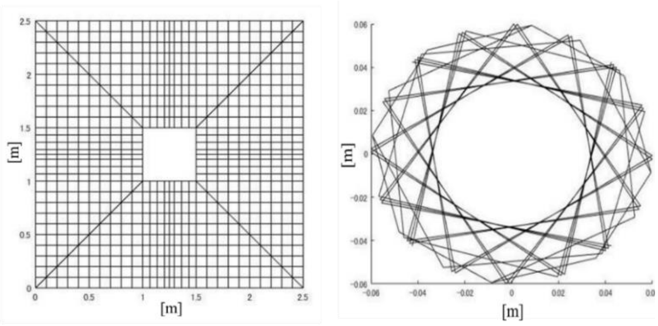

(a) **(b)**

Figure 2.12: Model of the sail: (a) deployed configuration and (b) completely folded inside the hub configuration.

For the force profile, a constant pulling force in all four corners in the diagonal outwards directions are applied to the corner nodes. The magnitude of this force is iteratively decided to best match the time until full deployment on ground and in space is achieved which is about 0.7 to 0.8 seconds. The force that is used for these simulations to achieve full deployment within 0.7 to 0.8 seconds is 1.5×10^{-5} kgm/s^2. Figure 2.12 shows the deployment sequence of the initial simulation result. The membrane properties used in this simulation are summarized in Table 2.1. Some parameters are references from references [81,82].

Table 2.1: Membrane properties used in the simulation.

Property [SI Unit]	Value
Young Modulus [Pa]	3.00×10^9
Density [kg/m^3]	1380
Poisson`s Ratio [-]	0.30
Thickness [µm]	25
Compression Stiffness Ratio (R_{CS}) [-]	1.00×10^{-7}
Contact Coefficient (k) [-]	0
Damping Coefficient (d) [-]	0
Folding Width [cm]	10
Fold Number	10

2.6.2. Results of Convex Tape Simulation

Four booms are placed to extend diagonally to achieve full deployment of membrane instead of a constant force. Each boom consists of two convex tapes. The detailed characteristic

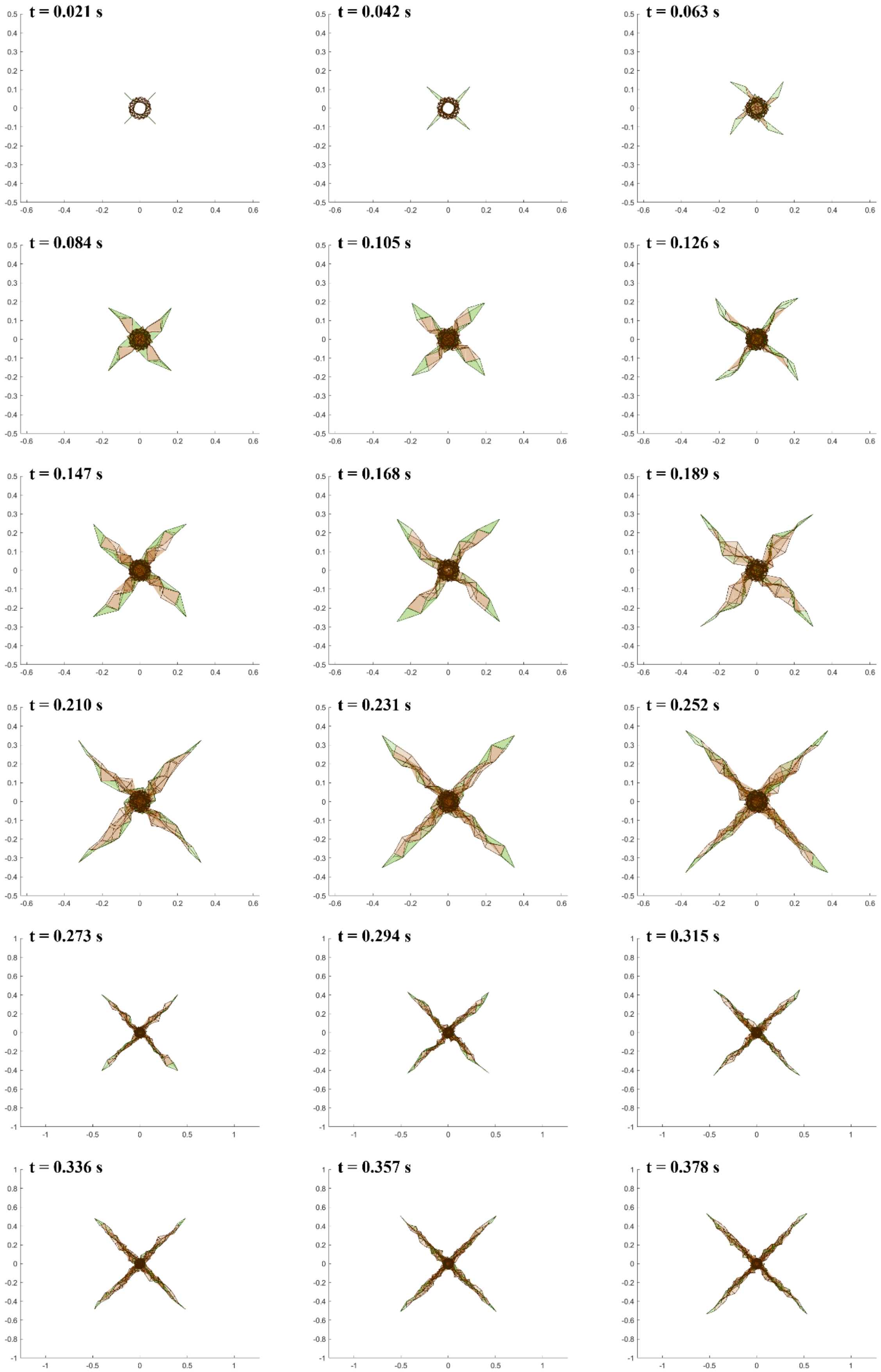
t = 0.021 s
t = 0.042 s
t = 0.063 s
t = 0.084 s
t = 0.105 s
t = 0.126 s
t = 0.147 s
t = 0.168 s
t = 0.189 s
t = 0.210 s
t = 0.231 s
t = 0.252 s
t = 0.273 s
t = 0.294 s
t = 0.315 s
t = 0.336 s
t = 0.357 s
t = 0.378 s

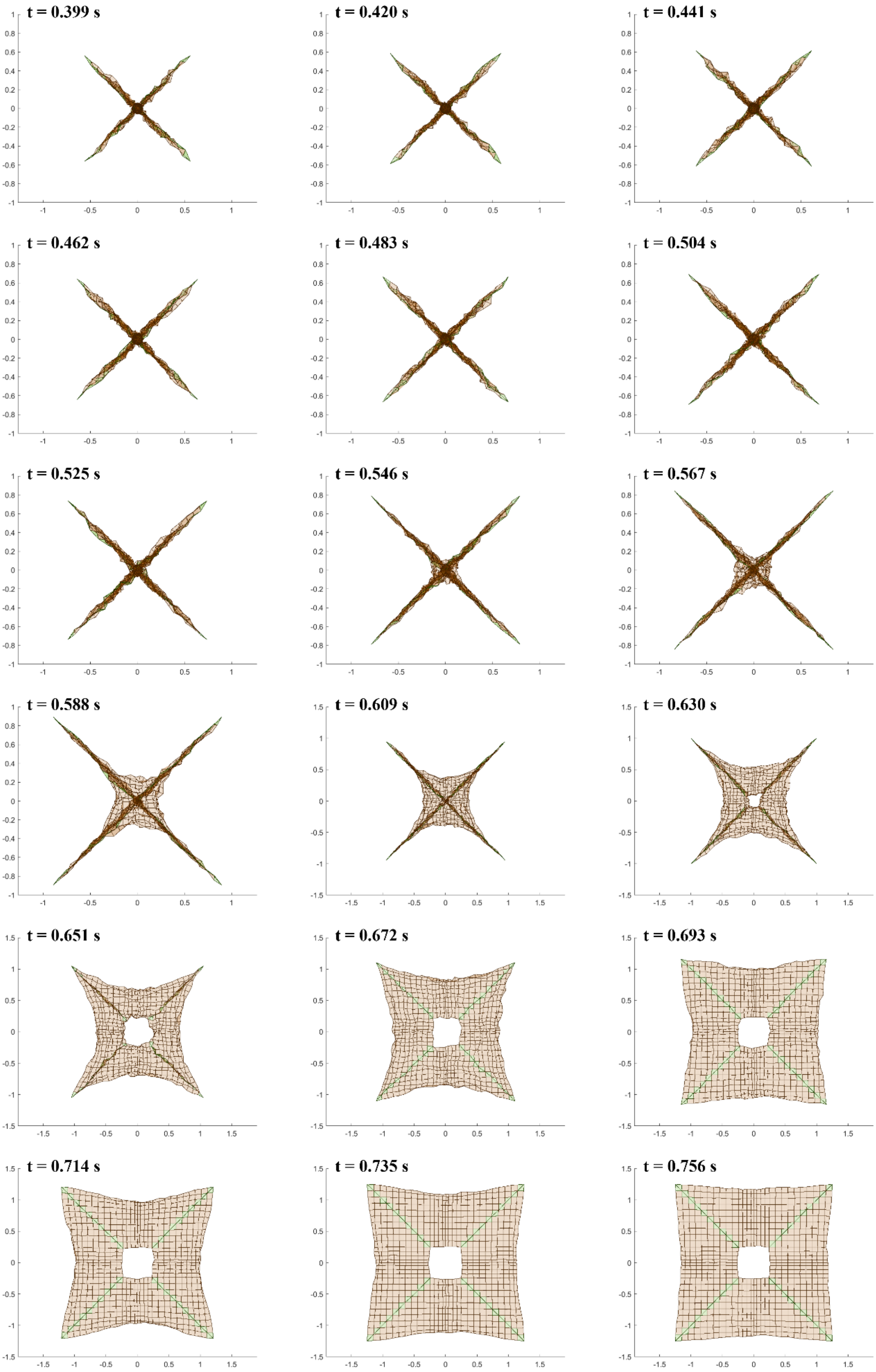

Figure 2.13: Initial simulation result of the DOM sail deployment with unrefined parameters.

Table 2.2: Convex tape characteristic values.

Property [SI Unit]	Value
Modulus of Longitudinal Elasticity [Pa]	200×10^9
Modulus of Lateral Elasticity [Pa]	78.5×10^9
Density[kg/m^3]	960
Poisson`s Ratio[-]	0.30
Damping Ratio[-]	0
Convex Tape Thickness [μm]	12
Radius of Convex Tape Arc [mm]	13.8
Height of Convex Tape [mm]	5
Flattened Width of Convex Tape [mm]	23
Internal Angle of Convex Tape [deg]	111
Length of each Convex Tape [m]	1.9

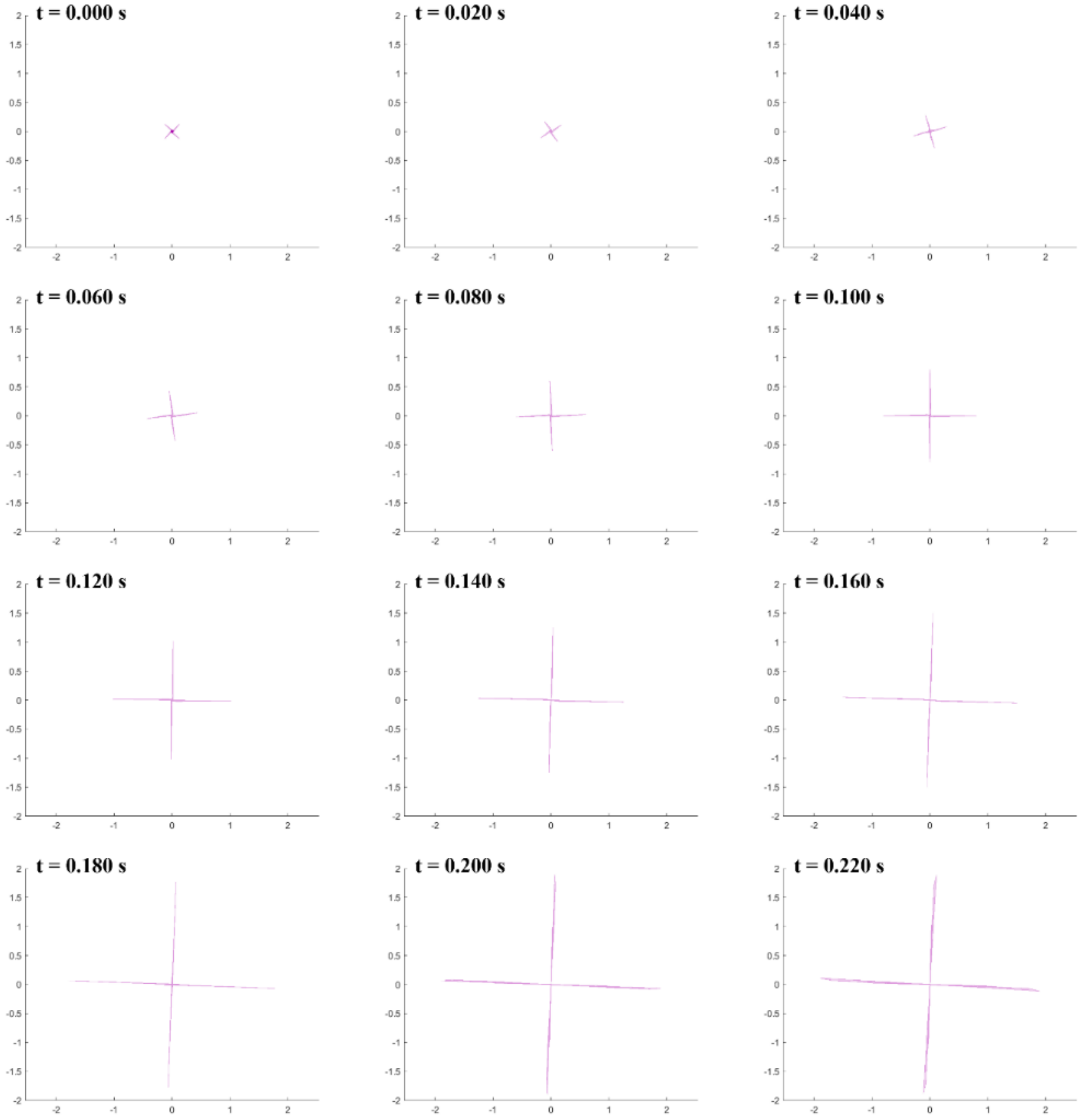

Figure 2.14: Extension sequence of the convex tapes.

values of the convex tape are shown in Table 2.2. The boom itself is modeled by dividing a single boom into 10 beam elements. The extension sequence is shown in Fig. 2.13.

2.6.3. Results of Fusion Model

The membrane deployment model and the convex tape extension model can be fused into a singular model using cable elements as connection between the tips of the convex tapes and the corners of the membrane. In the resultant fusion model, the membrane is intended to be deployed through the self-extending force of the convex tapes instead of pre-defined constant pulling force. Figure 2.14 shows the initial state of this model and Fig. 2.15 shows the initial deployment result of this model. The convex tape model is placed below the membrane model instead of superimposing the two models.

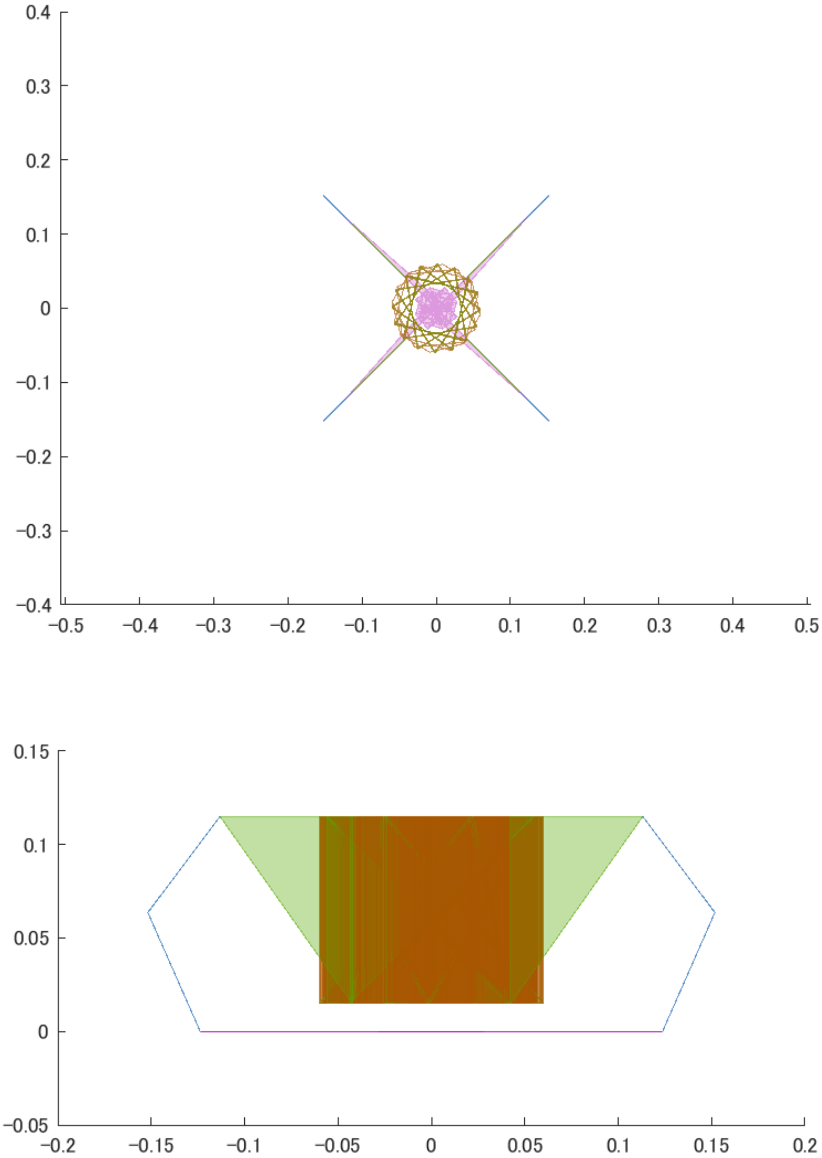

Figure 2.15: Top and side view of the initial state of the fused model.

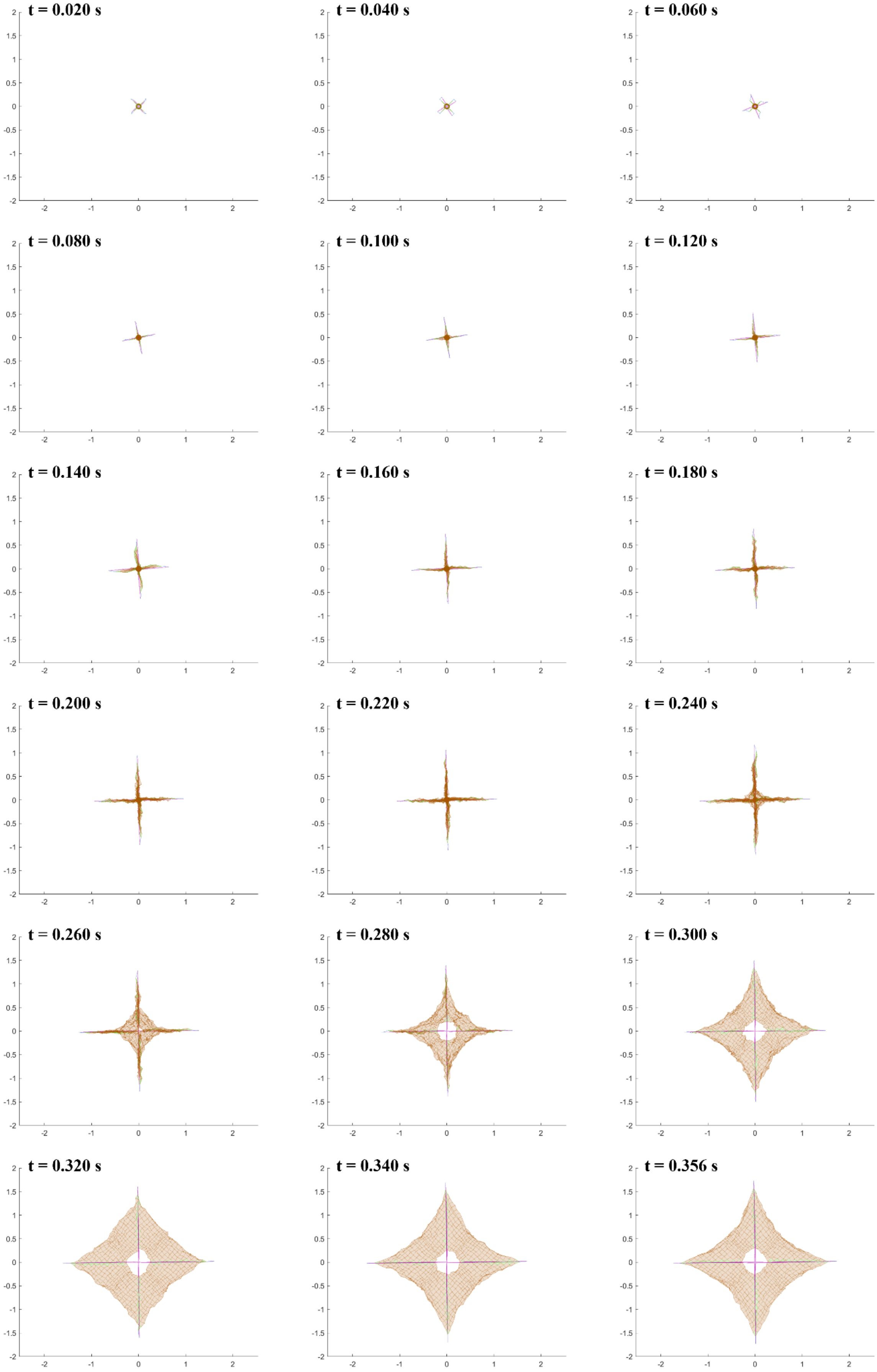
t = 0.020 s
t = 0.040 s
t = 0.060 s
t = 0.080 s
t = 0.100 s
t = 0.120 s
t = 0.140 s
t = 0.160 s
t = 0.180 s
t = 0.200 s
t = 0.220 s
t = 0.240 s
t = 0.260 s
t = 0.280 s
t = 0.300 s
t = 0.320 s
t = 0.340 s
t = 0.356 s

Figure 2.16: Deployment sequence of the fused model.

2.7. Summary

In this chapter, a mathematical model is presented for the simulation of membrane deployment behavior using convex tapes as the main force generation. Using conventional tension field theory as the basis, wrinkle/slack theory is built and the virtual deformation model, and then the stiffness reduction model that are used in this study are introduced for the membrane model. The wrinkle/slack criterion and the wrinkle/slack conditions are defined. In the stiffness reduction model in section 2.2.9, the parameters of ε_1 and ε_2 are newly introduced and hereinafter they will be referred to as the compressive stiffness ratio R_{cs}. Afterwards, the energy momentum method is implemented to increase computational convergence.

Following this, a convex tape model is presented as the main generation of pulling force for the membrane model deployment. In this model, a boom consisting of beam elements are generated and extended in a fixed direction. The strain energy per unit length of the convex tapes for this boom is calculated. This normalized strain energy is equivalent to the self-extending force of the convex tapes and is the deciding factor for the extension speed, and the time it takes for the completion of the extension.

Afterwards, the membrane model is improved with the addition of the contact restriction conditions between the membrane elements and the central hub elements. The contact conditions are defined, and the nodal forces of the element nodes that are detected to be within the hub are modified to push the nodes outwards. Two parameter coefficients k and d are introduced for this modification. They represent the spring constant and the damping ratio if this restriction is to be compared to the implementation of an omni-directional spring at the central hub element. Contact coefficient k and damping coefficient d will be the deciding factors on how much the nodes will be pushed out and consequently, how much rotational movement will be induced to the membrane during the deployment analysis.

3. Development of Separable De-Orbit Mechanism (SDOM)

Separable De-Orbit Mechanism (SDOM) is the name of the module that is developed for the specific pre-mission of ALE-1 to maneuver it and relocate to a lower orbit than its initial launch orbit. In this chapter design requirements, mission plan, system design, and mechanical design of SDOM are introduced.

3.7. Design Requirements

There are 5 design requirements for SDOM. Each of these requirements are described in the following subsections.

3.7.1. Separability

The most important design criterion for this proposed orbital maneuver system using a drag sail is separability. Drag sails are designed to completely de-orbit a satellite after its mission is completed. In fact, drag sails are designed with many safety measures to ensure this complete de-orbiting. In the case of only an altitude change, de-orbiting needs to stop after the desired lower altitude is reached. If not, the mission life on the reached lower altitude will be extremely short, due to exponential nature of de-orbiting rate at different altitudes due to atmospheric density. The easiest solution is to separate the drag sail from the satellite, so the generated drag force on the sail no longer applies to the satellite, but only to the sail itself. Since the ballistic coefficient of the sail side will be decreased by many folds due to less mass, it will de-orbit and burn up at re-entry and not pose further space debris. On the other hand, the satellite will have a much higher ballistic coefficient due to less area. Therefore, it will stay in-orbit longer, to conduct its main mission. Therefore, the upgraded system must have a function to separate the drag sail when the operator so desires.

3.7.2. Operability

Second most important design criterion is to have the satellite be operable even during the de-orbiting phase. Usually drag sails deploy after the satellite mission is finished, and the satellite is already considered to be debris at that point, however in the case of ALE-1, the satellite must still be able to communicate with ground station and generate enough power through solar cells to stay alive. If the sail is deployed immediately at one of the surfaces of the satellite, it is possible that it may interfere with antenna patterns and hinder the communication. Additionally, the solar cells around the satellite will be cut of from sunlight around half of the time on average considering the tumbling satellite model for analysis. However, this does not mean we can move the sail as far as possible. In fact, it should be as close to the satellite as possible that would let sufficient power generation happen. The intended way to move the sail away is through the use of a deployable boom consisting of convex tapes. It is common knowledge that convex tapes get more susceptible to bending the longer they get. Therefore, it is necessary to keep this boom length to the allowable minimum. After running simulations on the generated power in orbit, 2.5 m was decided for a good compromise between power generation and rigidity of the boom.

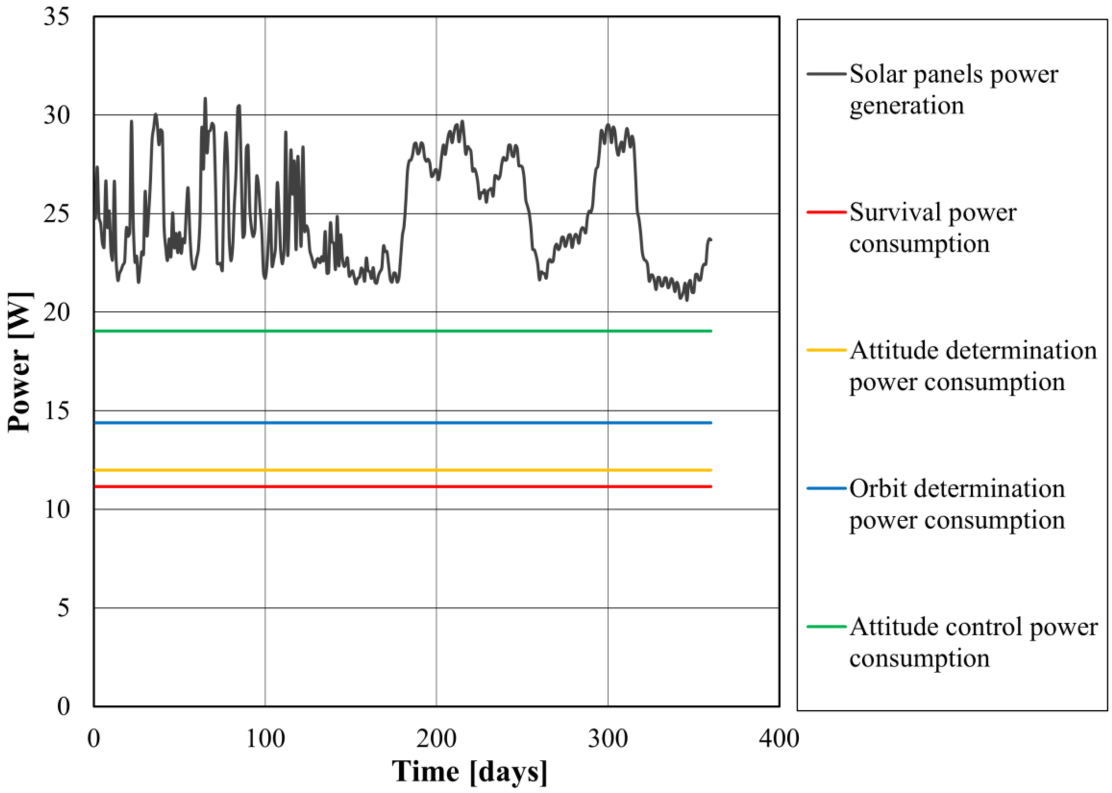

Figure 3.1: Daily mean solar power generation and its comparison to various daily mean power consumption levels for micro-satellite ALE-1 de-orbiting with a 2.5 m boom. (©JSASS)

Fig. 3.1 shows the results of in orbit power generation simulation with a sail that is 2.5 m away from the satellite. Here it is important to note that the sail size for this simulation was set to 2.5 m by 2.5 m which is the size of the sail in DOM2500. DOM2500 was chosen to be utilized due to mass budget restrictions. Although DOM4500 would yield a faster de-orbiting time, it was too big for the specific mission of ALE-1. DOM500, DOM1000 and DOM1500 on the other hand, are too small to effectively de-orbit a 70kg class micro-satellite from 500 km orbit. In Fig. 2.1 we see, power consumption levels for survival, with attitude determination available, with orbit determination available, and with attitude control available for the satellite. The power generation is always above all these consumption levels. Therefore, the with a 2.5 m long boom, and a 2.5 m by 2.5 m large sail, ALE-1 is estimated to have access to sufficient solar power generation even without any attitude altering inputs.

3.7.3. Passive Stability

Another possible deciding factor for the boom length would be the stability of the satellite system. With a sail at a distance of 2.5 m from the satellite, the whole system can be considered a two-mass system. Two-mass systems are susceptible to gravity gradient forces. The torque induced from these forces would be destabilizing torque considering the drag force direction. Figure 3.2 shows two cases of gravity gradient stabilized system and weather-cock stabilized system. For systems that are cruising lower than 500 km altitude, the dominant forces become aerodynamic forces and gravity gradient components. If the system can be weather cock stabilized, the effective drag area for the satellite would be larger, and the total de-orbiting time would be less. However, if the system is gravity gradient stabilized, the drag sail would effectively be useless. Although neither of these forces are large enough to restrict active attitude control, it is still desirable to have the system passively stabilize towards the better option.

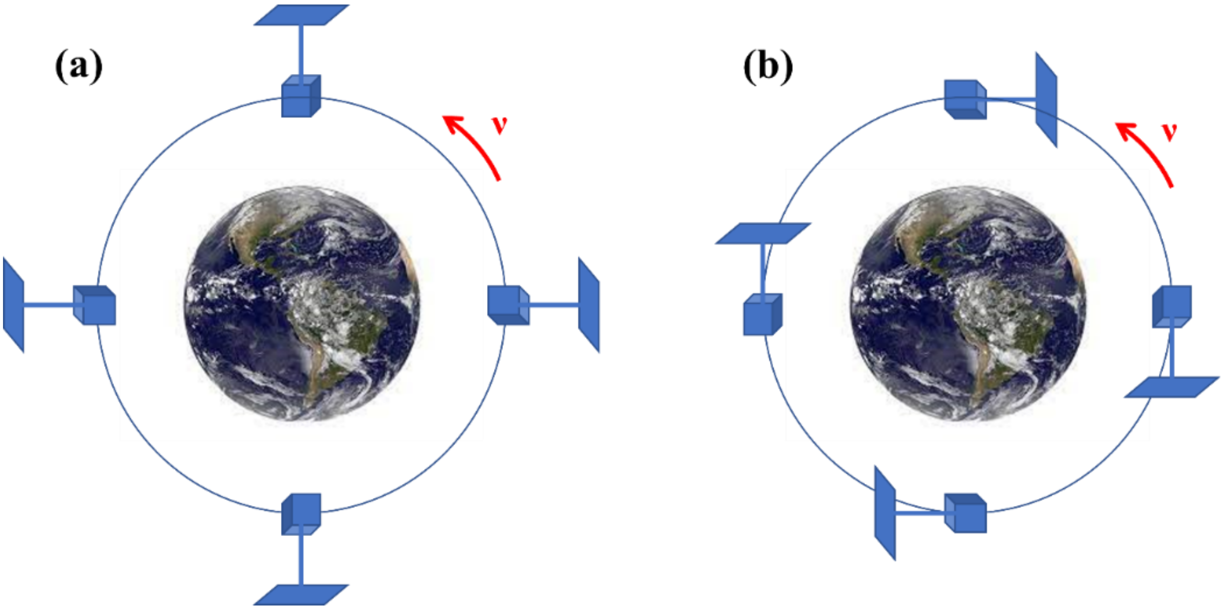

Figure 3.2: Representative stabilization states for ALE-1 with a deployed boom and sail with respect to the earth and the satellites velocity vector: (a) gravity gradient stable, (b) weather-cock stable.

Figure 3.3 shows the comparison of the magnitude of these forces with respect to the boom length for 500 km of altitude at weather cock stable attitude. T_{gg} stands for gravity gradient torque, and T_{ad} stands for aerodynamic drag torque. Up to 5 m of length for the boom, and for a sail of 2.5 m by 2.5 m, the aerodynamic drag torque is always larger by more than an order of magnitude than the gravity gradient torque. From this we see that a boom length of 2.5 m is acceptable for this system. The assumption for these results is that the center of pressure for this system will be close to the sail. Additionally, it is important to note that both of these torques heavily depend on the initial attitude of the satellite system. Fig 3.3 is the case for a satellite that is in the weather cock stable attitude. Since the system allows for active attitude control form the power generation aspect, the initial attitude can be altered to any attitude and these results can be achieved.

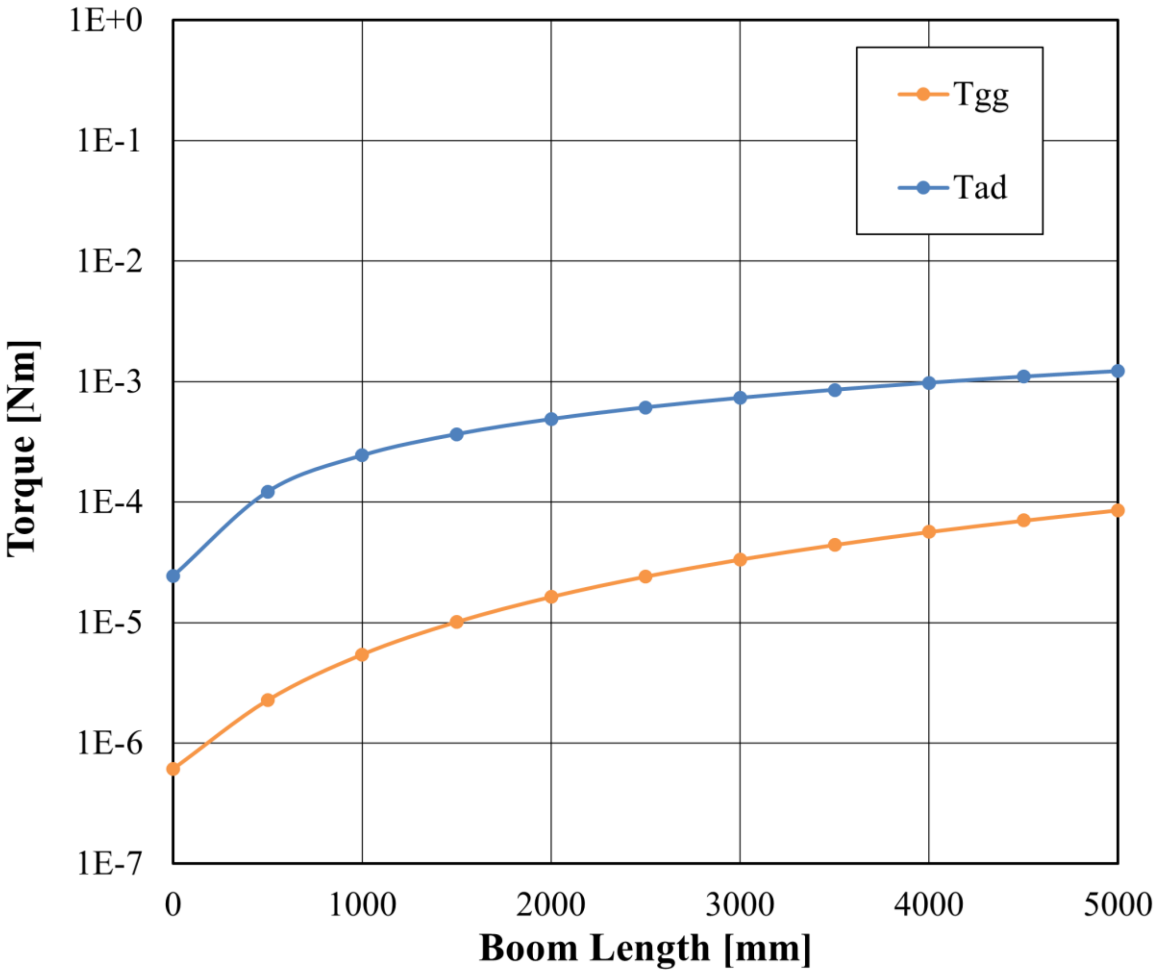

Figure 3.3: Comparison of the magnitudes of disturbance torques induces by aerodynamic drag forces and gravity gradient forces in relation to boom length with DOM2500 attached at the boom tip. (©JSASS)

3.7.4. Structural Resilience

The total mass budget spared for this system was 4 kg, of which 1.6 kg is used for DOM2500. Thus, for any added capability to the system the mass budget that can be used was 2.4 kg. As with all systems that are intended for space, this system also needed to withstand a rocket launch. When a rocket is launched, many forces act on it due to atmospheric resistance. This in turn induces a random vibration to its payloads specific to the rocket. All payloads need to clear the random vibration requirements to be able to ride the rocket. [83] Figure 3.4 shows the random vibration requirement for Epsilon 4.[84]

Although this profile is not a steep requirement for the satellite compared to other rockets, when considered in component levels it becomes concerning. Especially because a premature deployment of the sail, a premature deployment of the boom and a premature separation of the sail are all considered catastrophic failures not only for ALE-1 but for the whole rideshare on Epsilon 4. Therefore, it is necessary to make sure this system will safely go through with the rocket launch, and still be operable afterwards, all the while staying within the allowable mass budget. Additionally, it should not be disregarded that the operating conditions will be a thermal vacuum.

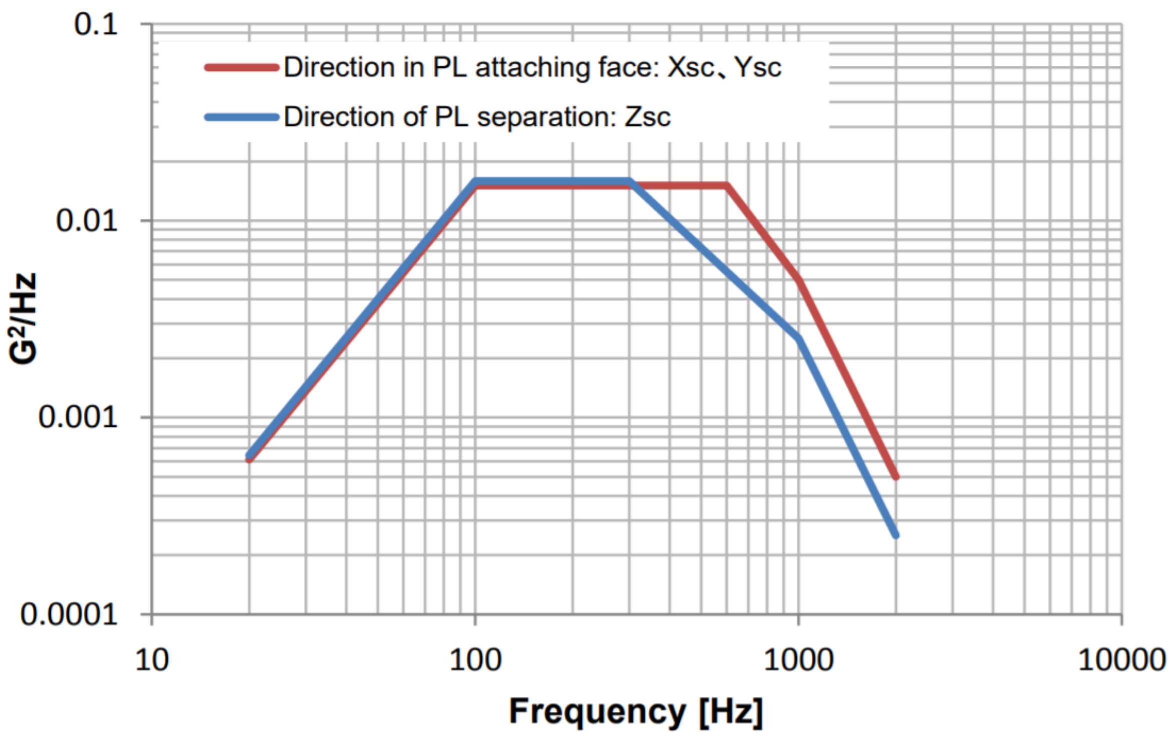

Figure 3.4: Random vibration requirement for the Epsilon launch Vehicle provided by JAXA. (©JAXA)

3.7.5. Observability

Lastly, this system should be observable for 2 reasons. First reason is the confirmation of all the intended functions. If this confirmation can be visual, it is even more reassuring. Second reason is the fact that this is a rare opportunity to send a drag sail to space and deploy it with a satellite that is still functional and is intended to stay functional. This rare chance provides a lot of opportunities to study the behavior of drag sails and systems that are utilizing drag sails. Therefore, for the further advancement of science and engineering, a system that is observed visually with capable tools is preferred over a system that only feedbacks whether functions are achieved or not.

3.8. Mission Plan

SDOM mission is planned in 5 phases. These phases are shown in Figure 3.5. Phase 0 is the “Default” phase where everything is safely stored inside a sturdy vessel fulfilling the structural resilience criteria discussed in section 3.1.3. At this phase, if the sail is initiated to deploy, it will not be able to deploy, if the boom is initiated to extend, it will not be able to extend and if the separation is initiated, nothing will separate. Phase 1 is the “Lid Open” phase. This is the phase where the lid is opened to prepare for the subsequent phases. Phase 2 is “Extension” phase where we extend a boom that is 2.5 m as the design criteria of operability in section 3.1.2. demands and passive stability in section 3.1.3. complies. At the base of this boom is the Micro-satellite ALE-1 and at the tip of this boom is the DOM2500. Phase 3 is the “Deployment” phase where the drag sail inside of DOM2500 is deployed perpendicular to the extended boom in the previous phase. This phase will last until a desired orbital altitude is reached. In the case of ALE-1 this will be an orbit that is lower than ISS throughout. Finally phase 4 is the “Separation” phase where the drag sail is separated together with the extended boom to fulfill the separability criteria discussed in section 3.1.1. Afterwards, the empty vessel stays at the satellite with no function, and the separated boom and sail are anticipated to quickly de-orbit and not cause any further debris.

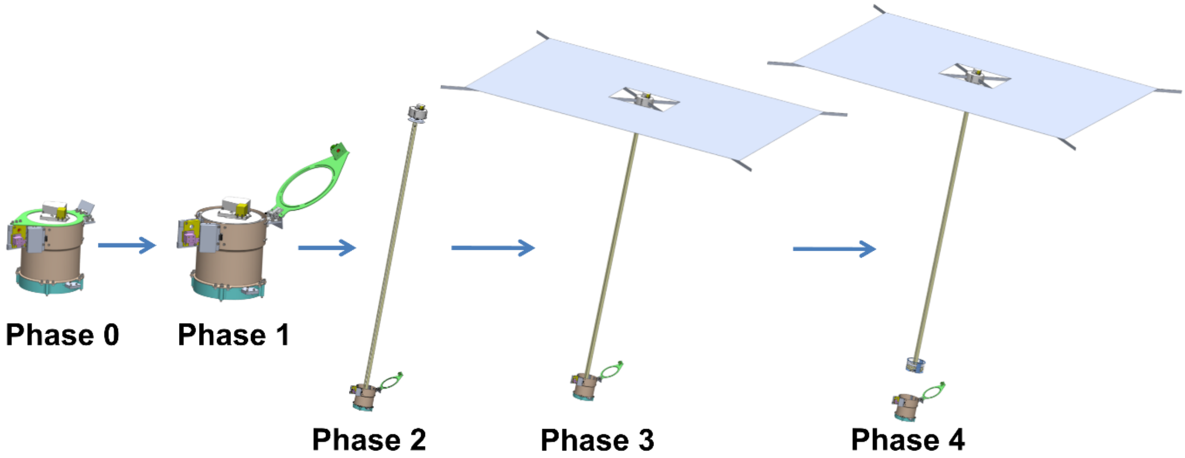

Figure 3.5: The phases of SDOM mission: (Phase 0) Storage phase, (Phase 1) Lid Open phase, (Phase 2) Extension phase, (Phase 3) Deployment phase and (Phase 4) Separation phase. (©IEEE)

With this mission plan the projected mission altitude is calculated as shown in Fig. 3.6. Tables 3.1 and 3.2 summarize the simulation environment and parameters used for this estimation. The de-orbiting of ALE-1 from 500 km altitude to sub 400 km altitude is projected to take approximately 650 days after the deployment of the drag sail. Although this duration is heavily dependent on the actual solar activity, it can serve as a basis for evaluation. As can be seen from Fig. 3.6, if the sail is kept and not separated, complete de-orbiting would be achieved shortly after (around 50 days) the 400 km altitude is reached. This is a very short time for the main mission of ALE-1. However, if the sail is separated, the remaining life on orbit is calculated to be 550 days. Which is a much more suitable time frame for the demonstration of artificial shooting star generation mission of ALE-1.

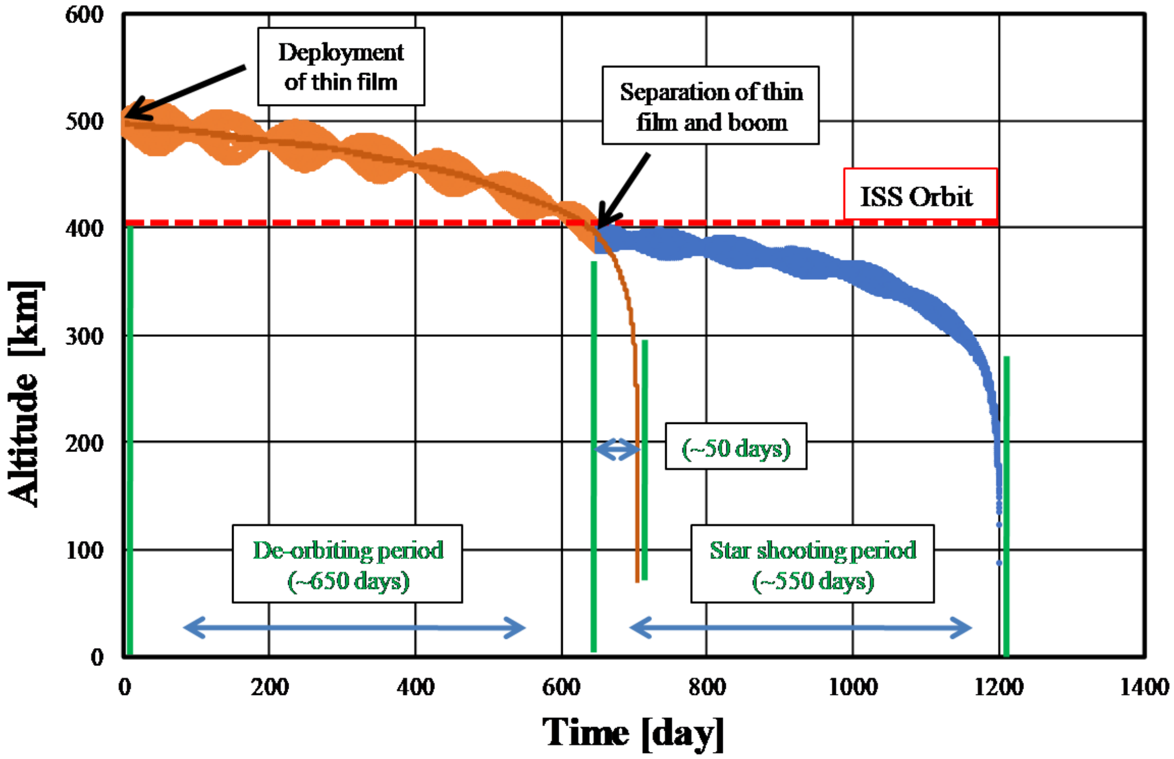

Figure 3.6: Projected orbital altitude estimation of ALE-1 using SDOM. (©JSASS)

Table 3.1. Environmental models used for the estimation of projected orbital altitude of ALE-1 using SDOM.

Section	Model
Earth gravity model	EGM-08, (degree, order) = (20, 20)
Sun/Moon model	Astronomical Almanac
Atmosphere model	NRLMSISE-00

Table 3.2. Parameters used for the estimation of projected orbital altitude of ALE-1 using SDOM.

Section	Parameter	Value
Atmospheric Drag	CD (drag coefficient) [-]	2.2
	Ap(daily geomagnetic planetary amplitude) [-]	-
	$F_{10.7}$(daily solar flux) [SFU]	-
	$F_{10.7,\ 81day}$(81-day average of $F_{10.7}$) [SFU]	-
Solar-radiation Pressure	c_R(radiation pressure coefficient) [-]	1.0+ε
	ε (emissivity) [-]	0.53
	P_{srp}(solar-radiation pressure) [N/m2]	4.57×10^{-6}
	ν (shadow function) [-]	0, 0.5, 1
Earth orientation parameters	xp, yp(polar motion) [deg]	0.0
Time system	$\Delta UT1$[s]	0.0
	ΔAT [s]	37.0

3.9. System Design

SDOM system is designed with 4 actions. For each action, two independent actuation systems are utilized: a nominal and a redundancy. Figure 3.7 shows a block layout of the SDOM system. Power is supplied from the power control unit to SDOM if the power switch for SDOM in the science handling unit is turned on. In Fig. 3.7 this power line is represented as the black network. Similar to the switch for the power, switched for each actuation for each action of SDOM are implemented and they can be actuated when signal is sent. This is represented with green lines in the figure. The switch for the power in general, and the switches for each individual actuation are controlled with different SCPU units to ensure that a malfunction in one single unit can not prematurely initiate any of the actuations. Additionally, each action is stopped by two inhibitors for redundancy, and both inhibitors can simultaneously be broken with each actuator.

3.10. Mechanical Design

DOM is used as a reference point for all the designs related to SDOM because it already has space demonstration and thus space heritage. As mentioned before, the chosen size of DOM for the mission of ALE-1 was DOM2500. Due to close relations between Tohoku University and the supplier of DOM, Nakashimada Engineering Works, it was possible to modify the outside of DOM2500 to fit in the SDOM better. First step is designing a vessel to hold

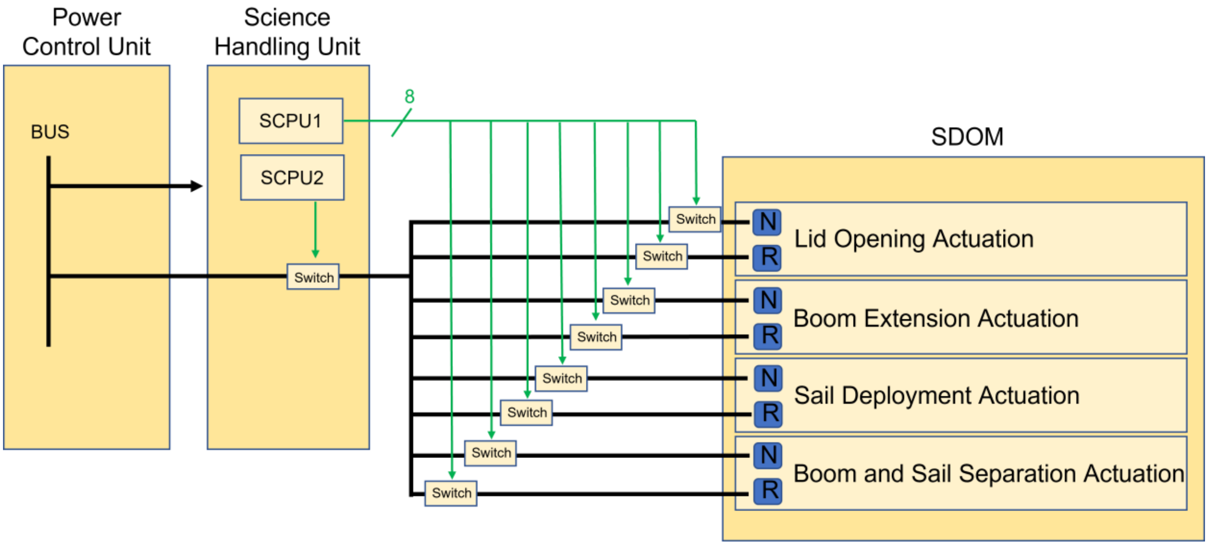

Figure 3.7: The block layout of SDOM system.

DOM2500 and all the rest of the mechanism. Figure 3.8 shows the main cylinder of SDOM. With a wall thickness of 1.5 mm and a radius of 174 mm, the main cylinder of SDOM is extremely thin when compared to its size. This kind of shell structure makes it weak in many aspects. The upper half is intended to have DOM2500 placed in it. This is depicted as the blue region in Fig. 3.8. The lower half is intended to house all the rest of the mechanisms including extension mechanism, separation mechanism and electrical assemblies. This is depicted as the red region inf Fig. 3.8. The lower half is intentionally designed narrower. At the necking down, a 45-degree section is left for DOM2500 to rest, with smoother edges to not hinder the movement of DOM2500 out of the cylinder when extension is initiated. When the lid is closed, DOM2500 is sandwiched between this neckdown and the lid. Four guides are placed inside the

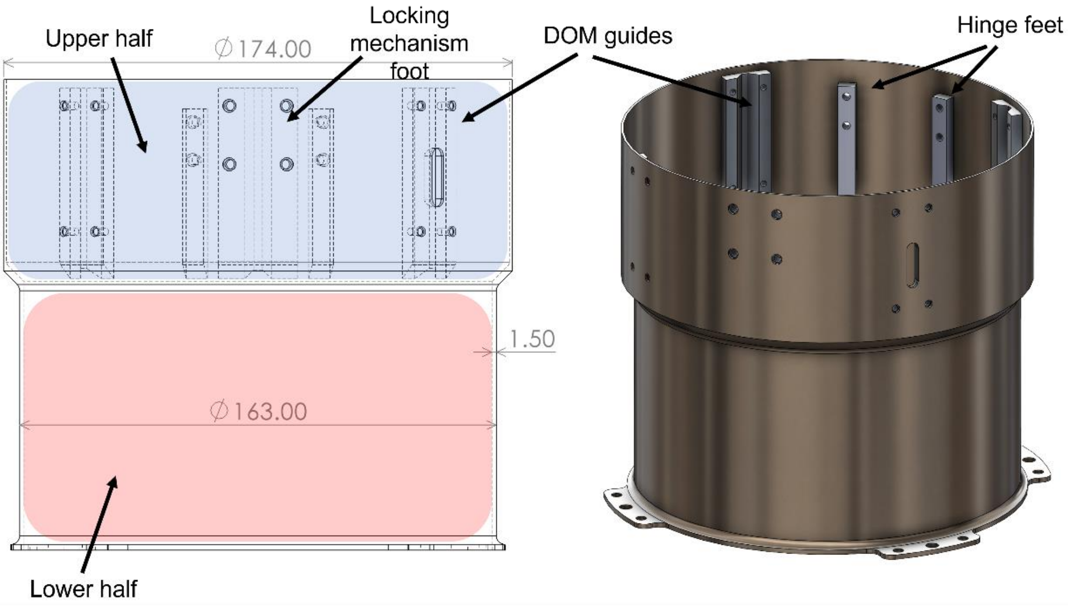

Figure 3.8: The main cylinder of SDOM.

main cylinder to prevent rotational freedom of DOM2500. These guides are manufactured as separate parts for ease of manufacturing and design flexibility. Additional guides are places to two opposite sides of the main cylinder as foot holds to outside mechanisms supporting the hinge for the lid and the locking mechanism of the lid.

Figure 3.9 shows DOM2500 used for ALE-1. The four pillars at the outer edges are additional items for this mission that go in the guides attached to the main cylinder to prevent rotational movement inside the main cylinder of SDOM. Also, the bottom plate is equipped with eight extensions with a 45-degree cylindrical taper, that would help establish a better fit at the main cylinders neckdown in addition to the tapers at the four pillars' bottoms. Additionally, a DC-DC converter was implemented at DOM2500 to ensure enough voltage is supplied for actuation.

Figure 3.10 shows the lid that would close the main cylinder of SDOM. In this figure, the inner side of the lid is shown. The lid is designed to have an extrusion exactly fitting to the top edge of DOM2500 to provide additional structural support to help dampen the vibrations induced by the rocket launch. At the back side (left on Fig 3.10) a plate is implemented to stop the lid from opening more than the allowable angle. Depending on the mission, the bend angle of this plate can be changed to adjust the lid opening angle. The lid is designed to be closed with the three screws on the front side. These screws are tightened to the lock assembly, so that when it is unlocked, a part of the lock assembly opens with the lid, and when it is locked, it is holding the lid closed. The lid is also designed with its middle hollowed out. This is to decrease the total height of the main cylinder and save mass. This way, the upper extrusions of DOM2500 do not have to be accounted for, as they can go through the lid.

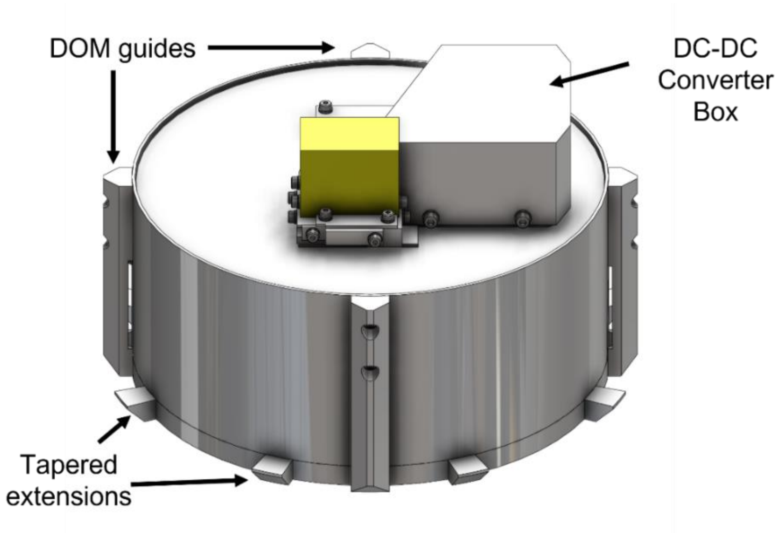

Figure 3.9: DOM2500 used for ALE-1 with its custom modifications.

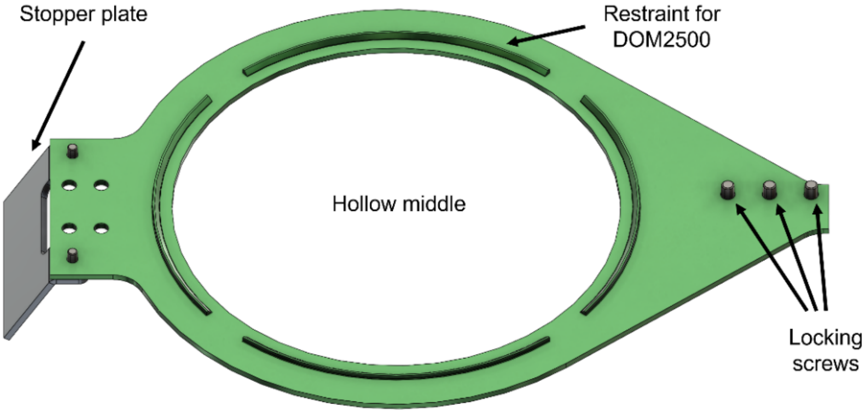

Figure 3.10: Lid of SDOM.

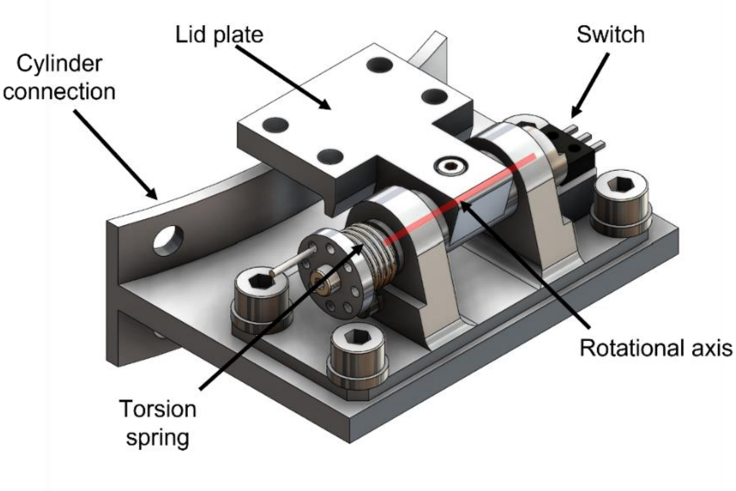

Fig 3.11: SDOM hinge for the lid.

Figure 3.11 shows the hinge assembly used for the lid. The lid attaches to the top four holes with screws. The base plate holding the hinge is attached to the main cylinders back side with use of previously mentioned hinge feet plates. The hinge itself is a recycled design from a previous mechanism used in another micro-satellite, RISESAT. Due to limited development time, and already demonstrated functionality after various testing, existing designs are recycled to increase success rate of the mission and cut down on development time. It utilizes a torsion spring that is already loaded. If the lock is let go, the lid is opened. This spring is visible in the figure. On the other side of the rotational axis of the hinge depicted in red in Fig 3.11, a switch is located that tracks whether the lid is open or not for confirmation.

On the other side of the main cylinder, the locking mechanism for the lid is situated. Figure 3.12 shows this mechanism from the front and from the back. Figure 3.13 shows the cross section at the centerline of the locking pin. In these figures, the lid and the parts connected to the lid are all marked green. Locking pin and the spring to push the locking pin are marked red. The chucks that are placed at the head of the pin to hold it at place are marked orange. The

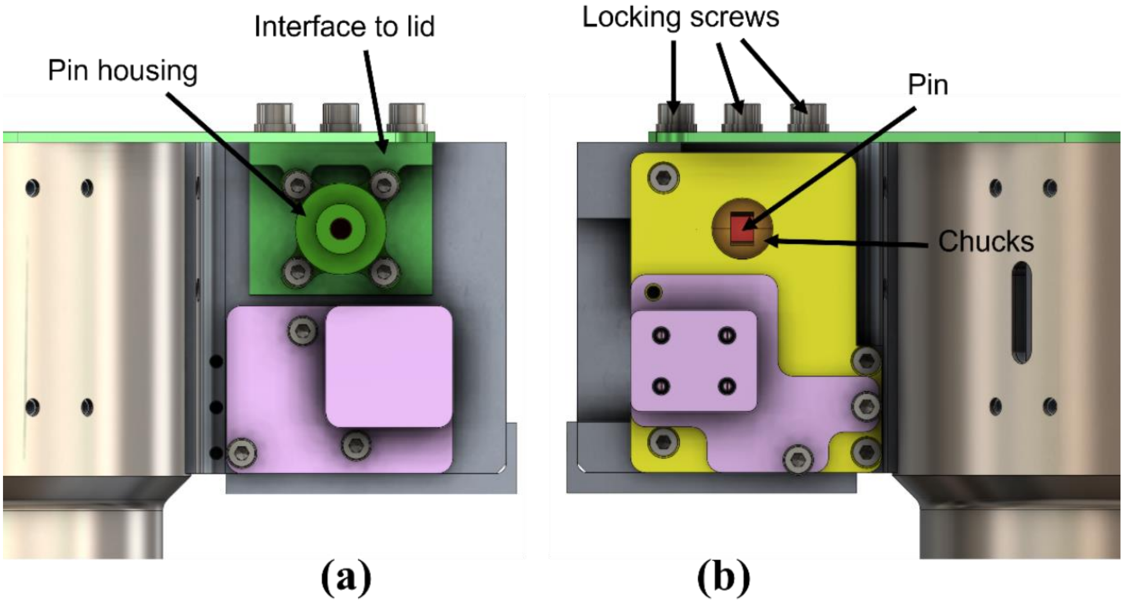

Figure 3.12: Locking mechanism of the lid of SDOM: (a) back view of the mechanism, (b) front view of the mechanism.

part that is connected to the main cylinder (cylinder to pin interface) is marked gray. The main cylinder is brown. And the lid stopper plate is gray. The pin is going through the green lid part, and the gray cylinder part. If this pin is in place, the lid cannot open. Before connecting the lid, the pin is assembled in locked configuration. The lid is closed as the last item of operation with three M4 screws. When the pin is released, the pin, its housing, and the pin interface to the lid are all opened together with the lid.

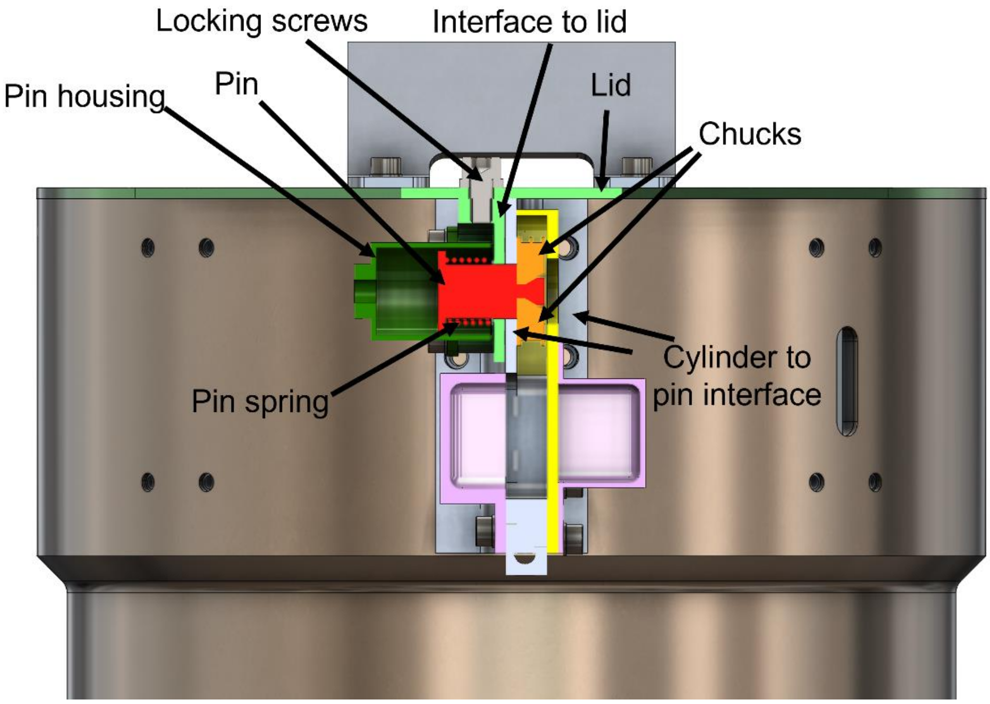

Figure 3.13: Section view of the locking mechanism of the lid of SDOM at the centerline of the locking pin.

The lid opening direction and the pin locking direction are perpendicular to each other. Doing so, the force that would help open the lid is avoided to affect the locking force. If the lid is tried to forcibly open, this force would be recompensed by the tensile strength of the pin. If the chucks are relaxed and the pin is released, the pin would move towards left in figure with help of the spring and stay within the green housing. For ease of assembly and as a safety, a screw can be inserted from the back of the housing to hold the pin in place. The spring force for this spring is 2.19 kgf.

Figure 3.14 shows more details on the mechanism to hold the chucks in place as wedges to the pin. The chucks exactly cover the pin head and wedge in from top and bottom sides. They are held pushed against each other by a Dyneema wire that is wrapped around them. This Dyneema wire is placed under tension for a period of time before assembly to make sure it will not elongate with the constant force acting on it during the stowage time. And then at the assembly, tension is applied to the wire using a simple ratchet and foot system. For redundancy, two Dyneema wires are used for the same pin assembly. In order to unlock the pin, both wires need to be cut.

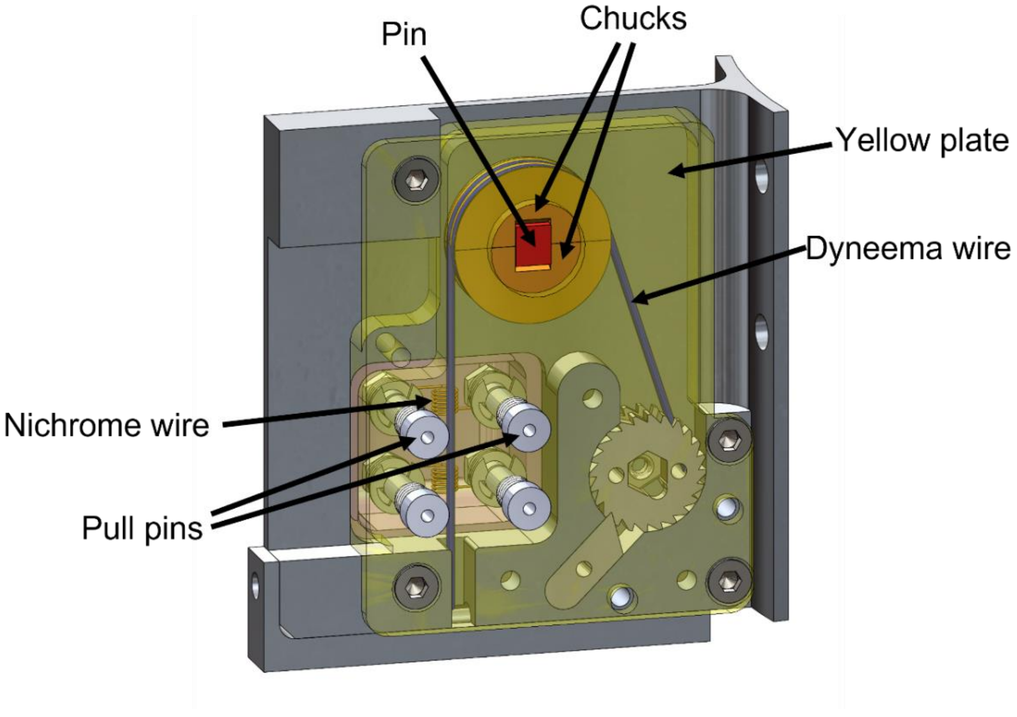

Figure 3.14: Detailed view the release mechanism for the pin locking mechanism of the SDOM lid.

Two pull pins holding a coiled nichrome wire in between them are tensioned against the transparent yellow plate, so that the nichrome wire is touching the tensioned Dyneema wire. When a current is shorted through the nichrome wires, they heat up and melt the Dyneema. For redundancy to ensure lock can open, two sets of this nichrome wire assembly are used. The transparent yellow plate is made of SEPLA material. This is to achieve electrical isolation between nichrome wire pull pins, as the rest of this pin locking sub-system is made of space grade aluminum materials. Purple parts in Figs 3.12 and 3.13 are cover plates to close of the nichrome wire assemblies. They can be taken off at any point to check the tension of the Dyneema wires.

For the extension mechanism, convex tapes are used as an extendable boom element. The convex tapes used are industrial grade and order-made, having more rigidity than conventional convex tapes available off the shelf commonly used for tape measures. Figure 3.15 shows the profile of the convex tapes that were used. Same convex tapes are used for the deployment of the sail as well. However, the configurations at which the tapes are assembled are different. For the sail deployment 2 tapes per diagonal of the sail are assembled as shown in Fig. 3.16 (a) with their concave sides touching each other. A total of 8 tapes are used for the sail. A total of

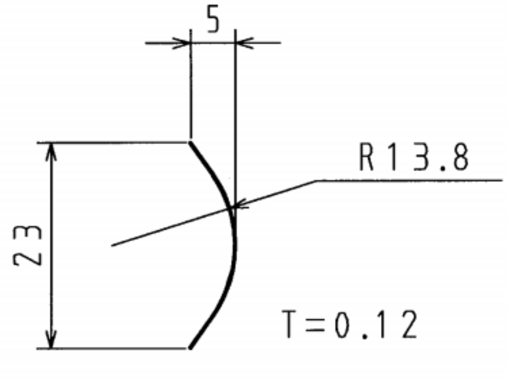

Figure 3.15: Convex tape profile.

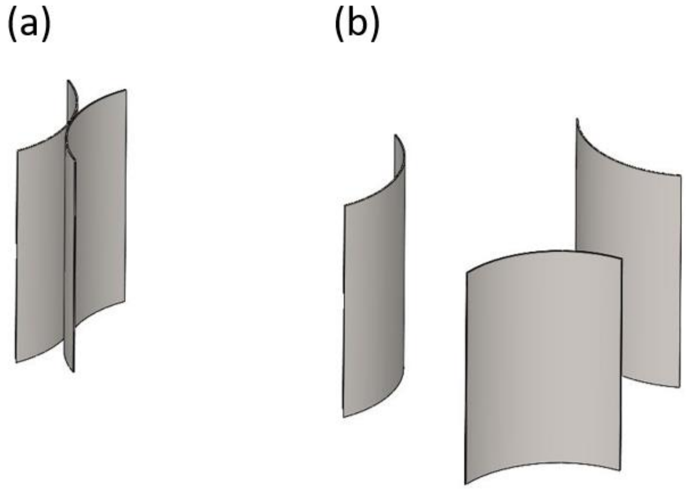

Figure 3.16: Convex tape alignments: (a) alignment for use in sail, (b) alignment for use in boom.

Table 3.3: Basic properties of used convex tapes.

Arc length	25 mm
Arc middle radius	13.8 mm
Thickness	0.12 mm
Material	SUS420J2
Young’s modulus	200,000 N/mm^2
Density	960 kg/m^3 or 48 g/m
Mast length	2500 mm × 3
Sail boom length	1900 mm × 2 × 4

three tapes are used for the boom element used for extendibility function, and they are assembled in a circular configuration with the convex sides facing each other at a 120-degree angle from each other as shown in Fig. 3.16 (b). Table 3.3 summarizes the properties of the convex tapes used for SDOM.

The tapes used for extension are each stored in their own coiler as their direction of extension and their alignment with respect to each other make it difficult to coil them together for storage. Figure 3.17 shows the coil assembly used for these tapes in both assembled and exploded view. The coil at which the convex tape is wound about is held on a shaft that extends from one side with the help of a bearing. Ideally, rotating parts are place on two bearings to ensure their shaft axis does not misalign, however in this case that would unnecessarily complicate the assembly while supplying an unneeded precision. Therefore, this was avoided to simplify the system and cut down on mass. Similarly, the coil assemblies are designed without outer walls around the coil itself. Instead, six rollers are placed with bearings on each end to help facilitate the extension of the tape. When convex tapes are coiled, along with the extending force on the extension direction, they apply a large expanding force on the radial direction. If not accounted for, this force can cause enough friction with the walls to stop the tapes from extending at all. The minimize this friction, the contact surface between a coiled tape and what is around it is reduced to six line-contacts with six rollers. And the rollers are placed on bearings to further lessen the hindrance of the radial force on the extension. The coil radius for the convex tape yields better extending force with a smaller coiling radius, however, it is not desired to have it less than the arc radius of the convex tape.[85] In this case the coiling radius is designed to be 30 mm. And the coil size is designed large enough to fit 5 m of convex tapes. Due to short development times, a longer boom length possibility was accounted for. The coil also is cut on one side to a hexagon socket so that a custom hexagonal tool can be fitted for the actual winding of the coils. As the coils are needed to be wound after assembled within the whole extension mechanism, it is necessary that the coils can be accessed from distance. The cover is screwed lastly from one side to the other side of the coil assembly, to keep the two sides together during a high random vibration environment to ensure rollers and bearings do not dislocate with the vibrating elastic deformations.

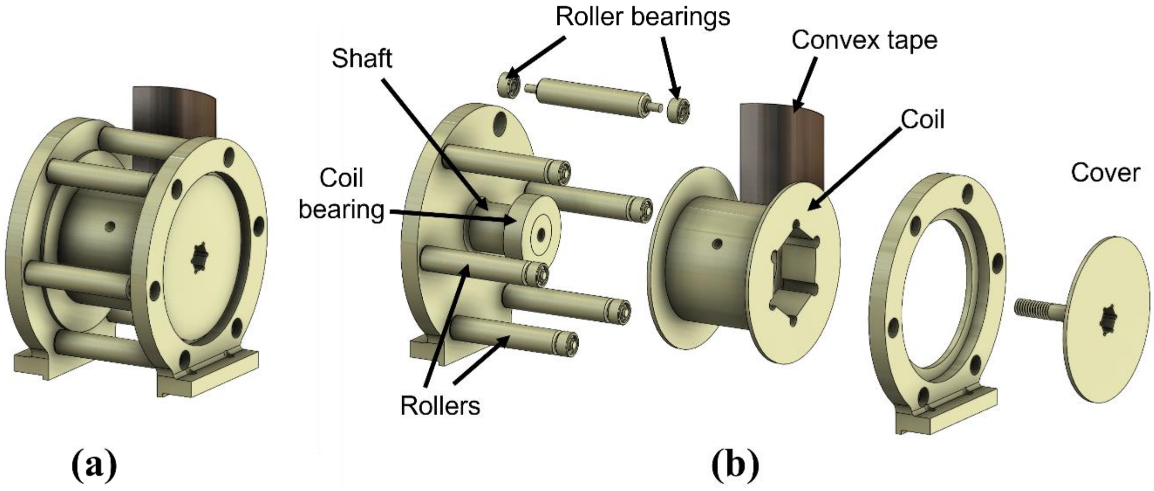

Figure 3.17: The coil assembly for the convex tapes for the boom: (a) assembled configuration, (b) exploded configuration.

The convex tapes are attached to the coil via flat-head screws. Although only a singular 2.5 m long tape is wound per coil, at the base, multiple shorter tapes are coiled and screwed together with the main one to supply rigidity at the point of connection. When convex tapes are coiled, they lose their convex shape in favor of a convex shape on the coil cylinder direction. The region where this change happens is called the ploy region and the most susceptible region to disturbing forces. In order to avoid the base of the boom buckling, this region is reinforced with extra layers of convex tapes.

Figure 3.18 shows the three coils assembled in what is named the separation cylinder. When separation occur, the entirety of this blue partial cylinder is separated from the satellite. Figure 3.18 (a) shows some components sectioned for a better view of the contents. The coil assemblies are rotationally offset from the walls by a degree to allow easy access to the coils even from outside of the separation cylinder after assembled. For clarity the coil assembly cover is hidden in Fig. 3.18. In Fig 3.18 (b) the gray cable winding cone is visible. This cone both acts as a semi separator between the bottom and the top of the separation cylinder, and as the bed for the cable that supplies power to DOM2500 2.5 m away. This cable is longer than 2.5 m and is wound around this cone. It is taken longer than 2.5 meters to account for the spiral winding if it and not cause tears on the cable. Figure 3.19 (a) shows this cable around the extended boom. As can be seen from Fig. 3.19 (b), DOM2500 side has another cone at the connection. The power and communication cable are gently stored between these cones and is pulled around the extended boom in a spiral fashion at the time of extension.

Figure 3.19 (c) shows the connection of the boom to the DOM2500 in more detail. The three convex tapes are connected to the same plate with two screws each without disturbing

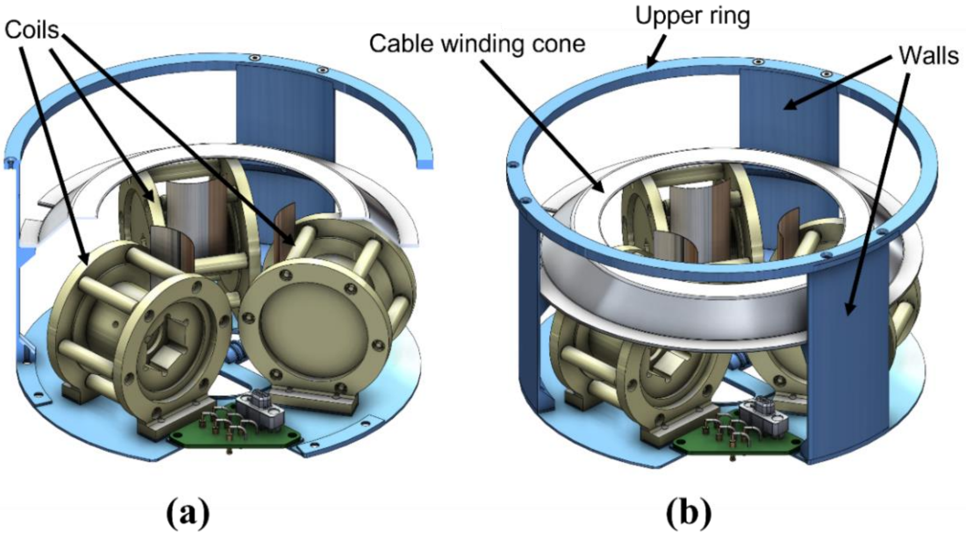

Figure 3.18: Separation cylinder containing coils for the SDOM boom: (a) partially sectioned view, (b) normal view.

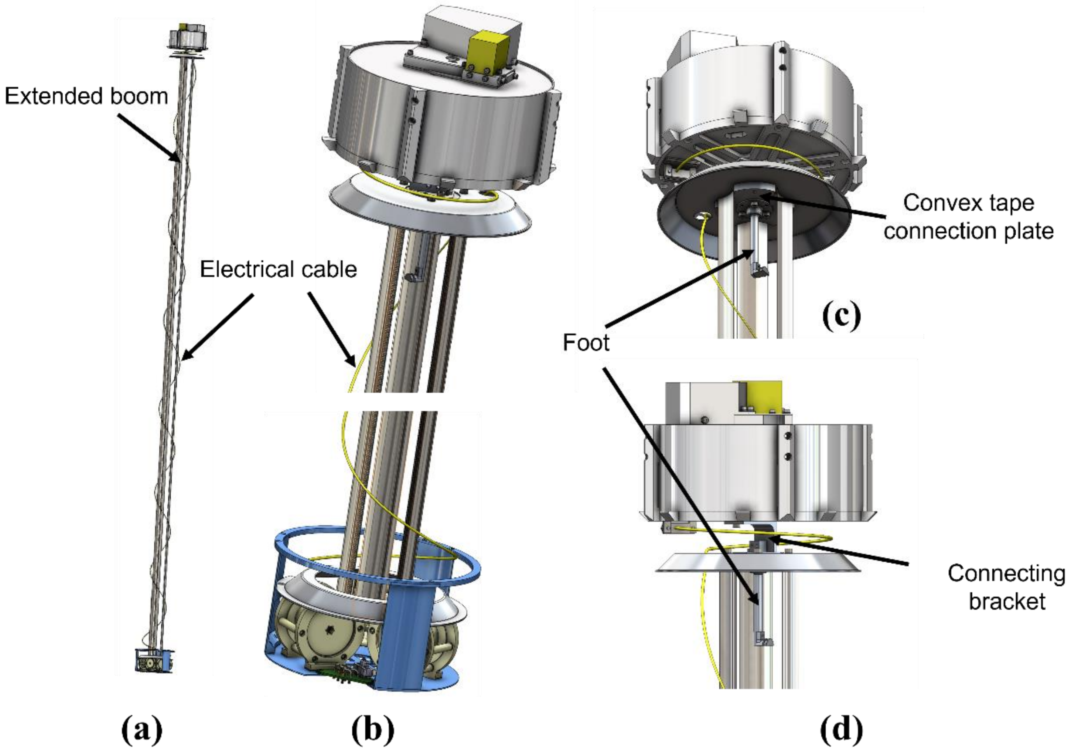

Figure 3.19: Different views of the boom of SDOM with DOM2500 at its tip and the separation cylinder at its bottom: (a) Complete extended view, (b) enlarged cut view of the extended configuration, (c) DOM2500 connection angled view, (d) DOM2500 connection orthogonal view.

their convex shapes. This connection plate has a foot extending below it. This foot is used to tie it down to the bottom of the separation cylinder to keep the convex tapes from extending with help of Dyneema wires. This will be explained in more detail further down. The cable is connected to the DOM2500 through a D-Sub connector at the bottom and accesses the satellite side through a hole at the conic plate. The DOM2500 is connected to the boom tip using simple brackets as shown in Fig. 3.19 (d).

At the base of the boom the cable connects to a custom designed printed circuit board (PCB) through another micro D-sub connector. The placement of this connector within the separation cylinder can be seen in Fig. 3.18. As the separation is intended to happen, an electrical connection between the two sides become an issue. Usually in space missions, zero-force connectors are used. However, any zero-force connector that was commercially available was too large to fit anywhere in this design, as well as too heavy for the mass budget of this system. In order to overcome this issue, a pair of custom PCBs are designed. The separation side has six conductive pins that can be pushed down. The pins used are VB-1-6-BC from MAC8. The PCB on the satellite side has six conductive pads to match the pins. When the separation cylinder is assembled to the main cylinder and held down to the bottom of SDOM, the pins are pushed against the pads and electrical connection is established. However, if the separation is initiated, no obstructive connection is available to hinder it. On the contrary, albeit very small, the pins will help push towards the separation. Figure 3.20 shows these PCBs in detail.

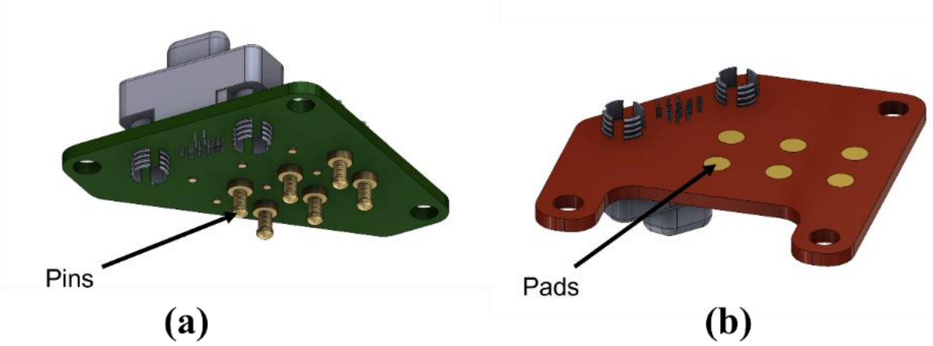

Figure 3.20: Custom designed PCBs for separable electrical connection: (a) boom and sail side, (b) satellite side.

Figure 3.21 shows SDOM main cylinder sectioned, separation cylinder partially sectioned with the coils for the boom hidden, DOM2500 hidden and the connection to DOM2500 partially sectioned. The foot of the DOM2500 connection exactly fits next to the semi cylindrical extrusion at the center of the separation cylinder bottom forming a longer semi-cylinder on the top side of the separation cylinder bottom. Below this is the bottom plate of SDOM, and another semi-cylinder extrusion on the other side of this plate. The foot of DOM2500 connection is tied down to this third semi-cylinder with help of a Dyneema wire. Similarly, the separation cylinder is tied down to this third semi-cylinder with help of a Dyneema wire on the other side.

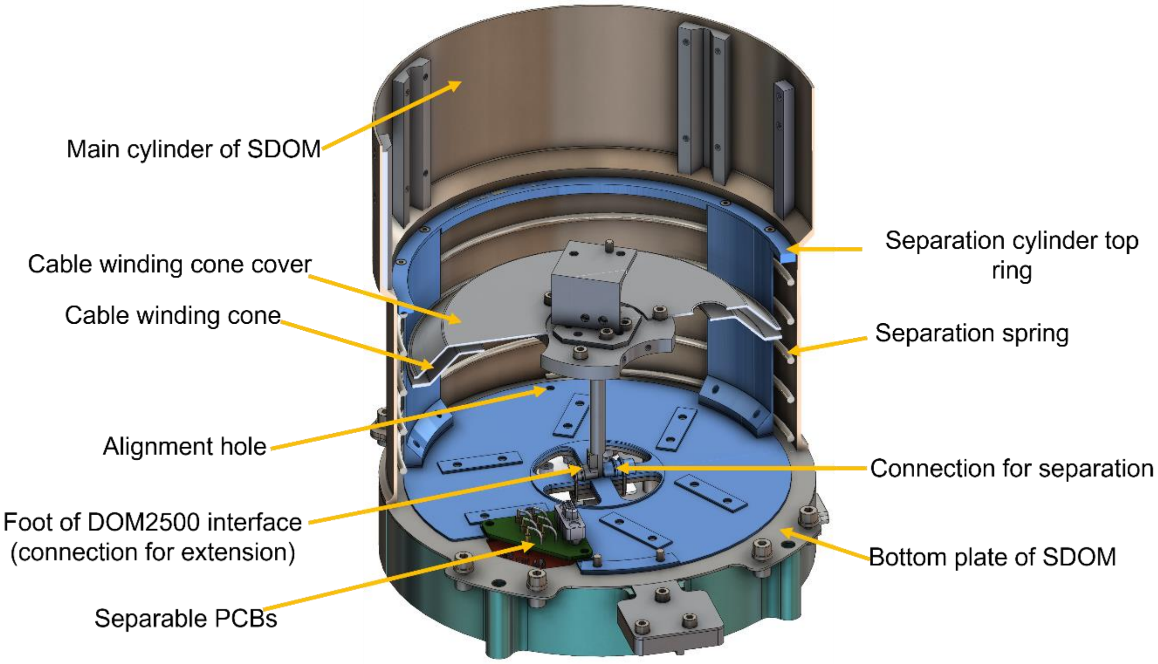

Figure 3.21: Partial sectioned view of SDOM assembly with several hidden components.

The separation force is supplied by the separation spring placed around the separation cylinder. When the extension Dyneema is melt down, DOM2500 becomes free, and the boom can extend. Consequently, when the separation Dyneema is melt down, the whole separation cylinder, including everything it contains, the boom, and the DOM2500 are pushed out of the SDOM main cylinder with help of the separation spring. This spring is designed so when it is at rest height, the bottom of the separation cylinder is out of the SDOM main cylinder. The spring is connected to the separating side; thus, it leaves the satellite as well. This design is chosen so there is no oscillating mechanical remnant left at the satellite side after the separation. There exists an alignment hole on the far side of the separation cylinder. A short pin is fed through here to assure the cylinder is in correct alignment with the bottom plate of SDOM, so that the electrical pins at the custom PCBs do not misalign during extreme vibration conditions.

On the bottom side of SDOM, the Dyneema wires that are used to prevent separation and extension are assembled into place with nichrome wires touching them similar to the lid pin-lock system. The purple line is one of the Dyneema wires in Fig. 3.22. Two nichrome wires per Dyneema wire are implemented for redundancy, and two Dyneema wires per connection are used for safety. DC-DC converters are implemented at close points to the nichrome wires to minimize cable length. This is done for the lid pin lock system and the DOM2500 as well. Nichrome wires are cut precise lengths to result in 1.1 Ohms of resistance. At 3.3 V, 3 A flows through them, which is above the necessary current by a safe margin for nichrome wires to get hot enough to melt the Dyneema. However, if the cable length leading up to them is tens of centimeters long, the total resistance of the circuit will be a different value, resulting in less current to flow through the nichrome wires. This is undesired. Therefore DC-DC converters are implemented per nichrome wire close to the nichrome wires.

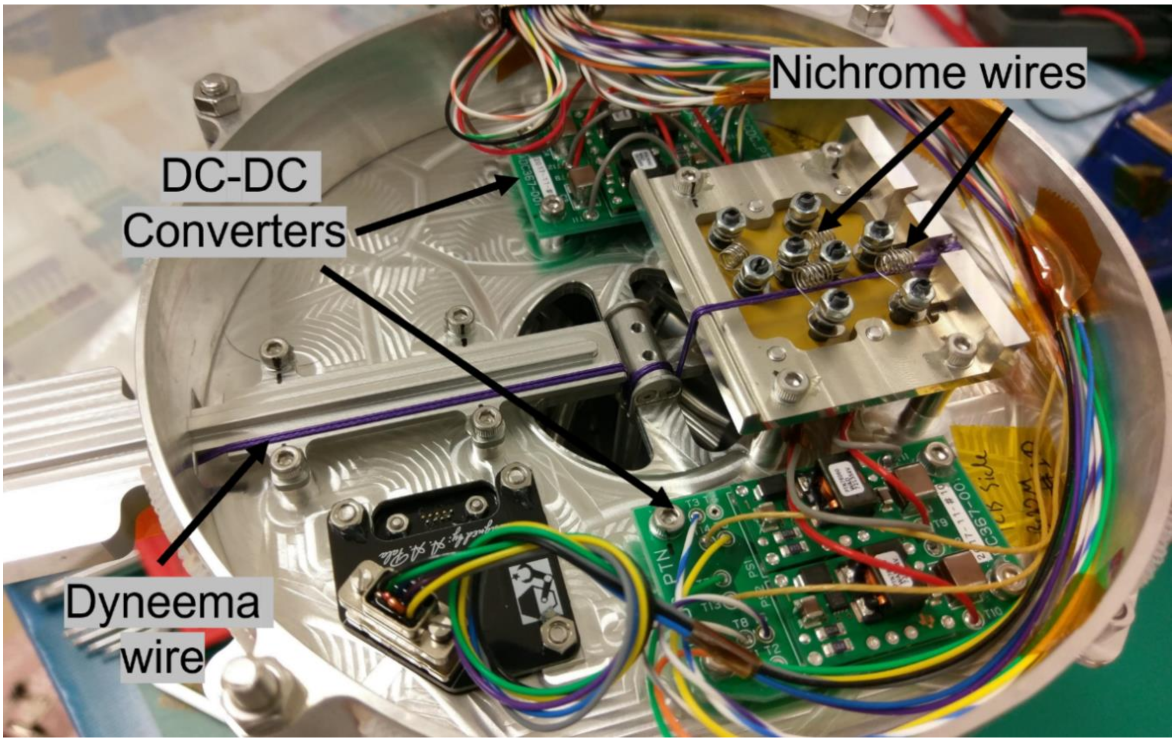

Figure 3.22: Bottom side of SDOM at semi-assembled configuration.

The ratchet and foot to tension the Dyneema wires on the bottom are implemented outside the main cylinder radius, so that tension on the Dyneema can be checked without disassembling the whole SDOM from the satellite. The bottom of the SDOM is elevated 30 mm with a spacer to allow room for the Dyneema cut mechanism between the satellite surface and the bottom of SDOM. After tightened to the satellite, the only electrical connection needed is a micro D-sub connector with 25 pins. Figure 3.23 shows SDOM assembled at flight configuration.

3.11. Observation Sub-systems

There are three systems implemented for observation of SDOM status. First one is a simple binary switch network for quick confirmation of the status during satellite operation. The data load is to be considered when downlinking from an orbiting satellite. Although it is possible to implement instruments that can take high resolution pictures and send back to the ground station, this kind of method will delay the confirmation possibly by days. In order to enable immediate confirmation, mechanical switches are implemented in various locations that are pushed down at the stored configuration and are released with each action that is completed. Thus, a total of 4-bits of binary information is sufficient to downlink with the satellite telemetry to confirm the SDOM status. Additional observation tools used are a laser range finder and a serial camera.

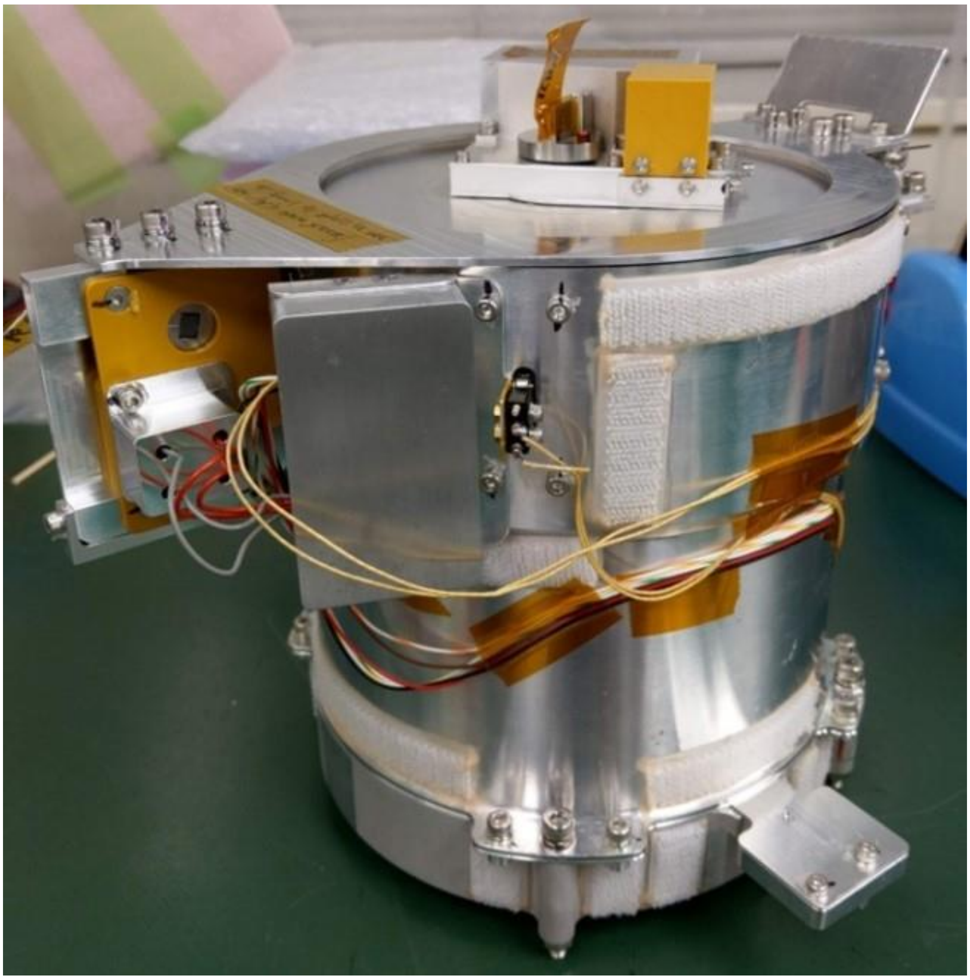

Figure 3.23: SDOM at full-assembled flight configuration. (©JSASS)

3.11.1. Time of Flight Camera System

A time of flight camera (TOF) is a type of laser range finder. For this mission, Sentis-M120-Laser from formerly Bluetechnix, now BECOM Electronics was used. This module was previously selected for use for the Hakuto lunar exploration rover project of the Space Robotics laboratory in Tohoku University. [86,87] For this project many tests to qualify the module for space-readiness were already conducted. [88,89,90] Additionally, with help of BECOM Electronics, the module was modified to perform better in a space environment. For the shirt development time of ALE-1, this was a huge advantage, and a big factor in choosing this module over others possible candidates.

TOFs calculate the distance by emitting a photon of light, and then recapturing that photon after it reflects on a surface. The time that passes during this window is measured and used to calculate the distance of the object that reflected the light, since the speed of light is constant and known. Figure 3.24 shows an example of the depth perception using TOF. The TOF uses 3 vertical-cavity surface-emitting laser diodes with the peak wavelength at 850 nm. Its field of view is 90° × 74° and the sensor array is 7.2 mm × 5.4 mm. Its resolution is 160 × 120 pixels.

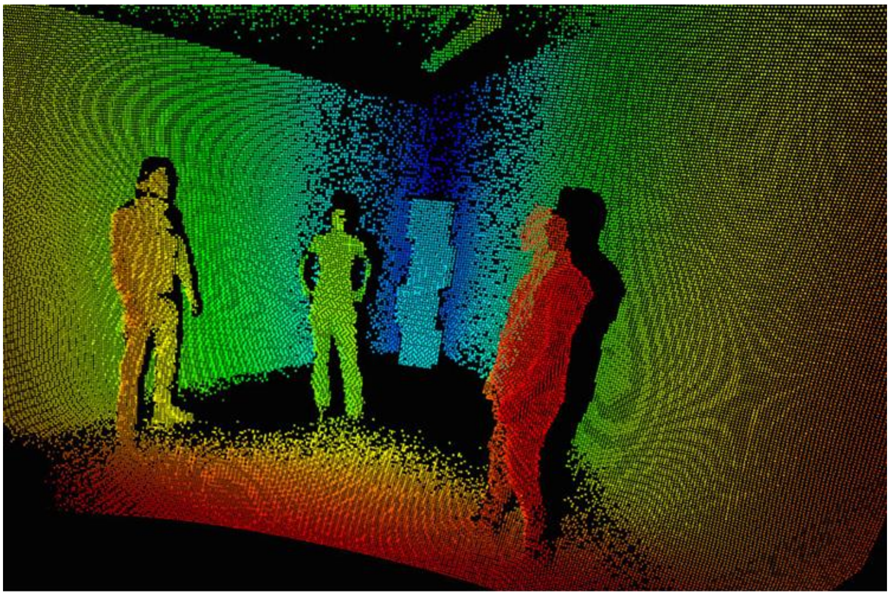

Figure 3.24: Example three dimensional point cloud data for time of flight sensor.

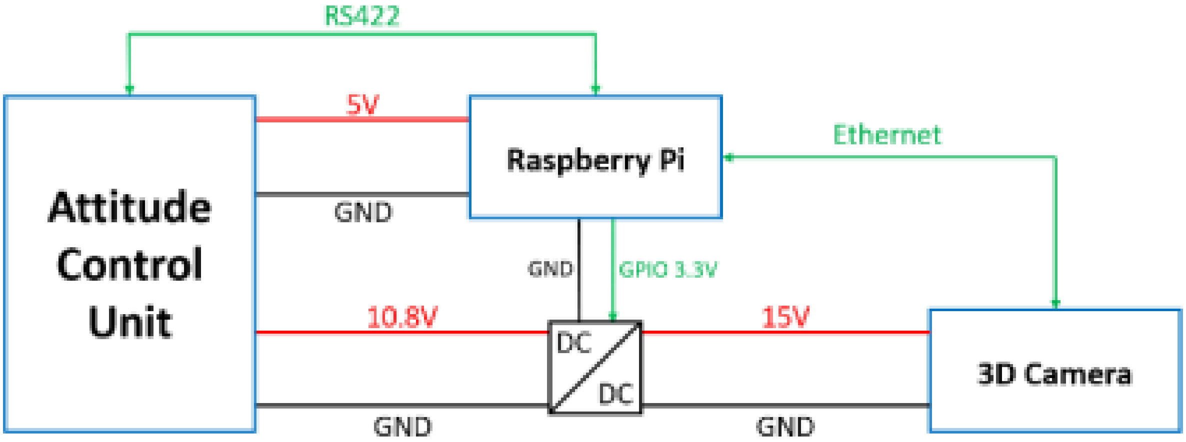

Figure 3.25: System architecture of time of flight camera system implemented on ALE-1.

The TOF used for this system uses the Continuous-Wave method to calculate the distance, instead of the pulsed source method. With Continuous-Wave method, instead of pulsed individual photons, a continuously modulated sinusoidal light wave is emitted. And the distances are estimated by calculating the phase-shift of the reflected signal. Further details on these methods can be found in references [91,92].

The TOF camera system used in this mission consist of a sensor, a Raspberry Pi 3B (RPi), and a DC-DC converter. The bus voltage of microsatellite ALE-1 is 10.8V whereas the TOF camera needs between 12V and 15V to properly function. The DC-DC converter is used for this voltage gain. RPi is used as the controller and interface for the TOF camera. The satellite bus system (specifically attitude control unit in this case) uses RS422 communication between sub-modules. However, the TOF camera uses an ethernet connection to effectively relay the acquired data as the data per second is high. Initially the acquired data is sent to RPi via ethernet cable using TCP/IP protocol. This data is then processed and stored in RPi and then compressed and fed back to the attitude control unit through RS422 communication, which can then be downlinked to the ground station in parts. RPi does not inherently possess RS422 communication. To overcome this, a USB to RS422 dongle is used. The system architecture is shown in Fig. 3.25.

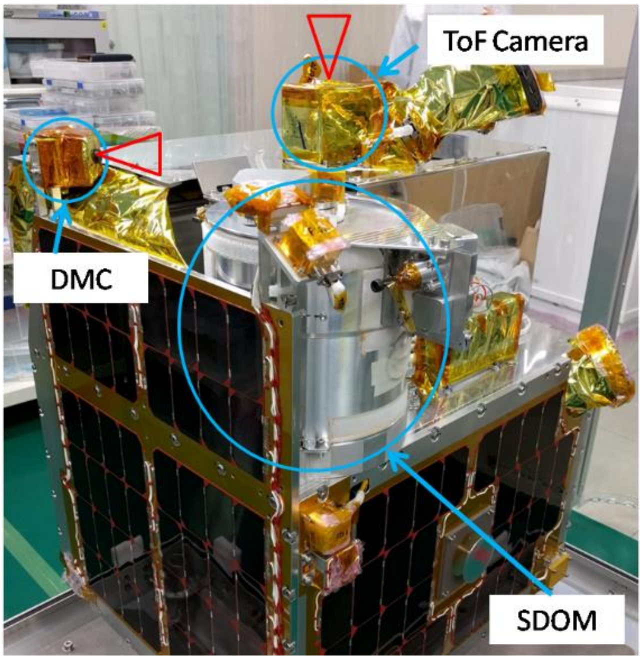

Figure 3.26: Flight configuration of ALE-1 with separable de-orbit mechanism (SDOM), time of flight (TOF) camera and DOM monitoring camera (DMC). (©JSASS)

Figure 3.26 shows the flight configuration of ALE-1. TOF Camera is located on top of the satellite with its angle of view pointing upwards. SDOM extends its boom along this direction and deploys its sail on a plane that has this direction as its normal vector. Figure 3.27 shows a representation of the intended field of view of the TOF camera from the cruising satellite. As shown in this figure, TOF camera can observe DOM2500 its sail deployed. It is also able to sample distance of the objects in its field of view, therefore it is possible to confirm the boom extension status with this camera as well. Additionally, the camera is intended to observe the deployment behavior of the sail, and any fluctuations on the sail during de-orbiting. The accuracy for the used TOF camera is within 1 cm and allows this observation. Lastly, we can confirm the separation using TOF camera as well. Figure 3.28 shows the TOF module that was used for the flight model of ALE-1.

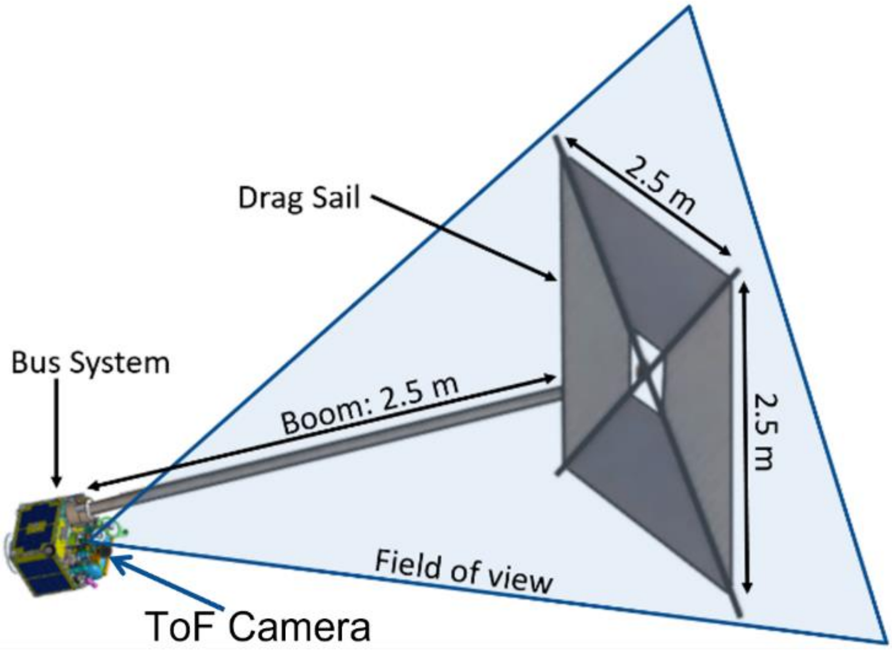

Figure 3.27: Representation of boom and sail within the field of view of TOF camera. (©JSASS)

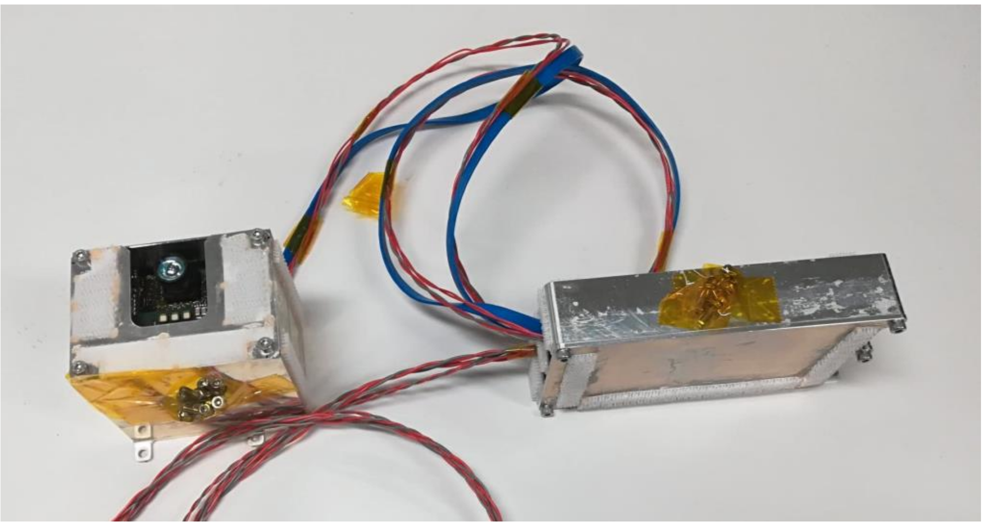

Figure 3.28: The time of flight camera sensor Sentis-M120-Laser and the Raspberry Pi 3B in their respective housing for ALE-1.

There are several modifications performed on the TOF camera and the sail of DOM2500 to enable better observation. First is the modification of the illuminator of the TOF camera. The default illuminator on the commercial off the shelf available TOF camera is an LED that emits light on all directions. For this mission, this integrated circuit part was swapped in favor of a high-power laser illuminator, that emits in a narrower field of view but with higher density. This increases the chances of a photon returning to the sensor greatly.

Second is the implementation of a filter on the sensor. The TOF camera is very susceptible to noise under direct sunlight. On earth, even on a cloudy day, outdoors TOF camera performs poorer than indoors. All the background illumination is accumulating to a lot of noise in the sensor. However, with the implementation of the filter on the sensor, that is specific to the wavelength that the camera emits, most of this background noise is eliminated. For use in space, such a filter is absolutely necessary, as the background radiation in space is much higher than on ground, and the camera would be bombarded with the complete spectrum of wavelengths at all times.

A third modification was implemented on the sail of DOM2500. The drag sail used for DOM2500 is a polyimide thin film that is aluminized. The aluminization process renders its surface reflective. For TOF camera to work, a mirror like reflective surface is undesirable, as the sent photon will be lost forever, if the angle of incidence is just a little above 0 degrees. To overcome this issue, retro reflective tapes were implemented on key point of the sail. Figure 3.29 shows the difference of reflection and retro-reflection.

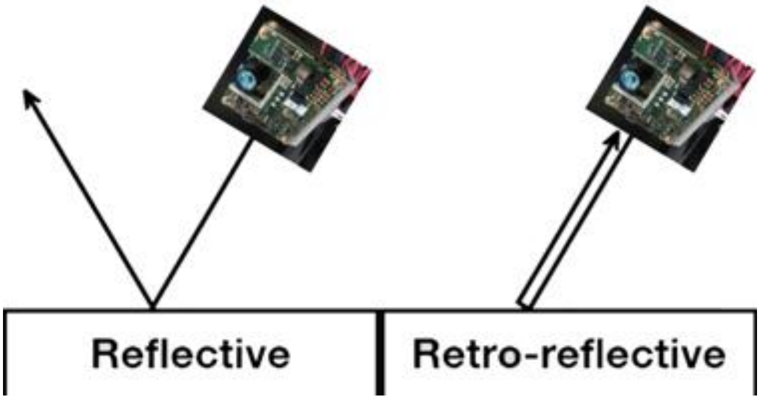

Figure 3.29: Difference between regular reflection and retro reflection.

Contrary to a reflective surface, on a retro reflective surface, the photon is reflected back to the source regardless of the angle of incidence. On normal surfaces, TOF camera works because most surfaces are more refractive than reflective. On a refractive surface the light is reflected back in all directions, with varying intensity. Therefore, a portion of it will reach back the sensor. However, if the sensor is pointed to a mirror, it will not register the mirror itself as an object but register the objects in the mirror as distant as they appear in the mirror.

The retro reflective material was taped to the sail outer edge, sail inner edge, and as point to a grid of 20 cm by 20 cm. This pattern is shown in Fig. 3.30.

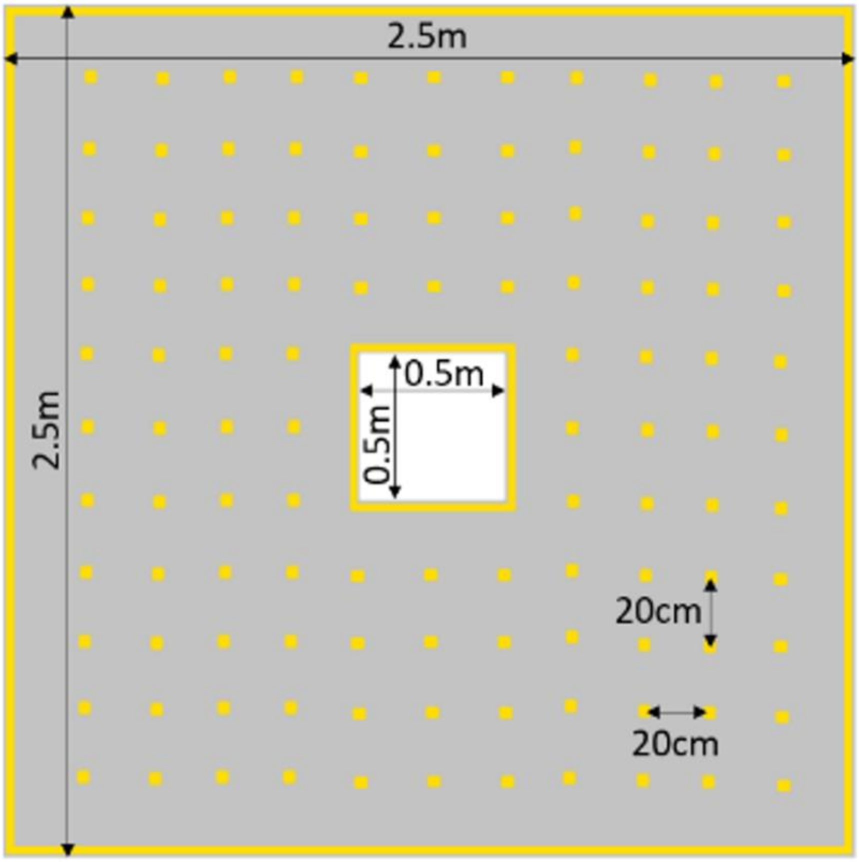

Figure 3.30: Retro-reflective taping pattern of the sail inside DOM2500 for ALE-1.

Lastly, all the unused components of RPi were desoldered to decrease potential point of failures.

3.11.2. DOM Monitoring Camera

Boom extension, sail deployment and separation can be observed by TOF camera. However, the lid status is outside of the field of view of this camera. An additional serial camera called DOM Monitoring Camera (DMC) is installed at the top of the satellite with its field of view containing SDOM. With DMC, we can confirm the lid status, as well as the extension, and separation status, as the lid of SDOM is designed hollow in the middle to allow for observation of the other side. Figure 3.31 shows the first light of DMC on ground after flight model of ALE-1 is assembled for reference. The stopper plate for the lid, as well as the top part of DOM2500 is visible on the right, and the TOF camera can be seen on the left. Although a narrower lens angle may provide better resolution for the SDOM, this image quality was sufficient for the visual confirmation of phases. Therefore, a wide angle fish eye lens with 116 degrees of field of view was implemented. The module used is, uCAM-III. It is the next step of status confirmation after binary switch states as a single image data is much lighter than a consecutive frame video with 3d point cloud data attached to it.

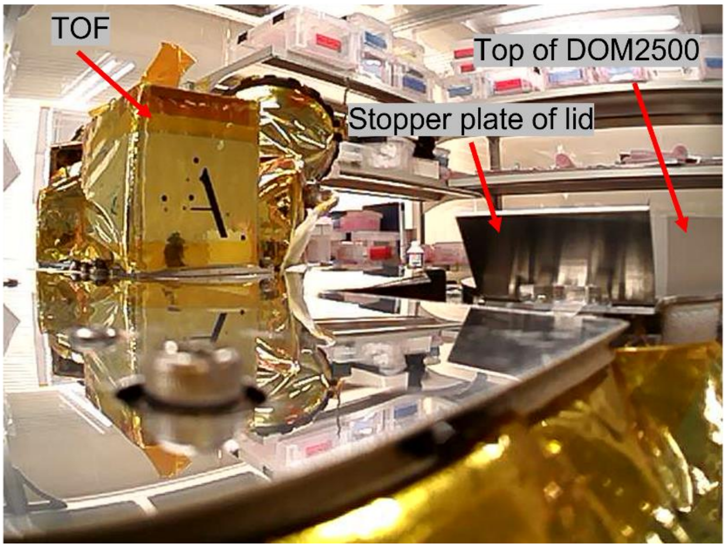

Figure 3.31: First light of DMC on ground at flight configuration of ALE-1.

3.12. Ground Tests and Evaluation

After many design iterations, all the subsystems were brought to a point of functionality. However, functionality on earth is not enough to vouch for functionality in space. Most basic two criteria for space missions are a vibration testing, and a thermal vacuum testing. If the SDOM systems are still functional after a vibration testing to the specifications of Epsilon 4 and a thermal vacuum testing, only then it is possible to claim its functionality. In this section all the test procedures and their results are elaborated.

Both the thermal vacuum testing simulating orbital conditions and the vibration testing simulating launch conditions are conducted twice on ALE-1 as a whole. For the SDOM, the passing criteria is first, surviving both tests with the lid closed intact, and second, still being able to go into all the planned mission phases without losing any functionality.

3.12.1. Lid Open Tests

The lid is the most important key point from the safety review point of view of JAXA, who is providing the ride for the ALE-1 in Epsilon 4. As mentioned before, a premature extension, deployment, or separation of the SDOM are all considered catastrophic failures in the scope of the Epsilon 4 mission, as the fairing contains many other ridesharing payloads.

After both tests, the lid stayed intact. Although this is sufficient for an evaluation of pass or fail, in order to quantify the safety of the lid lock, we measure the distance between the two chucks holding the lock pin in place. If the Dyneema wire holding the chucks in place loosens, the chucks would move a little further away from each other and create a gap in between.

Measuring for this value before and after test, provides any potential partial damage information. At every test we have confirmed the status of the chucks and confirmed that the chucks did not create a gap in between them. This result shows negligible or no elongation at the Dyneema rope tying the chucks together which is an ideal result.

As for the functionality test, SDOM is first placed horizontally on a surface. This is done to simulate the effects of on orbit weightlessness to the lid on opening direction. This allows the hinge spring the work only to open the lid and not also against the lids weight due to gravity. Also, SDOM is placed on a custom 3D printed stand to compensate for the irregular shape of its main cylinder and provide horizontal attitude. When the lid open signal is sent through the Science Handling Unit (SHU) of the satellite the lid opened as expected on both occasions. Figure 3.32 shows the sequence of the opening of SDOM lid at such a test.

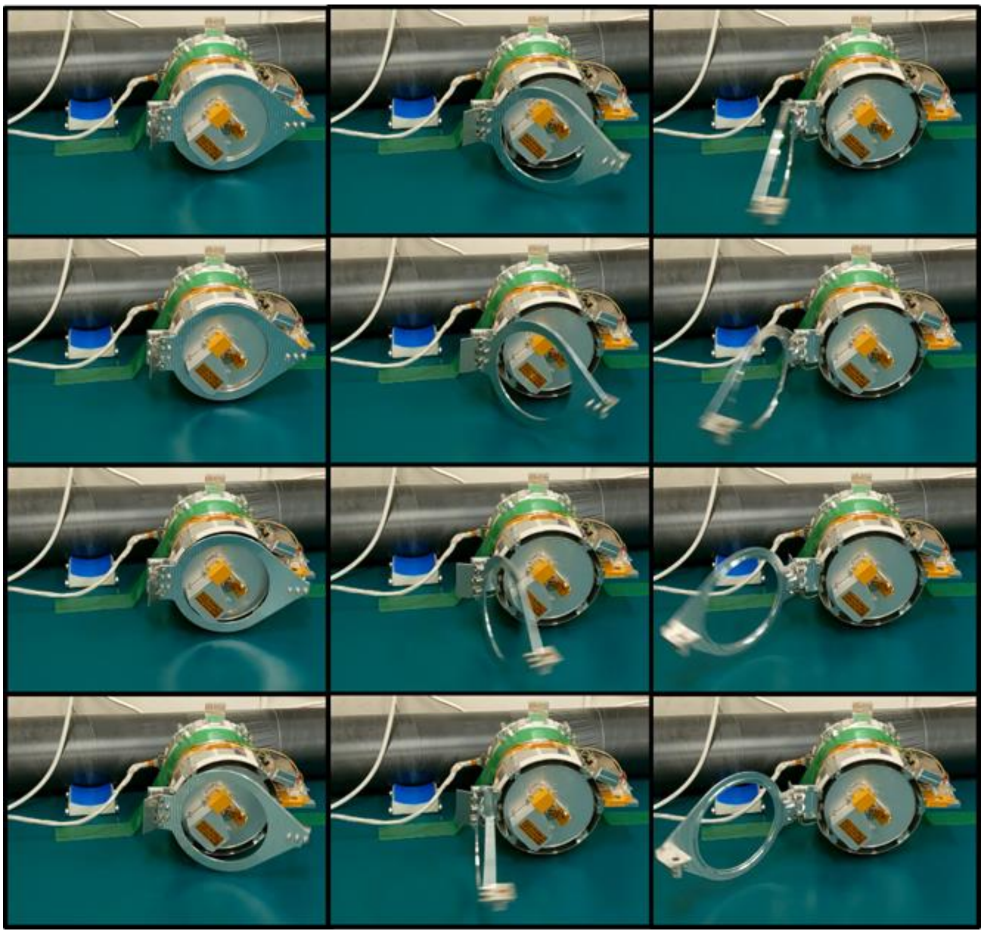

Figure 3.32: The opening sequence of SDOM lid during a successfully conducted ground experiment.

During the vibration test, a pickup accelerometer was placed near the pin of the locking mechanism in the movement direction of the pin to measure the response vibration at the pin. This response can be seen in Fig. 3.33. The maximum force acting on the Dyneema rope can then be calculated by the following Eq. 3.1:

$$F_{\text{dyneema rope}} = (G_{\text{rms}_{\text{at pin}}} \times m_{\text{pin}}) + F_{\text{pin spring}} \qquad (3.1)$$

The mass of the pin is 3.82 g. The G_{rms} at the pin is 9.02 G as can be read from Fig. 3.33, and force of the spring is calculated to be 2.19 kgf from specifications of the spring. From this, the maximum force acting on the Dyneema is calculated to be at 2.23 kgf. The Dyneema rope used in SDOM can withstand forces up to 68 kgf, and it is tensioned to a load higher than 2.23 before assembly for flight to account for natural elongation of the rope under tension as well.

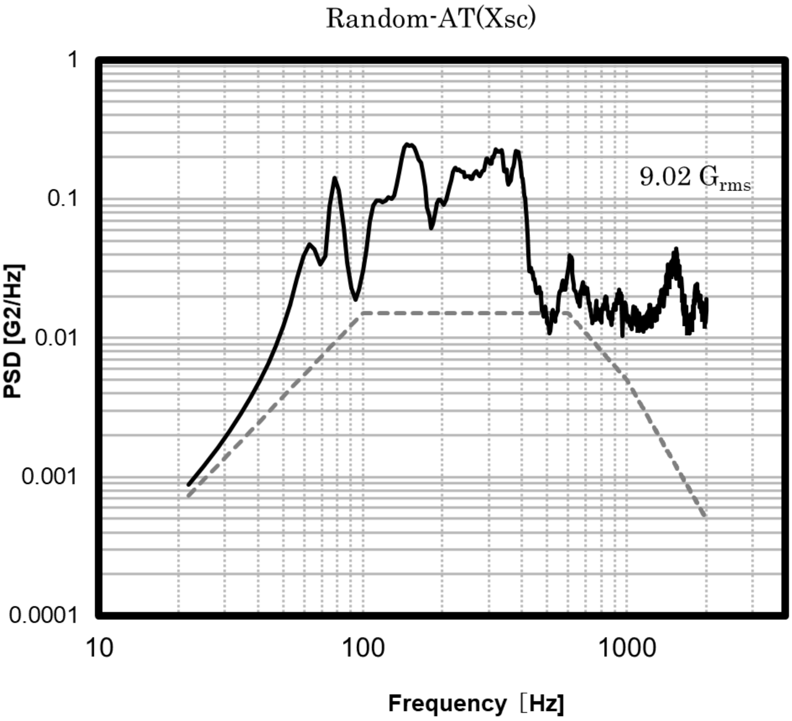

Figure 3.33: The random vibration response near the pin of SDOM lid locking mechanism at the direction of the locking pins movement for unlocking. (©JSASS)

3.12.2. Boom Extension Tests

The Dyneema rope that is holding back the extension is directly wound around parts that are extending away from each other. Any loosening on this Dyneema would not result in full extension but only a movement as much as the elongation of the rope which is in the order of millimeters at most and is negligible. However, the tension of the rope is checked through the externally accessible cover before and after tests nonetheless to make sure the rope has not loosened.

Extension tests are also conducted horizontal to the ground to simulate orbital weightless conditions. A cart system is utilized to hold the DOM2500 when the extending force acts to simulate lack of friction on space. DOM2500 will not be touching any surface while extending on weightless 3D space on orbit. A cart with wheels is not the same as no contact with any surface. However, it alleviates enough friction to enable movement. The remaining friction is negligible, because the existence of this friction is hindering the extension, and therefore forcing the extension experiment towards a safety margin by design. At these experimental conditions, extension signal is sent again through SHU simulating real communication conditions. Figure 3.34 shows the extension sequence partially from one experiment, and Fig. 3.35 shows the fully extended boom after separation with an undeployed sail. Unfortunately, due to the long size of the boom, video recording conditions were difficult and better images showing full extension sequence was not able to be acquired.

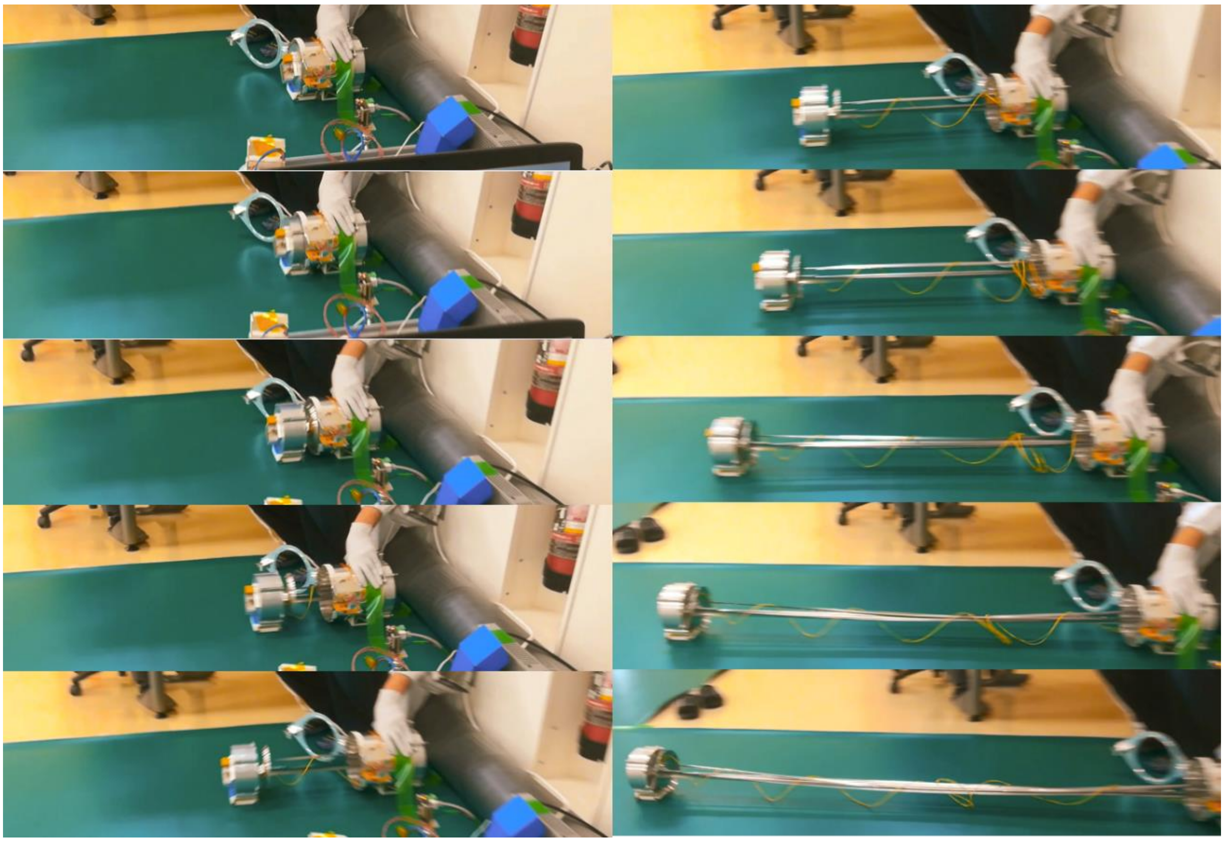

Figure 3.34: The partial sequence of SDOM boom extension.

Figure 3.35: Fully extended boom of SDOM after separation from the main cylinder with an undeployed sail. (©JSASS)

3.12.3. Sail Deployment Tests

For the sail deployment test, DOM2500 is mechanically separated from the boom. This is done so that the sail can be deployed in a horizontal to ground alignment which is closest to orbital conditions. However, the electrical connection is left intact. This is done so to test whether the signal reaches DOM2500 through the long cable going around the boom, and through the separable connectors. For this step, the necessary output power from the SHU is drastically higher when compared to the other actions of SDOM. This is believed to be due to

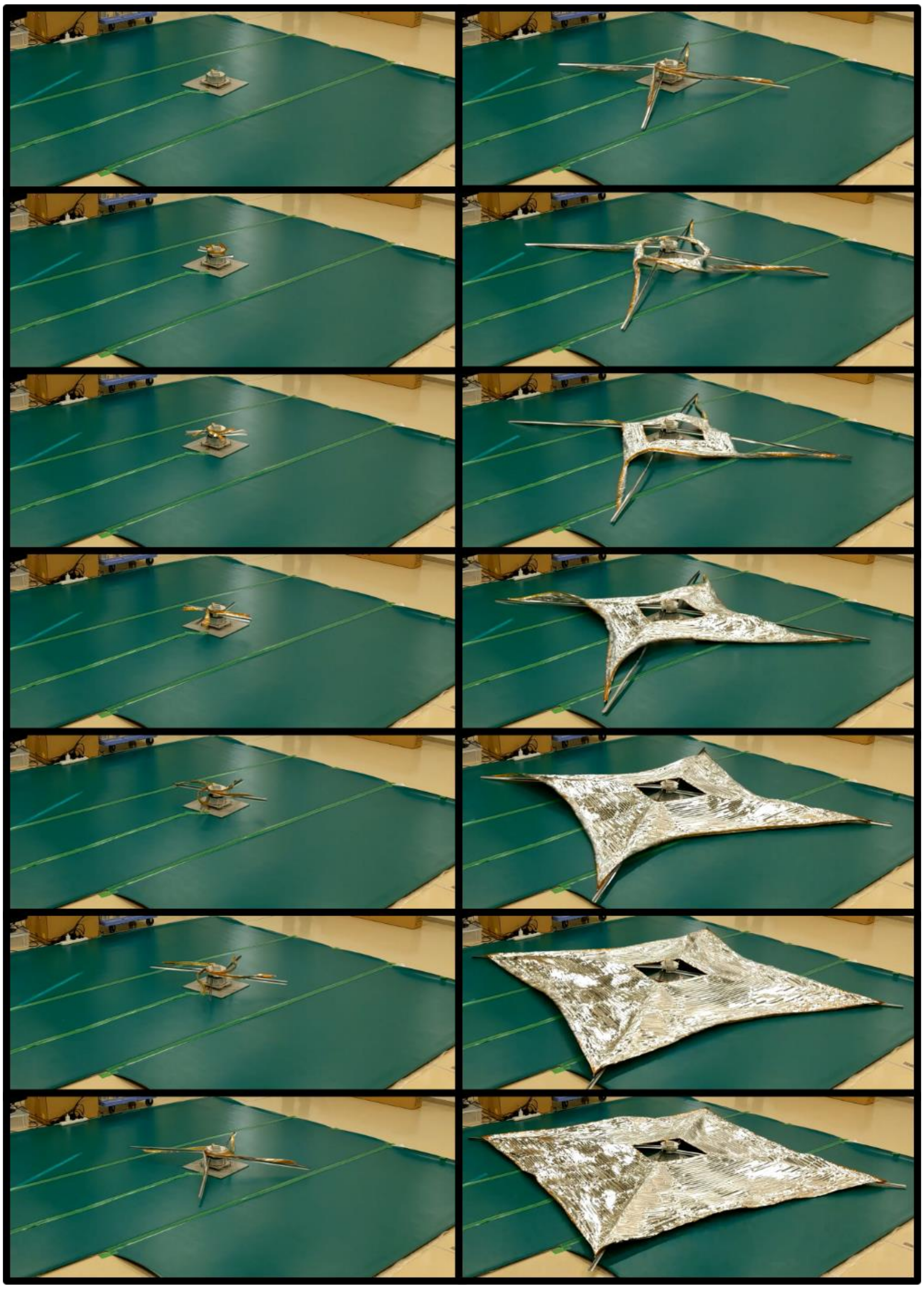

Figure 3.36: Deployment sequence of the sail of DOM2500 on ground through the electrical interface of SDOM.

the fact that the signal has to travel a long path and has to pass a contact pin type connection at the separable connector assembly. It does not pose a threat to the rest of the satellite as the output duration is as short as a few seconds and the total consumption therefore is not as extreme. However, it is necessary that the satellite can provide the required high levels of output wattage for this short duration. Figure 3.36 shows the deployment of DOM2500 through signals sent from SHU after vibration and thermal vacuum testing are conducted.

3.12.4. Separation tests

The separation Dyneema wire is tied almost identical to the extension Dyneema wire. Similar tension checking before and after thermal vacuum testing and vibration testing are conducted. The ground test is performed as with all the other tests, in a horizontal alignment, to simulate space conditions. However, unlike the extension, it is difficult to design a cart that would carry all the separating parts on wheels to decrease friction, due to limited space to place such a cart. Therefore, the test is conducted as it is. As the spring unloads and loses force, the separating side starts to have large contact with the inside of the main cylinder and the ground which results in high friction due to the weight of the separation cylinder, convex tape coils,

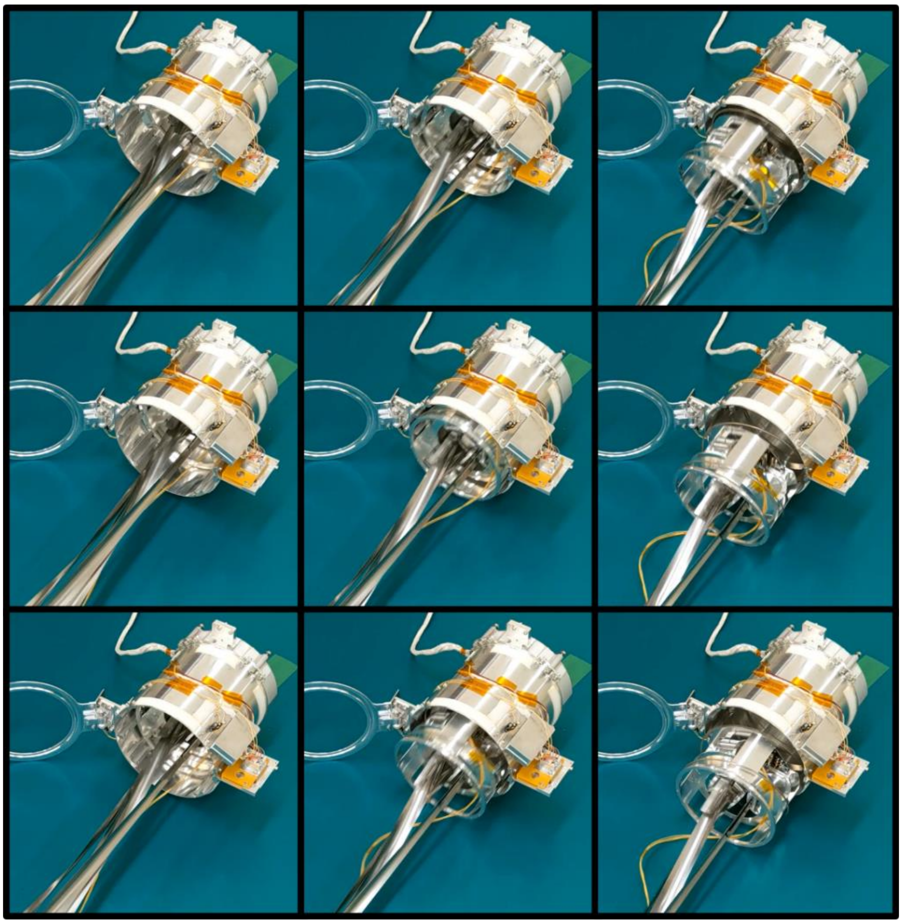

Figure 3.37: The sequence of images during the separation test of SDOM.

and the bottom of the boom itself. This results on the separating parts only partly leaving the main cylinder on earth before stopping. In orbital weightlessness these conditions do not apply. The main aim of this test is to confirm the separation force provided by the separation spring is sufficient. The spring was able to force the contents of SDOM related to boom out of the main cylinder. This was deemed sufficient for a complete separation in-orbit. Figure 3.36 shows this sequence.

3.13. In-Orbit Demonstration

3.13.1. Mission History

ALE-1 was launched into orbit in 18th of January 2019. Important events and their dates are shown in the timeline in Fig. 3.38. As with all satellite missions, initial procedure is a system check to ensure the satellite did not lose functionality at the launch. After confirmation, regular operation of the satellite is started. For ALE-1 the first mission would be the orbital maneuver and therefore SDOM mission. With some delays due to time consuming confirmations, SDOM mission was initiated in 10th of June 2019 with the transmission of lid open signal. Unfortunately, Immediate confirmation of lid opening at the time of command execution could

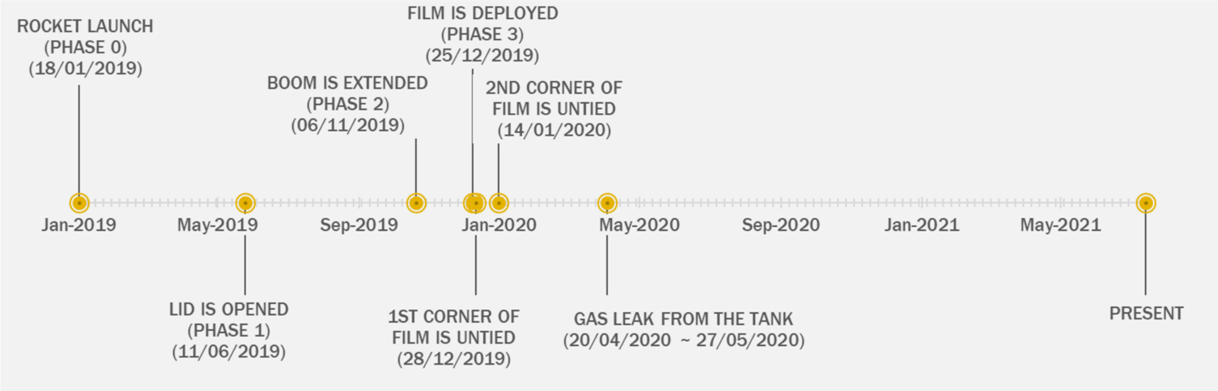

Figure 3.38: SDOM mission history and important events that occurred at ALE-1. (©IEEE)

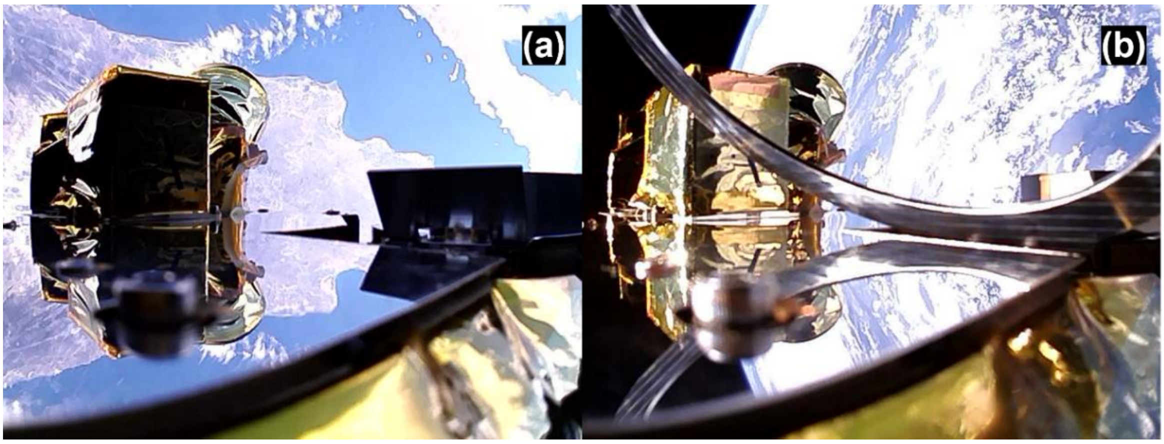

Figure 3.39: In orbit DMC pictures at different phases of SDOM mission: (a) at phase 0 when SDOM is in storage mode, (b) at phase 1 where the lid of SDOM is open. (©IEEE)

not be confirmed as the lid switch state did not change. The following day, 11th of June 2019, the switch state was confirmed to change, and the taken DMC picture showed the lid open. The lid is believed to open with delay. Figure 3.39 shows in-orbit DMC pictures before and after the lid opening.

3.13.2. Boom Extension

Following the lid opening, full system check of the satellite was conducted once more. On 3rd of July 2019, the boom extension signal was sent. However, boom extension could not be confirmed immediately either. On the following day, 4th of July 2019, the redundancy actuation signal was sent, but boom extension could still not be confirmed. It was strongly believed that the holding mechanism was released however extension was not successful. From this point onward, ALE-1 was put under periodical observation period. During this period many actions were tried to kickstart the extension. At first, the reaction wheels in ALE-1 were utilized to give sudden momentum changes to the satellite to possibly move the internal parts of SDOM to help facilitate the release of a possible jamming. Shocks were induced to the satellite with 3 reaction wheels in 3 different axes, but the extension could not be confirmed. Reaction wheels take longer to accelerate than to decelerate. In order to increase the magnitude of the shock, a similar procedure was taken in the reverse direction with sudden deceleration of the reaction wheels as the next step. Extension could still not be confirmed. Figure 3.40 shows the reaction wheel input, spin rate of the satellite in response measured by the fiber optical gyro-sensor (FOG) on-board, and the corresponding roll, pitch and yaw angles in one of these trials. Although the output spin of the satellite is slow, due to the distance between SDOM and satellite center of mass, the output torque at SDOM is higher.

As a next step, shooting a blank cartridge with the star shooting mechanism was tried as it could induce a sudden shock with the release of high-pressure gas from the tank without the metal pellet that would normally be pushed out. However, this did not help the boom to extend either. As a last step continuous heating and cooling of the SDOM through actively facing the sun and deep space was tried. Several cycles of thermal expansion and thermal contraction was used to overcome any friction in the internal system. Most structural elements in the SDOM are aluminum (A7075-T6), however convex tapes and some other key components are stainless steel. Different thermal expansion coefficient between different materials was thought to cause small movements. Especially an expansion of convex tape housing was hoped to lessen radial friction to facilitate an extension, however the boom did not extend following this either.

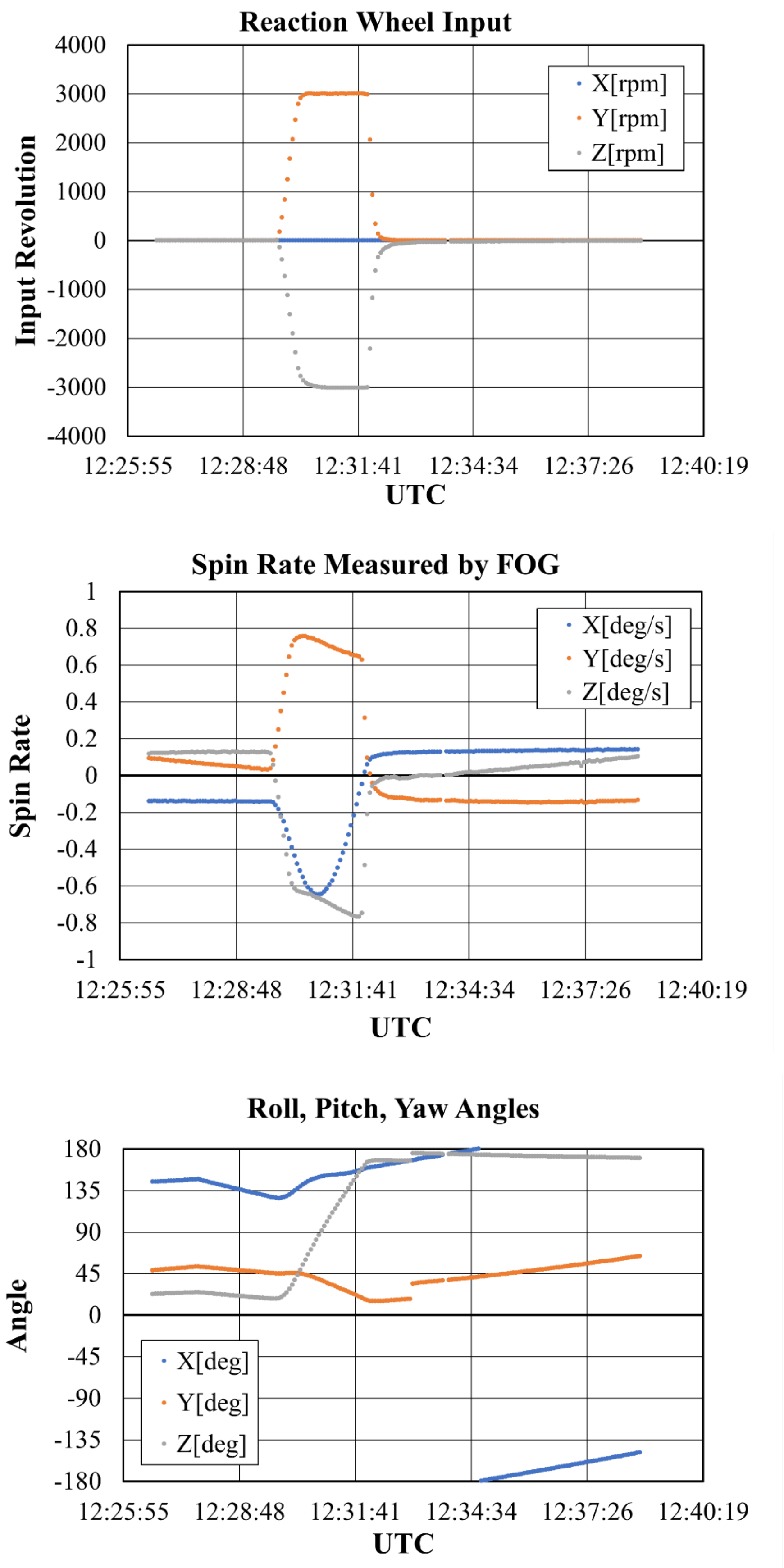

Figure 3.40: Representative case for a reaction wheel induce shock trial to facilitate boom extension of SDOM: (a) the input rotation to the reaction wheels, (b) spin rate of the satellite in response measured by the FOG, (c) corresponding roll, pitch, and yaw angles.

After all these actions, ALE-1 was put under deep observation, without performing any actions but only periodical observation of its status. On 6th of November 2019, during one of these routine observations, the boom was confirmed to be extended through a DMC picture. Figure 3.41 shows this picture and the TOF image taken shortly after.

The data from TOF camera after calibration shows the bottom of the DOM2500 at 2.3 meters distance. Because the TOF camera is located 0.2 m above the bottom of the boom, this value is in fact the value for fully extended boom when observed through the TOF camera, confirming the full success of the extension of the boom.

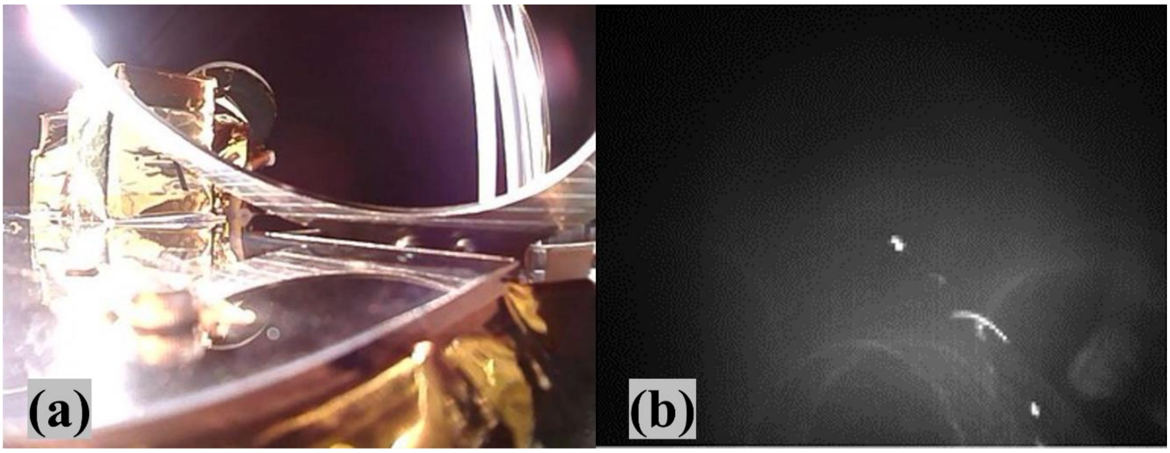

Figure 3.41: Confirmation of the extension of boom: (a) the earliest DMC picture showing the extended boom and (b) the corresponding TOF picture. (©IEEE)

Before moving on to the sail deployment, some experimentation was conducted at this stage to investigate the possible vibrations of the system and the rigidity of the boom. Attitude logs taken by the attitude control unit (ACU) of ALE-1 were used for analysis. Figure 3.42 shows the three individual axis rotations and the nominal rotation of the tumbling satellite before boom extension. Through a Fourier transform we can go to the frequency domain. Figure 3.43 shows the frequency domain of this data. In comparison Figs 3.43 and 3.44 show the time domain and frequency domain of the tumbling satellite after boom extension was confirmed. Although it cannot be claimed that it is immediately after the extension, as confirmation could have been late. The system may have dissipated some of the energy and damped most of the initial oscillation at this point. The frequency domain figures are zoomed in to lower frequencies to show better resolution at more interesting band of the frequencies. Comparing the frequency domain in each case, we see that the frequencies have a wider distribution after the extension, however the dominance is at very low frequencies still. In fact, if the boom is oscillating, the peak value at 5e-4 would correspond to roughly 30 minutes of period, which is the period of the satellite. This would suggest the boom is moving with the satellite. Similarly comparing

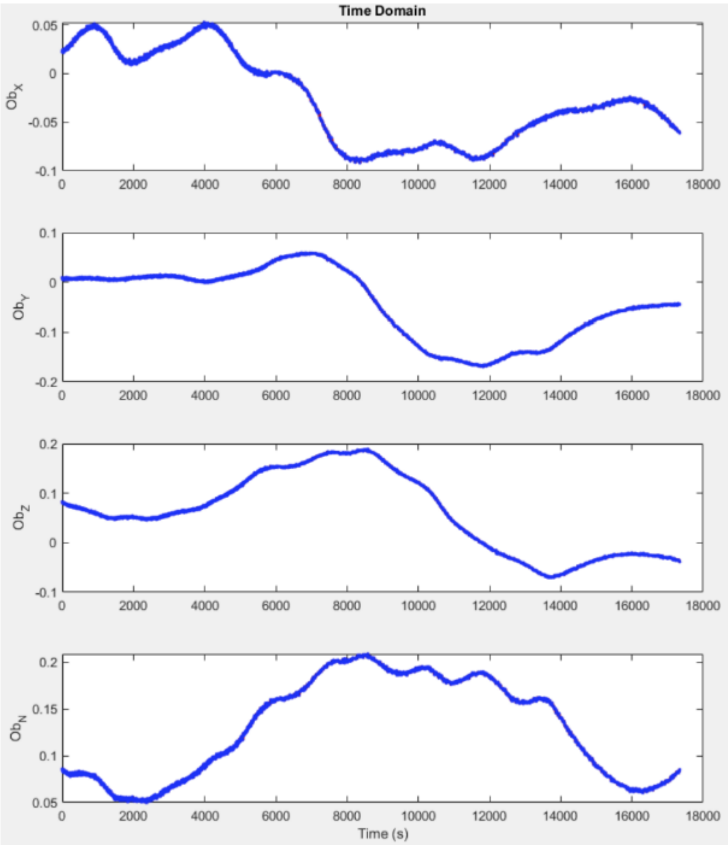

Figure 3.42: Rotations of tumbling satellite before extension of boom in time domain.

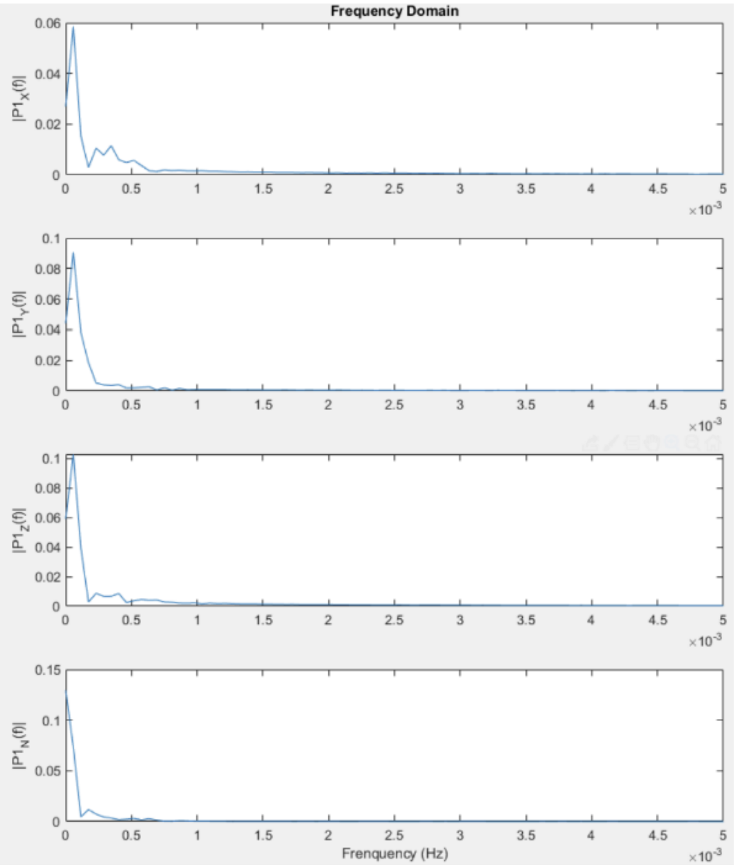

Figure 3.43: Rotations of tumbling satellite before extension of boom in frequency domain.

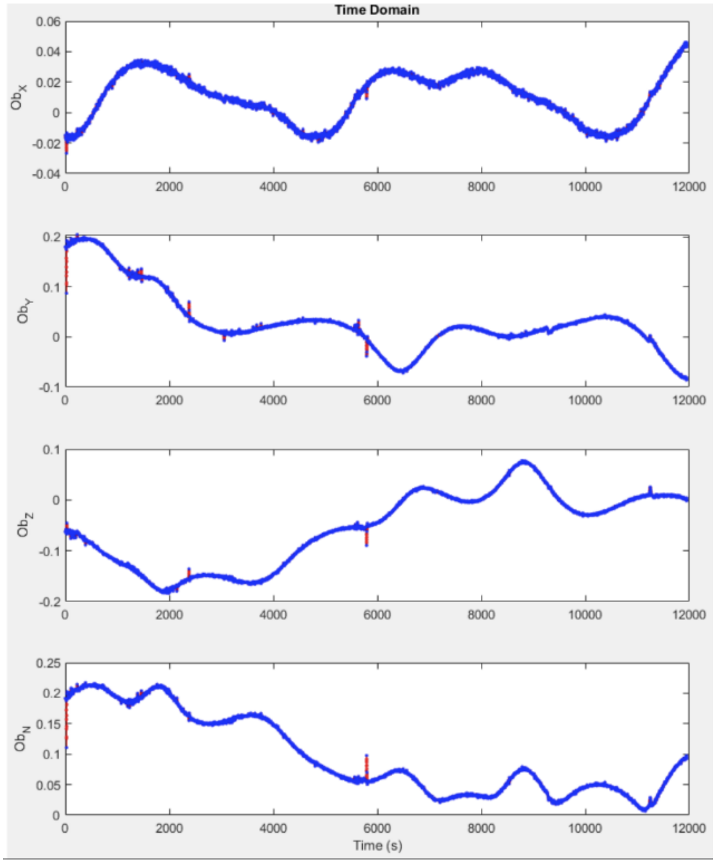

Figure 3.44: Rotations of tumbling satellite after extension of boom in time domain.

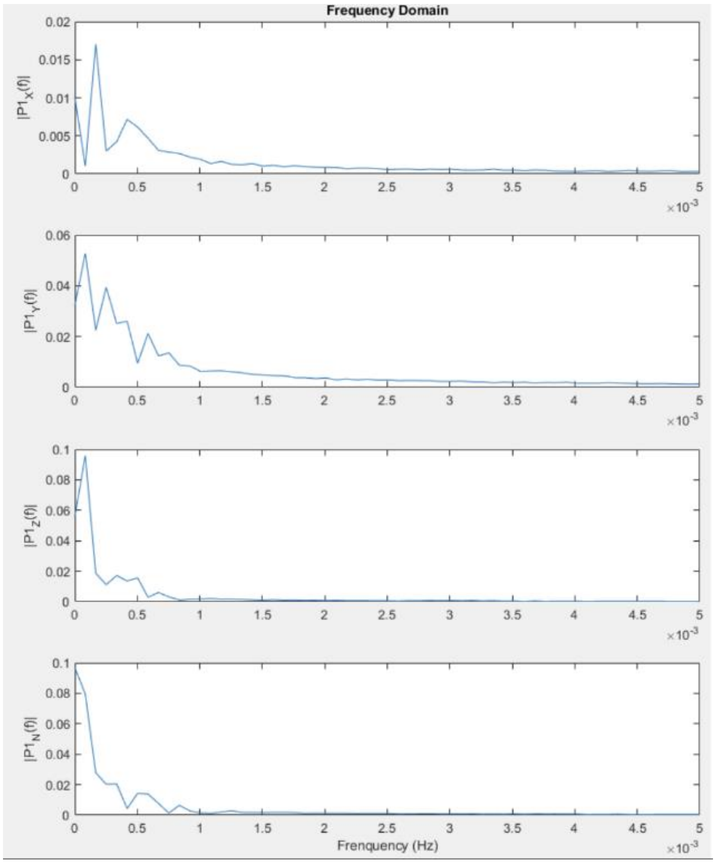

Figure 3.45: Rotations of tumbling satellite after extension of boom in frequency domain.

various TOF images over time, shows no change in the location of the bottom of the DOM2500 within its field of view. From these data, it is concluded that at this phase the boom is rigid and in fact not oscillating for all intents and purposes within the scope of ALE-1 operation.

This result gives confidence that the boom will not bend and cause a catastrophic failure if the satellite attitude is tried to be controlled by inputs through reaction wheels. This is important for two reasons: First, it enables the estimation of the moment of inertia of this system. Second, it enables attitude control help when the de-orbiting phase is started.

The moment of inertia of ALE-1 was estimated through measuring the spin response of the satellite to the reaction wheel inputs through FOG. Table 3.4 summarizes the mass moments of inertia at principal axes of the satellite before and after extension of the boom calculated from in-orbit data, measurement from the ground values at mass property test before flight, and calculation using parallel axis theorem, and applying simplifications to mass distribution of parts that change their relative position in the satellite.

Table 3.4: Mass moments of inertia of ALE-1 at different phases of SDOM mission.

	Mass property test before flight	Parallel axis theorem with simplifications for extended boom	In orbit estimation	
			Default	Extended
J_{xx}	2.96 kg/m^2	15.94 kg/m^2	2.89 kg/m^2	16.54 kg/m^2
J_{yy}	3.03 kg/m^2	16.02 kg/m^2	2.92 kg/m^2	16.42 kg/m^2
J_{zz}	2.21 kg/m^2	2.21 kg/m^2	2.17 kg/m^2	2.21 kg/m^2

3.13.3. Deployment of the Sail

The sail deployment signal was sent on 24th of December 2019 during the night phase of the orbit. TOF camera can collect better data in the night phase and the sail deployment was intended to be recorded. However, the power requirement for the sail deployment actuation was too high and internal breakers of the satellite went down to avoid damage to the system. First option to avoid this would be to decrease power usage during deployment. Although the system was taken to a bare minimum, the total power usage was still above the threshold of the breaker. The next largest power consumer in the system is TOF camera itself when turned on. Turning it off would bring the consumption rate to below the threshold, however valuable data acquisition would be sacrificed in the process. The other option was to conduct deployment in the day phase of the orbit, where the satellite is generating power through solar sails, which then contribute to raise the threshold for the breakers. This would result in lesser quality data from the TOF camera, yet lesser quality data is preferable to no data at all.

On 25th of December 2019, sail deployment signal was sent once more during the day phase, and the deployment of the sail was confirmed immediately with the sail switch state change. Following this, the data logged by the TOF camera was downlinked over several days. A total of 127 frames were captured with a framerate of 10 frames per second including the deployment of the sail. Figure 3.45 shows the deployment sequence from these frames. Frame ID for each frame is denoted on the top right corner. The corresponding timestamp t is denoted on the top left corner of each frame in seconds. Frames 1 through 14 are identical to frame 15 with no detectable movement. The deployment starts at a time between t=1.5 and t=1.6 seconds and completes within 0.8 seconds. For comparison Fig. 3.46 shows the deployment sequence of the engineering model of DOM2500 on earth.

For easier comparison, the timestamps for ground experiment are shifted 1.5 seconds to match the deployment in space. As can be seen from both figures, the deployment in space and on ground are very similar in nature. Both take about 0.7 to 0.8 seconds to fully deploy, and the footprint of deployment at every timestamp are similar. In fact, differences are more clearly observed after the deployment is completed. On earth, mainly due to effects of gravity and by a small portion due to higher air resistance, the sail stabilizes in a constant shape very fast. Whereas in space, the sail is movement continues after deployment is completed. If the complete deployment is observed, the sail is seemingly getting larger and smaller with a period of about 1.5 seconds. Additionally, the whole sail is rotating in the clockwise direction. This is due to angular momentum accumulated in the coil during the deployment sequence when the convex tapes used for the deployment of the sail are extending. Further analysis on both accounts is conducted.

3.13.3.1. Deployment Percentage

As discussed above, after deployment the sail is seemingly getting larger and smaller. As a first step, in order to quantify how much deployment has actually occurred, the deployed is calculated. Ideally this area is to be calculated from the TOF data acquired, but the TOF data acquired proved to be extremely noisy to accurately calculate the area of the film in the image. As discussed in section 3.7.3., the deployment had to be conducted in day period of the orbit. In fact, sun can be observed as pitch black pixels on the top right of the deployment sequence images. Against all the physical filters applied to the camera, the data had extreme noise in

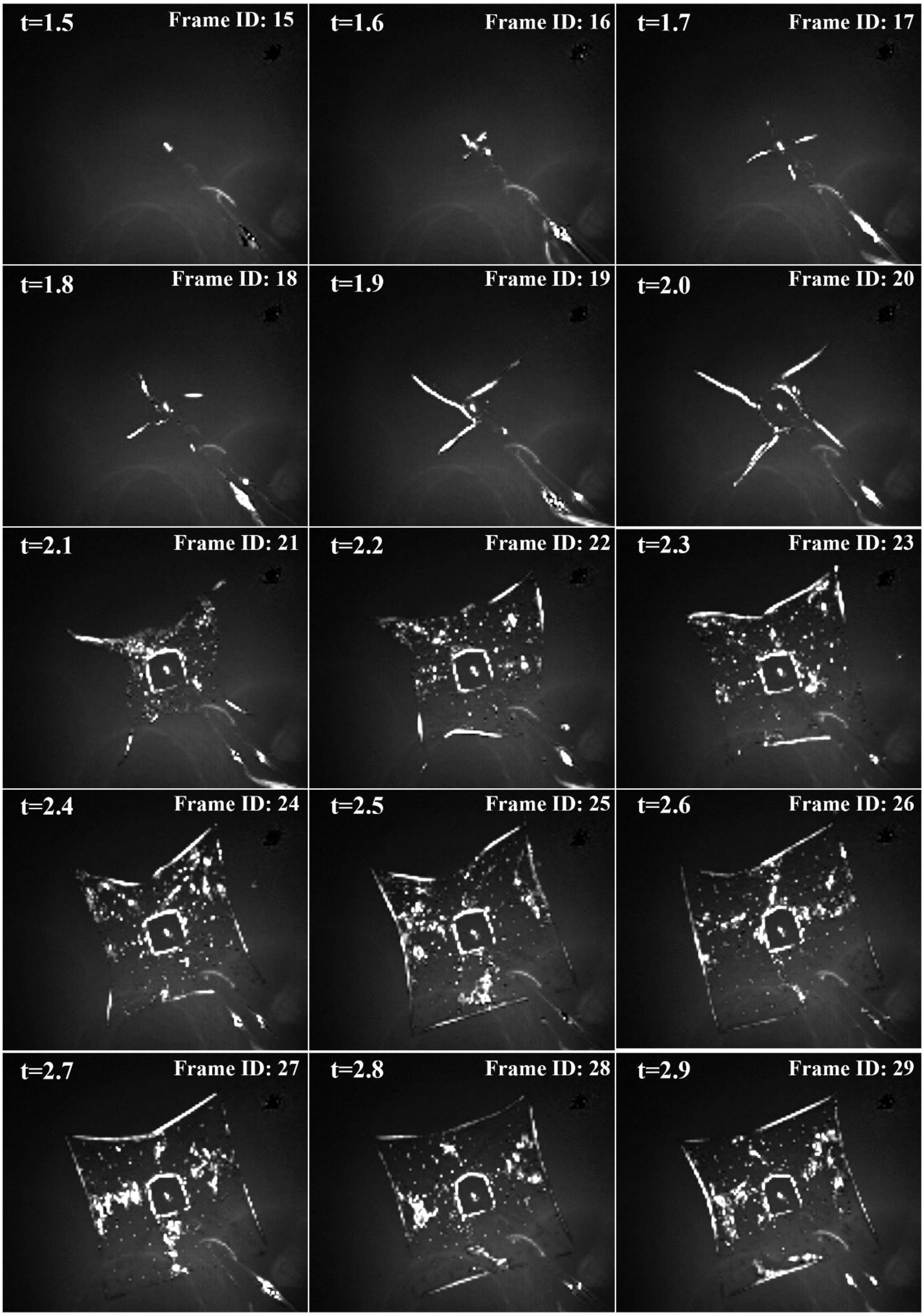

Figure 3.46: Image sequence of the sail deployment of DOM2500 used for SDOM in-orbit taken by TOF.

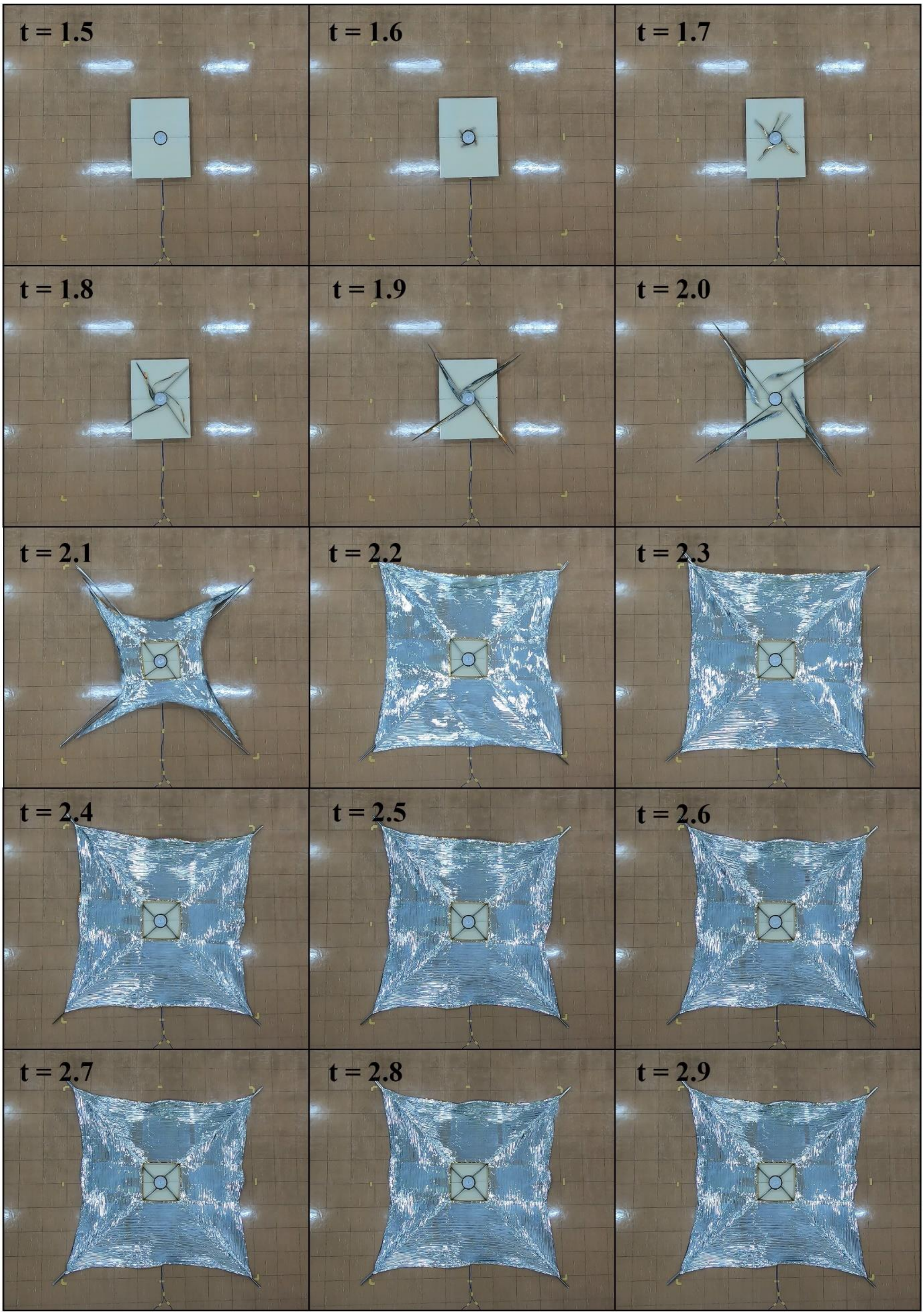

Figure 3.47: Image sequence of the sail deployment of engineering model of DOM2500 on earth.

space to accurately depict the exact distance of each point. Many points were extremely underestimated due to stray photons reaching the sensor instead of the photons emitted by the sensor itself.

Additionally, many of the emitted photons are reflected back from the housing of the camera itself. Although housing was designed to the requirements defined in the instruction manual of the TOF while considering these kinds of possibilities, the measures taken were ultimately not sufficient. However, even though the distance data is not as reliable as expected, the visual appearance of the film is very distinguishable. Using this, it is possible to estimate an area comparison with a control image taken on ground with the same positioning of the sail and the camera as the space.

The design value for the deployment plane of the sail is 0.2 meters higher than the bottom of DOM2500. This makes the film deployment plane, 2.5 meters away from the TOF camera. Additionally, the sail is connected to the convex tapes used for deployment only at the tips through Dyneema wires. Considering the length of these convex tapes and the length of the Dyneema wires used for the aforementioned connections, we can replicate a deployed sail on ground and observe through TOF camera for a control image. Figure 3.47 shows this image.

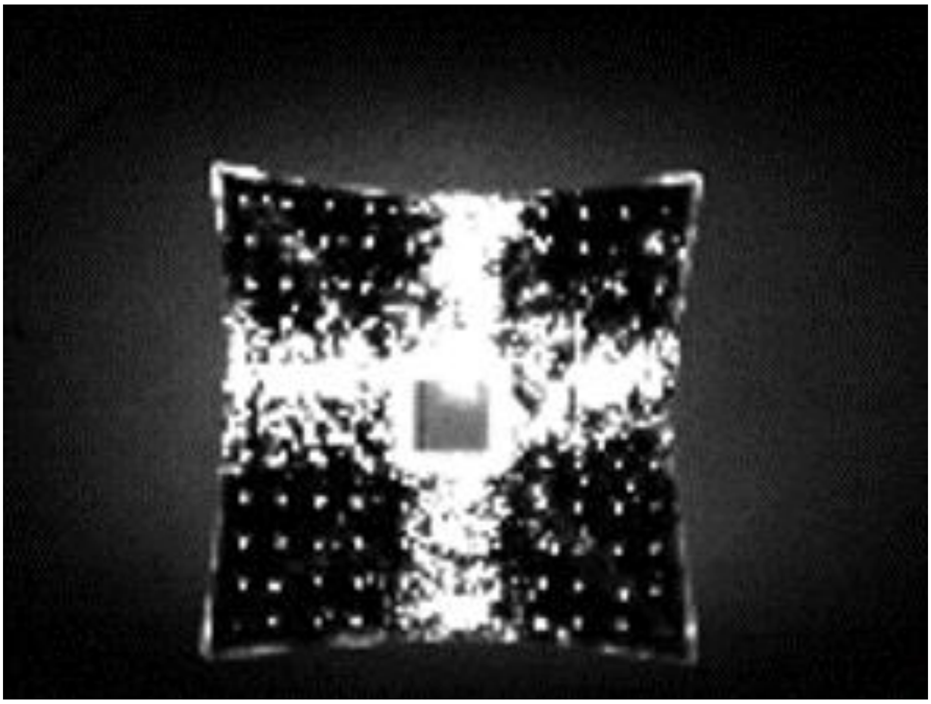

Figure 3.48: Control image of the replicated deployed sail taken on ground with TOF at same position conditions.

The area of the film in Fig. 3.47 is considered fully deployed. Using this control image as 100%, the deployment of each frame from the TOF data acquired in space are calculated and plotted into Fig 3.48. From this figure, it can be seen that the sail is seemed to be deployed at most 87% of design value and it get smaller as much as 66% of the design value at the initial deployment oscillation. This oscillation is damped over time and although the data does not continue until the stabilization point, it can be estimated to be around 75%.

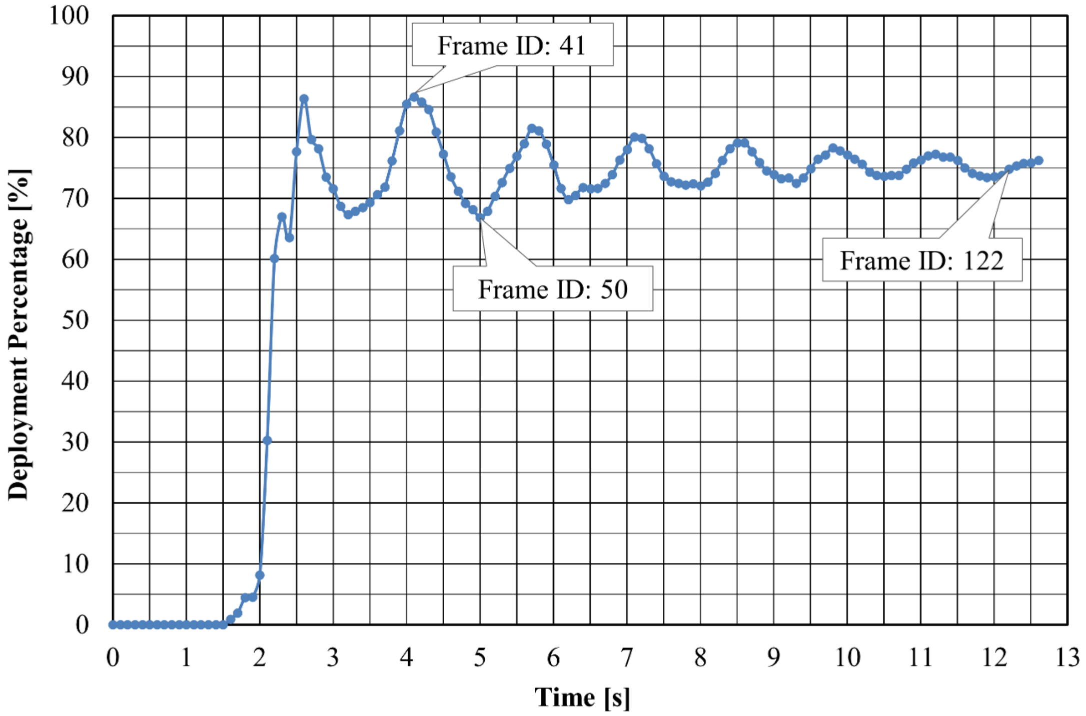

Figure 3.49: The calculated deployment percentage per frame during deployment of the sail in space.

For further investigation of the possible reasons behind this, the 3D point cloud data acquired by TOF is inspected for each frame. For discussion, three frames are selected with highest deployment percentage, lowest deployment percentage, and a percentage that is close to the stability point. These are frames 41, 50 and 122.

Figure 3.49 shows the point cloud for the highest deployment percentage yielding frame, and Fig. 3.50 shows the corresponding amplitude image from the TOF camera. For better visualization, a plane that is the size of the theoretical film is drawn at the theoretical distance of 2.5 m from the camera. As can be observed most of the points are severely underestimated from the camera.

It is important to consider the points with a higher Z distance value as more accurate. A higher Z distance corresponds to a longer time of flight between the emitted photon and the captured photon. Realistically, most of these points should have similar time of flight, and

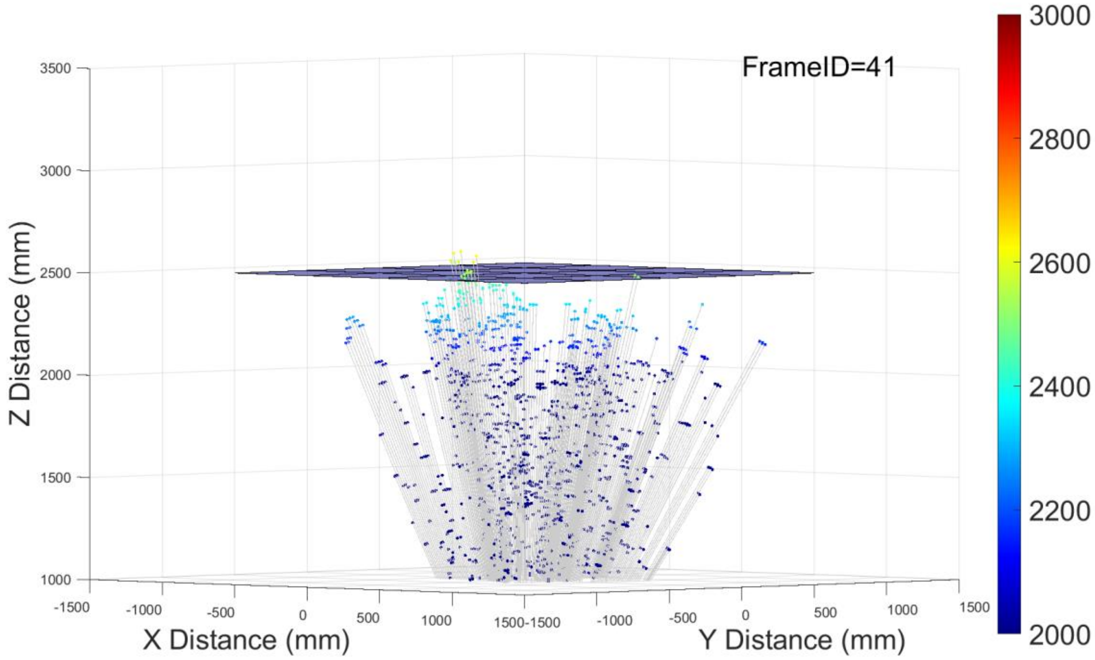

Figure 3.50: 3D point cloud data from TOF for the highest deployment percentage yielding frame.

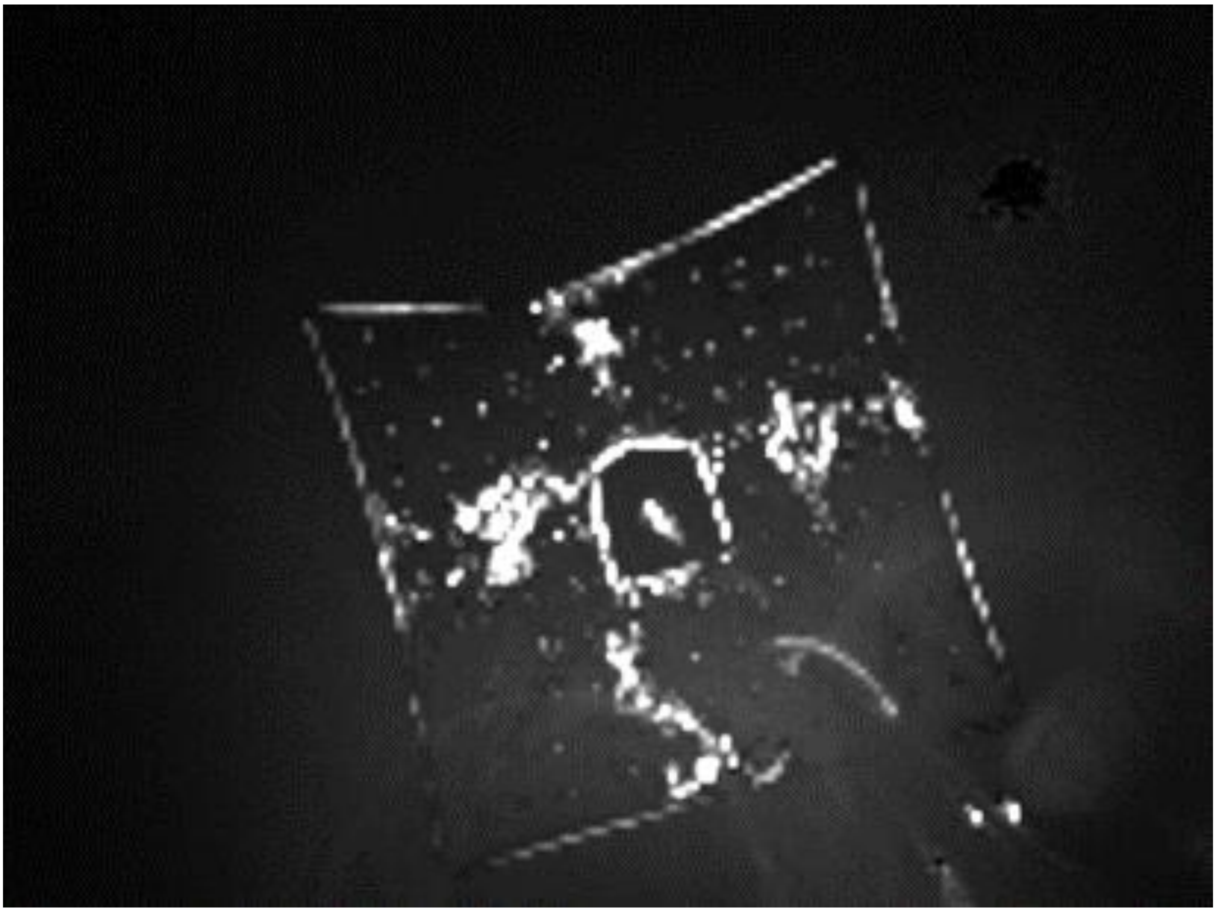

Figure 3.51: TOF amplitude image for the highest deployment percentage yielding frame.

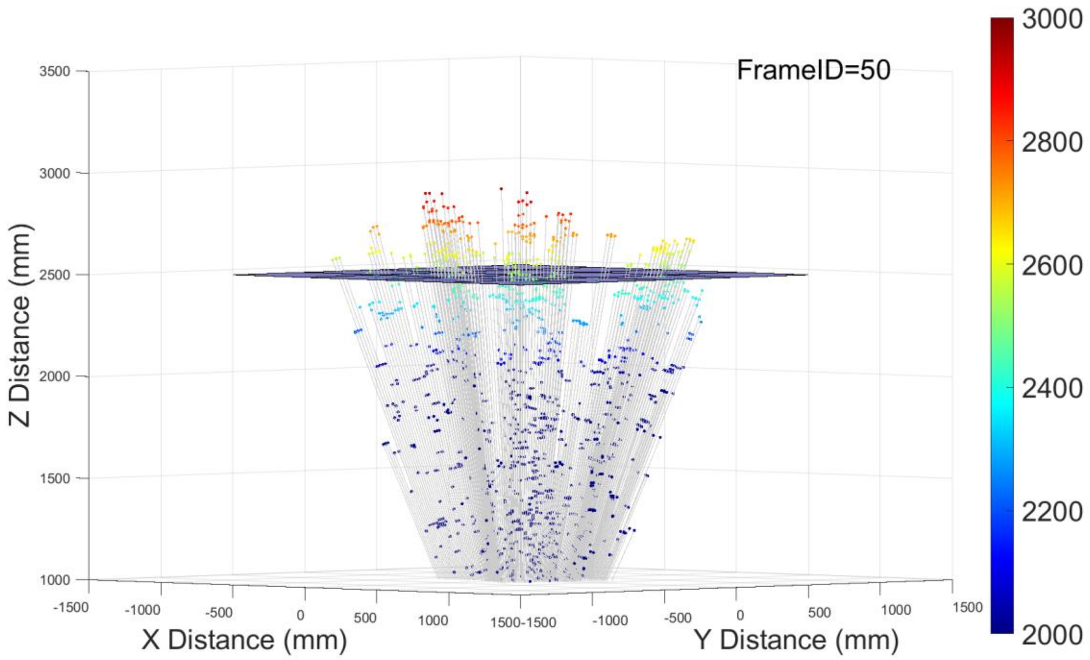

Figure 3.52: 3D point cloud data from TOF for the lowest deployment percentage yielding frame.

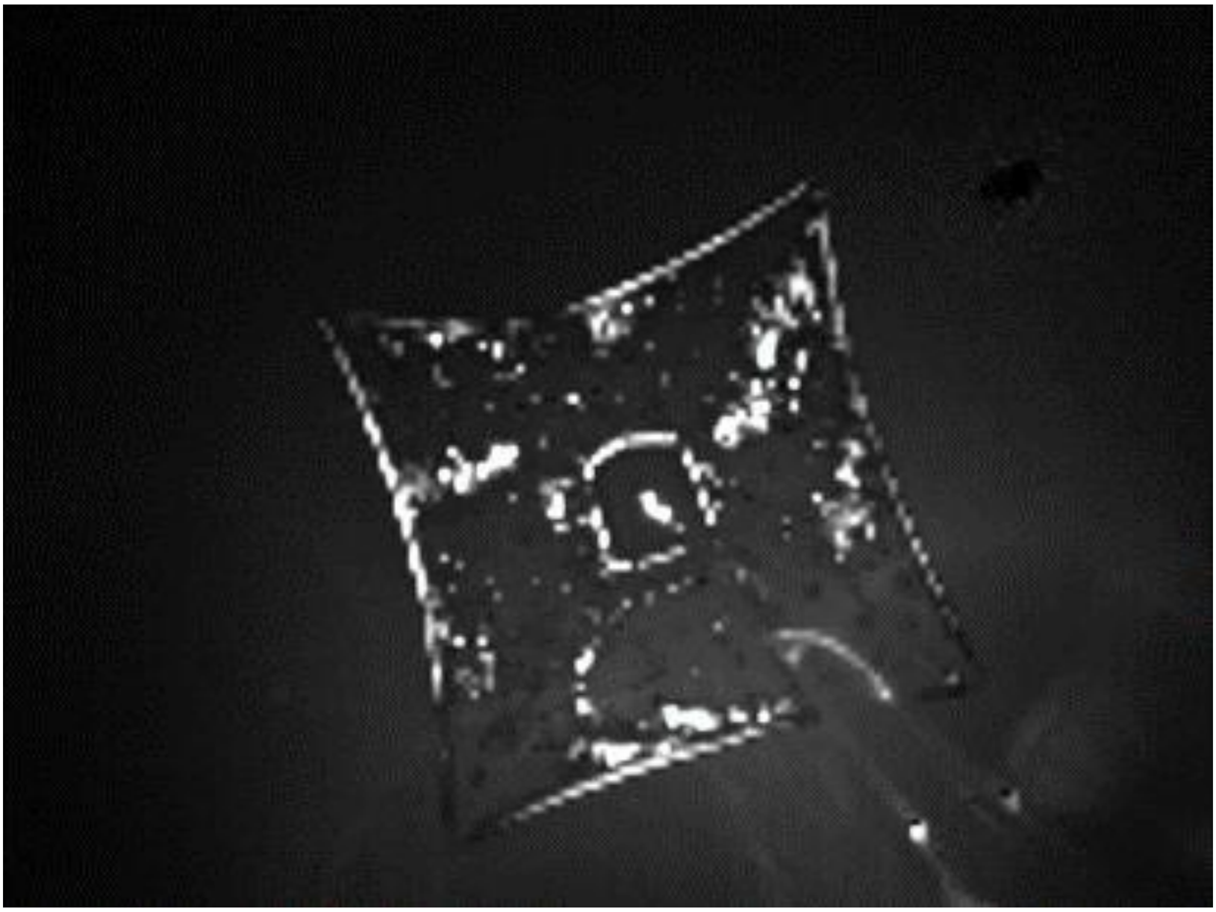

Figure 3.53: TOF amplitude image for the lowest deployment percentage yielding frame.

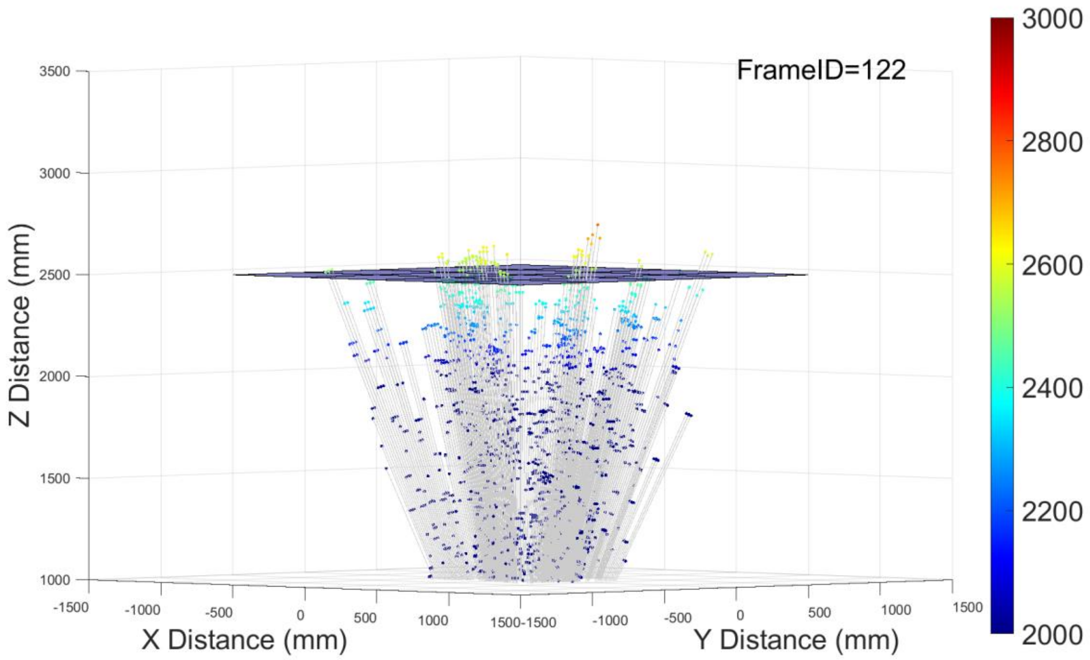

Figure 3.54: 3D point cloud data from TOF for the closest to stability deployment percentage yielding frame.

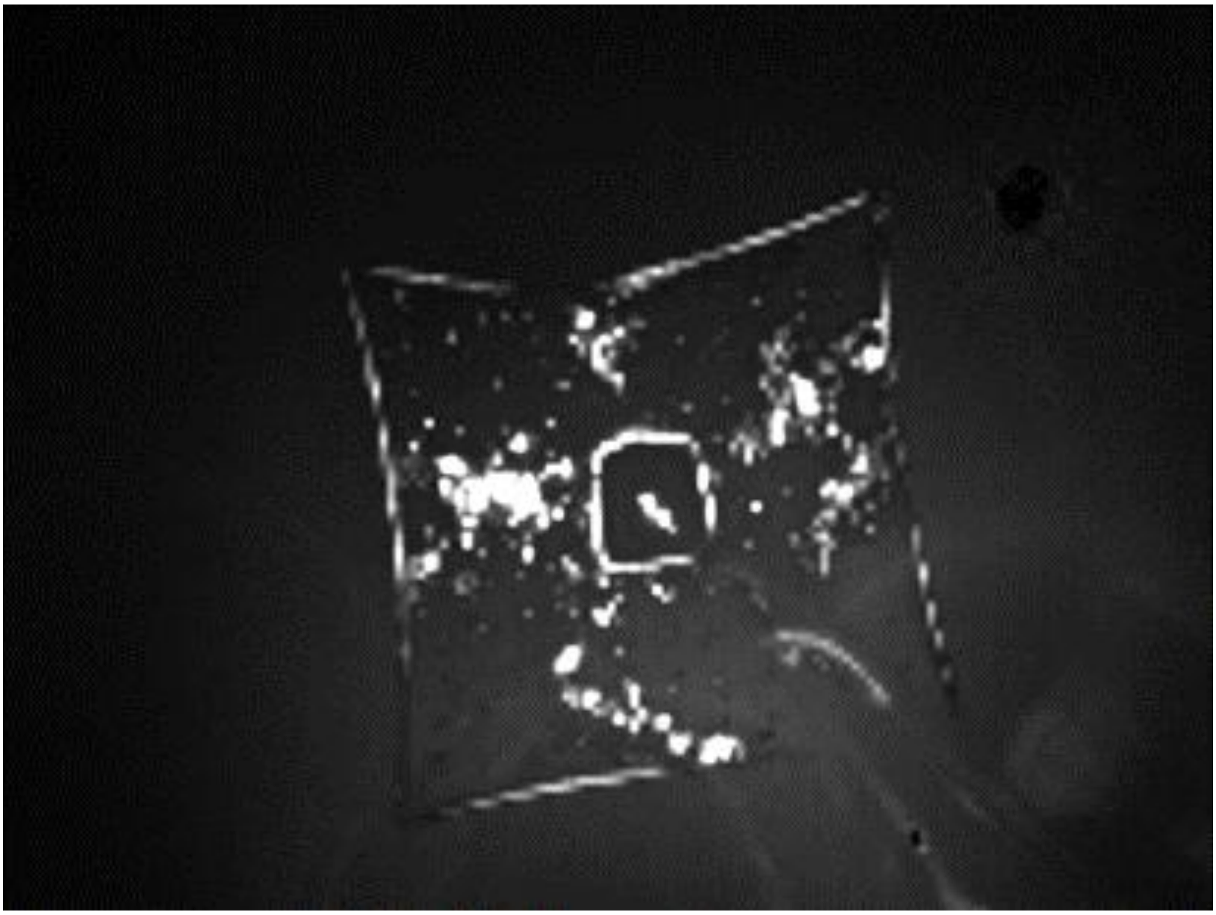

Figure 3.55: TOF amplitude image for the closest to stability deployment percentage yielding frame.

therefore similar Z distances, however, for each pixel any stray photon hitting the sensor prematurely causes underestimation of the distance for that particular point.

In comparison, overestimation of a point can only occur, if the emitted photon is lost, and a stray photon takes longer than the theoretical time-of-flight of that lost photon to reach the sensor. With such enormous background radiation levels, this is highly unlikely. Therefore, for the rest of this analysis, point that are estimated to be further away from the camera are considered more accurate. For figure 3.49, it can be seen that the points that are situated furthest away from the camera are situated around 2.5 meters of distance.

Figure 3.51 shows a similar figure for the lowest deployment percentage yielding frame and Fig. 3.52 shows the corresponding amplitude image from the TOF camera. In this frame, it can be seen that the points that are furthest away from the camera can be found around 2.8 meters of distance. The color scale is synchronized throughout the figures to observe the difference better. From this figure, it can be inferred that the film is in fact not situated in 2.5 meters of distance as designed but further away at least partially.

Looking at the deployment video, the sail movement can be considered as moving away from the camera while curving outwards and returning back towards the camera becoming flatter. At Frame ID: 41, the sail appears flattest, which in turn would also be closest to the camera, and at Frame ID: 50, the sail appears most curved and in turn further away from the camera. The shrinkage of projected film area on to the camera due to curving and the smaller appearance of the sail due to further away location are considered to be the reasons for the sail’s low deployment percentage.

Figure 3.53 shows a similar figure for the frame with a deployment percentage that is close to the stabilization percentage of 75% and Fig. 3.54 shows the corresponding amplitude image from the TOF camera. The points that are furthest away from the camera in this figure can be found around 2.65 meters. From this, it can be inferred that the sail stabilizes in a curved attitude and further away from the satellite than intended.

3.7.3.2. Torsional vibration of the boom

The convex tapes used for the sail deployment are wound around a coil inside DOM2500 at storage. During deployment, this coil is rotating with increasing speed and gaining angular momentum. When the deployment is finished, this angular momentum is then transferred to the whole sail and the sail is seen to be rotating in the clockwise direction when observed from the satellite. This rotation can also be observed in the later portions of the deployment of the sail.

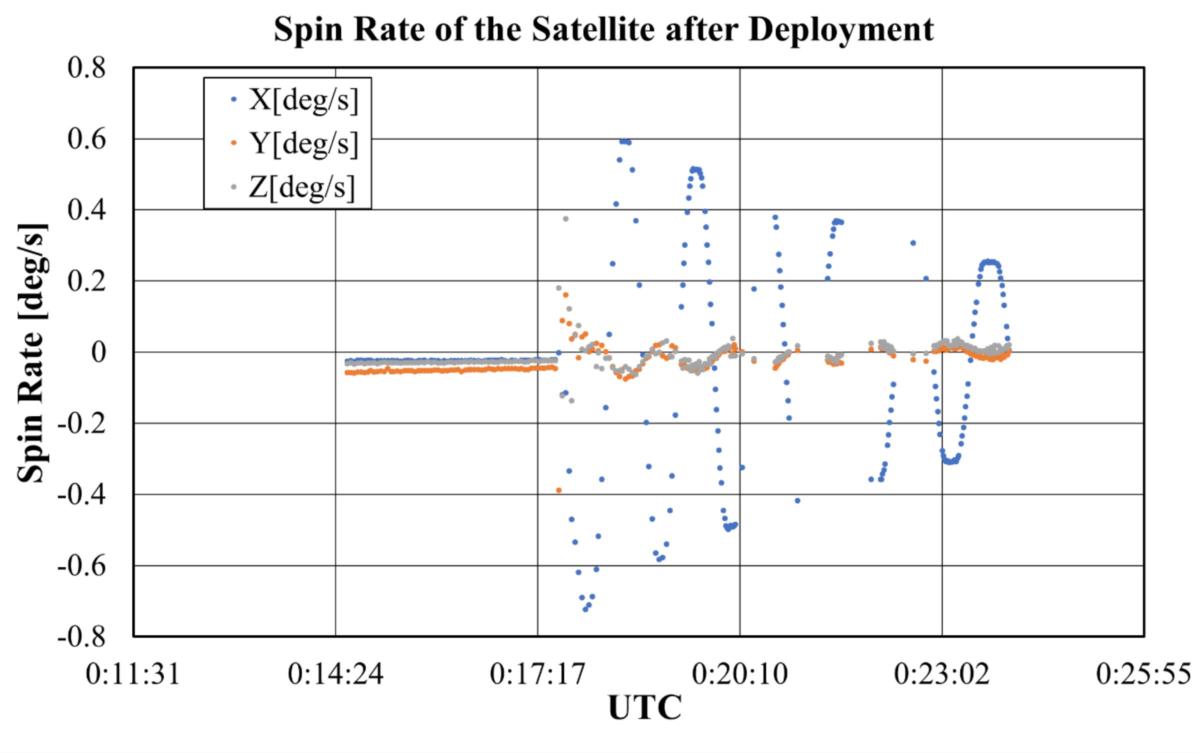

Figure 3.56: Spin rate of the satellite during deployment of the sail measured with the ACU.

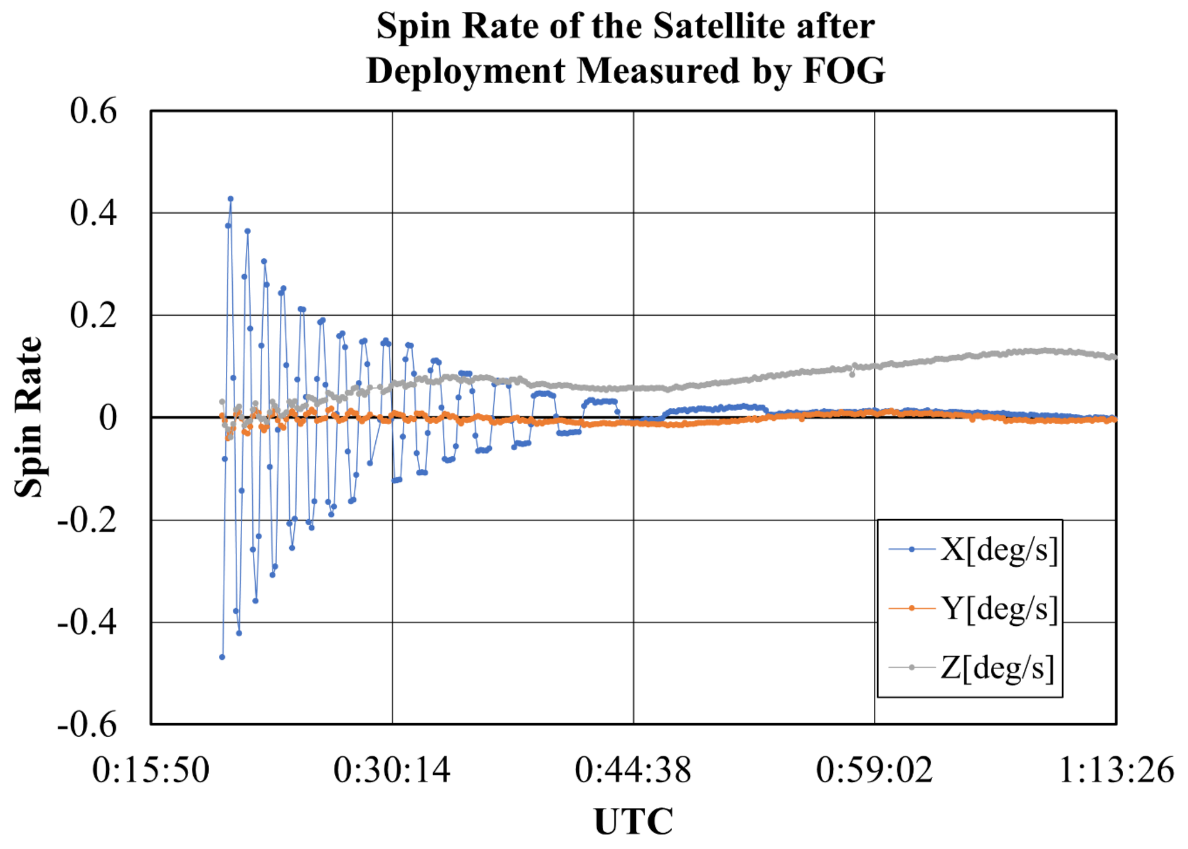

Figure 3.57: Spin rate of the satellite shortly after the deployment measured with FOG.

The rotational movement of the satellite is also logged through ACU of the satellite during deployment and logged with FOG immediately after deployment. Figures 3.55 and 3.56 show these logs. From these figures it is clearly observed that with the deployment of the sail, an oscillating rotation is induced to the satellite in the direction of the boom extension. The reason for this, is the torsional vibration of the boom with the excitation from the angular momentum of the deployment. The boom is acting as a shaft, and the sail and the satellite are acting as rotating mass elements. From these figures we can read the period of this vibration to be about 60 seconds.

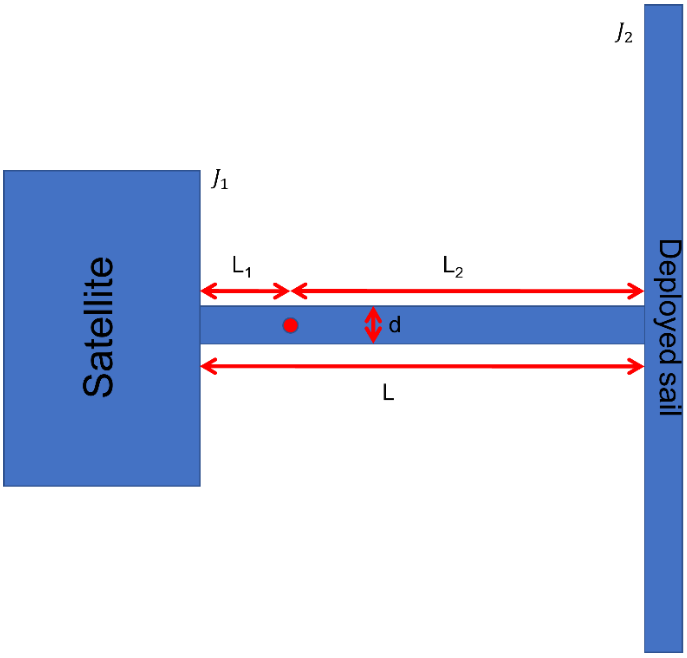

Figure 3.58: Simplified system of ALE-1 for torsional vibration analysis.

Figure 3.57: represents a simplified system of ALE-1. The red dot in this figure represents the stationary node where no movement can be observed by an outside observer. The frequency of the torsional vibration of a free shaft with two masses at each end is given by Eq.3.2:

$$F = \frac{1}{2\pi}\sqrt{C\,\frac{(J_1+J_2)}{(J_1 J_2)}} \tag{3.2}$$

Where F is the natural frequency of the system, J_1 and J_2 are the corresponding mass moment of inertia of the two masses, and C is the torsional stiffness of shaft connecting the two masses defined as:

$$C = I_p \frac{G}{L} \tag{3.3}$$

In Eq. 3.3, I_p is the moment of inertia of the shaft, G is the modulus of rigidity of the shaft which is specific to the material, and the L is the length of the shaft. The term I_pG together is called the torsional rigidity. Frequency F can be calculated from the period of the oscillation, and the respective mass moment of inertia J values at the axis where the boom resides can be calculated using the parallel axis theorem. G is specific to the material and is 77 GPa for steel used in convex tapes. Using all these values we can solve for an I_p for the boom element of SDOM which is: 3.23×10^{-13} m^4. From these we can calculate an equivalent diameter and mass table for other materials in case of solid shaft each yielding the same torsional rigidity as the SDOM boom. Table 3.5 summarizes this.

Table 3.5: Equivalent diameters and masses for different booms of same length.

	SDOM boom	Solid steel	Solid aluminum	Solid CFRP
Diameter	50mm	1.35mm	1.75mm	1.66mm
Mass	360g	27.6g	16.9g	8.7g

By comparison, from a torsional rigidity point of view, a boom made of convex tapes is more than 10 times more massive as a solid shaft, however convex tapes do provide lateral rigidity with more efficiency than solid shafts. Convex tapes are inherently weakest to the torsional disturbance, and this weakness is clearly seen from Table 3.5. Additionally, solid shafts can not self-extend, and therefore are irrelevant as far as deployable space structures are concerned.

The position of the standing node of the torsional vibration as well as the ratio of the angles of twist for each side for the system defined in Fig. 3.57 are given by the following Eq. 3.4:

$$\frac{L_2}{L_1} = \frac{J_1}{J_2} = \frac{a_2}{a_1} \tag{3.4}$$

From this, because $L_1 + L_2$ is known to be 2.5 m, L_1 is calculated to be 0.46 m. Similarly, by calculating the area under the first wave in Fig. 3.56 through integration, the total angle of twist can be calculated to be 13.962 degrees at the satellite side. This will then correspond to 61.402 degrees at the sail side using Eq. 3.4. Knowing this angle allows the calculation of the torque caused to the satellite system by the deployment of DOM2500 to be 0.013 Nm through the following Eq. 3.5:

$$T_2 = \frac{GI_P}{L_2} a_2 \tag{3.5}$$

3.7.4. Post-Deployment of the Sail

Shortly after the sail deployment, the sail connection with the convex tape frame was lost on one of the corners. The loss was confirmed on 28th of December 2019, 3 days after the sail deployment. The sail status image confirming this can be seen in Fig. 3.58. Following this, on 14th of January 2020, another corner connection of the sail was confirmed to be lost. At this state, the drag sail was only connected at two corners. Figure 3.59 shows the confirming image of this state taken by the TOF camera. The convex tapes that deployed the sail can be clearly observed in this figure as well.

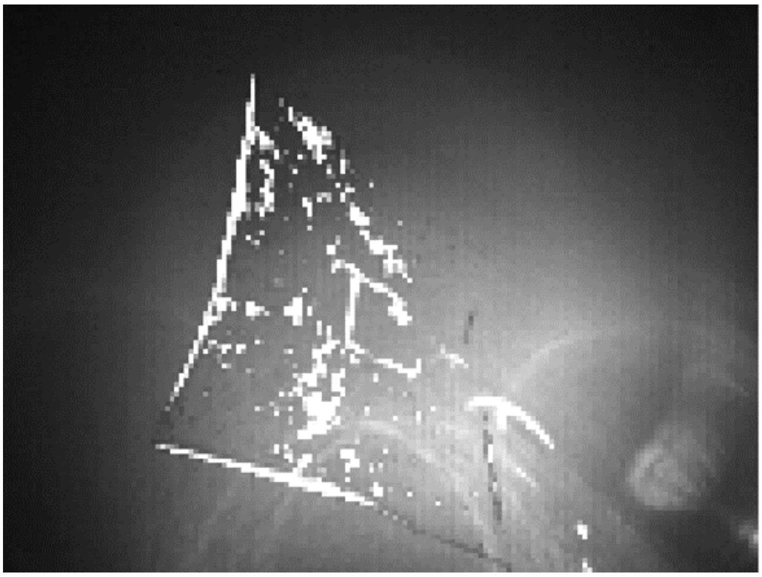

Figure 3.59: The amplitude image acquired by TOF camera confirming the loss of the first corner of the film. (©IEEE)

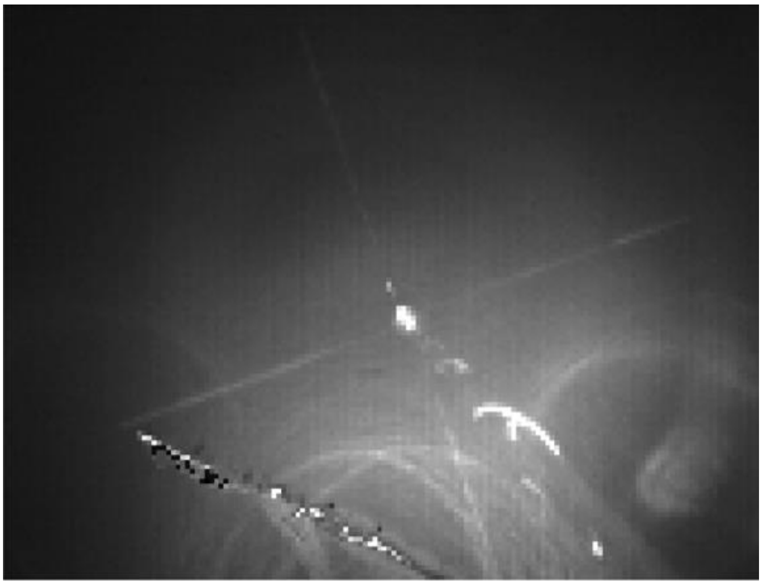

Figure 3.60: The amplitude image acquired by TOF camera confirming the loss of the second corner of the film. (©IEEE)

From this point onwards, the sail is free to move around the axis that goes through the two connection points left. Additionally, due to less tension on the film, the size of the film is expected to be even smaller than the previously estimated 75%. The boom is 2.5 meters long and the sail is 2.5 m by 2.5 m wide when completely flat. Considering the shrinkage of the sail, it is unlikely that the sail can reach the satellite and cause a catastrophic failure. In fact, Fig. 3.60 shows a picture of the sail taken by the DMC at a time when the sail was located between the DOM2500 and the satellite, and it is observed that the sail does not reach the satellite.

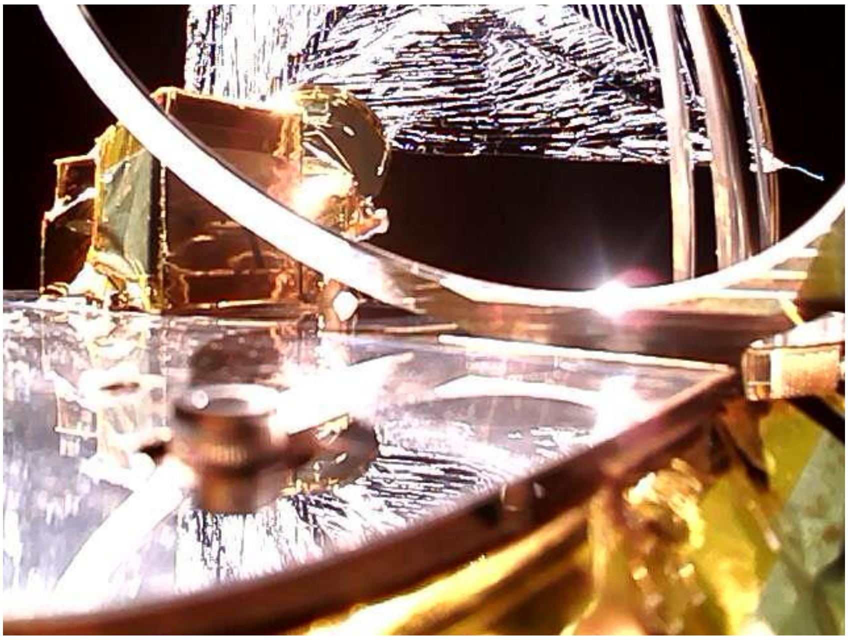

Figure 3.61: DMC picture showing the sail coming between DOM2500 at the tip of the boom and the satellite main body. (©IEEE)

From this point onwards, ALE-1 was left to de-orbit on its own. Although many observations of the sail with the TOF camera was planned, none could be realized due to the sail situation. However, the de-orbiting rate of ALE-1 was observed to change with the deployment of the sail. Figure 3.61 shows the semi-major axis of ALE-1 with regards to time in UTC. This graph is drawn using the two-line element set (TLE). ALE-1 has descended about 17 km in the 19 months since the deployment of the drag sail.

The discontinuous change in de-orbiting rate right before January 2020 coincides with the deployment of the sail. The small jump in semi-major axis around April of 2020 coincides with the gas leak from the satellite. This leak is from the tank that is used for the artificial star shooting mission equipment on-board from. The reason for this leak was a malfunction in the gas output control system, and it was noticed at routine pressure checks of the tanks. When the control system was restarted, the malfunction disappeared.

Although the sail was broken in a very short time after deployment, the de-orbiting rate is still much higher than before its deployment. This state of the sail is referred to as a drag-flag from this point onwards. The descent rate of ALE-1 is difficult to quantify, because it is difficult to simulate the orbit descent considering complicated influences of the unstable sail status of ALE-1, solar activity and atmospheric changes.

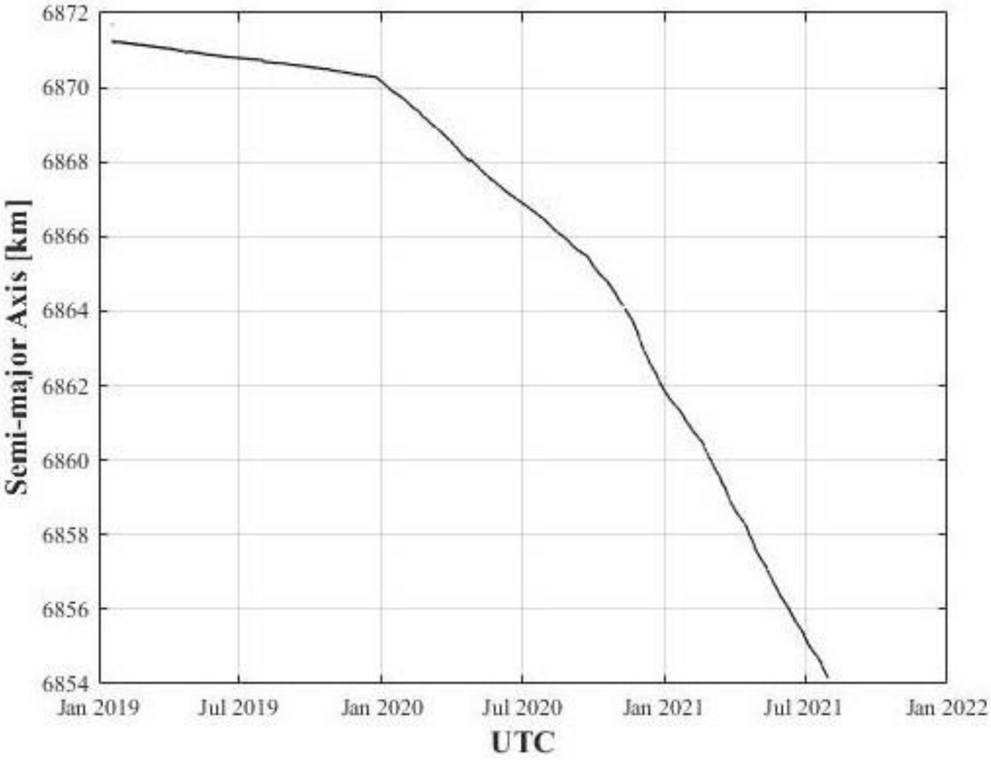

Figure 3.62: The trajectory history of ALE-1 based on two-line elements. (©IEEE)

In general, the perturbation acceleration of a flying object in the upper atmosphere is given by the following Eq. 3.5:

$$\mathrm{a}_{\mathrm{drag}} = -\frac{1}{2}\mathrm{C}_{\mathrm{D}}\rho\frac{A}{m}\mathrm{v}_{\mathrm{rel}}^{2} \tag{3.5}$$

where ρ is the atmospheric density, C_D is the drag coefficient, A is the cross-sectional area of the satellite, and m is the satellite mass. ALE-1's mass is 68.16 kg according to pre-launch measurements (65.29 kg after SDOM separation); therefore, m is taken to be 68.16 kg. CD is a dimensionless quantity and is taken to be 2.2 for satellites in-orbit. A is 6.0 m^2 at theoretical maximum deployment of the sail, however, since the film is not deployed ideally into a completely flat state and is in a drag-flag state, it is impossible to measure the cross-sectional area value. Therefore, to estimate the orbit descent, first an effective A needs to be estimated for the case of ALE-1.s

From the de-orbiting data of 19 months from January 2020 until July 2021, we can calculate an effective drag area for this drag-flag and use this value to further estimate the deorbiting of ALE-1 until sub 400 km orbit. In order to do this, a series of simulations are run with varying drag area values from 1.3-1.7 m^2 with increments of 0.5 m^2. The environmental model used for these simulations are summarized in Table 3.6 and the parameters used in the simulations are summarized in Table 3.7. Figure 3.62 shows the comparison of these simulations to the TLE.

Table 3.6: Environmental model used for simulation.

Section	Model
Atmospheric drag	EGM2008, (degree, order) = (40,40)
Sun / Moon model	Astronomical Almanac
Atmosphere model	NRLMSISE-00

Table 3.7: Parameters used for simulation.

Section	Parameter	Value
Atmospheric drag	C_D (drag coefficient)	2.2
	Ap (daily geomagnetic planetary amplitude) [-]	-
	$F_{10.7}$ (daily solar flux) [SFU]	-
	$F_{10.7,81day}$ 81day (81-day average of F10.7) [SFU]	-
Solar-radiation pressure	C_R (radiation pressure coefficient) [-]	1.53
	P_{srp} (solar-radiation pressure) [N/m^2]	4.57×10^{-6}
	Shadow function	0, 0.5, 1
Earth orientation parameters	Xp, yp (polar function) [deg]	0.0
Time system	UTI [s]	0.0
	⊿ AT [s]	37.0
Duration	2020/05/28 20:00:00 ~ 2021/07/31 00:00:00	

The simulations were performed starting from the time the gas leak was confirmed to finish until the end of July 2021. As can be seen from the graph, the predicted values in the simulations show similar behavior to the TLE trajectory history, although the rate of descent varies with each A. At the first half of this descent, an effective drag area of 1.5 m2 seems to match better with the TLE, while on the second half of the descent, an effective drag area of 1.65 m2 seems to match better with the TLE. Using this it is concluded that the effective drag area A for the case of ALE-1 is between 1.5 m^2 and 1.65 m^2.

From this conclusion, further simulations were run using the values 1.5~1.65 m^2 varying with 0.5 m^2 increments until complete de-orbiting was achieved. Figure 3.63 shows these results. If the orbit descent of ALE-1 continues at a similar rate to the estimated effective area A of 1.5~1.65 m^2, it can be expected that ALE-1 will reach below 400 km of altitude in sometime October to November of 2022 depending on the A. Relatedly, complete de-orbiting could be achieved as early as January of 2023 if separation of the drag-flag is not performed. As this is undesired, it is necessary to monitor periodically and initiate the separation as soon as the desired altitude is reached.

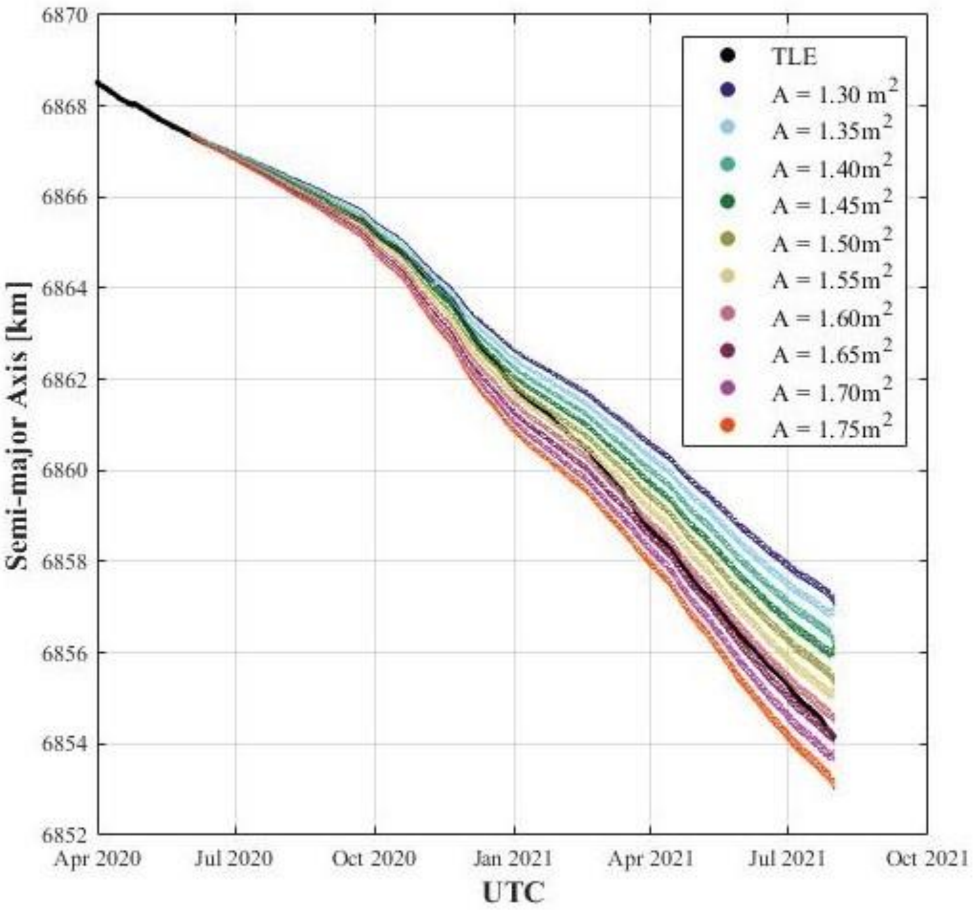

Figure 3.63: Comparison of simulations with varying effective drag area to the TLE. (©IEEE)

These results are very different than the initial simulations run at section 2. The effective drag area is a very dominant factor on the de-orbiting time of a satellite and the main reason for the SDOM mission of ALE-1 to still continue is the fact that the effective drag area for ALE-1 decreased substantially with the breaking of sail connections.

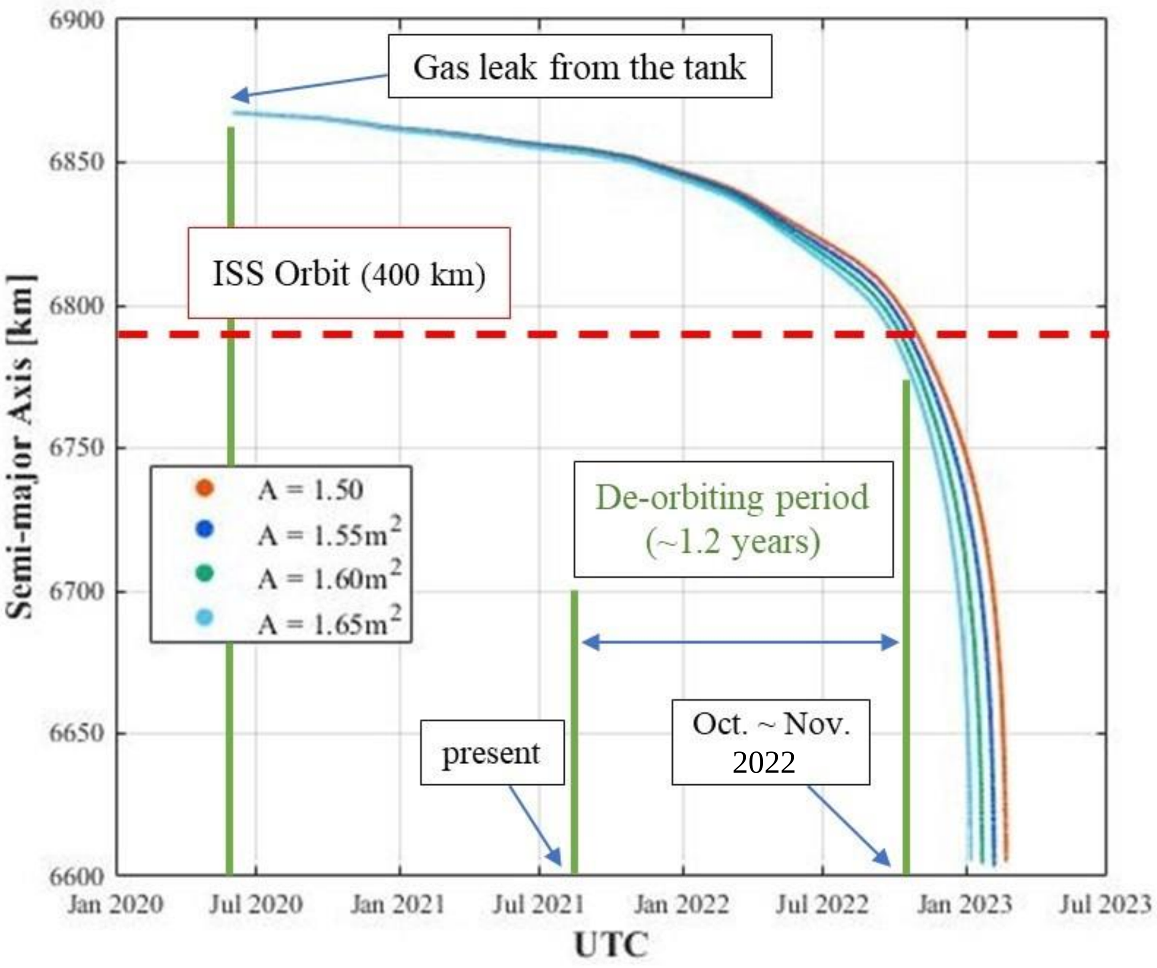

Figure 3.64: Estimated projection of the future de-orbiting of ALE-1 at the drag-flag state. (©IEEE)

3.8. Summary

In this chapter, the development and in-orbit demonstration of Separable De-Orbit Mechanism (SDOM) is explained. The various design requirements for the SDOM in general and specific to the ALE-1 mission are presented and the design choices for these criteria are explained. The membrane size is chosen as 2.5 m by 2.5 m to enable realistic de-orbiting of the micro-satellite ALE-1. The mast length is chosen to be 2.5 m to enable operability during de-orbiting.

A serial camera (DMC) is implemented to confirm the lid opening, boom extension and membrane separation actions. Additionally, a time-of-flight camera (TOF) system is integrated to observe the deployment behavior, and membrane status afterwards. The whole system of SDOM is then subjected to ground experiments, where the successful actuation of each phase was confirmed.

After the launch of ALE-1, the SDOM mission was also initiated shortly after. The lid was opened and after the confirmation of this, the boom extension signal was sent. After about 5 months of delay, the boom extension was also confirmed. After confirmation of the relative rigidity of the boom, membrane deployment was initiated. The membrane was deployed, and the deployment behavior was optically recorded by the TOF as monochromatic images and as 3D point cloud data including the distance information. This kind of data acquisition for the membrane deployment behavior in space is the first of its kind. The deployment took 0.7 to 0.8 seconds. The oscillation of membrane was observed after the complete deployment was achieved. The comparison of deployment images in-orbit and on-ground show similarities in deployment times and intermediary membrane shapes during deployment. However, they show disparity after the deployment where the membrane oscillates in-orbit, and is stationary on-ground. This oscillation was further investigated with the 3D data acquired from the TOF and an out-of-plane oscillation of the membrane was detected. This is an unexpected behavior. Deployment experiments and observations cannot be repeatedly performed in outer space with ease. Therefore, the data acquired is extremely valuable as control data and contribute to the future academic development of this field.

The membrane deployment percentage is investigated. Compared to membrane deployed on-ground, the membrane deployed in space is estimated to reach less are. This is due to several reasons. One reason is the fact that control data is taken on-ground, and the membrane is subject to gravity on-ground that flatten its folds more to show larger deployment area. Another reason is the fact that membrane is oscillating out of plane, which causes a curve to the membrane and lessens its projected area on the sensor. And finally, the fact that the membrane moves in the normal to the sensor direction which places the membrane further than the sensor which decreases its projected area.

Additionally, the torsional vibration of the boom is investigated. An equivalent moment of inertia is calculated for the SDOM boom from the measurement data, and the boom is concluded to be extremely weak against twisting force. The torque imparted by the DOM2500 on the main satellite is calculated to be 0.013 Nm in space.

Post-deployment analysis was conducted on the membrane. Two of the four membrane corner connections were broken shortly after deployment. However, a clear change in the de-orbiting rate of the satellite was detected from the telemetry data. In order to quantify this change, de-orbiting simulations were run for the ALE-1 system. Comparing the telemetry to the simulation results, an effective drag area for the ALE-1 system was estimated to be between

$1.5\ m^2$ and $1.65\ m^2$. This is about ¼ as effective as a flat membrane normal to the velocity direction, and ½ as effective as a tumbling satellite with a flat membrane. Use of potential drag-flags instead of drag sails are left to be investigated as future work.

Currently, ALE-1 is approaching its separation phase. The separation is estimated to be conducted in October to November of the year 2022 when the satellite is expected to reach below ISS orbit. This would equate 650 to 700 days after deployment. Although the initial simulation results were estimating 550 days for the completion of the orbital maneuver, the unexpected failure at the membrane corners have delayed this. Given the lower resulting effective area of a quarter, this is still a short time frame. The reason for this is increased solar activity, and the change in the current altitude of ISS itself.

4. Model Parameter Identification with In-Obit Flight Demonstration

Ground simulation work for mechanical movements is usually conducted using finite element analysis. This kind of analysis yields more accurate results if more parameters are included and considered. Although this increases computational cost of the simulation, for relatively smaller scale projects such as SDOM, with the help of modern computational power, it is possible to include very realistic models. These models usually contain parameters that are not easily calculated for space environment. Finetuning the simulation according to the ground experimental results do not always equate a realistic simulation environment for space. Therefore, it is necessary to tune the parameters of the simulation environment to space variables. Some of these variables can only be experimentally determined and show differences depending on the environment. It is important to use real mission data for the determination of these parameters. For this step, the data obtained for SDOM deployment in space is very valuable.

4.7. Parameter-tuning of the Membrane Model

To gain computational time, tuning of membrane is conducted without convex tapes first.

4.7.1. Fine-tuning of the Contact Coefficient

Figures 3.46 and 3.47 show the deployment sequence in space and on ground respectively. When compared to these figures, the initial simulation deployment shown in Fig. 2.11 is very linear. Additionally, in real deployment, the sail is first released from the wrapped configuration to a partially rotated star configuration as seen on Figs 5.10 (t=2.0) and 5.9 (t=2.0), and following this, the 2 cm folds are unfolded. This behavior is also not apparent in the initial simulation result. In order to improve this simulation result, the contact coefficient of the inner hub contact restriction model is adjusted.

With increased contact coefficient value, more rotation is induced to the membrane in general. Additionally, with increased pushing away from the hub, the inner layers of folds of the membrane start passing through the outer layers and move and unfold towards outside prematurely due to lack of tangibility between elements. It is important to match a good rotation rate for the membrane to match real rotation induced in the in-orbit deployment.

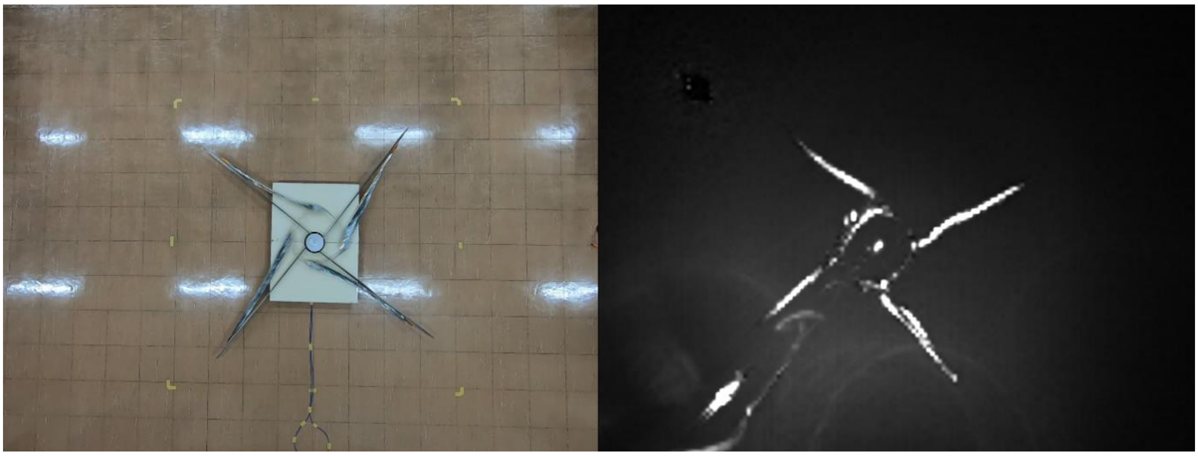

Figure 4.1: Initial formation of the inner hole and the star shape of the membrane during deployment experiments.

In order to balance out the rotational movement of the sail better to the general deployment, and to decrease the overshoot of the sail towards outside, the contact coefficient for the hub is varied as k = [10000, 1000, 50, 25, 20, 15, 10, 5]. Figure 4.1 shows reference frames to compare from the ground experiment and the in-orbit deployment data. For better comparison, the in-orbit result is mirrored. Figures 4.2 and 4.3 show comparison of the simulation results at key timepoints, and Figs. 4.4~4.11 show the complete simulation sequences with 0.02 second intervals up to 0.72 s. The most realistic result occurs at k = 10 which is Fig. 4.10.

As can be observed from Fig. 4.2, with high contact coefficient values, the inner layers of membrane are pushed outward excessively, and the membrane over-deploys prematurely. Following this, the membrane shrinks back at later stages of the deployment before full deployment is achieved. This is undesired and unrealistic behavior. Additionally, from Fig. 4.3, it can be observed that the membrane deploys with the induced rotation at lower values of contact coefficient k. Here it is important to note the appearance of the inner hole of the membrane and the general shape of the membrane at this instant. At k = 10, the membrane shape and the inner hole formation bears closest resemblance to the in-orbit and ground experiment results.

With a lower contact coefficient for the central hub model, the sail does not overextend further than the pulling corners. The sail is still prematurely unfolding from the inner layers, but this is less than the previous simulation result with a higher contact coefficient value. The rotational movement of the sail is also induced to some extent. Especially, at t = 0.56 s in Fig. 4.10. the sail is resemblant of the right-angled star shaped folded configuration shown in Fig. 2.9 (f). After this shape is achieved, ideally the sail should unfold starting from the inner most folds, propagating towards the outward layers, as the inner most square is tensioned closer to its maximum allowance before the outer layers. This can be seen in Figs. 3.46 and 3.47, where the inner square hole is fully deployed at t = 2.1 in both figures where the rest of the film is still only partially deployed. Following the inner folds, rest of the folds propagate to unfold in order towards outside. However, in this simulation, the smaller folds of the sail have already mostly unfolded at t = 0.60 and the sail is only overlapping itself as 2 layers when looked from the vertical angle as in the figure. This kind of fold, or the type of unfolding of the said fold does not occur in the real sail during deployment. Instead the membrane stay folded until the intermediary star-shape is achieved through unwrapping, and then the folds start to open up.

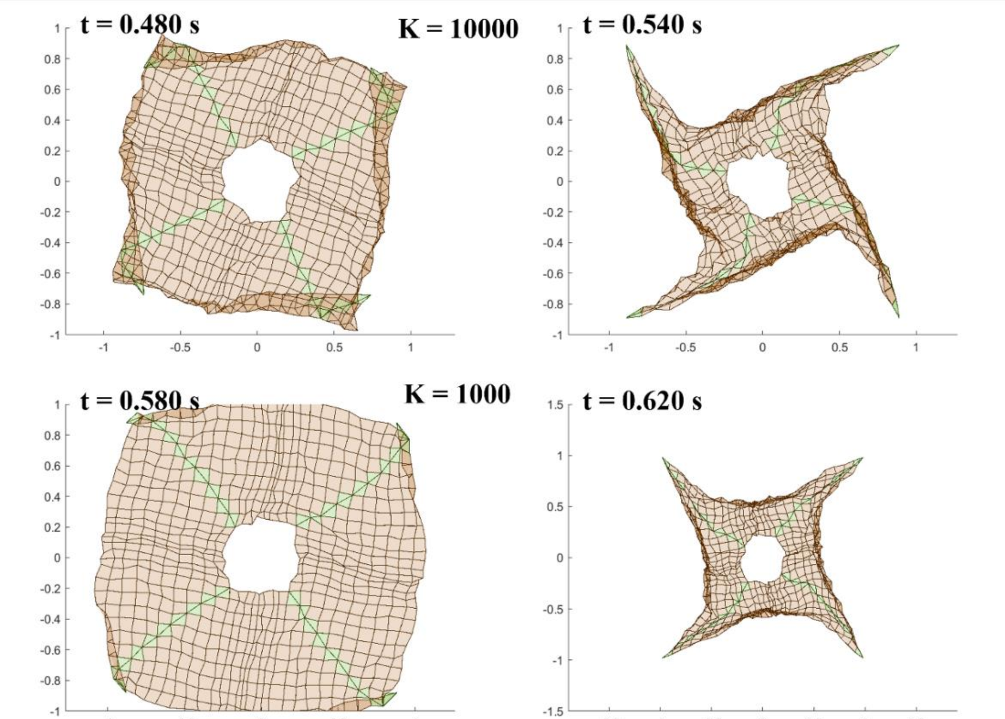

Figure 4.2: Over-deployment and subsequent shrinkage of the membrane at high contact coefficient values k.

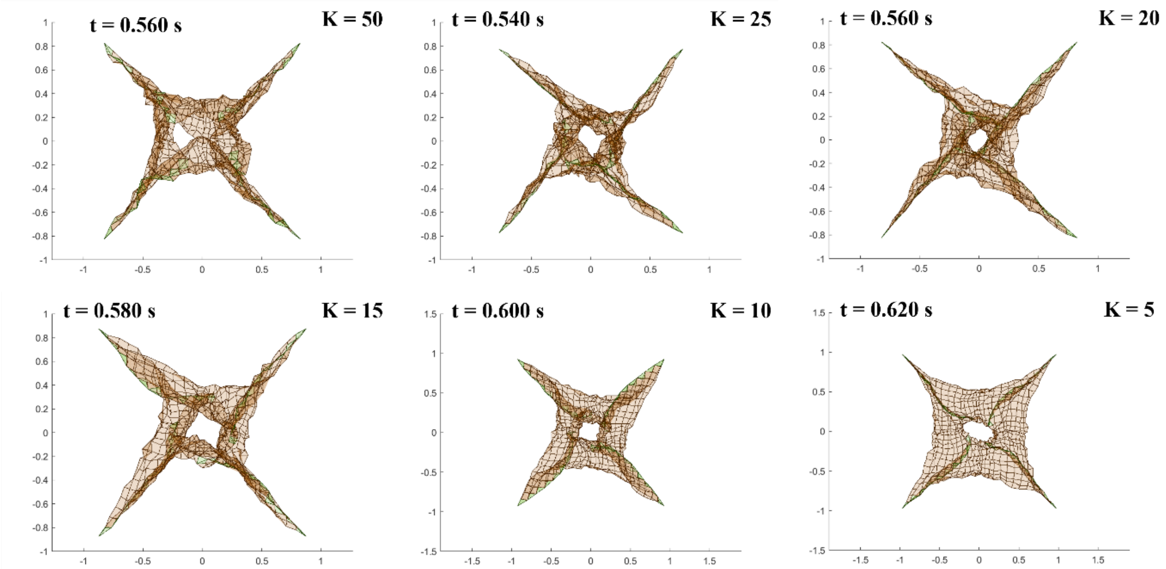

Figure 4.3: Shape of inner hole at appearance and the formation of rotational star shape.

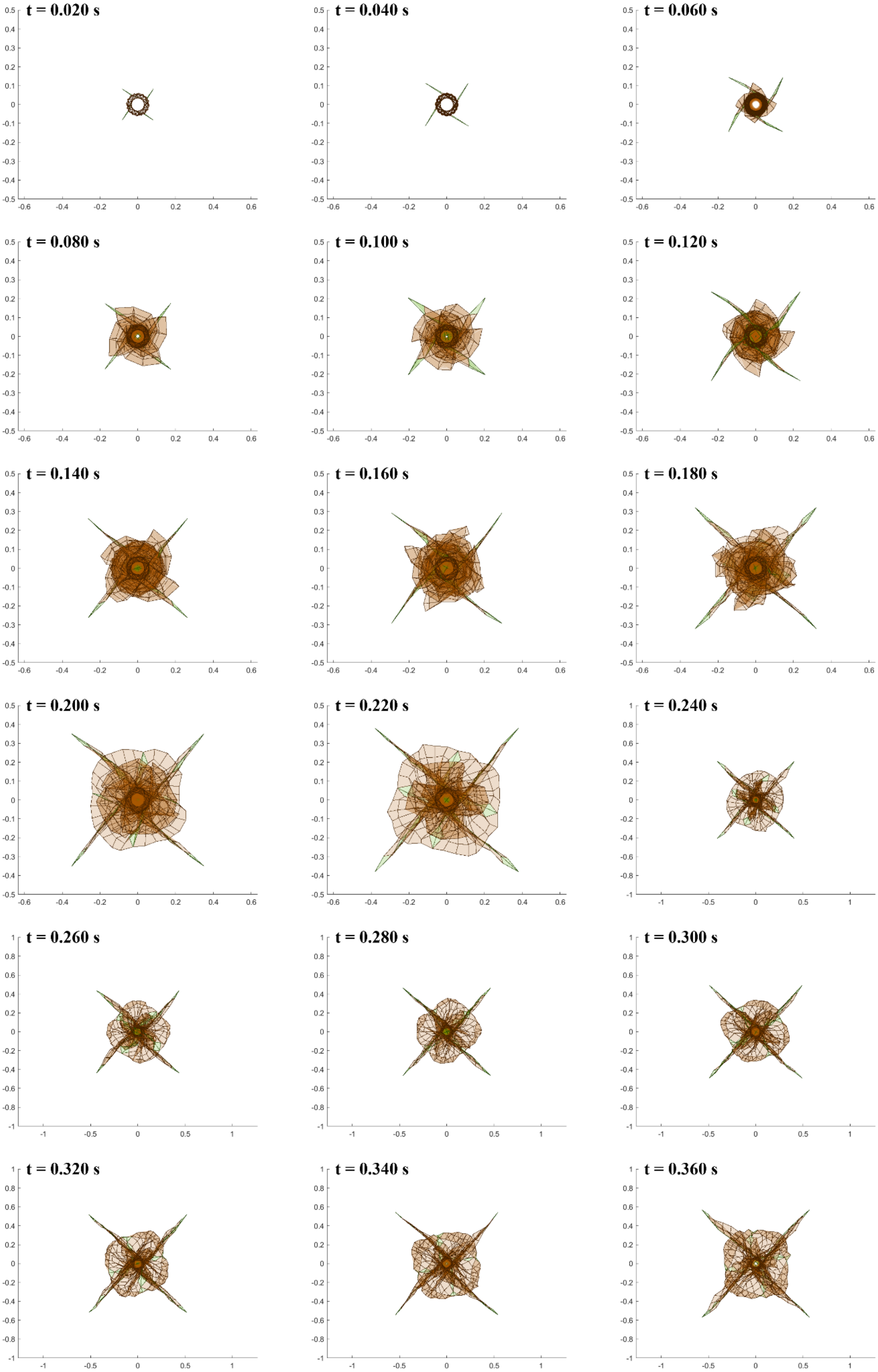
t = 0.020 s
t = 0.040 s
t = 0.060 s
t = 0.080 s
t = 0.100 s
t = 0.120 s
t = 0.140 s
t = 0.160 s
t = 0.180 s
t = 0.200 s
t = 0.220 s
t = 0.240 s
t = 0.260 s
t = 0.280 s
t = 0.300 s
t = 0.320 s
t = 0.340 s
t = 0.360 s
0.5 0.4 0.3 0.2 0.1 0 -0.1 -0.2 -0.3 -0.4 -0.5
-0.6 -0.4 -0.2 0 0.2 0.4 0.6
1 0.8 0.6 0.4 0.2 0 -0.2 -0.4 -0.6 -0.8 -1
-1 -0.5 0 0.5 1

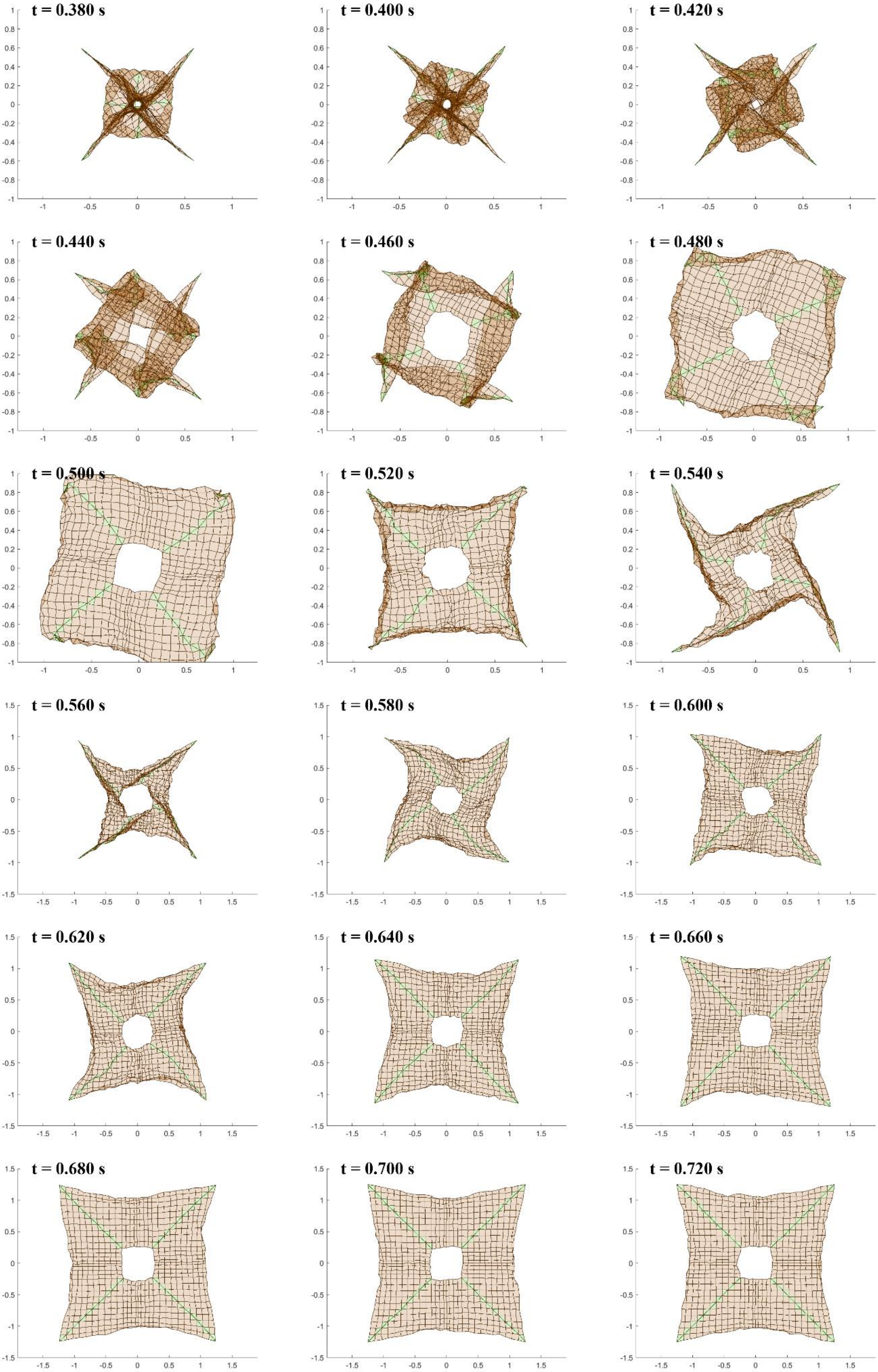

Figure 4.4: Simulation result of sail deployment for SDOM with the contact coefficient for the central hub k = 10000.

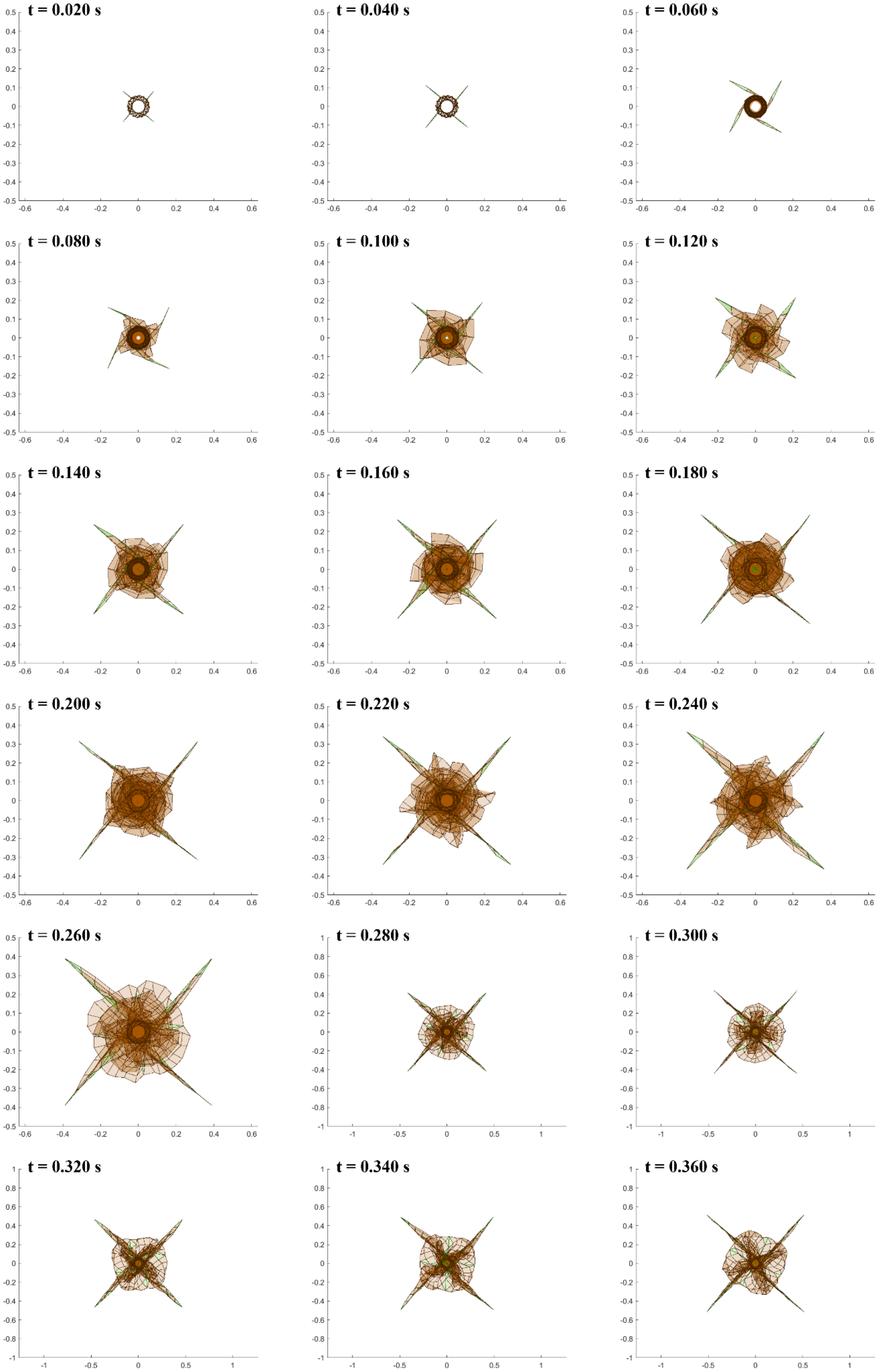
t = 0.020 s
t = 0.040 s
t = 0.060 s
t = 0.080 s
t = 0.100 s
t = 0.120 s
t = 0.140 s
t = 0.160 s
t = 0.180 s
t = 0.200 s
t = 0.220 s
t = 0.240 s
t = 0.260 s
t = 0.280 s
t = 0.300 s
t = 0.320 s
t = 0.340 s
t = 0.360 s
0.5 0.4 0.3 0.2 0.1 0 -0.1 -0.2 -0.3 -0.4 -0.5
-0.6 -0.4 -0.2 0 0.2 0.4 0.6
1 0.8 0.6 0.4 0.2 0 -0.2 -0.4 -0.6 -0.8 -1
-1 -0.5 0 0.5 1

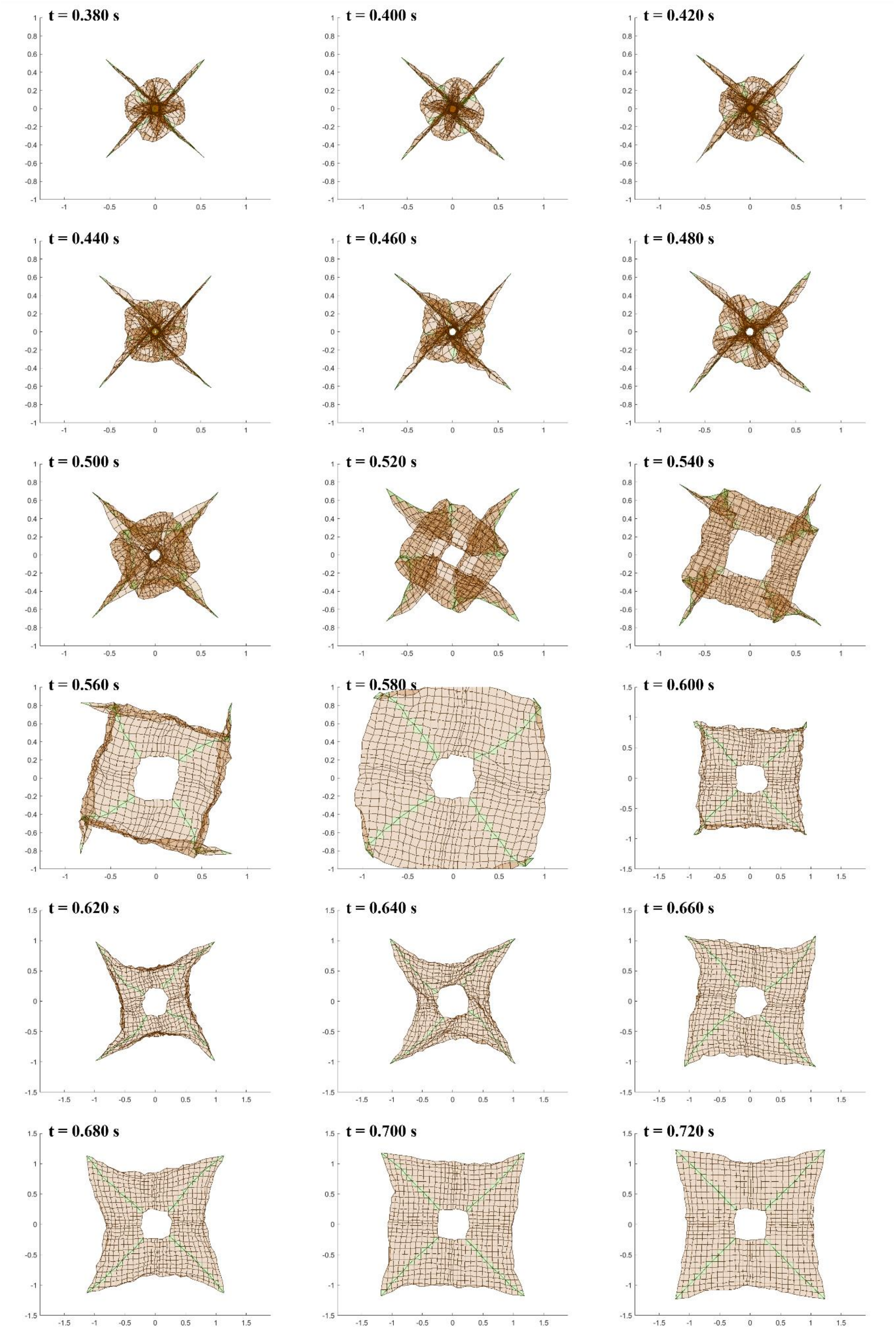

Figure 4.5: Simulation result of sail deployment for SDOM with the contact coefficient for the central hub k = 1000.

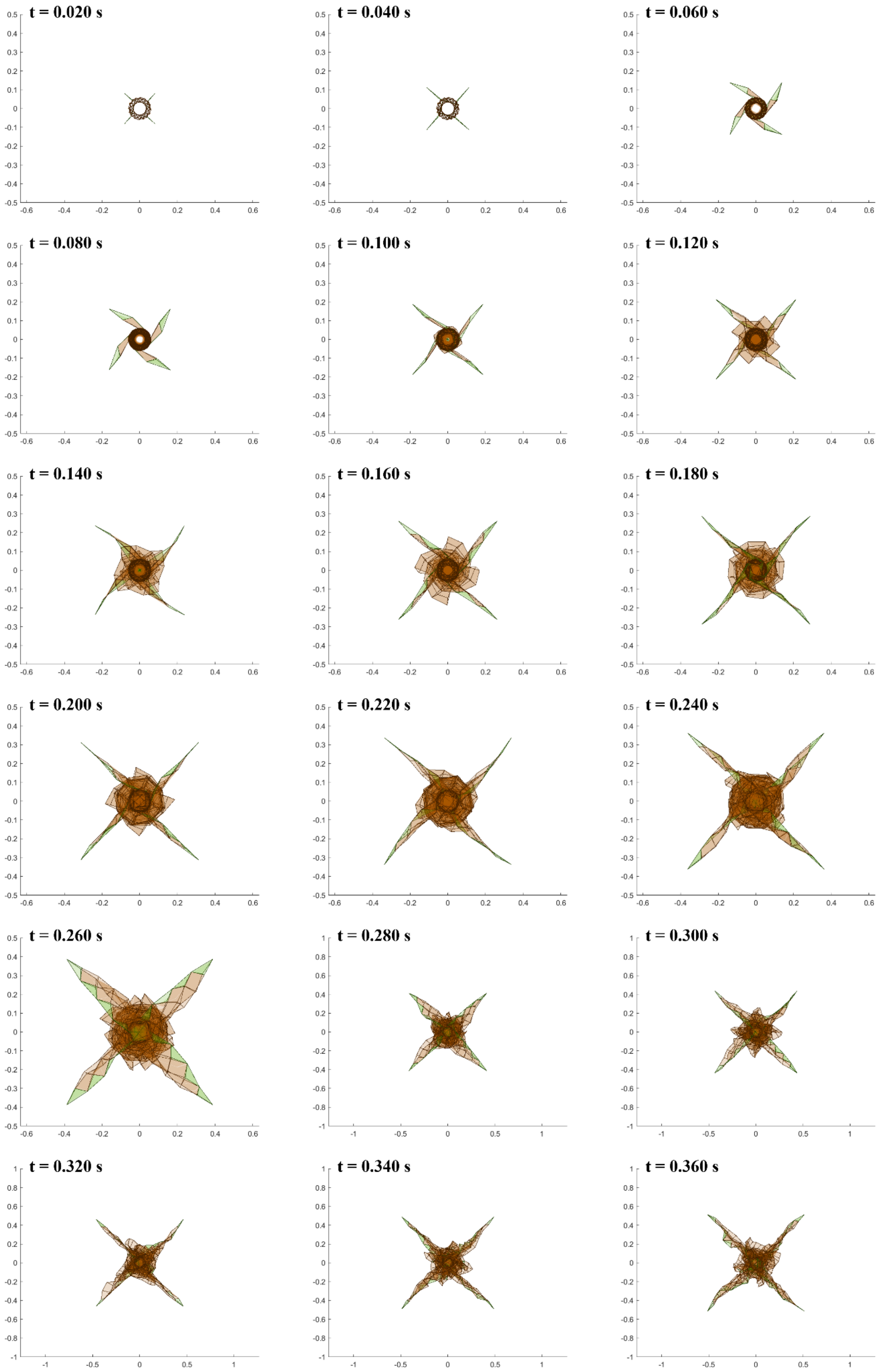
t = 0.020 s
t = 0.040 s
t = 0.060 s
t = 0.080 s
t = 0.100 s
t = 0.120 s
t = 0.140 s
t = 0.160 s
t = 0.180 s
t = 0.200 s
t = 0.220 s
t = 0.240 s
t = 0.260 s
t = 0.280 s
t = 0.300 s
t = 0.320 s
t = 0.340 s
t = 0.360 s
0.5
0.4
0.3
0.2
0.1
0
-0.1
-0.2
-0.3
-0.4
-0.5
-0.6
-0.4
-0.2
0
0.2
0.4
0.6
1
0.8
0.6
0.4
0.2
0
-0.2
-0.4
-0.6
-0.8
-1
-1
-0.5
0
0.5
1

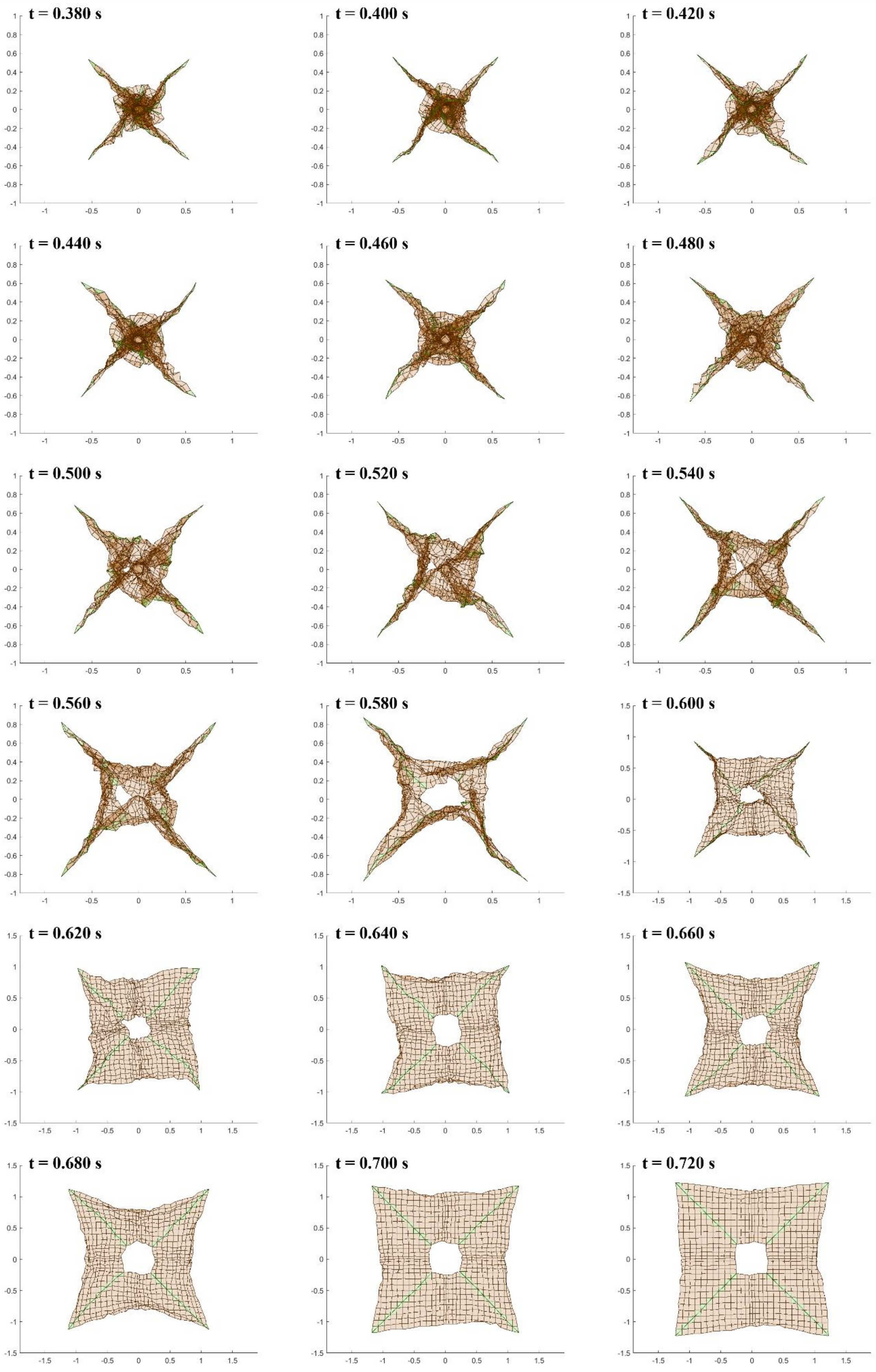
t = 0.380 s
t = 0.400 s
t = 0.420 s
t = 0.440 s
t = 0.460 s
t = 0.480 s
t = 0.500 s
t = 0.520 s
t = 0.540 s
t = 0.560 s
t = 0.580 s
t = 0.600 s
t = 0.620 s
t = 0.640 s
t = 0.660 s
t = 0.680 s
t = 0.700 s
t = 0.720 s

Figure 4.6: Simulation result of sail deployment for SDOM with the contact coefficient for the central hub k = 50.

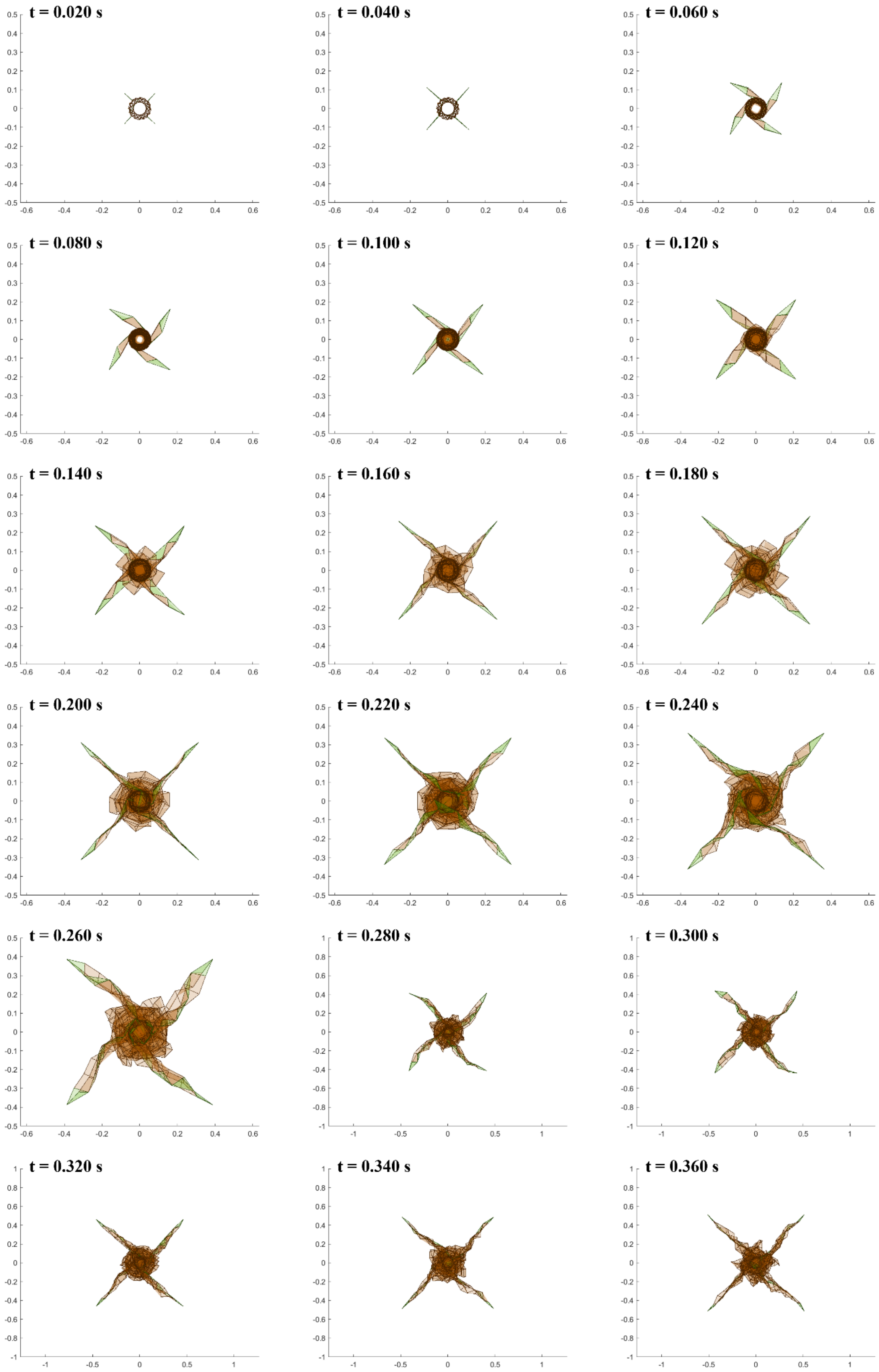
t = 0.020 s
t = 0.040 s
t = 0.060 s
t = 0.080 s
t = 0.100 s
t = 0.120 s
t = 0.140 s
t = 0.160 s
t = 0.180 s
t = 0.200 s
t = 0.220 s
t = 0.240 s
t = 0.260 s
t = 0.280 s
t = 0.300 s
t = 0.320 s
t = 0.340 s
t = 0.360 s
0.5
0.4
0.3
0.2
0.1
0
-0.1
-0.2
-0.3
-0.4
-0.5
-0.6
-0.4
-0.2
0
0.2
0.4
0.6
1
0.8
0.6
0.4
0.2
0
-0.2
-0.4
-0.6
-0.8
-1
-1
-0.5
0
0.5
1

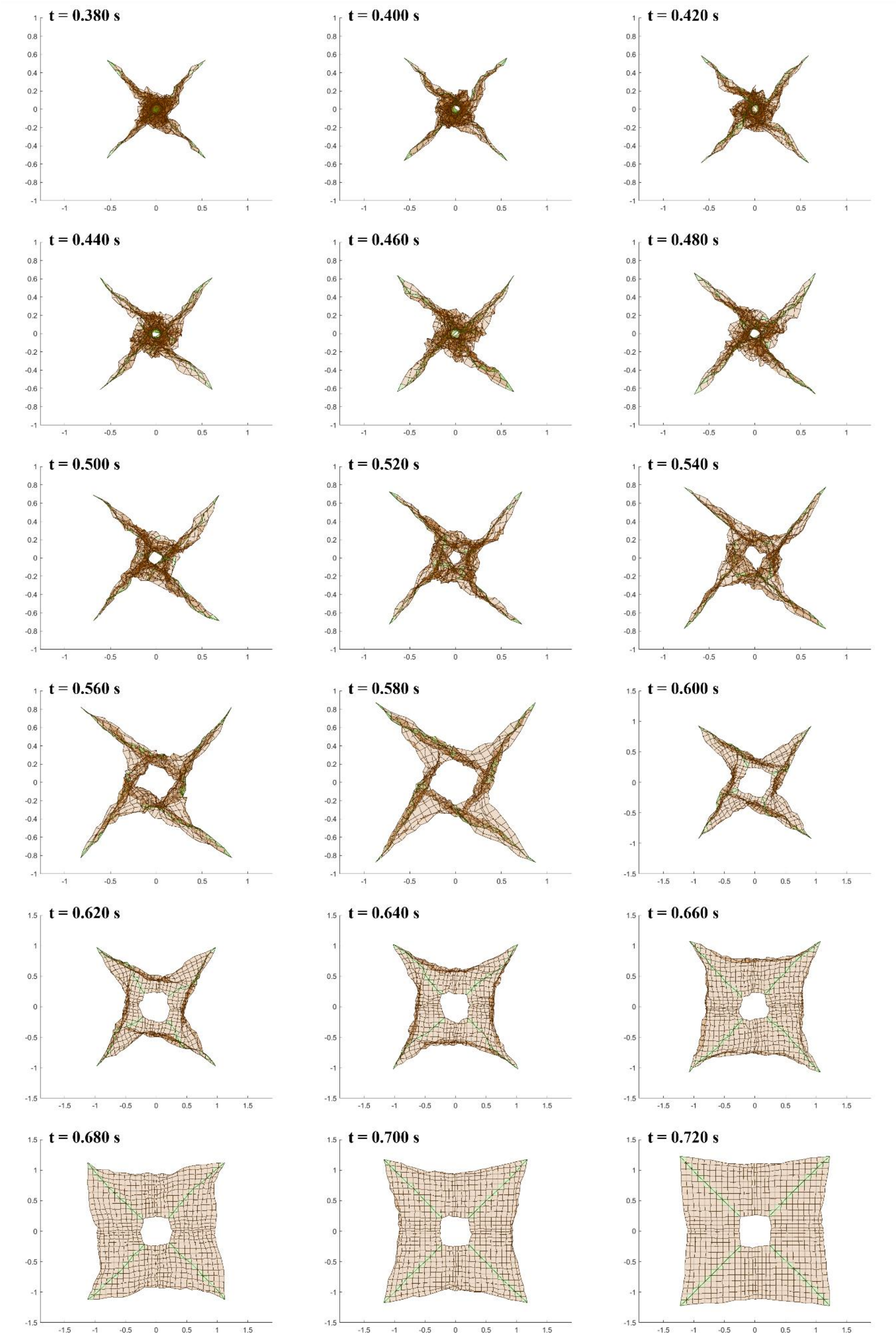

Figure 4.7: Simulation result of sail deployment for SDOM with the contact coefficient for the central hub k = 25.

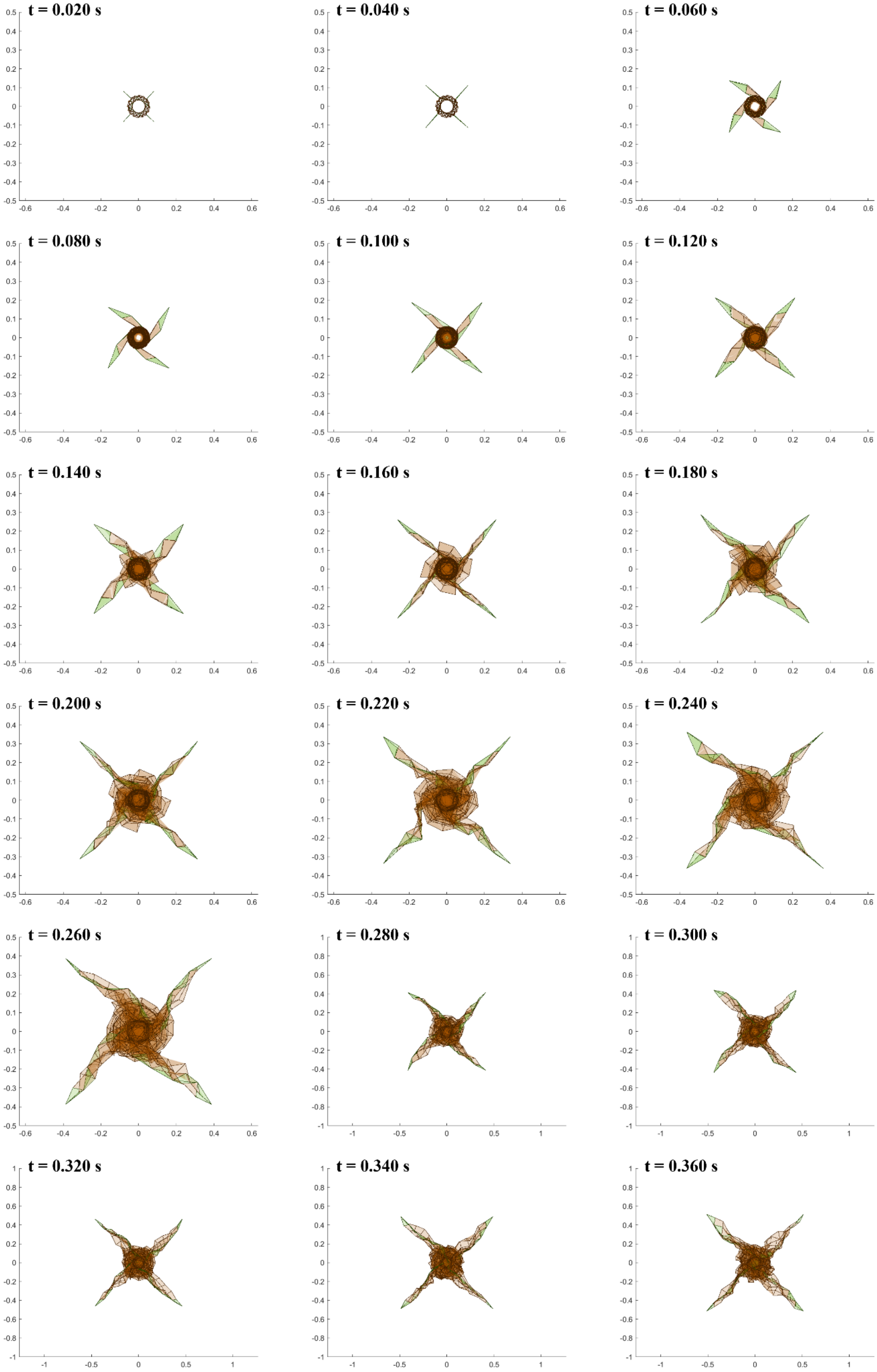
t = 0.020 s
t = 0.040 s
t = 0.060 s
t = 0.080 s
t = 0.100 s
t = 0.120 s
t = 0.140 s
t = 0.160 s
t = 0.180 s
t = 0.200 s
t = 0.220 s
t = 0.240 s
t = 0.260 s
t = 0.280 s
t = 0.300 s
t = 0.320 s
t = 0.340 s
t = 0.360 s
0.5
0.4
0.3
0.2
0.1
0
-0.1
-0.2
-0.3
-0.4
-0.5
-0.6
-0.4
-0.2
0
0.2
0.4
0.6
1
0.8
0.6
0.4
0.2
0
-0.2
-0.4
-0.6
-0.8
-1
-1
-0.5
0
0.5
1

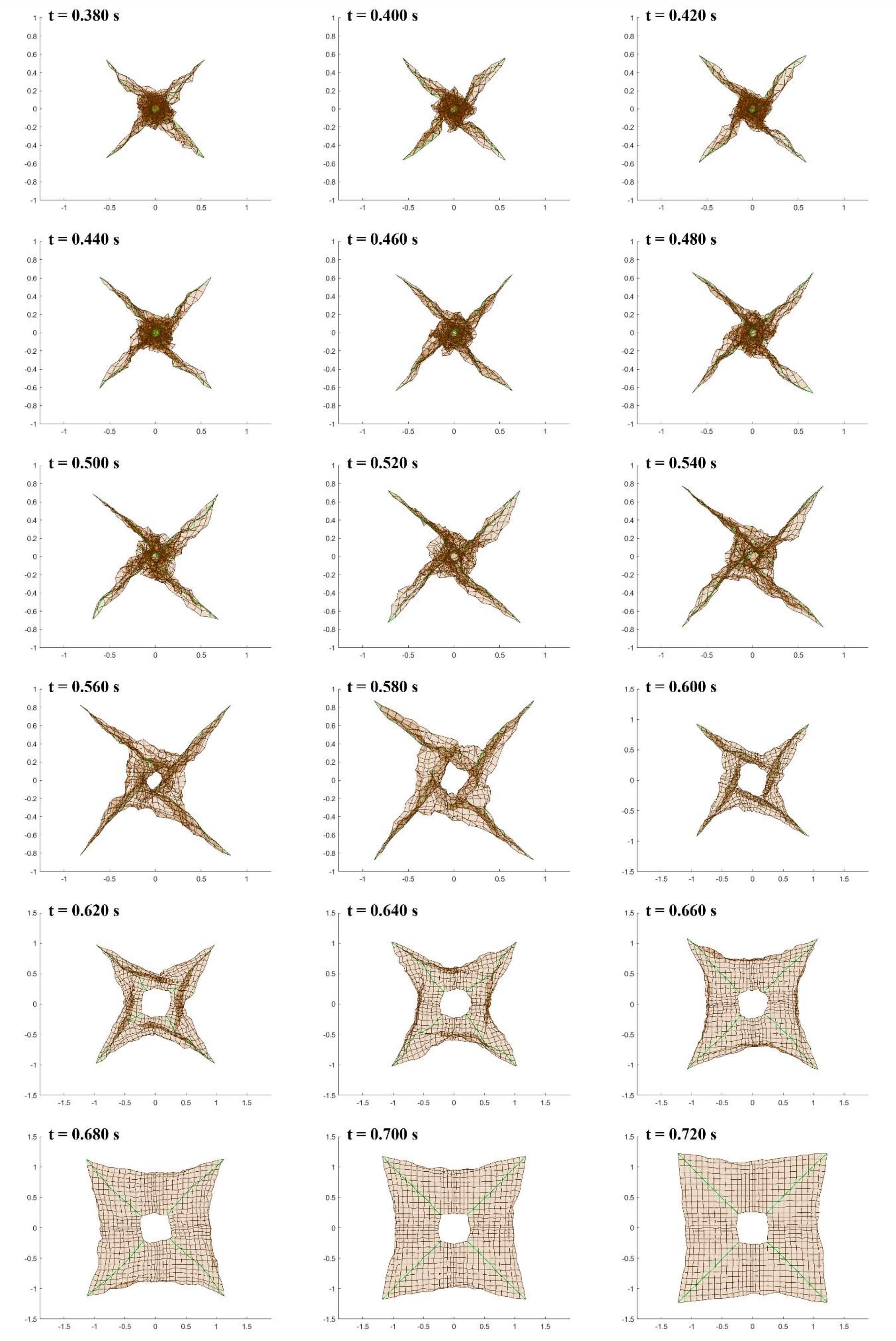

Figure 4.8: Simulation result of sail deployment for SDOM with the contact coefficient for the central hub k = 20.

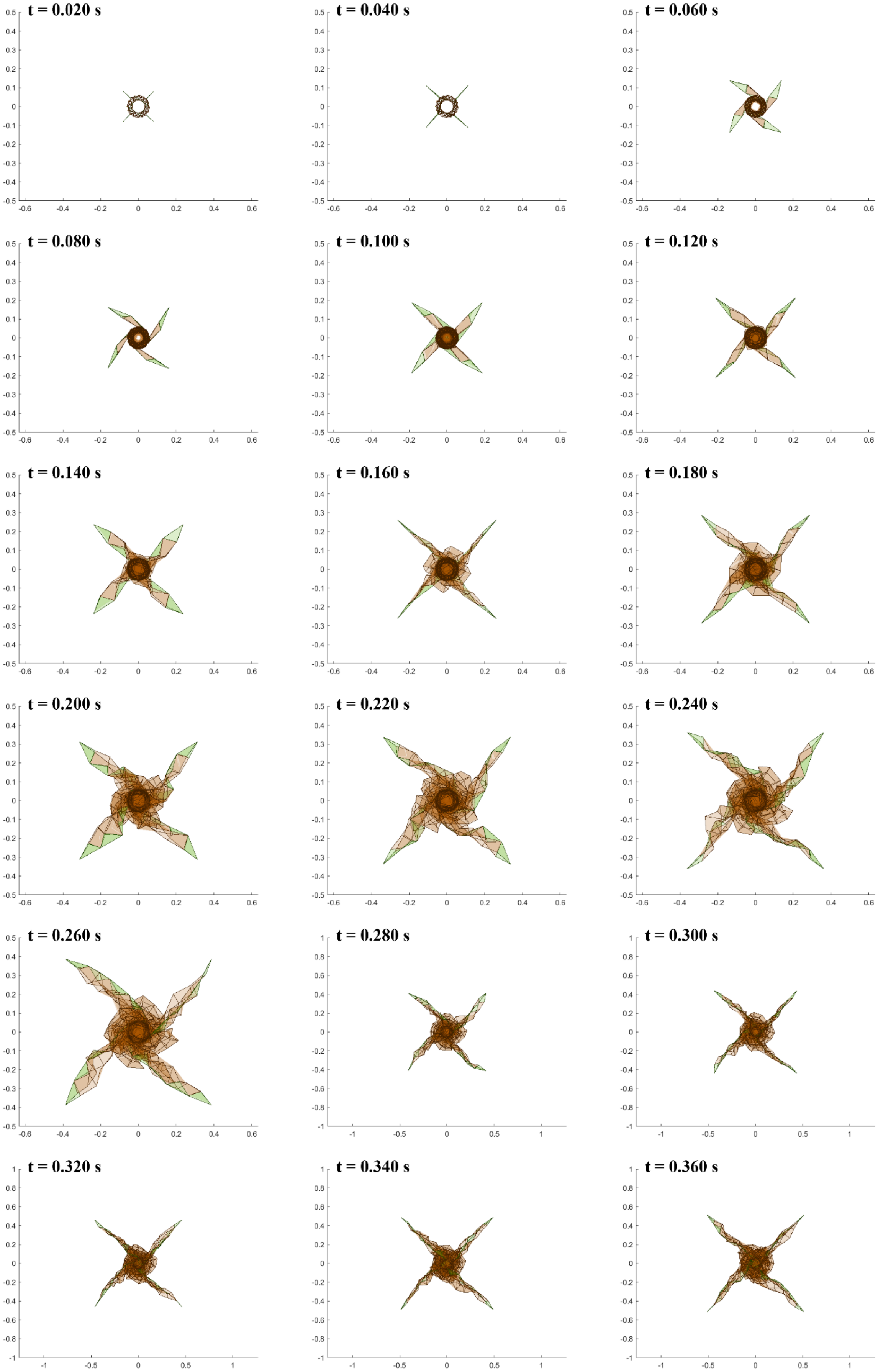
t = 0.020 s
t = 0.040 s
t = 0.060 s
t = 0.080 s
t = 0.100 s
t = 0.120 s
t = 0.140 s
t = 0.160 s
t = 0.180 s
t = 0.200 s
t = 0.220 s
t = 0.240 s
t = 0.260 s
t = 0.280 s
t = 0.300 s
t = 0.320 s
t = 0.340 s
t = 0.360 s
0.5
0.4
0.3
0.2
0.1
0
-0.1
-0.2
-0.3
-0.4
-0.5
-0.6
-0.4
-0.2
0
0.2
0.4
0.6
1
0.8
0.6
0.4
0.2
0
-0.2
-0.4
-0.6
-0.8
-1
-1
-0.5
0
0.5
1

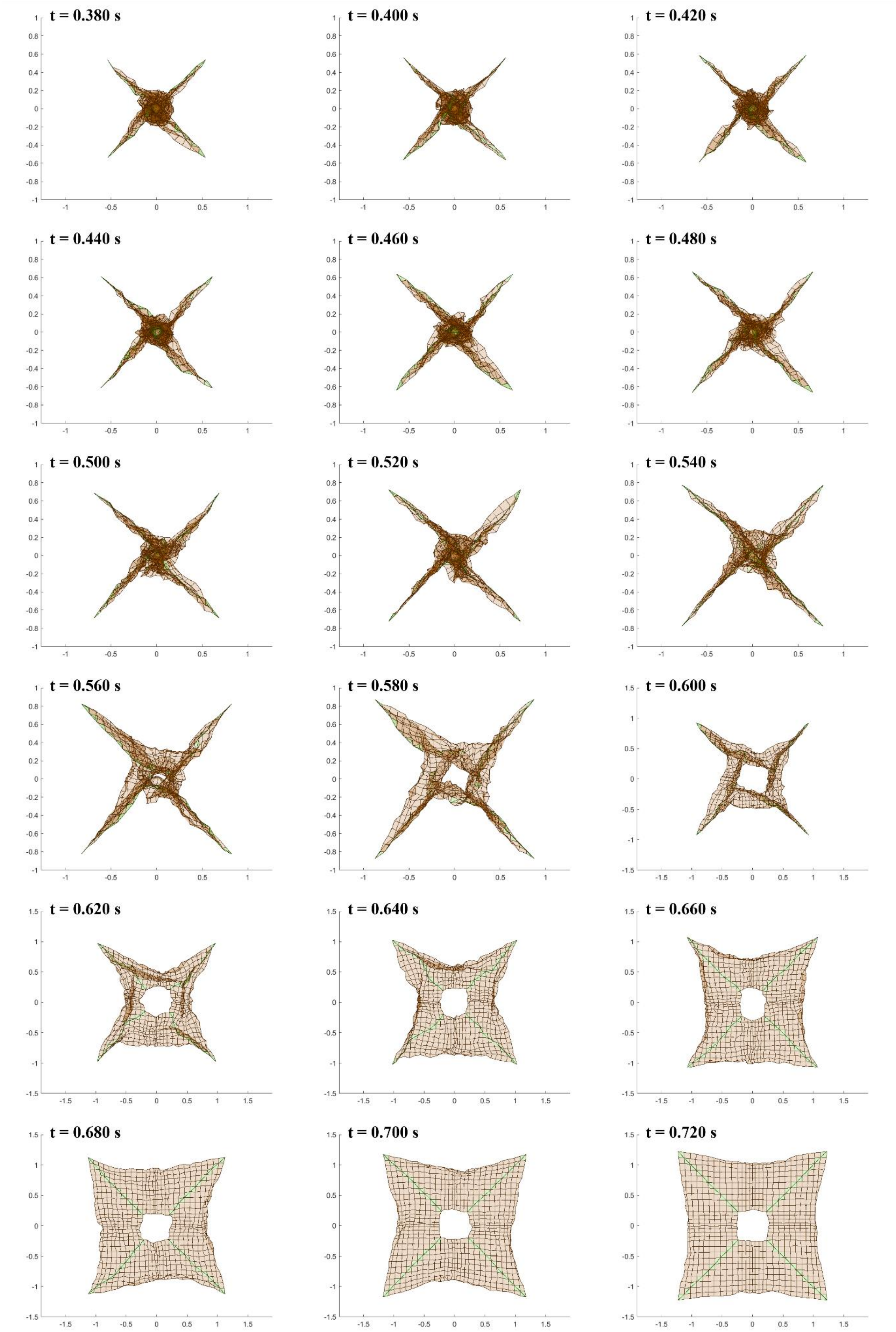

t = 0.380 s
t = 0.400 s
t = 0.420 s
t = 0.440 s
t = 0.460 s
t = 0.480 s
t = 0.500 s
t = 0.520 s
t = 0.540 s
t = 0.560 s
t = 0.580 s
t = 0.600 s
t = 0.620 s
t = 0.640 s
t = 0.660 s
t = 0.680 s
t = 0.700 s
t = 0.720 s

Figure 4.9: Simulation result of sail deployment for SDOM with the contact coefficient for the central hub k = 15.

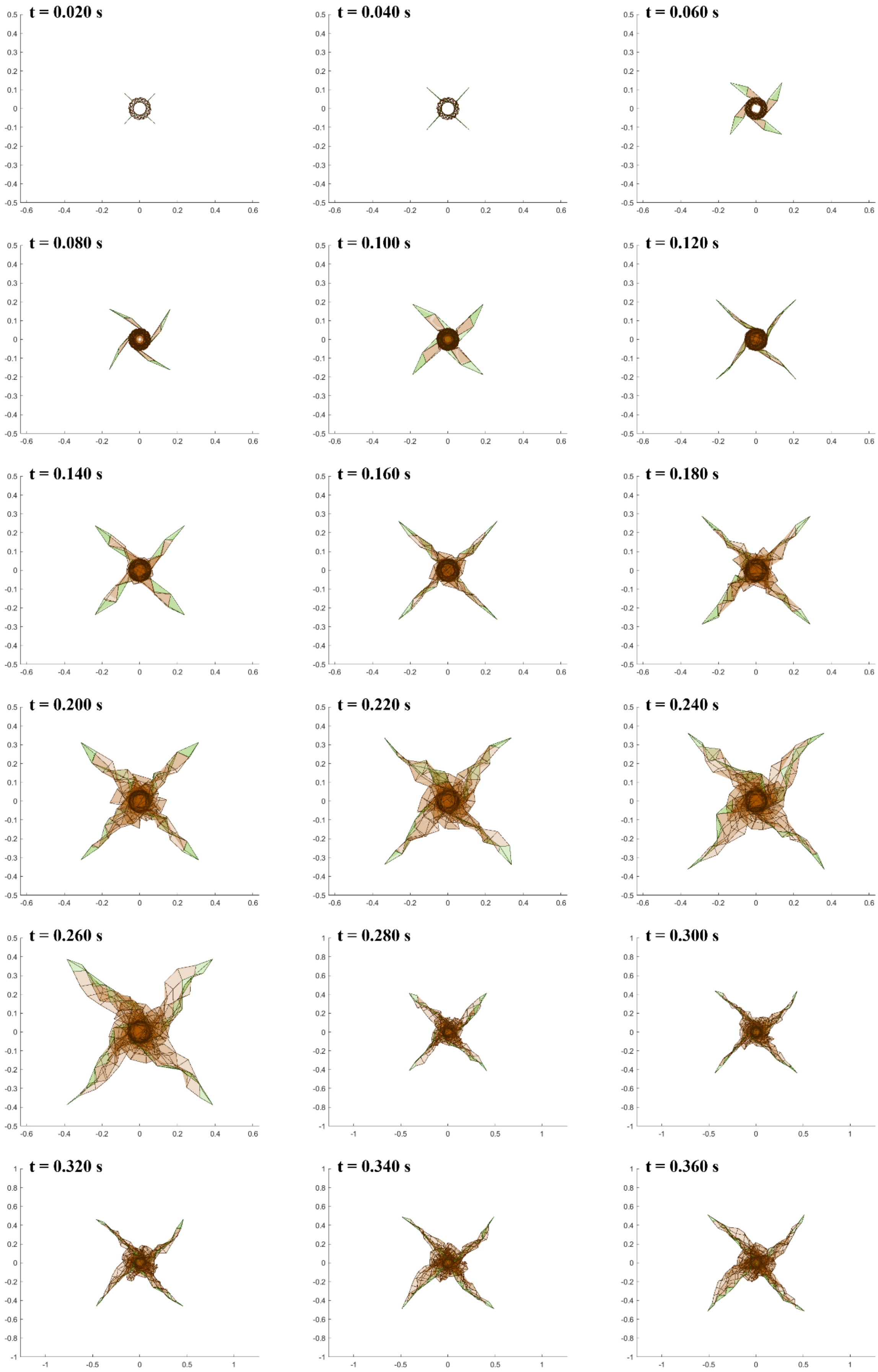
t = 0.020 s
t = 0.040 s
t = 0.060 s
t = 0.080 s
t = 0.100 s
t = 0.120 s
t = 0.140 s
t = 0.160 s
t = 0.180 s
t = 0.200 s
t = 0.220 s
t = 0.240 s
t = 0.260 s
t = 0.280 s
t = 0.300 s
t = 0.320 s
t = 0.340 s
t = 0.360 s
0.5
0.4
0.3
0.2
0.1
0
-0.1
-0.2
-0.3
-0.4
-0.5
-0.6
-0.4
-0.2
0
0.2
0.4
0.6
1
0.8
0.6
0.4
0.2
0
-0.2
-0.4
-0.6
-0.8
-1
-1
-0.5
0
0.5
1

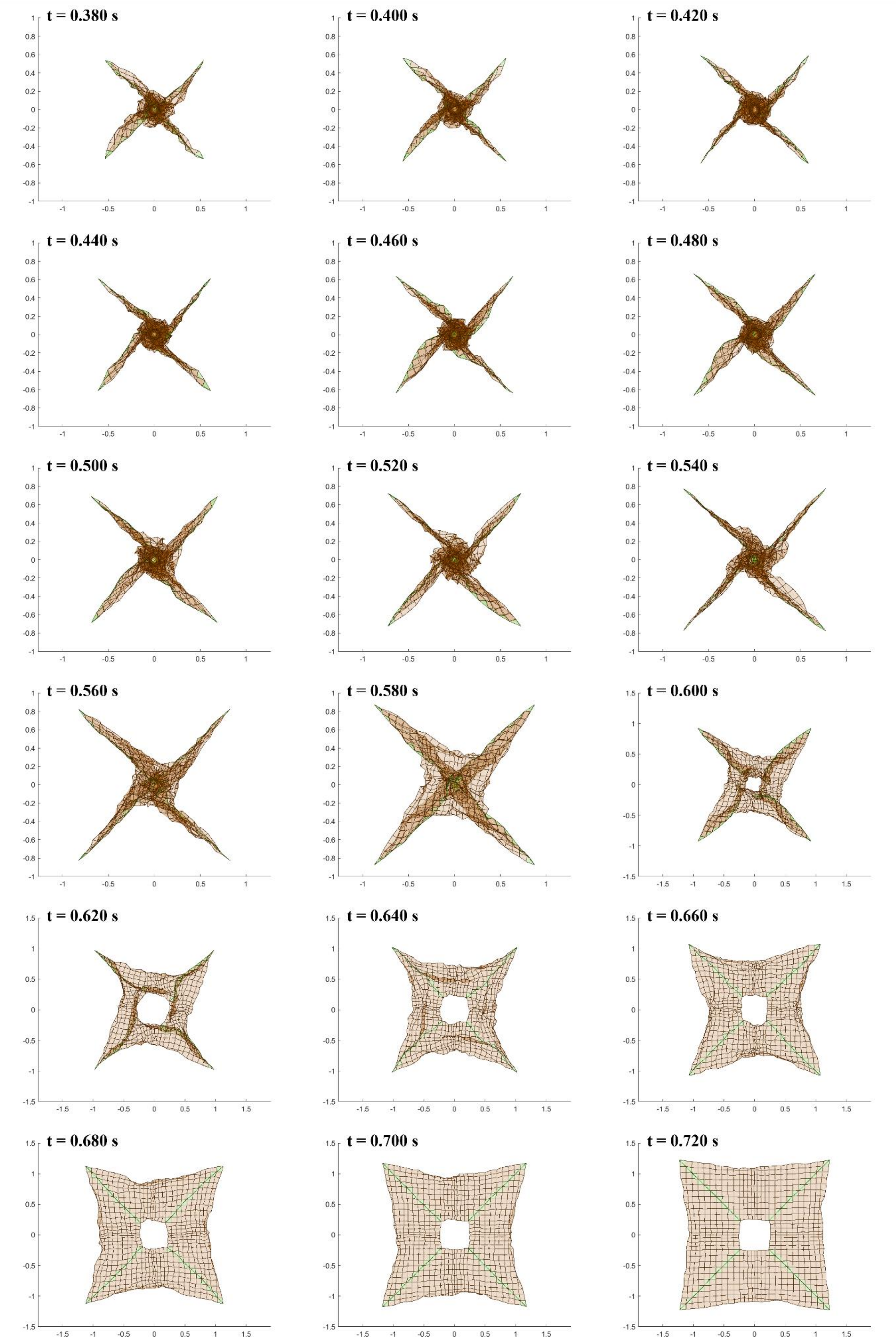

Figure 4.10: Simulation result of sail deployment for SDOM with the contact coefficient for the central hub k = 10.

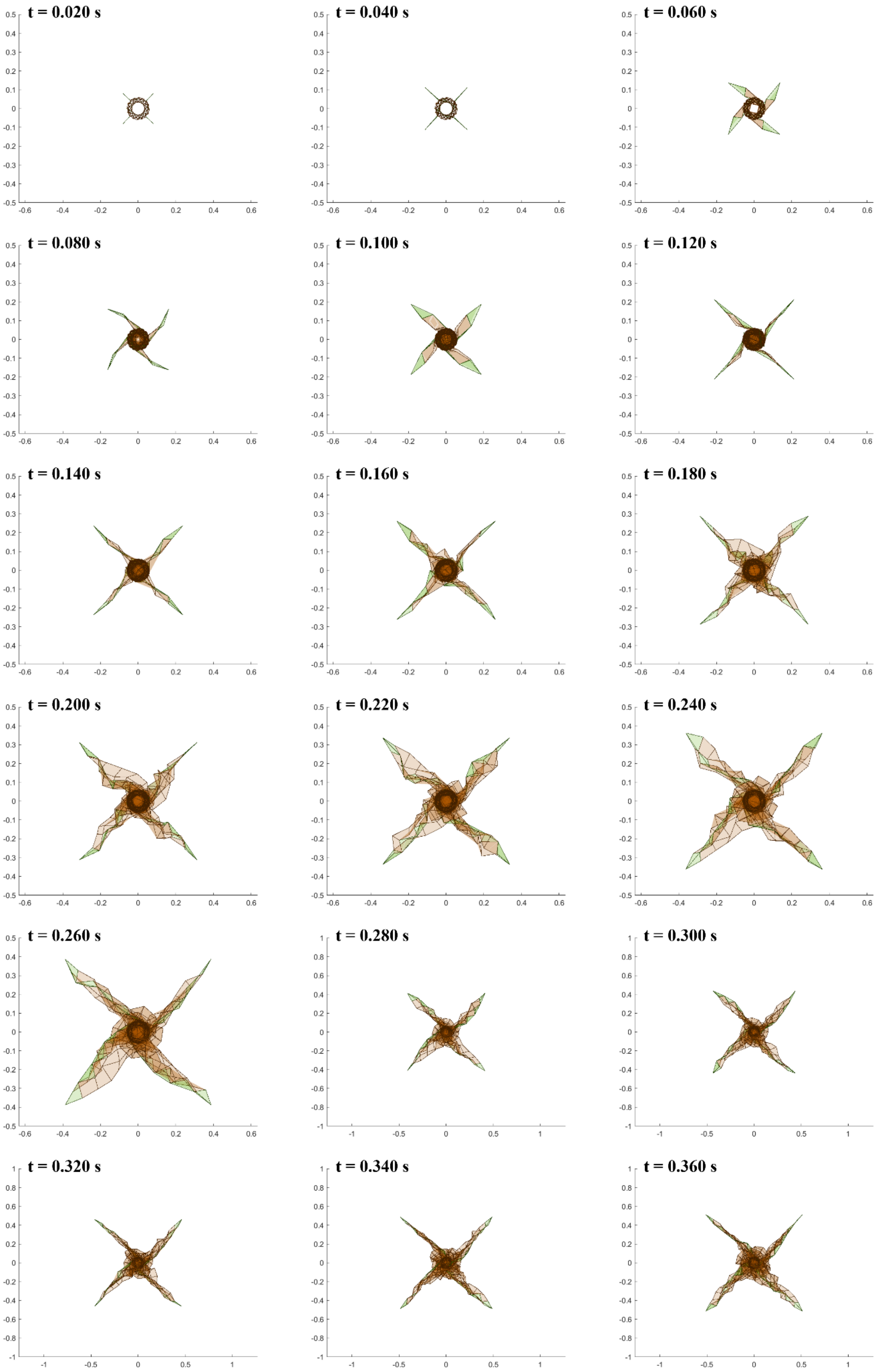
t = 0.020 s
t = 0.040 s
t = 0.060 s
t = 0.080 s
t = 0.100 s
t = 0.120 s
t = 0.140 s
t = 0.160 s
t = 0.180 s
t = 0.200 s
t = 0.220 s
t = 0.240 s
t = 0.260 s
t = 0.280 s
t = 0.300 s
t = 0.320 s
t = 0.340 s
t = 0.360 s
0.5
0.4
0.3
0.2
0.1
0
-0.1
-0.2
-0.3
-0.4
-0.5
-0.6
-0.4
-0.2
0
0.2
0.4
0.6
1
0.8
0.6
0.4
0.2
0
-0.2
-0.4
-0.6
-0.8
-1
-1
-0.5
0
0.5
1

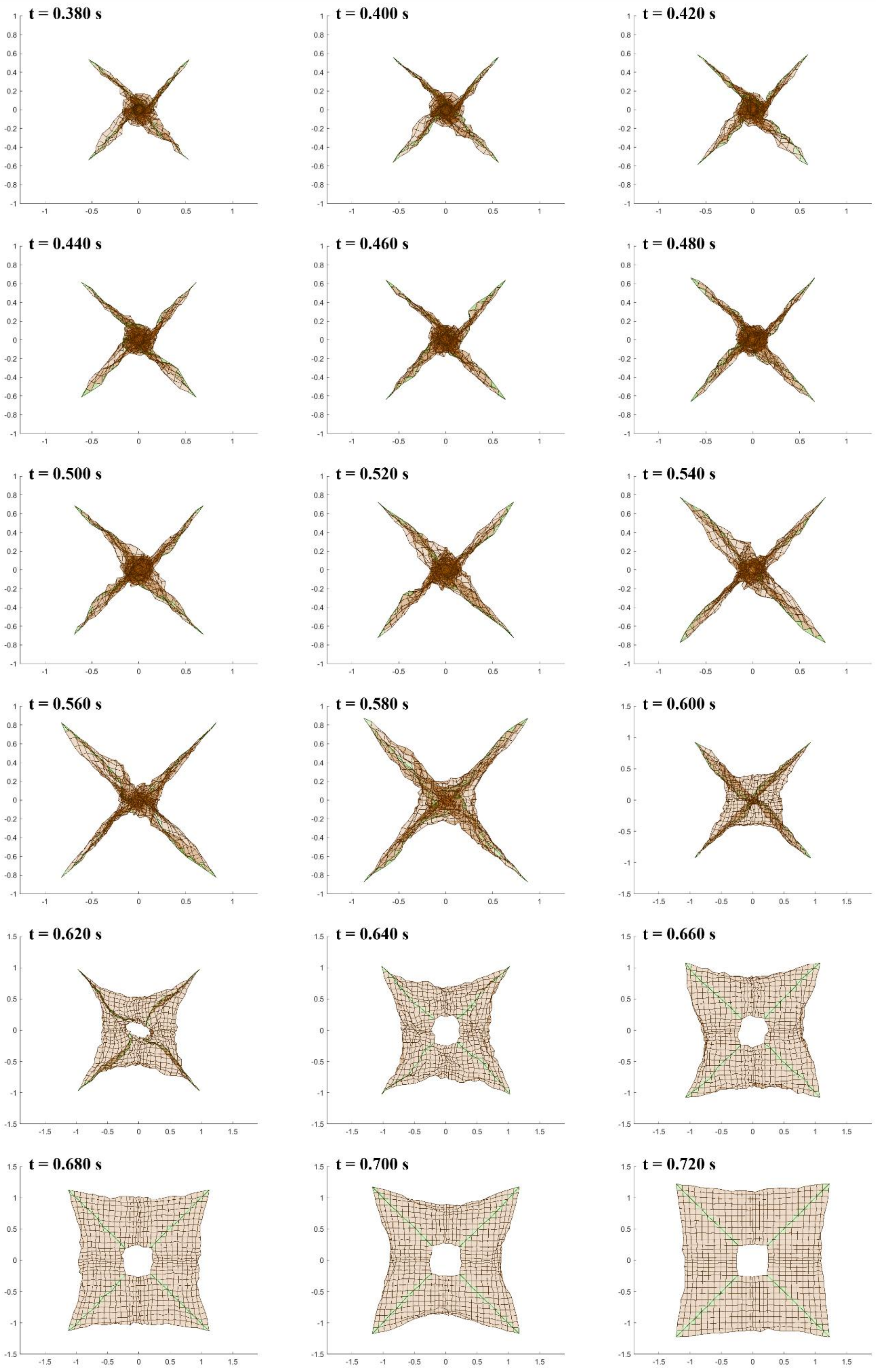

Figure 4.11: Simulation result of sail deployment for SDOM with the contact coefficient for the central hub k = 5.

4.7.2. Damping Coefficient

Following this simulation, a damping coefficient for the spring model of the hub was explored varying as d = [10-4, 10-5, 10-6, 10-7]. At these values the effects of the inclusion of a damping coefficient were close to negligible. At the magnitude of 10^{-1} or higher the effects were noticeable however not constructive towards the goal that is aimed in this work. Also, the magnitude of the damping coefficient is realistically close to the magnitude of the step time for the integration calculations which is 10^{-5}seconds. This is because, the damping coefficient is modeled as a fraction of the integration time in the mathematical model. Thus, a damping coefficient with magnitude 10^{-3} or higher is in fact unrealistic. Additionally, the computational time has increased drastically with the inclusion of this damping. Considering the additional cost it brings and the negligible results it provides, the damping coefficient for the spring model of the central hub contact restriction was disregarded and deemed as an unsignificant parameter for this analysis. It can be excluded from the mathematical model altogether for the future. Figure 4.13 shows the comparison of these damping ratios at t = 0.6 s and Figs. 4.14~4.17 show the full results for reference.

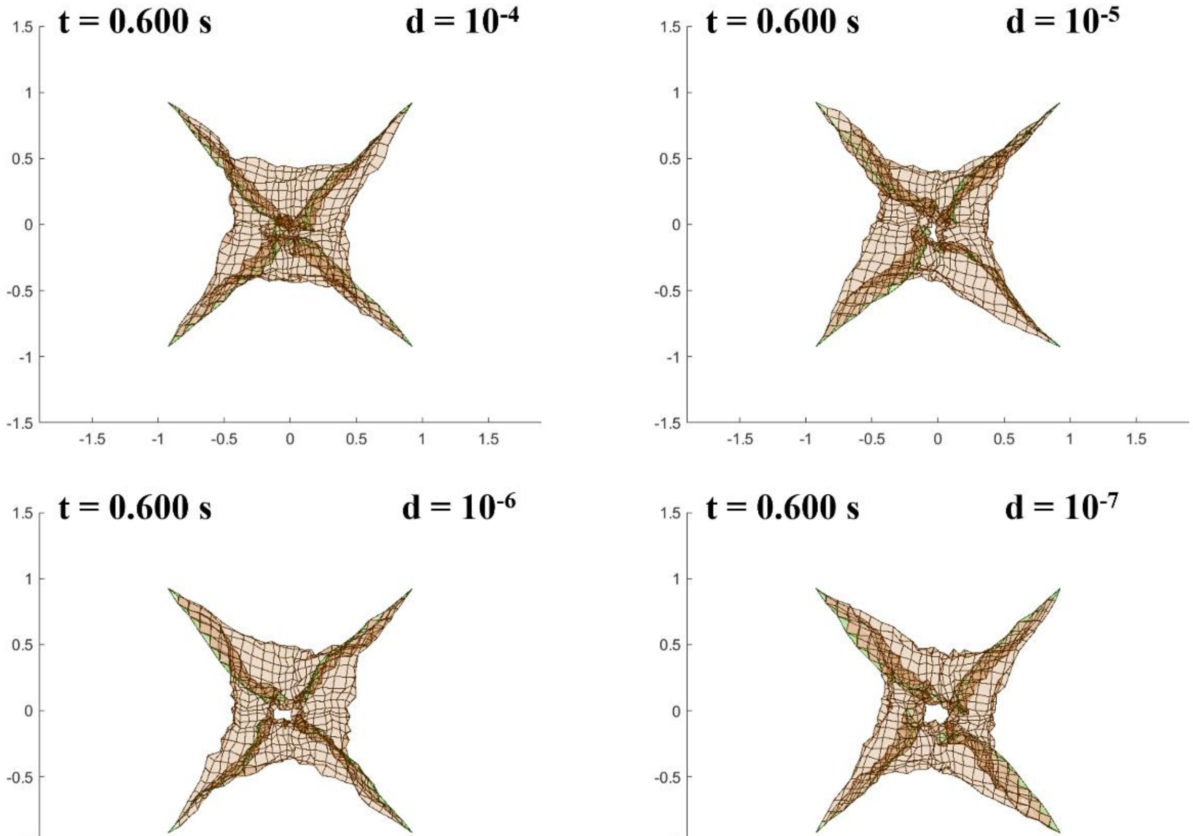

Figure 4.12: Comparison of different damping coefficients.

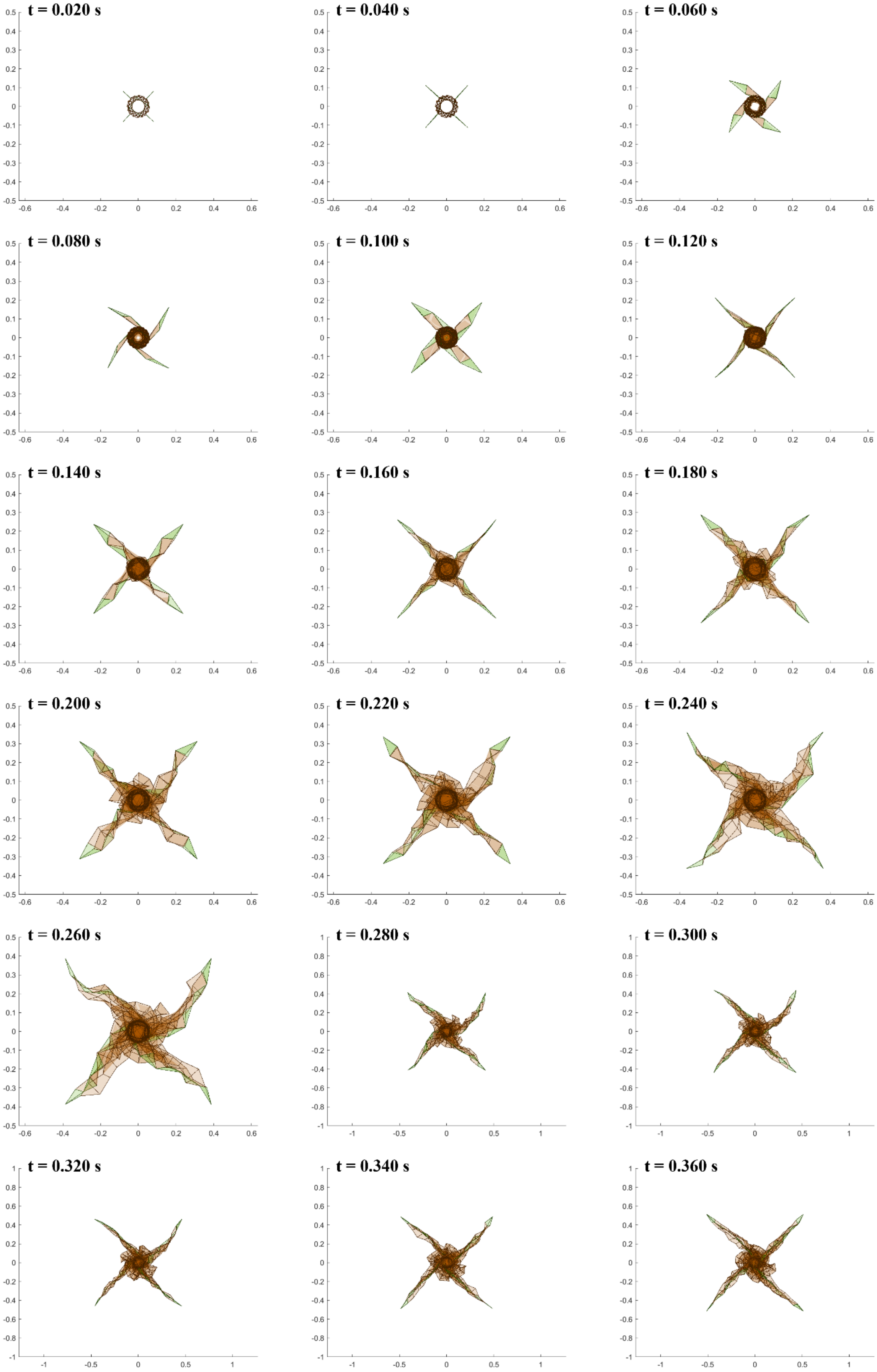
t = 0.020 s

t = 0.040 s

t = 0.060 s

t = 0.080 s

t = 0.100 s

t = 0.120 s

t = 0.140 s

t = 0.160 s

t = 0.180 s

t = 0.200 s

t = 0.220 s

t = 0.240 s

t = 0.260 s

t = 0.280 s

t = 0.300 s

t = 0.320 s

t = 0.340 s

t = 0.360 s

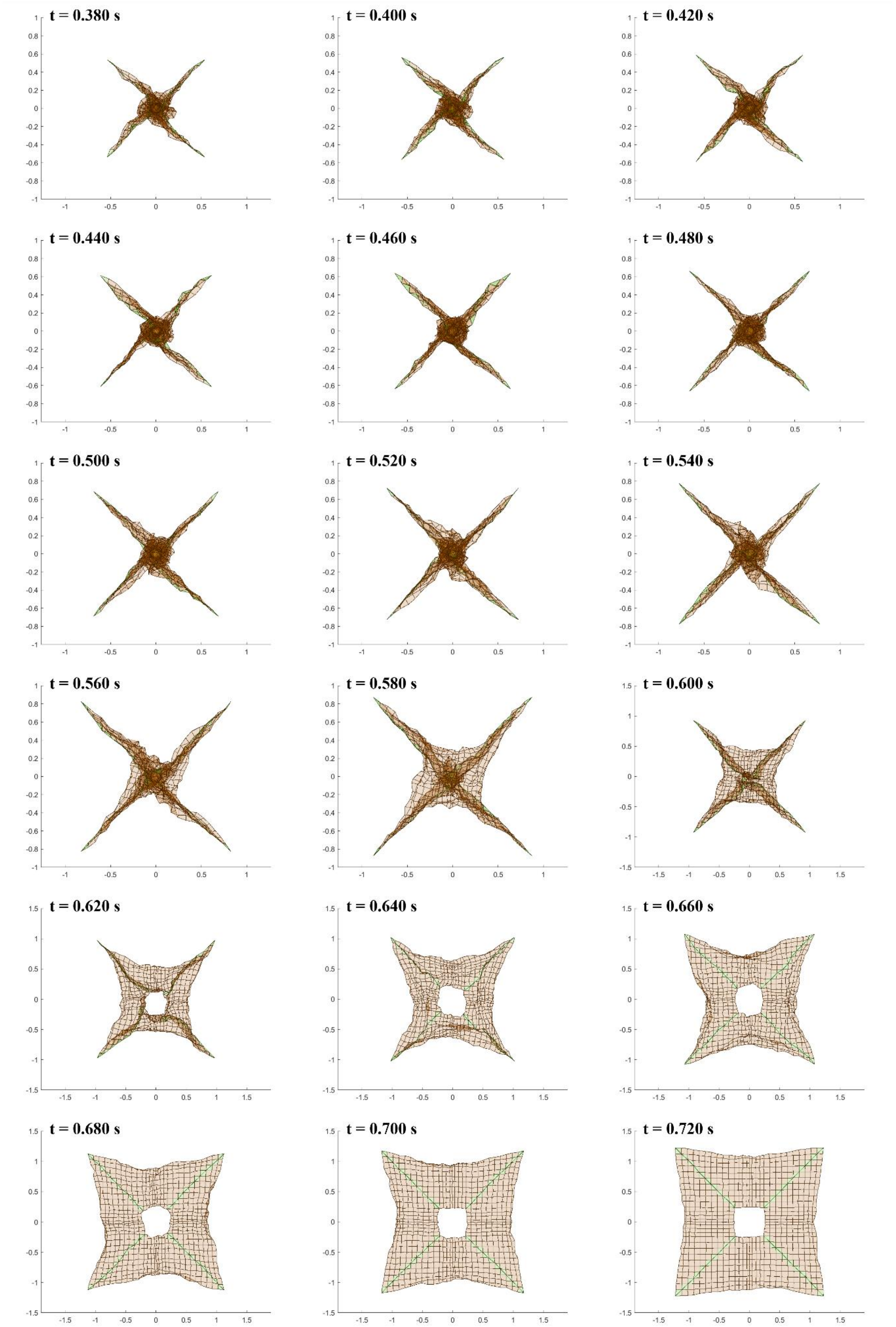

Figure 4.13: Simulation result of the sail deployment for SDOM with the central hub model parameters as k = 20 and d = 10^{-4}.

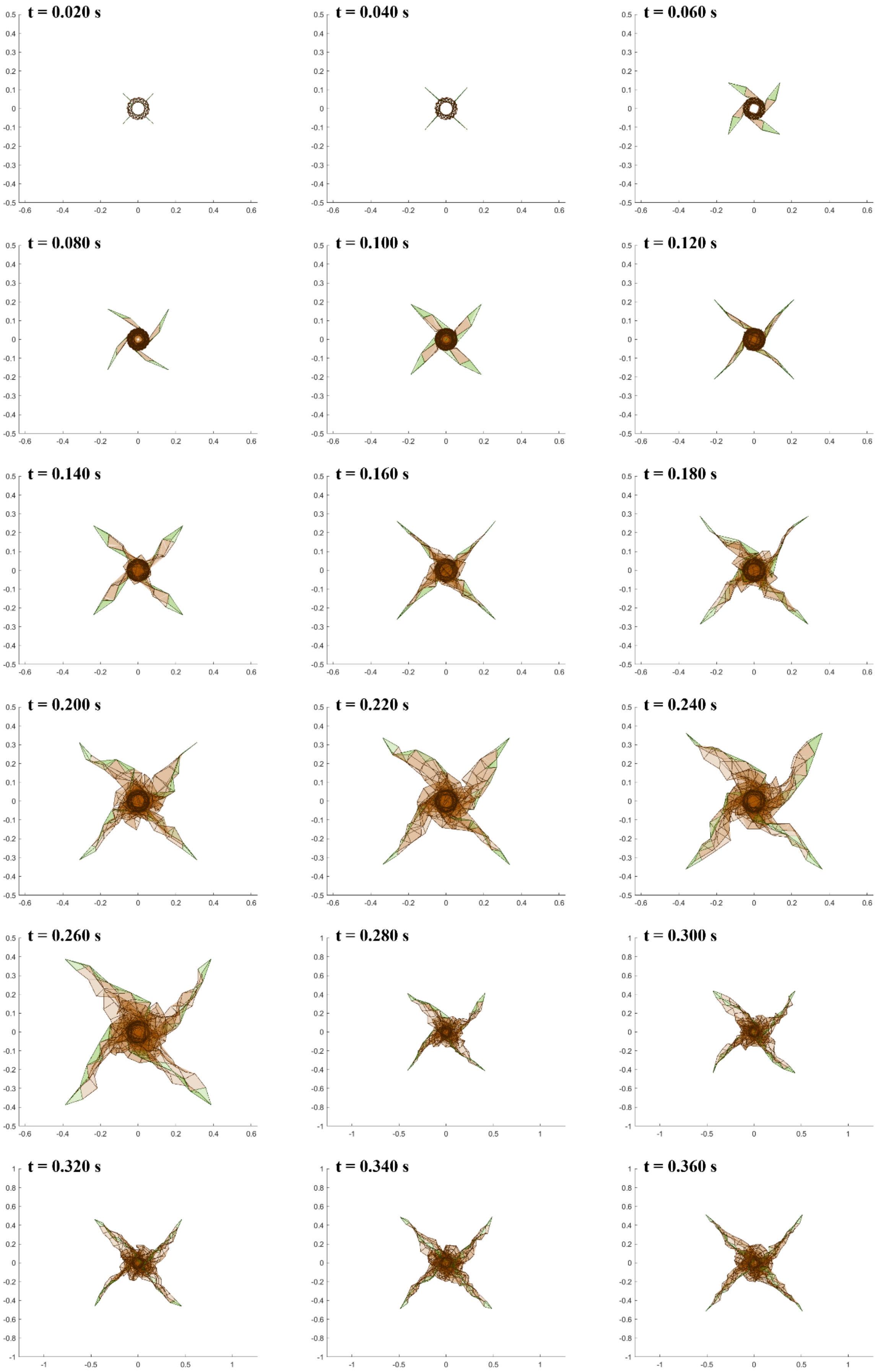
t = 0.020 s
t = 0.040 s
t = 0.060 s
t = 0.080 s
t = 0.100 s
t = 0.120 s
t = 0.140 s
t = 0.160 s
t = 0.180 s
t = 0.200 s
t = 0.220 s
t = 0.240 s
t = 0.260 s
t = 0.280 s
t = 0.300 s
t = 0.320 s
t = 0.340 s
t = 0.360 s
0.5
0.4
0.3
0.2
0.1
0
-0.1
-0.2
-0.3
-0.4
-0.5
-0.6
-0.4
-0.2
0
0.2
0.4
0.6
1
0.8
0.6
0.4
0.2
0
-0.2
-0.4
-0.6
-0.8
-1
-1
-0.5
0
0.5
1

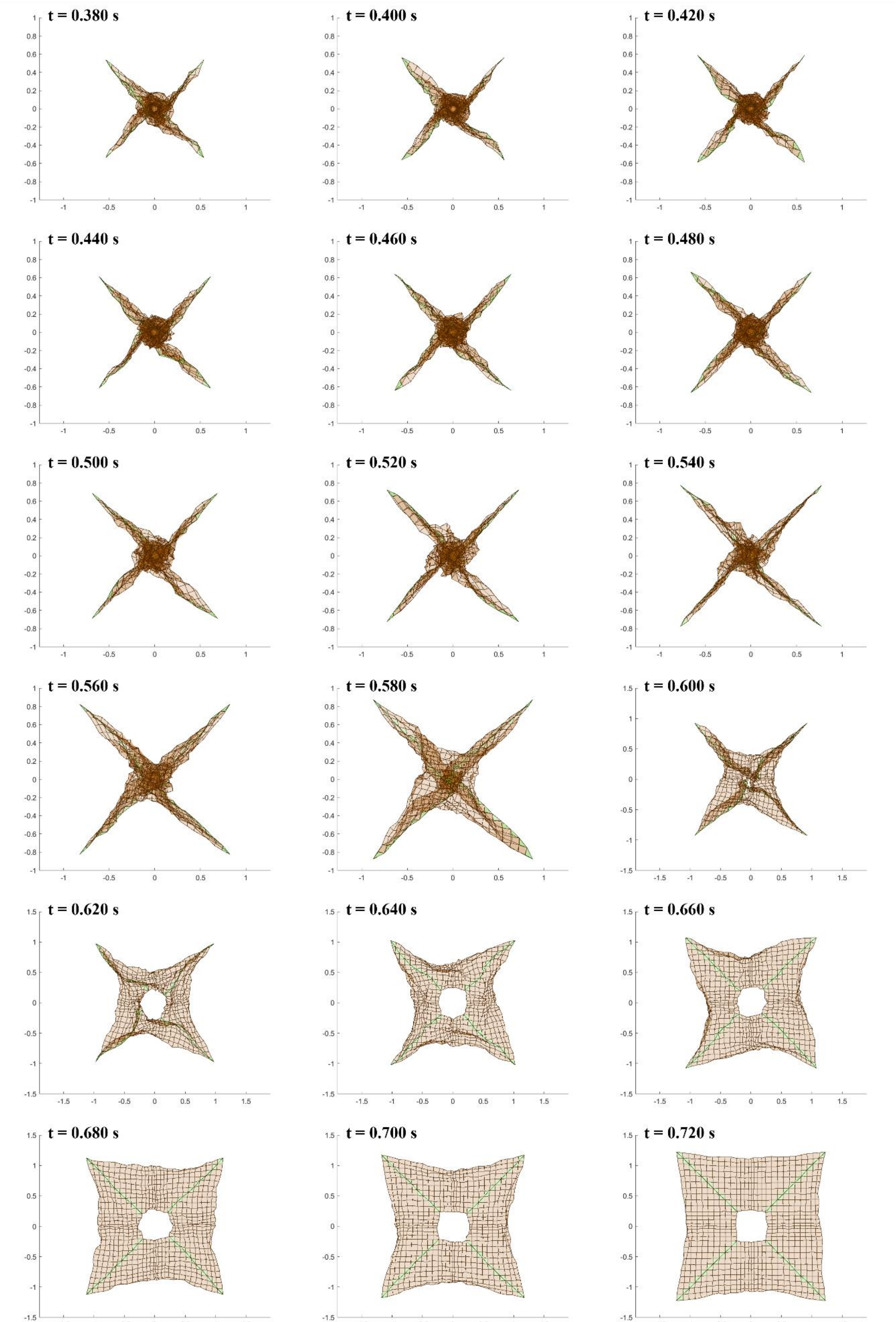

Figure 4.14: Simulation result of the sail deployment for SDOM with the central hub model parameters as k = 20 and d = 10^{-5}.

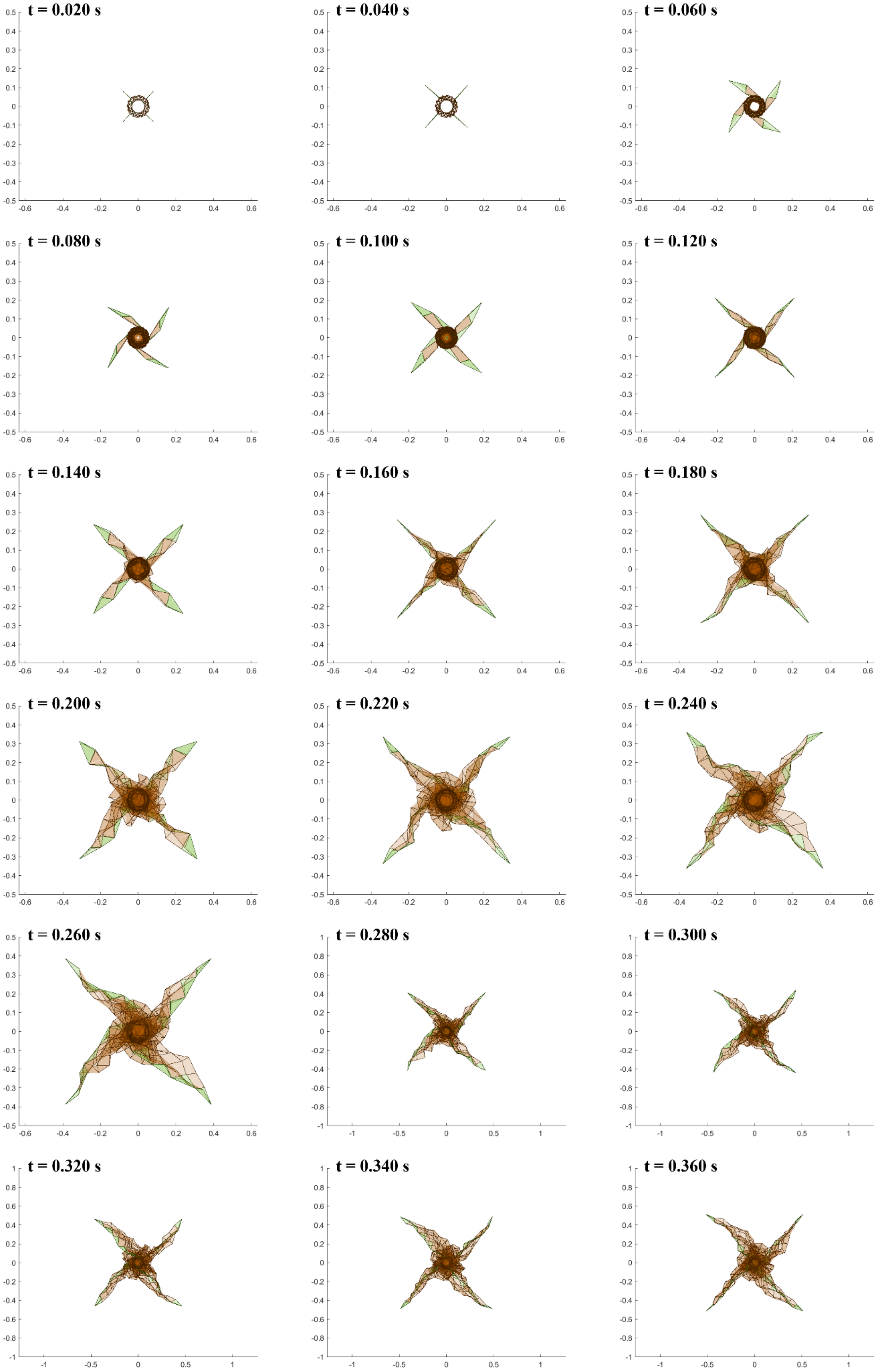
t = 0.020 s
t = 0.040 s
t = 0.060 s
t = 0.080 s
t = 0.100 s
t = 0.120 s
t = 0.140 s
t = 0.160 s
t = 0.180 s
t = 0.200 s
t = 0.220 s
t = 0.240 s
t = 0.260 s
t = 0.280 s
t = 0.300 s
t = 0.320 s
t = 0.340 s
t = 0.360 s
0.5
0.4
0.3
0.2
0.1
0
-0.1
-0.2
-0.3
-0.4
-0.5
-0.6
-0.4
-0.2
0
0.2
0.4
0.6
1
0.8
0.6
0.4
0.2
0
-0.2
-0.4
-0.6
-0.8
-1
-1
-0.5
0
0.5
1

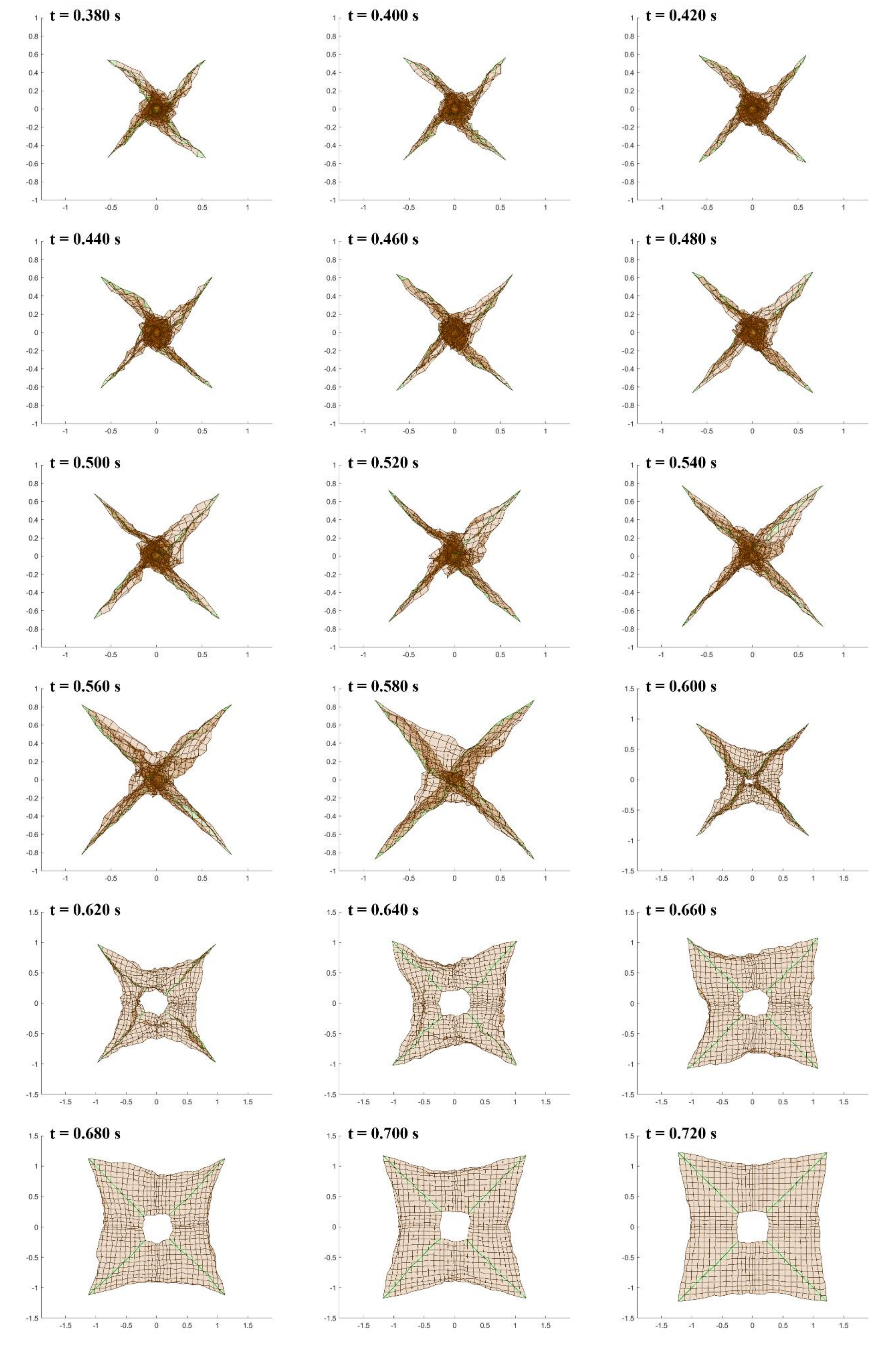

Figure 4.15: Simulation result of the sail deployment for SDOM with the central hub model parameters as k = 20 and d = 10^{-6}.

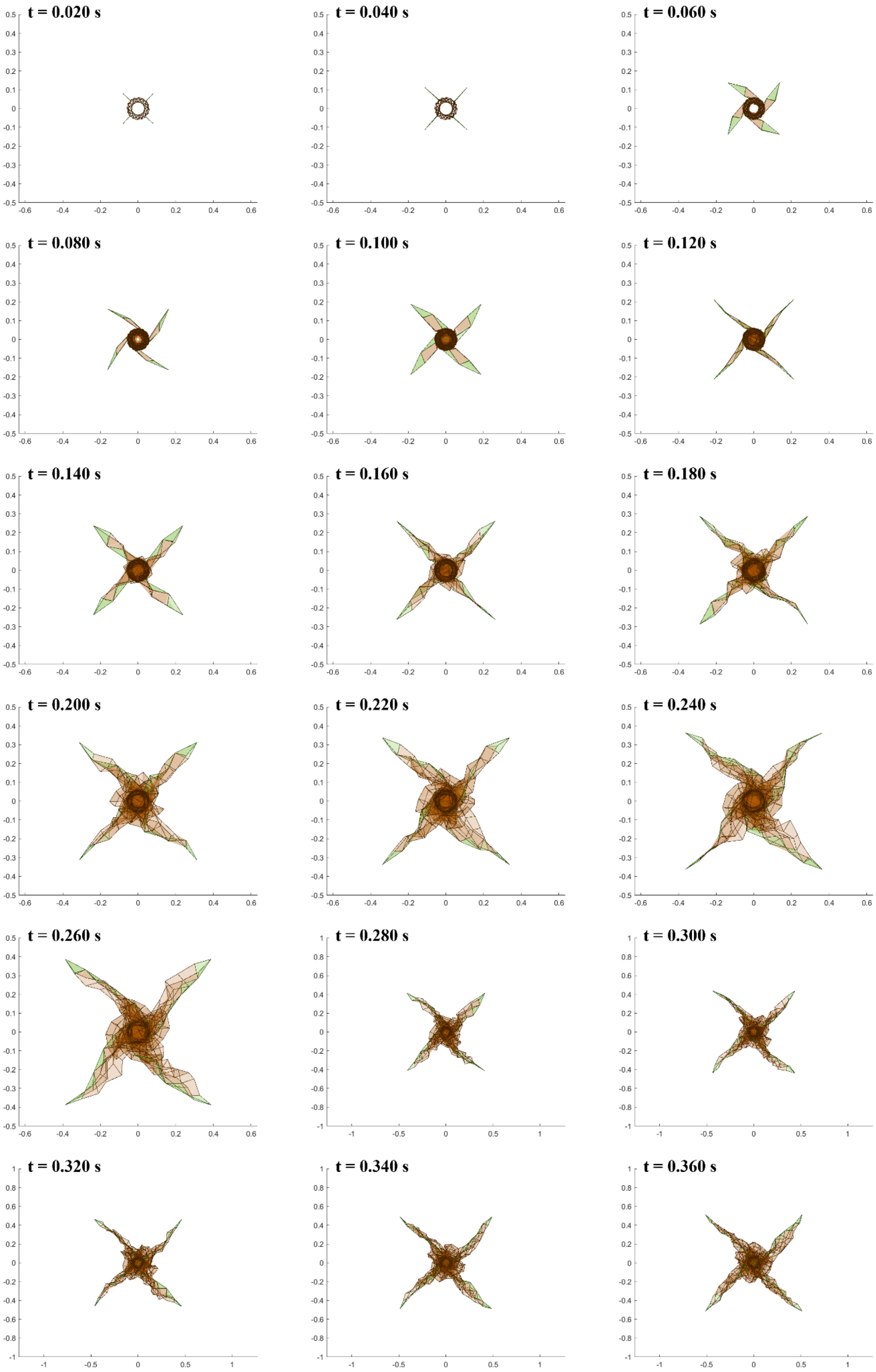
t = 0.020 s
t = 0.040 s
t = 0.060 s
t = 0.080 s
t = 0.100 s
t = 0.120 s
t = 0.140 s
t = 0.160 s
t = 0.180 s
t = 0.200 s
t = 0.220 s
t = 0.240 s
t = 0.260 s
t = 0.280 s
t = 0.300 s
t = 0.320 s
t = 0.340 s
t = 0.360 s
0.5
0.4
0.3
0.2
0.1
0
-0.1
-0.2
-0.3
-0.4
-0.5
-0.6
-0.4
-0.2
0
0.2
0.4
0.6
1
0.8
0.6
0.4
0.2
0
-0.2
-0.4
-0.6
-0.8
-1
-1
-0.5
0
0.5
1

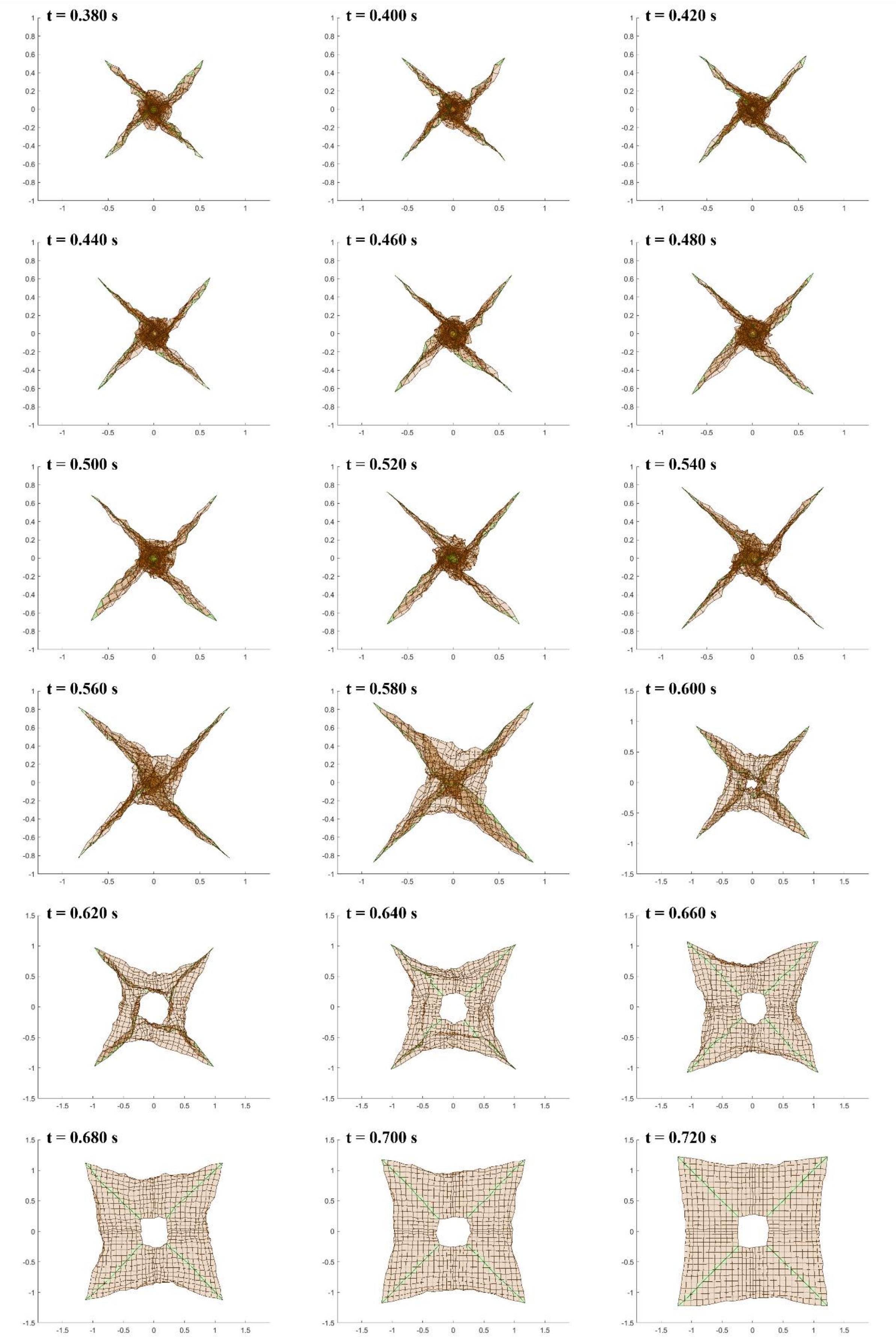

Figure 4.16: Simulation result of the sail deployment for SDOM with the central hub model parameters as k = 20 and d = 10^{-7}.

4.7.3. Fine-tuning of the Compression Stiffness Ratio

After the inclusion of the contact restriction between the sail and the hub, its rotation rate to its unwrapping rate was balanced and the overshoot of the sail further outwards than the pulled corners during deployment was restrained. As the next step in this work, the untimely unfolding of the internal layers of the folded film is to be minimized. This unfolding is not only due to the lack of contact restriction between elements. In fact, it is also present at the pulled diagonals of the sail which are the outmost layers and are to be least affected by the lack of contact restriction between elements. In Figs. 3.46 and 3.47, when the corners are pulled, they are fully folded until complete unwrapping into the star shape is achieved. However, in the simulation, the diagonals of the film already start to unfold and widen. In order to reinforce the sail at the folds so that they show some resilience to unfolding while being pulled, the compression stiffness ratio of the sail was varied as the dominant parameter. Initial value for this parameter up to this point was 10^{-7}. This small value is chosen due to the assumptions made in the mathematical model used in this simulation with the stiffness reduction model. The compression stiffness value is taken as a small fraction of the tension stiffness value. The theory assumes a small fraction; however, the magnitude of this smallness is in fact important in the analysis. Under the conditions of $k = 10$ and $d = 0$, compression stiffness ratio was varied as $R_{cs} = [10^{-2}, 10^{-3}, 10^{-4}, 10^{-5}, 10^{-8}]$ in addition to the 10^{-7}. At smaller values of compression stiffness ratio R_{cs}, the premature unfolding of the membrane is still observed. Figure 4.17 show this comparison at the formation of the inner hole and the star shape. However, at larger values of compression stiffness ratio R_{cs}, the premature unfolding of the membrane before the formation of the inner hole and the star shape does not occur. Figure 4.18 show the comparison between the compression stiffness ratios $R_{cs} = 10^{-2}$ and $R_{cs} = 10^{-3}$. In this figure it can be observed that, although the formation of the inner hole and the relative star shape is better when $R_{cs} = 10^{-2}$, the unfolding of the membrane is over-inhibited at the later stages of the deployment. In comparison, at $R_{cs} = 10^{-3}$, the unfolding occurs naturally after the formation of the inner hole and the star shape starting from the inner layers of the membrane fold close to the in-orbit and ground experiment results.

Figures 4.19 ~ 4.23 show the complete simulated deployment sequences under the above conditions. The closest results to the real deployment is deemed to occur at $R_{cs} = 10^{-3}$ in Fig. 4.20. In this figure, it is observed that the folds stay folded, until the force pulling from the corners directly acts towards the unfolding as the tension in the sail increases. Before this, the force is only working towards the unwrapping of the sail around the central hub. Up to $t = 0.58$ s,

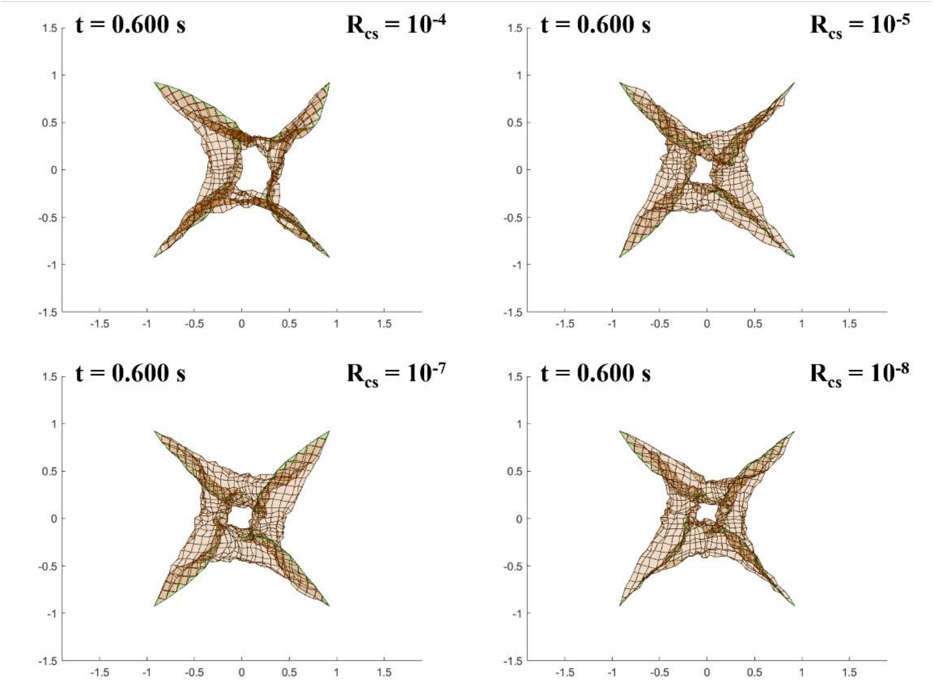

Figure 4.17: Comparison of smaller compression stiffness ratio values $R_{cs.}$.

the folds of the sail do not flatten. However, there is still no contact restriction between elements of the sail. Some premature unwrapping is still observed from the inner layers. This unwrapping starts from the 4 other end points of the sail that occur after the star-shaped fold is rotated around the hub. Figure 2.9 (h) shows these end points. When the folded sail is wrapped around the inner hub, these pseudo-end-points appear for the right angled star shaped sail. Because there is no contact restriction between the elements of the model, the elements themselves are free to cross over each other. This results in these other end points that occur after folding, to start unfolding from the inner side. This can be seen from t = 0.10s, to t = 0.36s. From t = 0.38s, the central elements and nodes of the sail become very chaotic. This is due to the fact that the rotation of the sail around the central hub, is not synchronizing with the deployment (unwrapping) rate of the sail. When the forces are finally applying tension to the sail to propagate flattening of folds, the inner corners of the sail corresponding to the outer corners are placed at the opposite quadrants of the sail. This is undesired and reworking of the contact coefficient parameter is needed to rebalance the rotation rate with the new compression stiffness ratio value.

In comparison, with an even higher compression stiffness value, the star shape is even more apparent as can be seen in Fig. 4.19. However, some folds of the membrane do not unfold at all until considerable tension is applied to the membrane as can be seen from t = 0.62s to t = 0.68s. This is unrealistic. Folded membrane unfolds to an extent uniformly even when no tension is applied. It does not flatten completely, but it does not stay fully folded, or non-

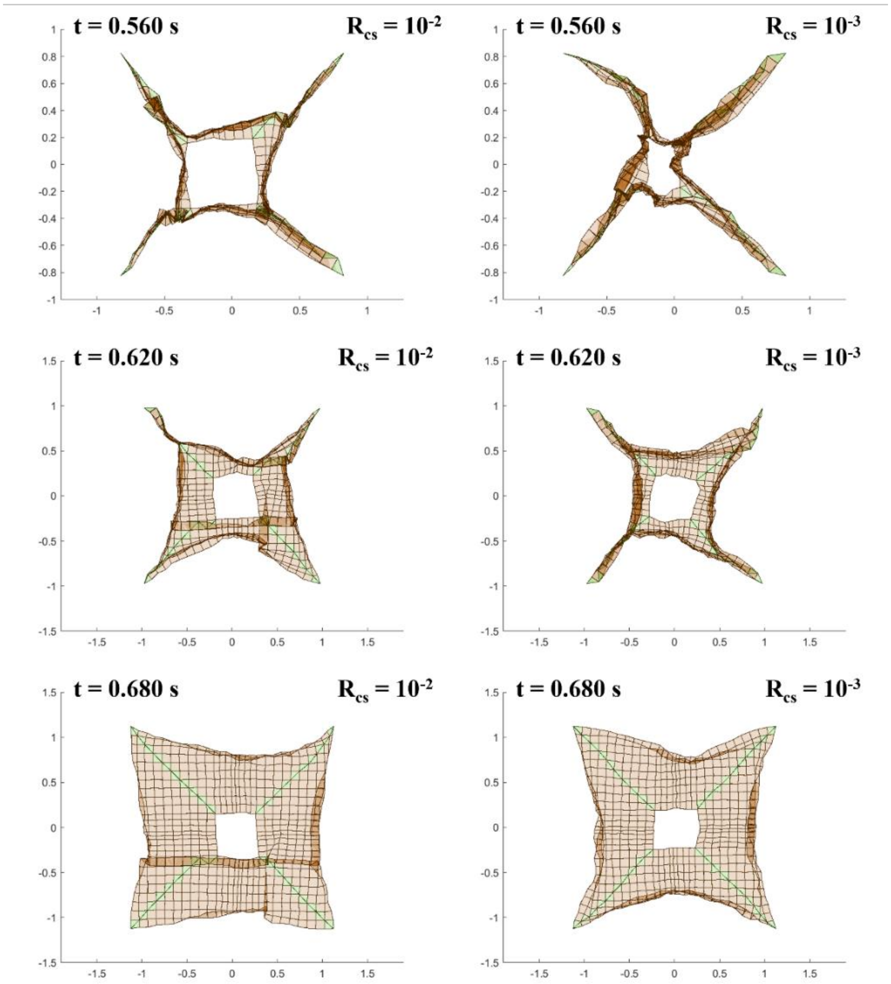

Figure 4.18: Comparison of larger compression stiffness ratio values R_{cs}..

uniformly folded. Values of R_{cs} that are higher than 10^{-3} still allow for considerable premature unfolding of the membrane as can be seen from Figs. 4.21 to 4.23 and are therefore undesired.

With increased compressive stiffness ratio, the folds are staying folded longer, and only unfolding after complete unwrapping from the circular shape is achieved. The elements are still able to overlap and go through each other, therefore complete unwrapping to the star shape does not completely reflect reality. However, an improvement from previous iterations is the fact that, although premature unwrapping of inner end points of the sail could not be avoided due to unrestricted movements through elements, the unfolding at this stage was prevented. Additionally, with these parameters the unfolding of the sail occurs from the inner most folds moving along the outwards radial direction, instead of the previous unfolding from the middle folds into a large singular fold, which then slides over itself towards outwards radial direction.

From these, it is clearly seen that the compressive stiffness ratio, not only relates to the element shape and size through compressive rigidity value it will provide, but also relates to the resistance to the unfolding between elements.

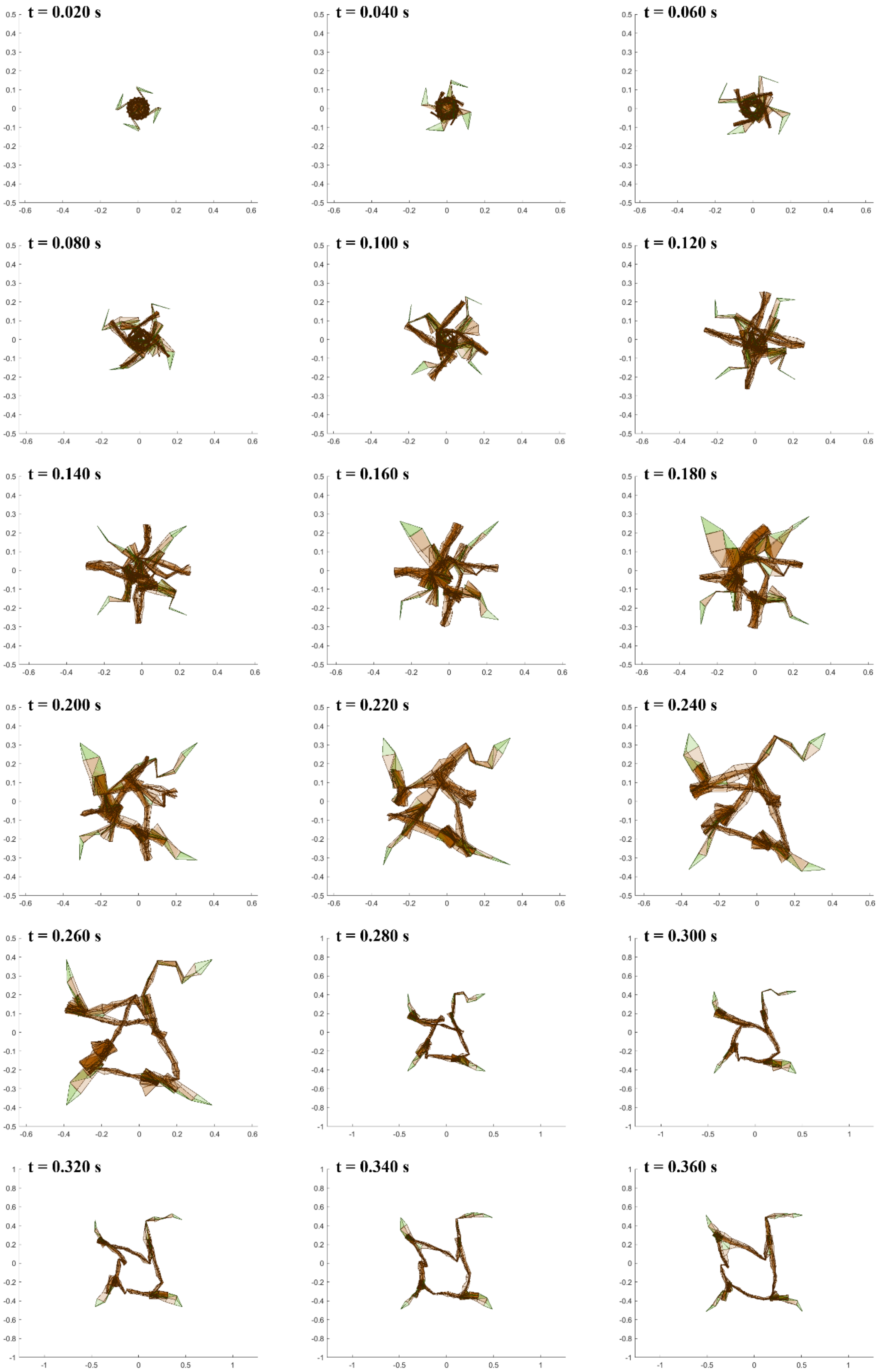
t = 0.020 s
t = 0.040 s
t = 0.060 s
t = 0.080 s
t = 0.100 s
t = 0.120 s
t = 0.140 s
t = 0.160 s
t = 0.180 s
t = 0.200 s
t = 0.220 s
t = 0.240 s
t = 0.260 s
t = 0.280 s
t = 0.300 s
t = 0.320 s
t = 0.340 s
t = 0.360 s
0.5
0.4
0.3
0.2
0.1
0
-0.1
-0.2
-0.3
-0.4
-0.5
-0.6
-0.4
-0.2
0
0.2
0.4
0.6
1
0.8
0.6
0.4
0.2
0
-0.2
-0.4
-0.6
-0.8
-1
-1
-0.5
0
0.5
1

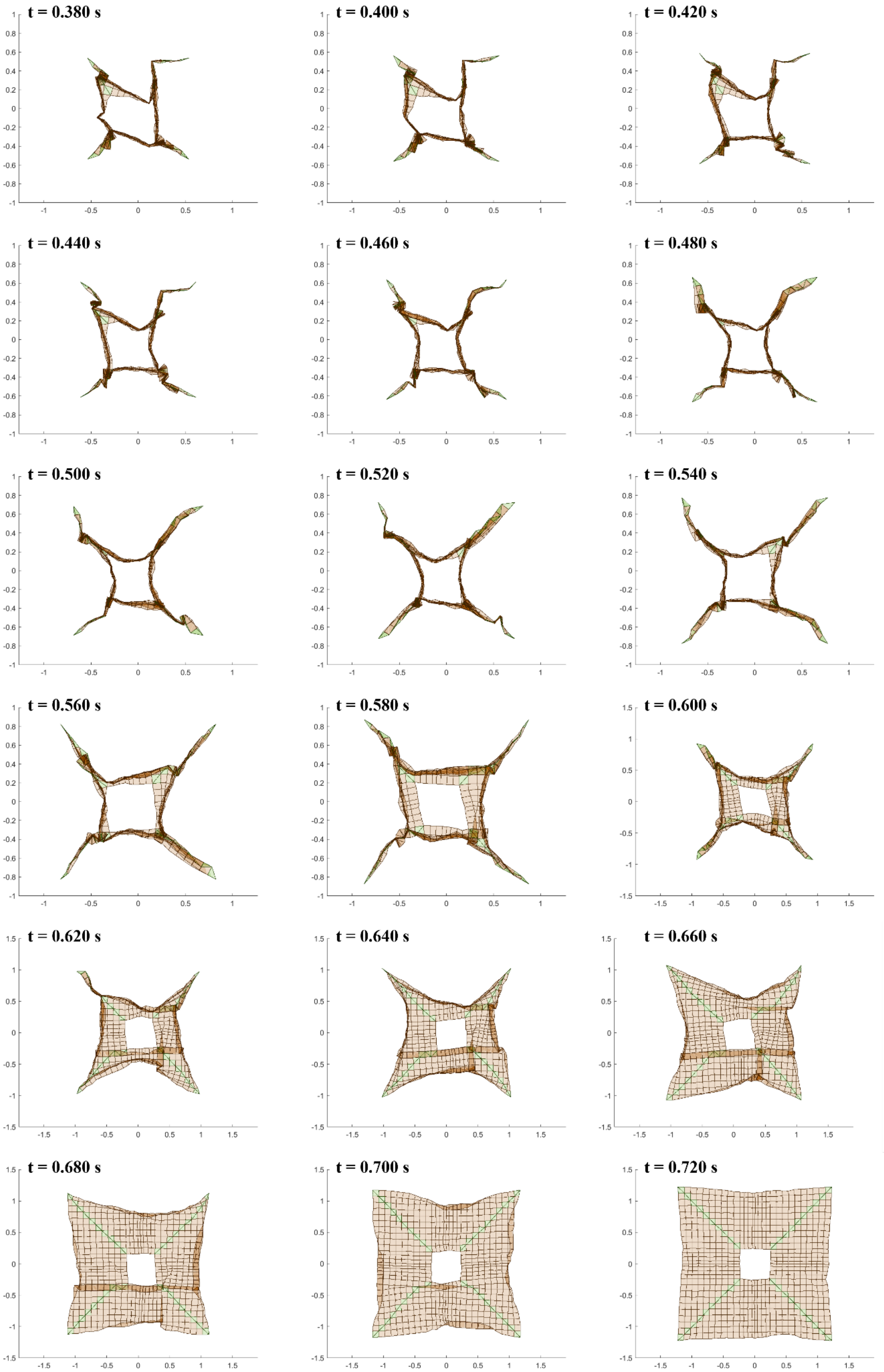

Figure 4.19: Simulation result of sail deployment for SDOM with the central hub model parameters as k = 10 and d = 0 and the compression stiffness ratio $R_{cs} = 10^{-2}$.

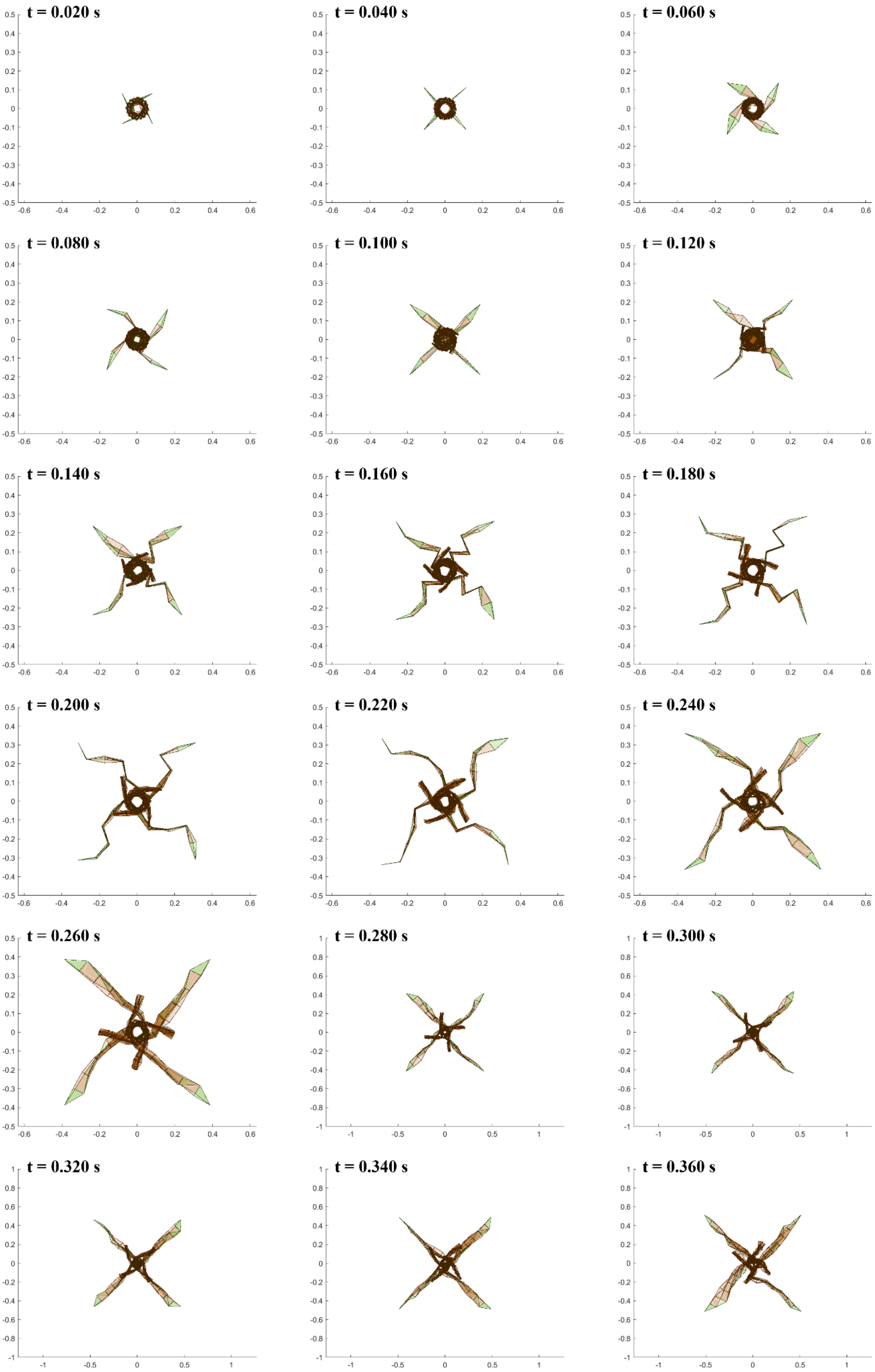
t = 0.020 s
t = 0.040 s
t = 0.060 s
t = 0.080 s
t = 0.100 s
t = 0.120 s
t = 0.140 s
t = 0.160 s
t = 0.180 s
t = 0.200 s
t = 0.220 s
t = 0.240 s
t = 0.260 s
t = 0.280 s
t = 0.300 s
t = 0.320 s
t = 0.340 s
t = 0.360 s

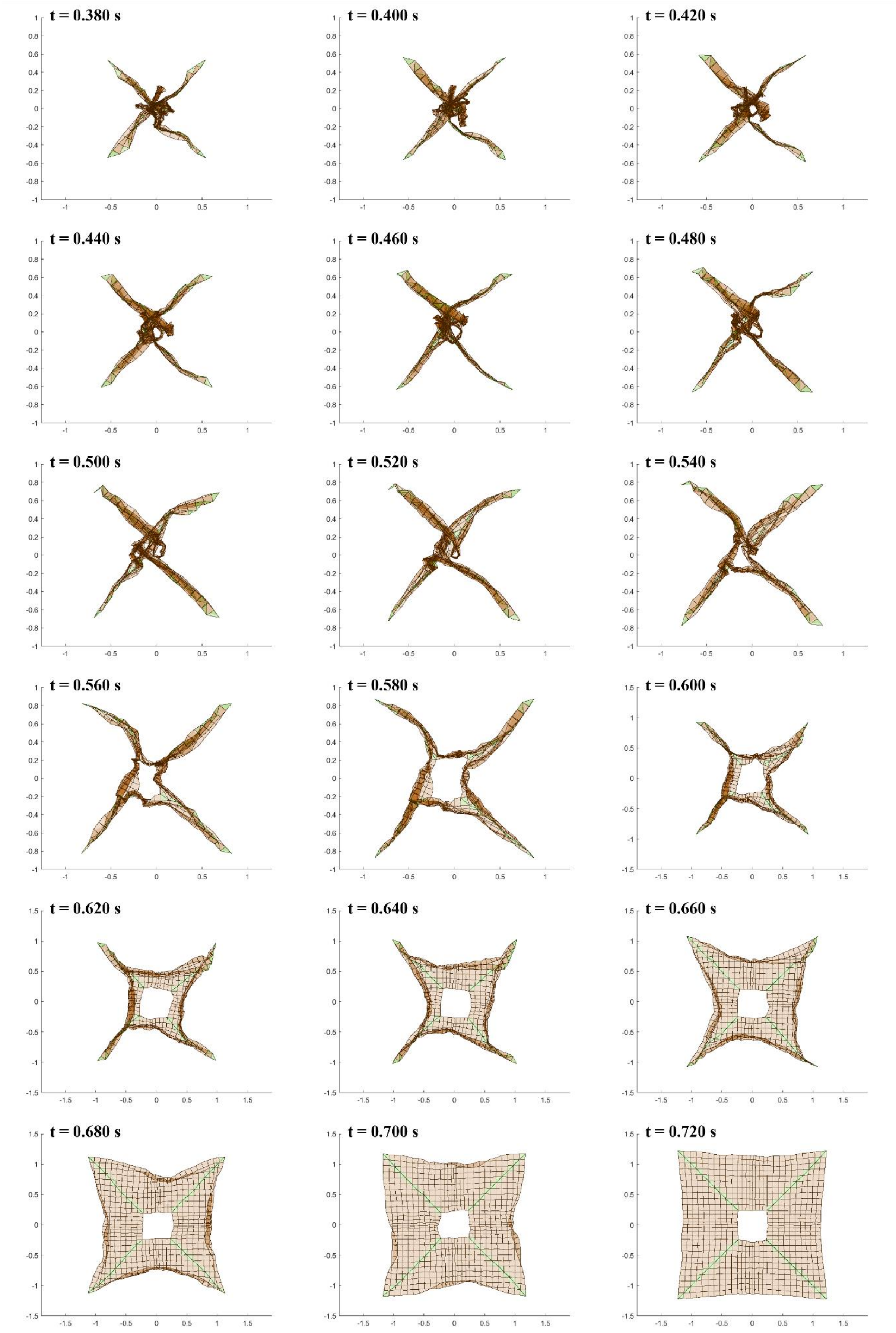
t = 0.380 s

t = 0.400 s

t = 0.420 s

t = 0.440 s

t = 0.460 s

t = 0.480 s

t = 0.500 s

t = 0.520 s

t = 0.540 s

t = 0.560 s

t = 0.580 s

t = 0.600 s

t = 0.620 s

t = 0.640 s

t = 0.660 s

t = 0.680 s

t = 0.700 s

t = 0.720 s

Figure 4.20: Simulation result of sail deployment for SDOM with the central hub model parameters as k = 10 and d = 0 and the compression stiffness ratio $R_{cs} = 10^{-3}$.

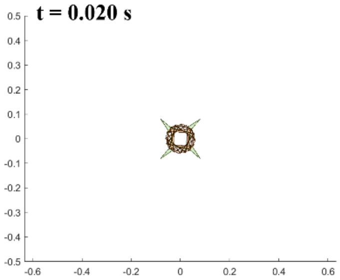

t = 0.020 s

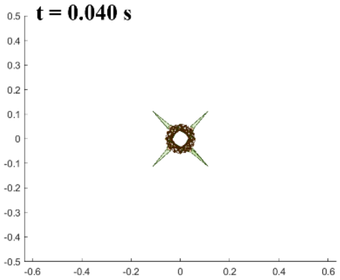

t = 0.040 s

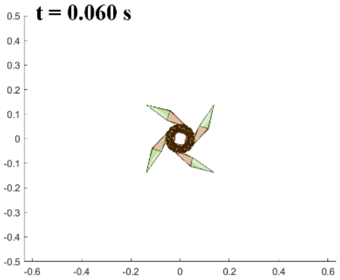

t = 0.060 s

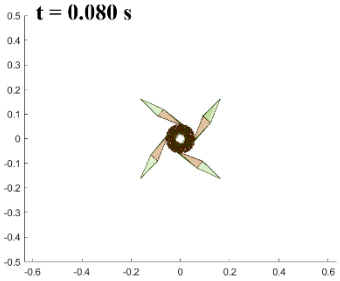

t = 0.080 s

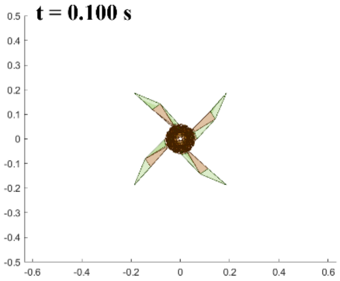

t = 0.100 s

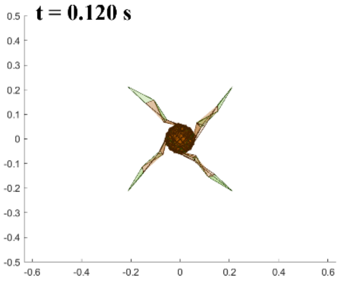

t = 0.120 s

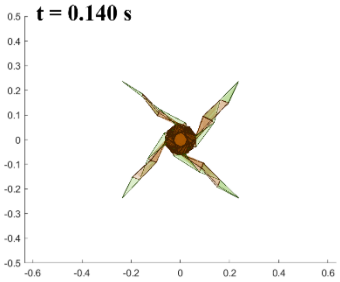

t = 0.140 s

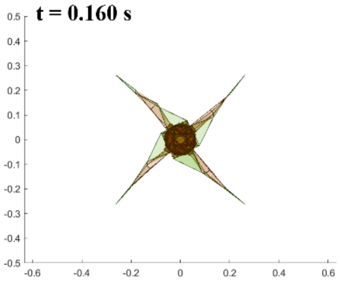

t = 0.160 s

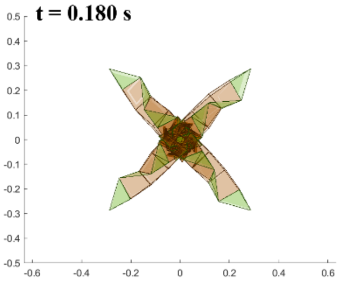

t = 0.180 s

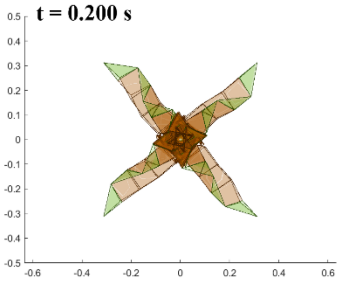

t = 0.200 s

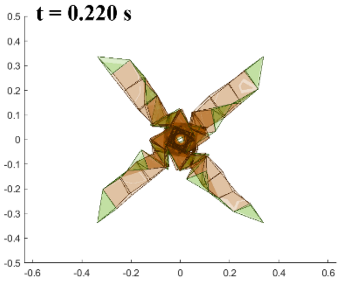

t = 0.220 s

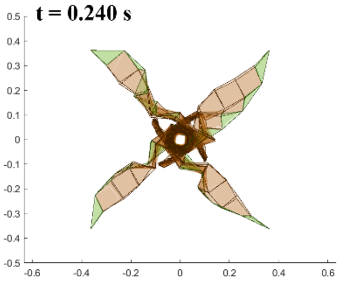

t = 0.240 s

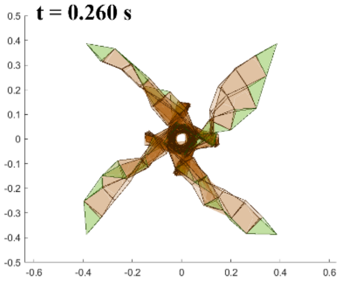

t = 0.260 s

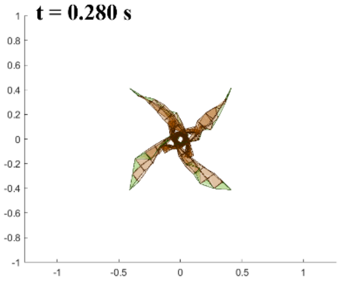

t = 0.280 s

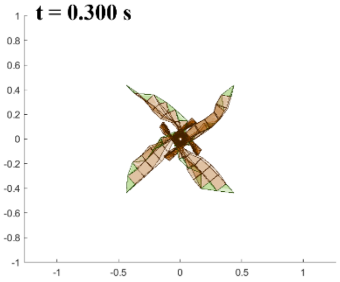

t = 0.300 s

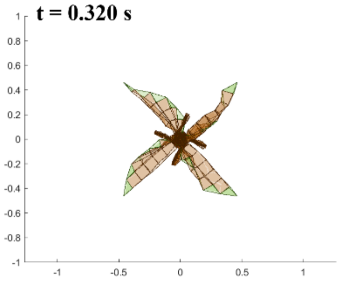

t = 0.320 s

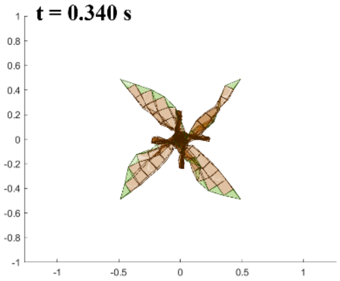

t = 0.340 s

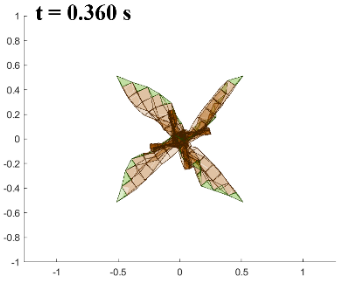

t = 0.360 s

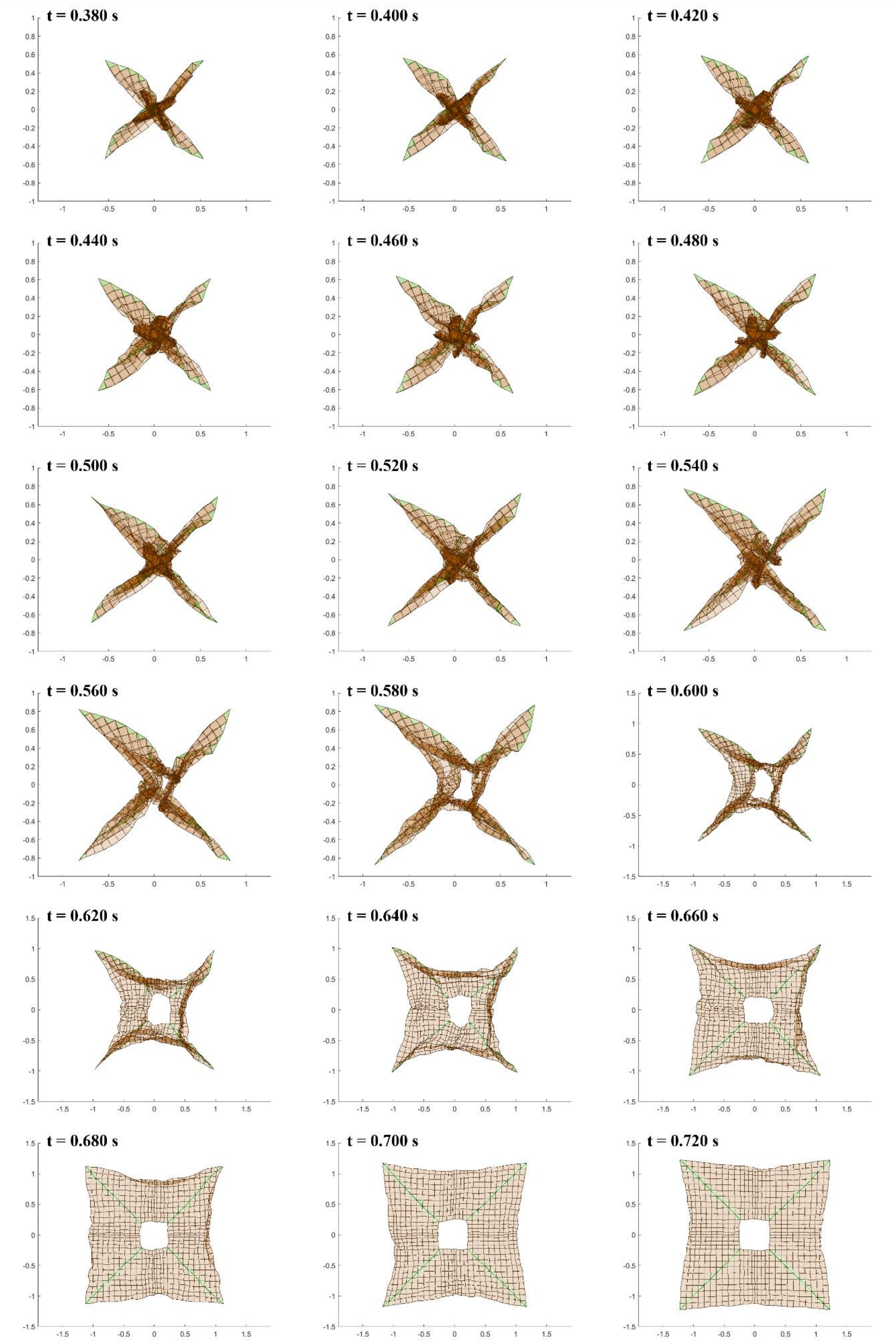

Figure 4.21: Simulation result of sail deployment for SDOM with the central hub model parameters as k = 10 and d = 0 and the compression stiffness ratio $R_{cs} = 10^{-4}$.

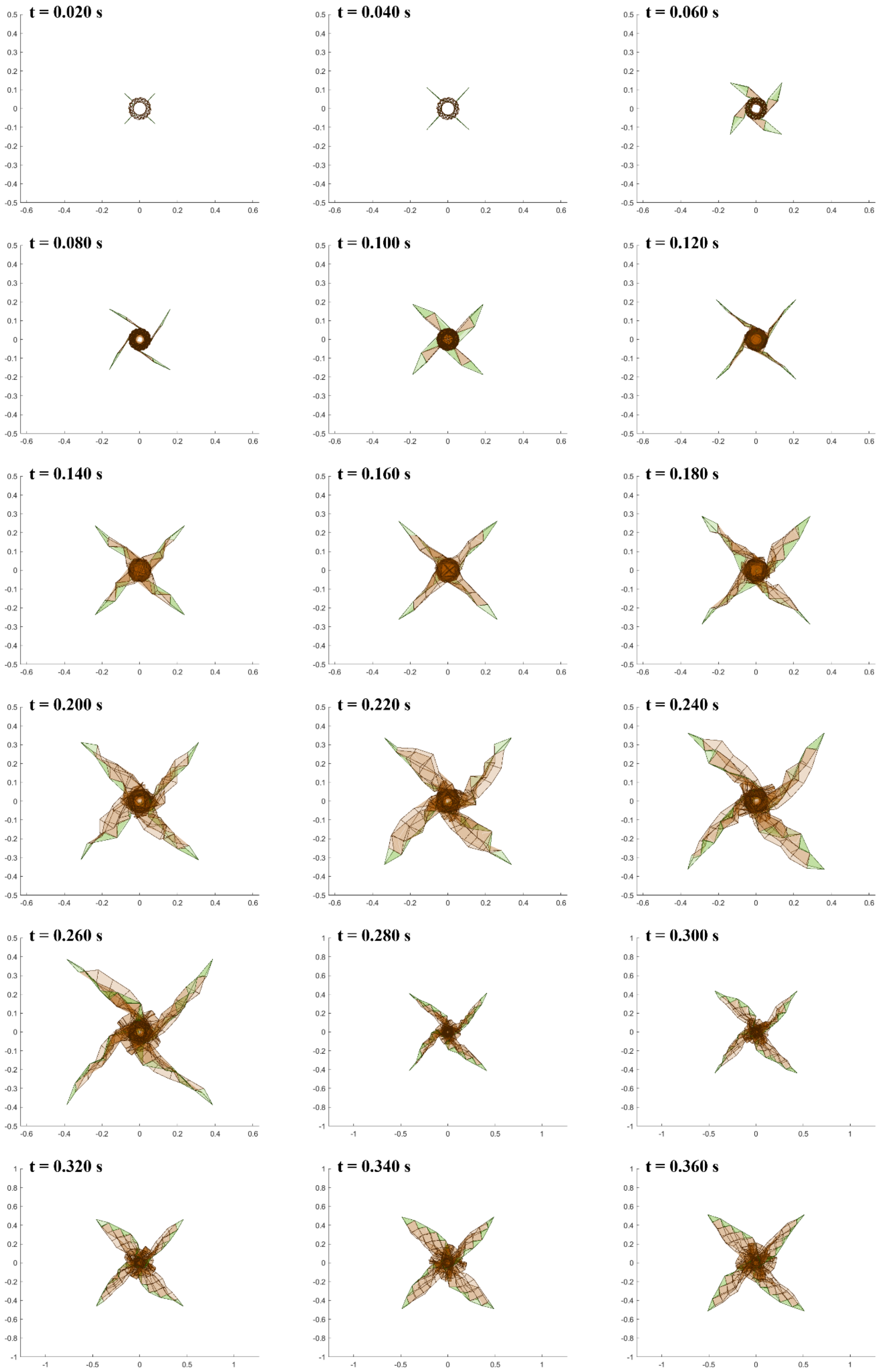
t = 0.020 s
t = 0.040 s
t = 0.060 s
t = 0.080 s
t = 0.100 s
t = 0.120 s
t = 0.140 s
t = 0.160 s
t = 0.180 s
t = 0.200 s
t = 0.220 s
t = 0.240 s
t = 0.260 s
t = 0.280 s
t = 0.300 s
t = 0.320 s
t = 0.340 s
t = 0.360 s
0.5
0.4
0.3
0.2
0.1
0
-0.1
-0.2
-0.3
-0.4
-0.5
-0.6
0.6
1
0.8
-0.8
-1
-0.5

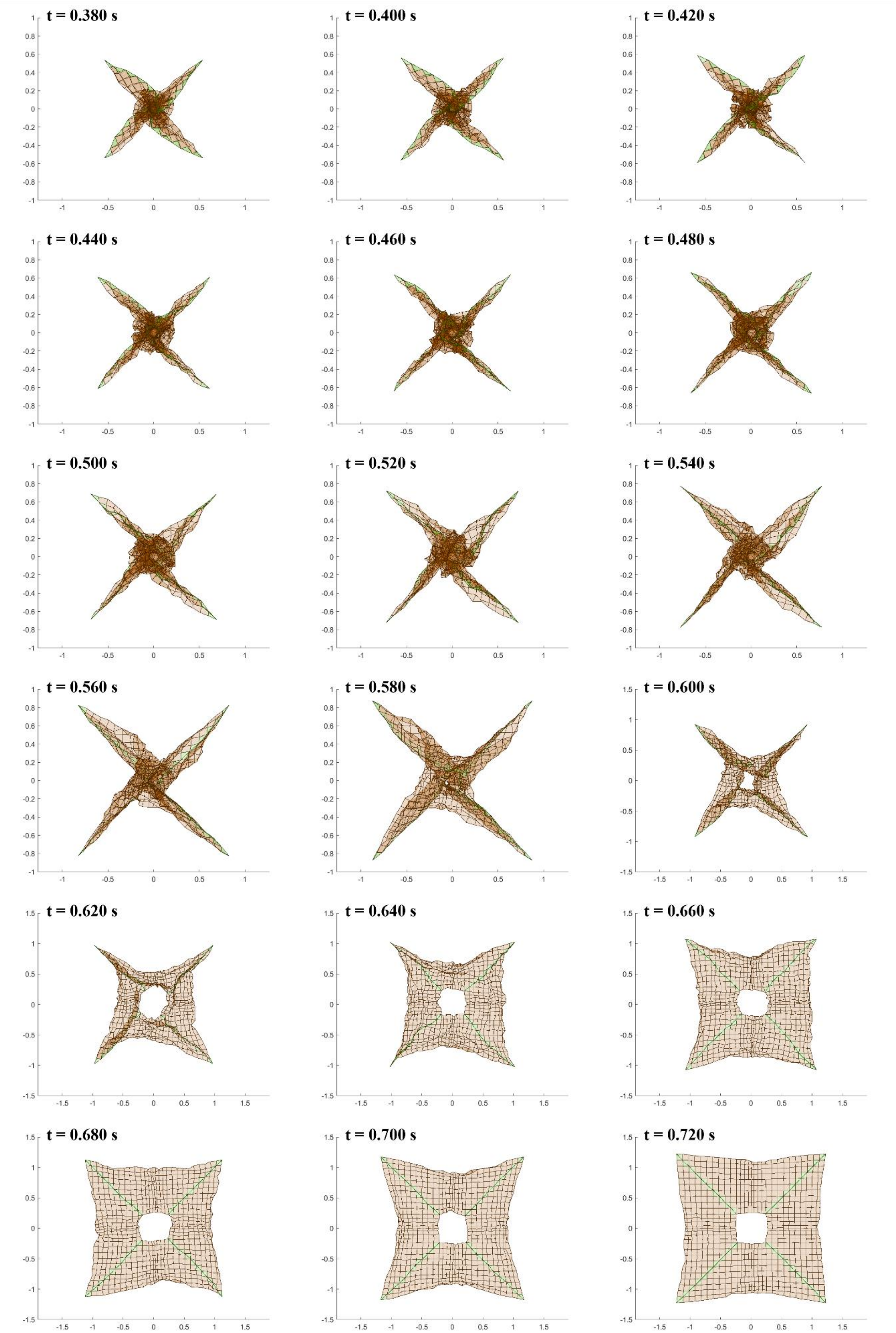

Figure 4.22: Simulation result of sail deployment for SDOM with the central hub model parameters as k = 10 and d = 0 and the compression stiffness ratio $R_{cs} = 10^{-5}$.

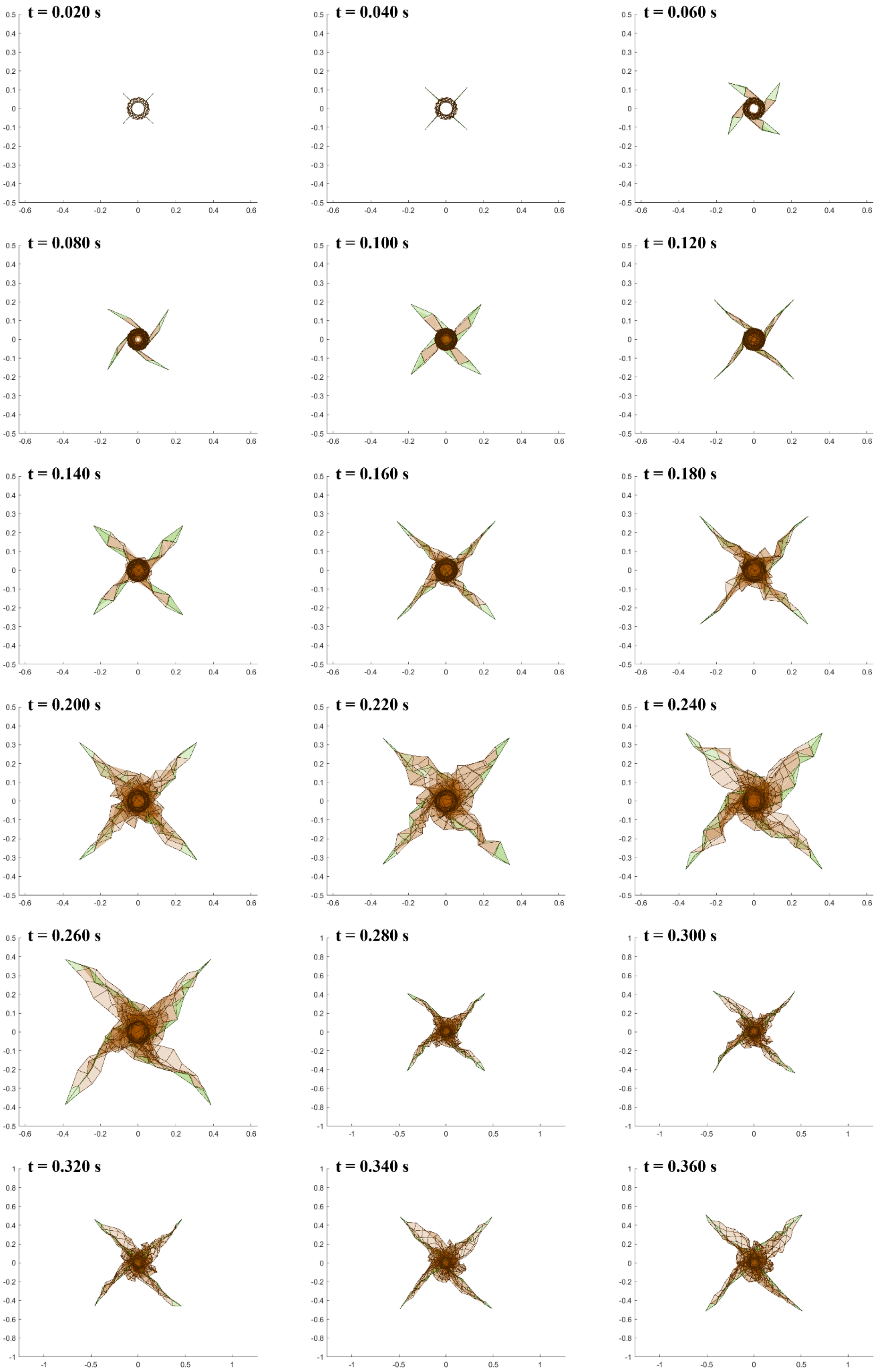
t = 0.020 s
t = 0.040 s
t = 0.060 s
t = 0.080 s
t = 0.100 s
t = 0.120 s
t = 0.140 s
t = 0.160 s
t = 0.180 s
t = 0.200 s
t = 0.220 s
t = 0.240 s
t = 0.260 s
t = 0.280 s
t = 0.300 s
t = 0.320 s
t = 0.340 s
t = 0.360 s
0.5 0.4 0.3 0.2 0.1 0 -0.1 -0.2 -0.3 -0.4 -0.5
-0.6 -0.4 -0.2 0 0.2 0.4 0.6
1 0.8 0.6 0.4 0.2 0 -0.2 -0.4 -0.6 -0.8 -1
-1 -0.5 0 0.5 1

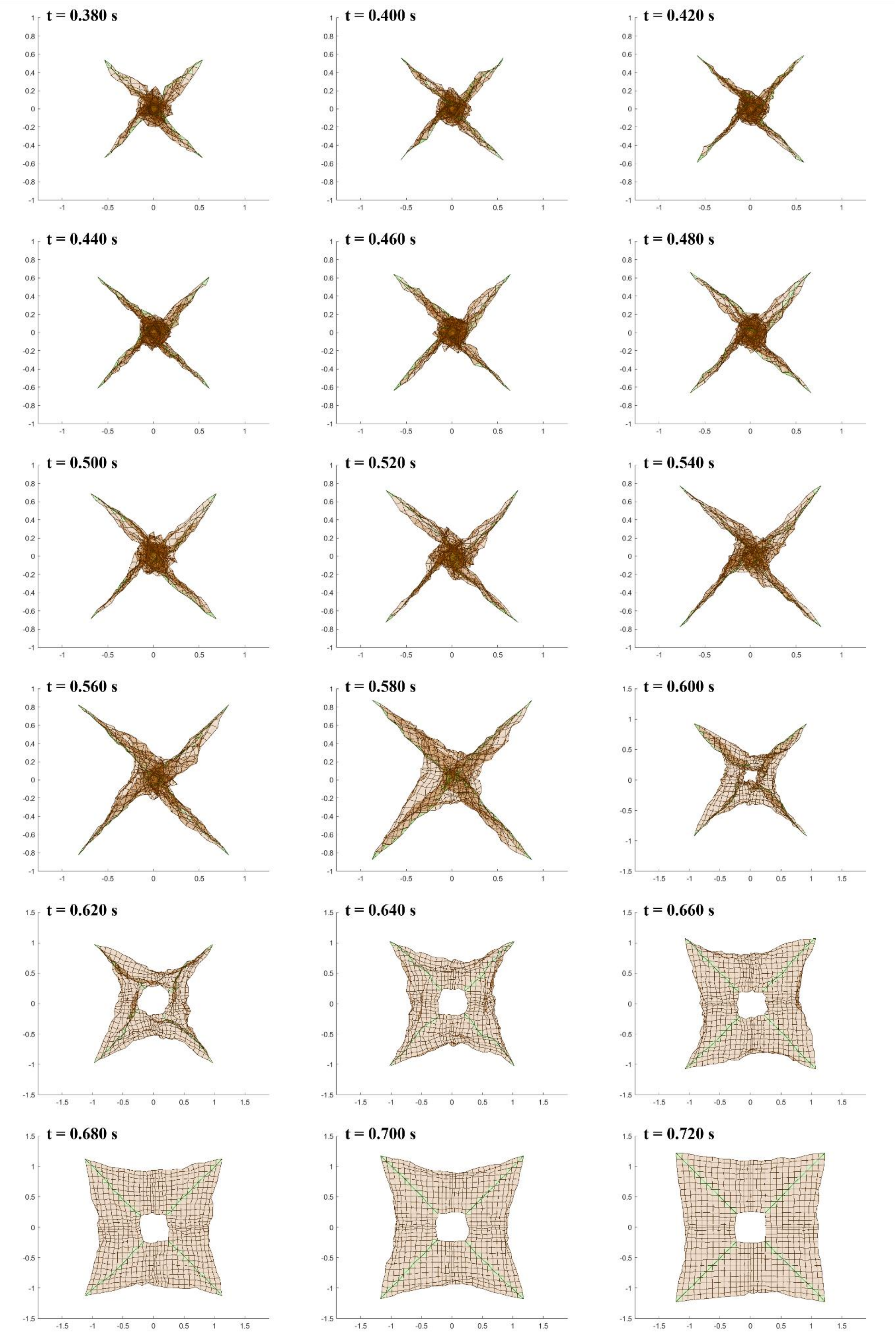

Figure 4.23: Simulation result of sail deployment for SDOM with the central hub model parameters as k = 10 and d = 0 and the compression stiffness ratio $R_{cs} = 10^{-8}$.

4.1.4. Re-tuning of the Contact Coefficient

In order to acquire the most realistic resulting combination, the newly found parameter of $R_{cs} = 10^{-3}$ was again splashed with varying k = [0, 15, 20, 25, 50] in addition to the previous result with 10. A deployment with the correct unfolding order starting from inner most folds moving towards outer folds after full unwrapping can be observed even with k = 0 which disregards the contact restriction of the inner hub. From this, it can be concluded that the unfolding order is more dependent on the compressive stiffness ratio. However, the rotational movement of the unwrapping cannot be confirmed without the contact restriction with the hub.

For better comparison, a side-by-side layout of all the results at t = 0.52, t = 0.58, t = 0.64 and t = 0.70 are given in Figs. 4.24 and 4.25. From these figures it can be observed that the inner hole and the star shape formation during deployment is best at values of k = 15 and k = 20. At lower values of k, the rotational pace and the deployment pace desynchronize, and the desired inner hole and star shape formation cannot be observed. This is most apparent at the instances of t = 0.52 s and t = 0.58 s. On the other hand, at higher values of k, the unfolding of the membrane does not occur sequentially between the folded layers, and the premature unfolding can be observed t = 0.58 s. Additionally at k = 50, the desynchronization of the rotational pace and the deployment pace of the membrane is also observed at t = 0.52 s. Between k = 15 and k = 20, although little difference can be seen in the former stages of deployment, at t = 0.64 s, when k = 20, the outer most layers of the membrane are less continuous and show a buckling behavior at the outer edges of the membrane as opposed to a the continuous bending behavior observed at t = 0.64 s when k = 15. This is closer to the in-orbit deployment results shown in Fig. 3.45 at t = 2.2 to 2.5.

Additionally, the rotation number of the pseudo corners are measured and graphed with vary contact coefficient k values. Figure 4.26 show this graph. The rotational wrapping number of the pseudo corners in the case of DOM2500 used for the deployment is 1.25 revolutions around the hub. The closest rotational unwrapping is measured for the contact coefficient value k of 20. In conclusion, the most realistic parameters for the membrane model are identified as k = 20, d = 0, and $R_{cs} = 10^{-3}$.

Figures 4.27 ~ 4.31 show the results for all the simulations with varied k. The closest simulation result to the real deployment with k = 20 is shown in Fig. 4.29. In this result, the right-angled star shape can clearly be confirmed from t = 0.54 to t = 0.58. From this point onwards, the inner folds start to flatten first similar to the ground experiment and in-orbit results, with the inner square hole fully deployed around t = 0.60. In comparison in Fig. 4.27,

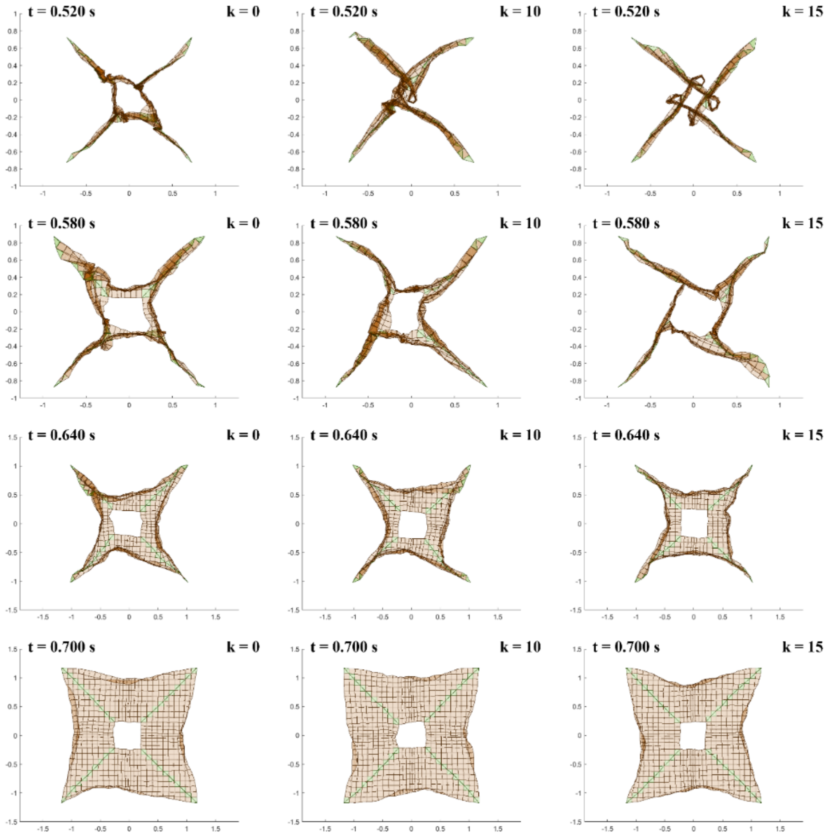

Figure 4.24: Side-by-side comparison of the membrane unfolding at contact coefficient values of k = 0, 10, 15.

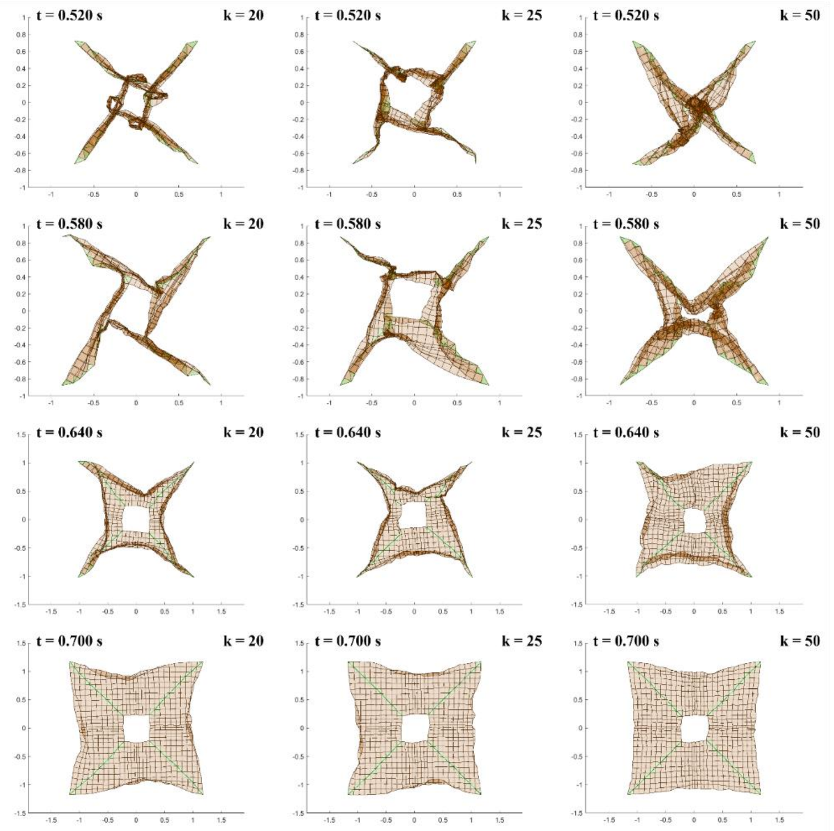

Figure 4.25: Side-by-side comparison of the membrane unfolding at contact coefficient values of k = 20, 25, 50.

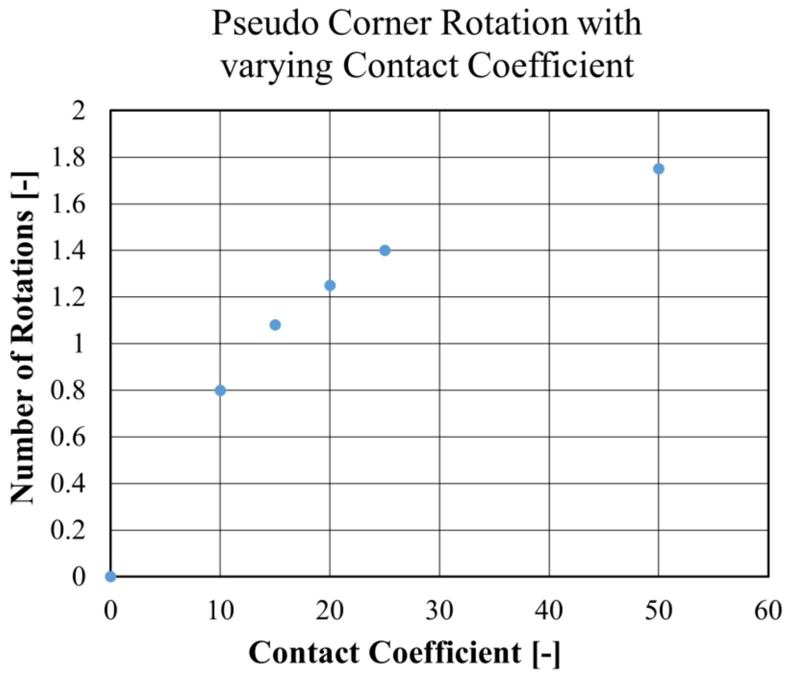

Figure 4.26: Number of rotations for the unwrapping pseudo corners with varying contact coefficient values k.

with no central hub outward force, the membrane is still only unwrapping before unfolding, however the unwrapping motion is not circular due to lack of contact restriction between elements. On the other hand, with higher or lower spring constants, the inner pseudo corners of the folded membrane overshoot or undershoot to unwrap and result in an inner square hole that is not clear. The desired behavior is most apparent in Fig 4.29 at t = 0.50s to t = 0.60s.

4.8. Parameter-tuning of the Convex Tape Model

In the initial simulation for convex tape extension conducted in chapter two, the fully extended state is achieved in 0.2 s as shown in Fig. 2.12. In comparison, the initial simulation result with the fusion model is fully deployed in 0.356 s as shown in Fig. 2.14. The addition of membrane slows down the extension of the convex tape. However, in the real experiment result that was conducted in-orbit presented in chapter 3, the deployment is achieved in ~0.7 s as can be seen in Fig. 3.46. The mechanism of DOM2500 is built in a way that allows the convex tapes to first latch into extendable position and then start extension freely. Considering this initial movement, the simulation model of convex tapes are also built to start from the free-to-extend position, and the initial latching movement is disregarded. In Fig. 3.46, the latching occurs between t = 1.5 s to t= 1.6 s, and the extension starts immediately after. Due to limited frame rate of 10 fps, the resolution of the exact value is unfortunately 0.1 s and more accurate time value could not be obtained. It is necessary to tune the parameters of the convex tape model to achieve more accurate extension times than the initial result.

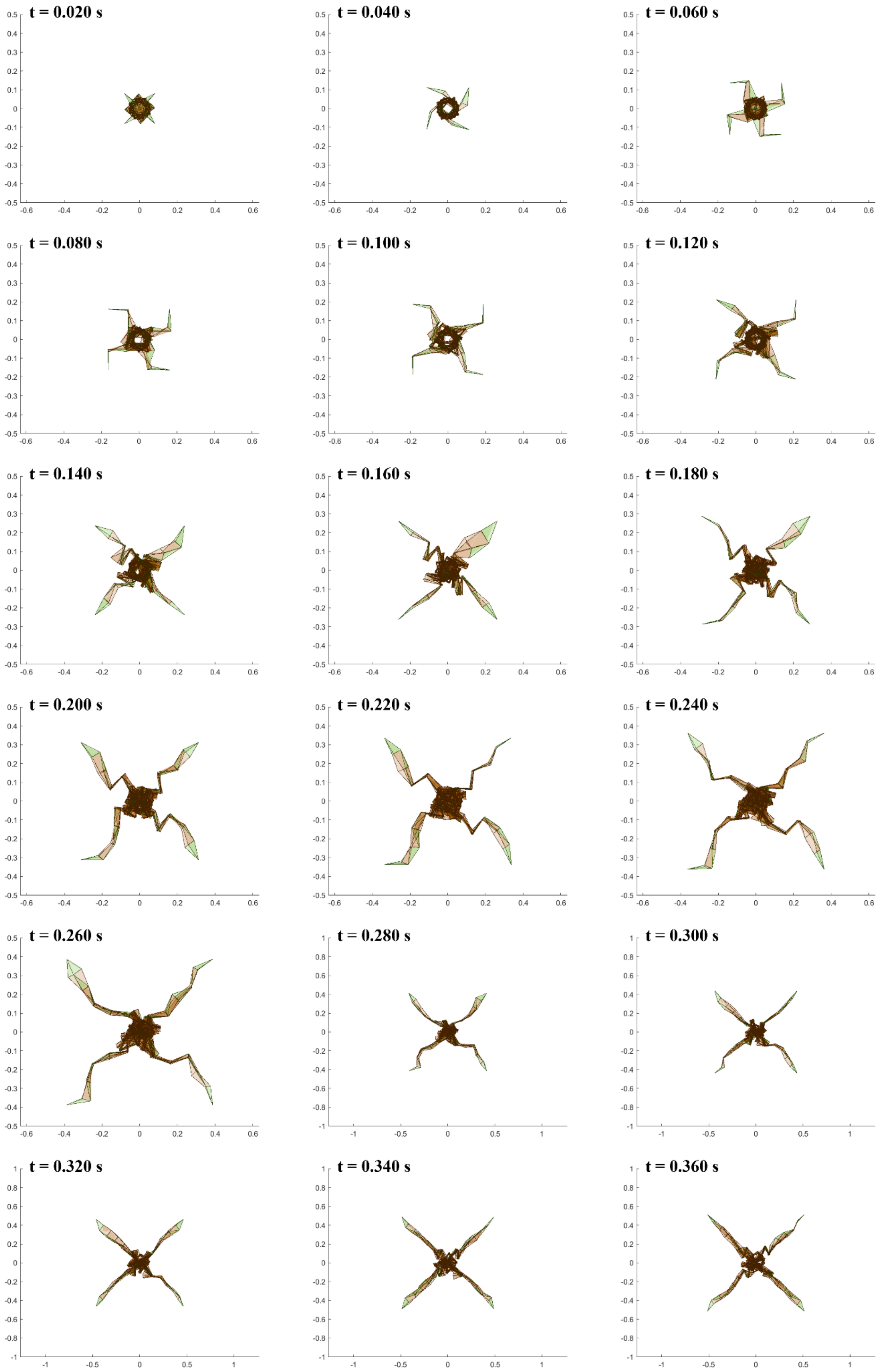
t = 0.020 s
t = 0.040 s
t = 0.060 s
t = 0.080 s
t = 0.100 s
t = 0.120 s
t = 0.140 s
t = 0.160 s
t = 0.180 s
t = 0.200 s
t = 0.220 s
t = 0.240 s
t = 0.260 s
t = 0.280 s
t = 0.300 s
t = 0.320 s
t = 0.340 s
t = 0.360 s
0.5
0.4
0.3
0.2
0.1
0
-0.1
-0.2
-0.3
-0.4
-0.5
-0.6
-0.4
-0.2
0
0.2
0.4
0.6
1
0.8
0.6
0.4
0.2
0
-0.2
-0.4
-0.6
-0.8
-1
-1
-0.5
0
0.5
1

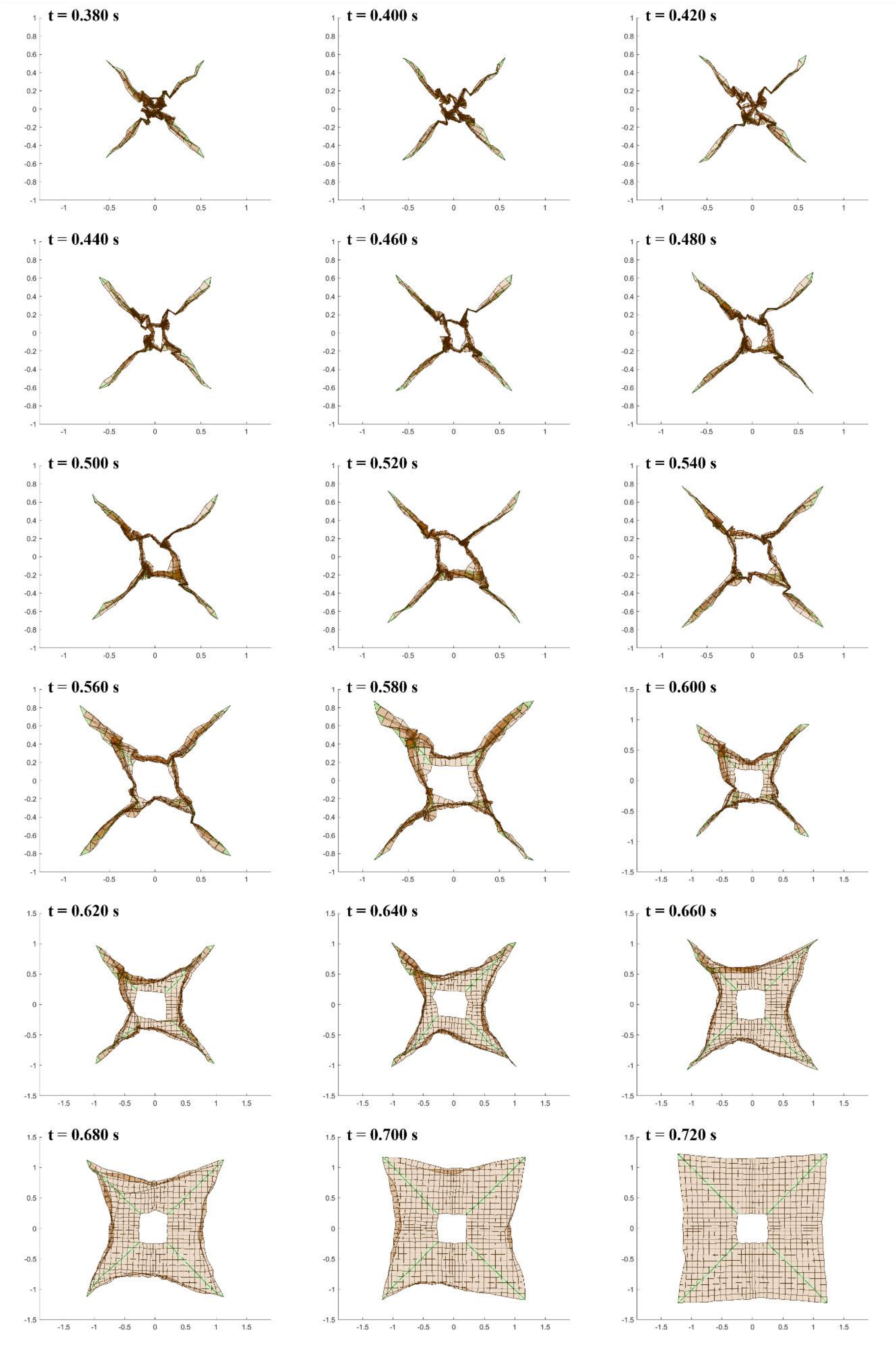
t = 0.380 s

t = 0.400 s

t = 0.420 s

t = 0.440 s

t = 0.460 s

t = 0.480 s

t = 0.500 s

t = 0.520 s

t = 0.540 s

t = 0.560 s

t = 0.580 s

t = 0.600 s

t = 0.620 s

t = 0.640 s

t = 0.660 s

t = 0.680 s

t = 0.700 s

t = 0.720 s

Figure 4.27: Simulation result of sail deployment for SDOM with the central hub model parameters as k = 0 and d = 0 and the compression stiffness ratio $R_{cs} = 10^{-3}$.

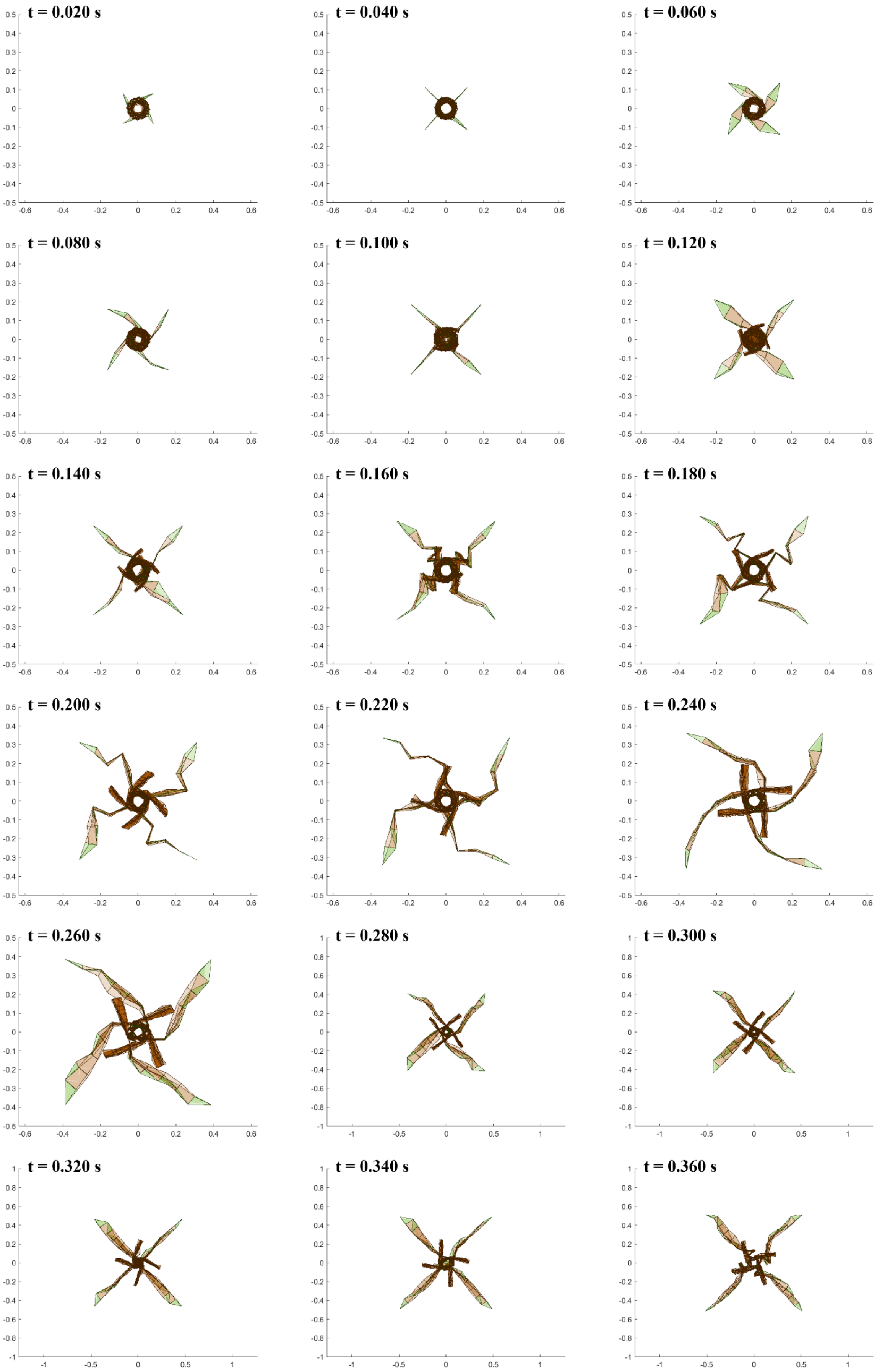
t = 0.020 s
t = 0.040 s
t = 0.060 s
t = 0.080 s
t = 0.100 s
t = 0.120 s
t = 0.140 s
t = 0.160 s
t = 0.180 s
t = 0.200 s
t = 0.220 s
t = 0.240 s
t = 0.260 s
t = 0.280 s
t = 0.300 s
t = 0.320 s
t = 0.340 s
t = 0.360 s
0.5
0.4
0.3
0.2
0.1
0
-0.1
-0.2
-0.3
-0.4
-0.5
-0.6
0.6
1
0.8
0.6
-0.8
-1
-0.5
0.5

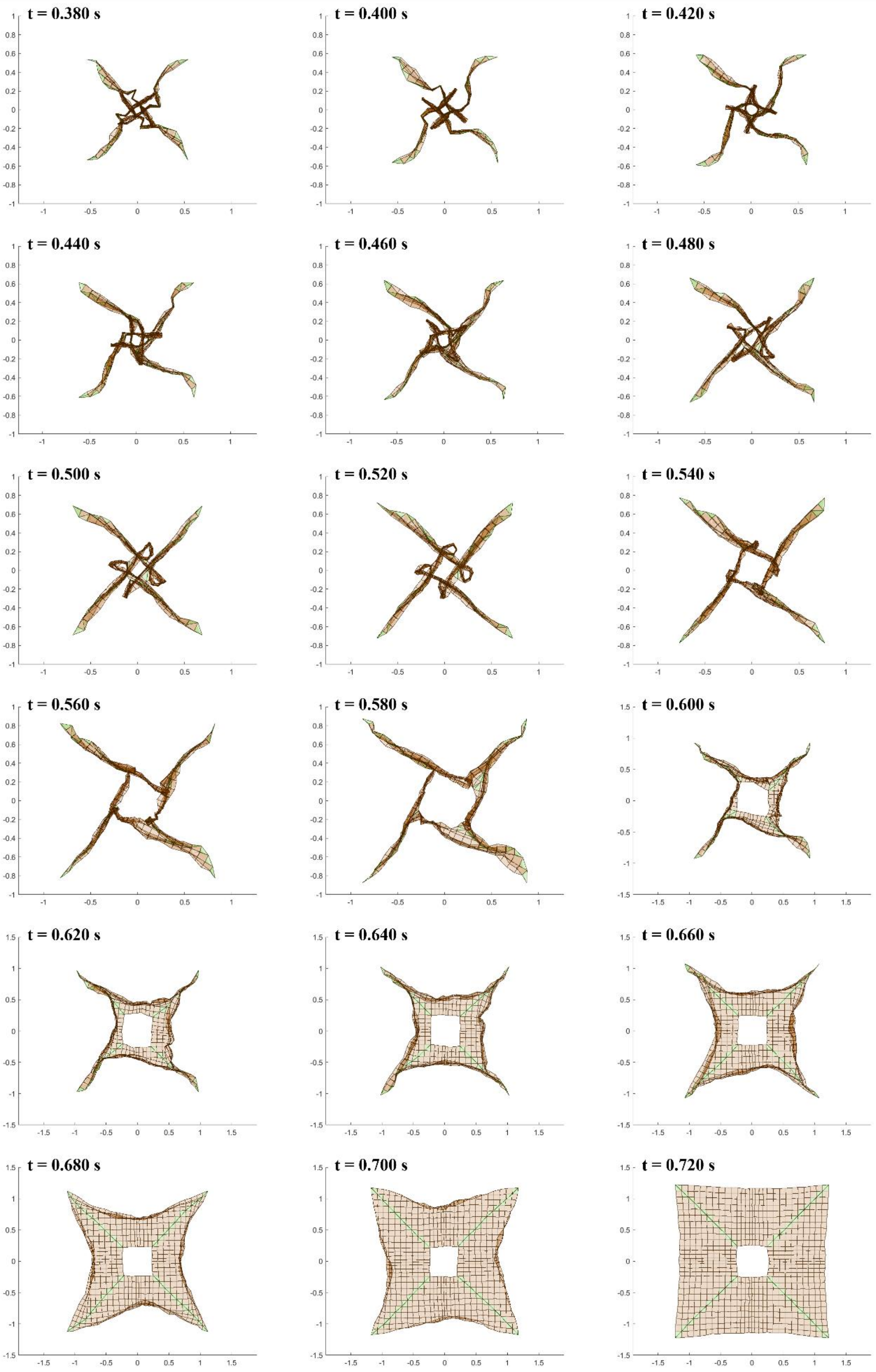

Figure 4.28: Simulation result of sail deployment for SDOM with the central hub model parameters as k = 15 and d = 0 and the compression stiffness ratio $R_{cs} = 10^{-3}$.

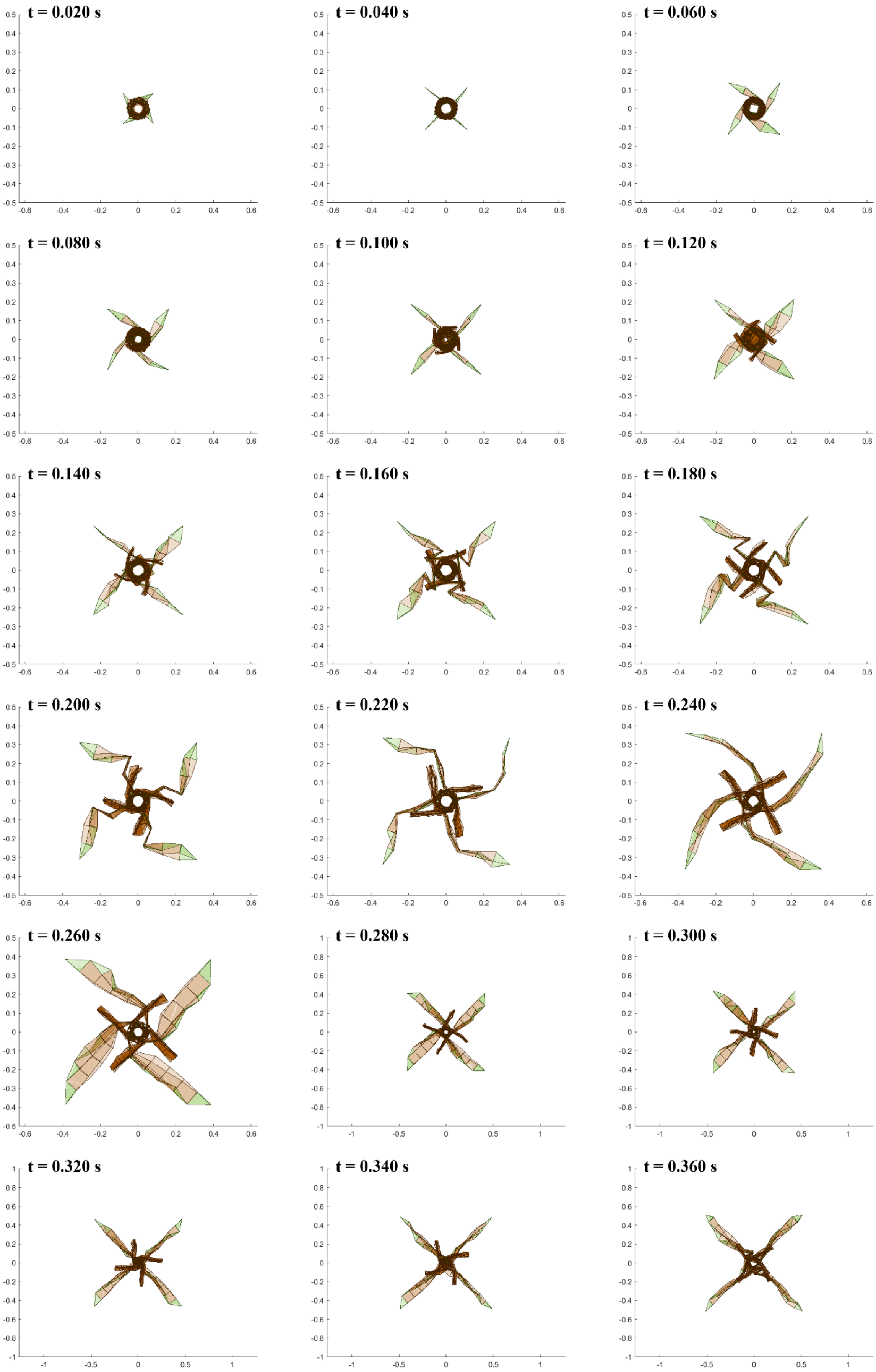
t = 0.020 s
t = 0.040 s
t = 0.060 s
t = 0.080 s
t = 0.100 s
t = 0.120 s
t = 0.140 s
t = 0.160 s
t = 0.180 s
t = 0.200 s
t = 0.220 s
t = 0.240 s
t = 0.260 s
t = 0.280 s
t = 0.300 s
t = 0.320 s
t = 0.340 s
t = 0.360 s
0.5
0.4
0.3
0.2
0.1
0
-0.1
-0.2
-0.3
-0.4
-0.5
-0.6
-0.4
-0.2
0
0.2
0.4
0.6
1
0.8
0.6
0.4
0.2
0
-0.2
-0.4
-0.6
-0.8
-1
-1
-0.5
0
0.5
1

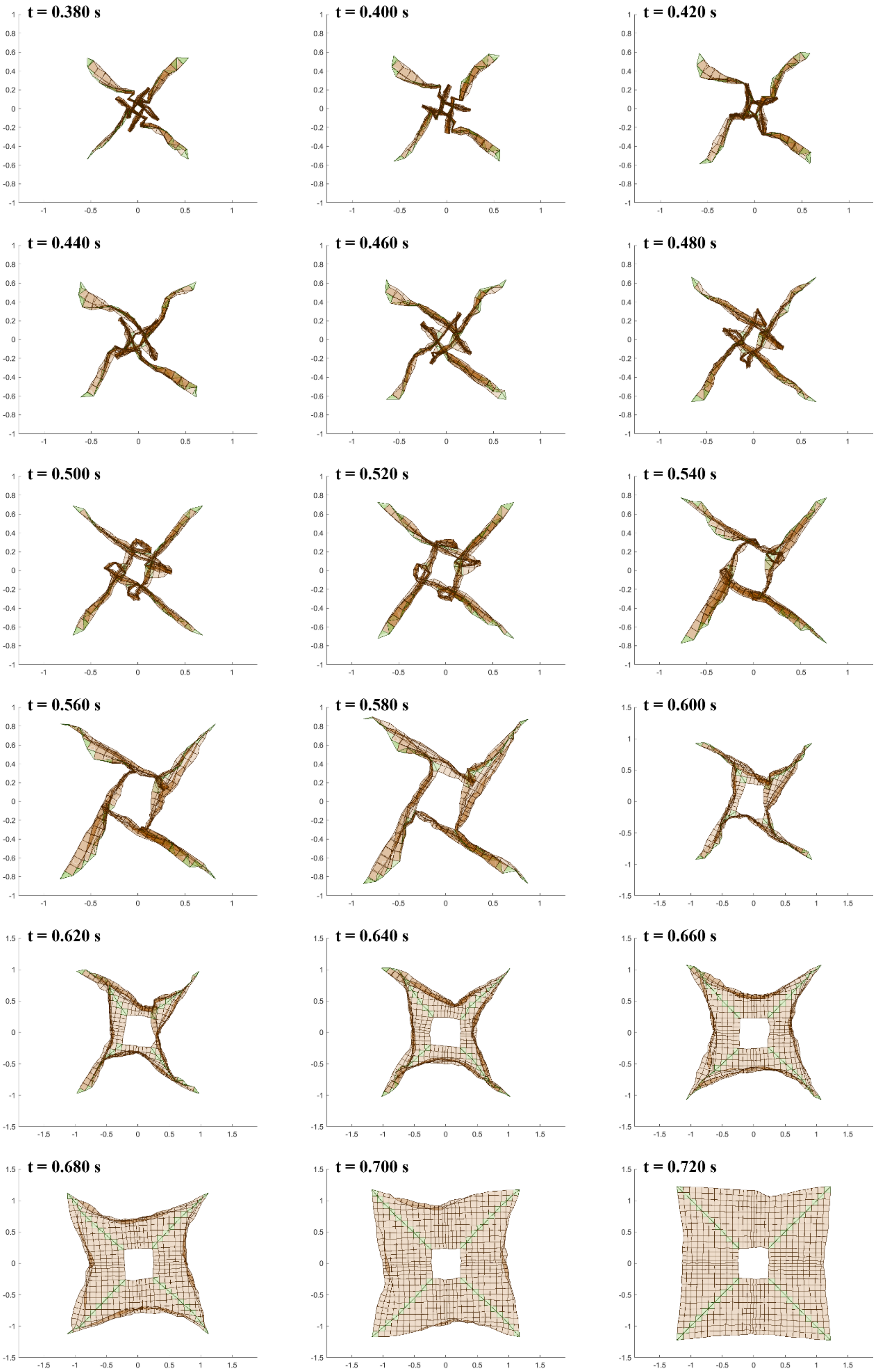

Figure 4.29: Simulation result of sail deployment for SDOM with the central hub model parameters as k = 20 and d = 0 and the compression stiffness ratio $R_{cs} = 10^{-3}$.

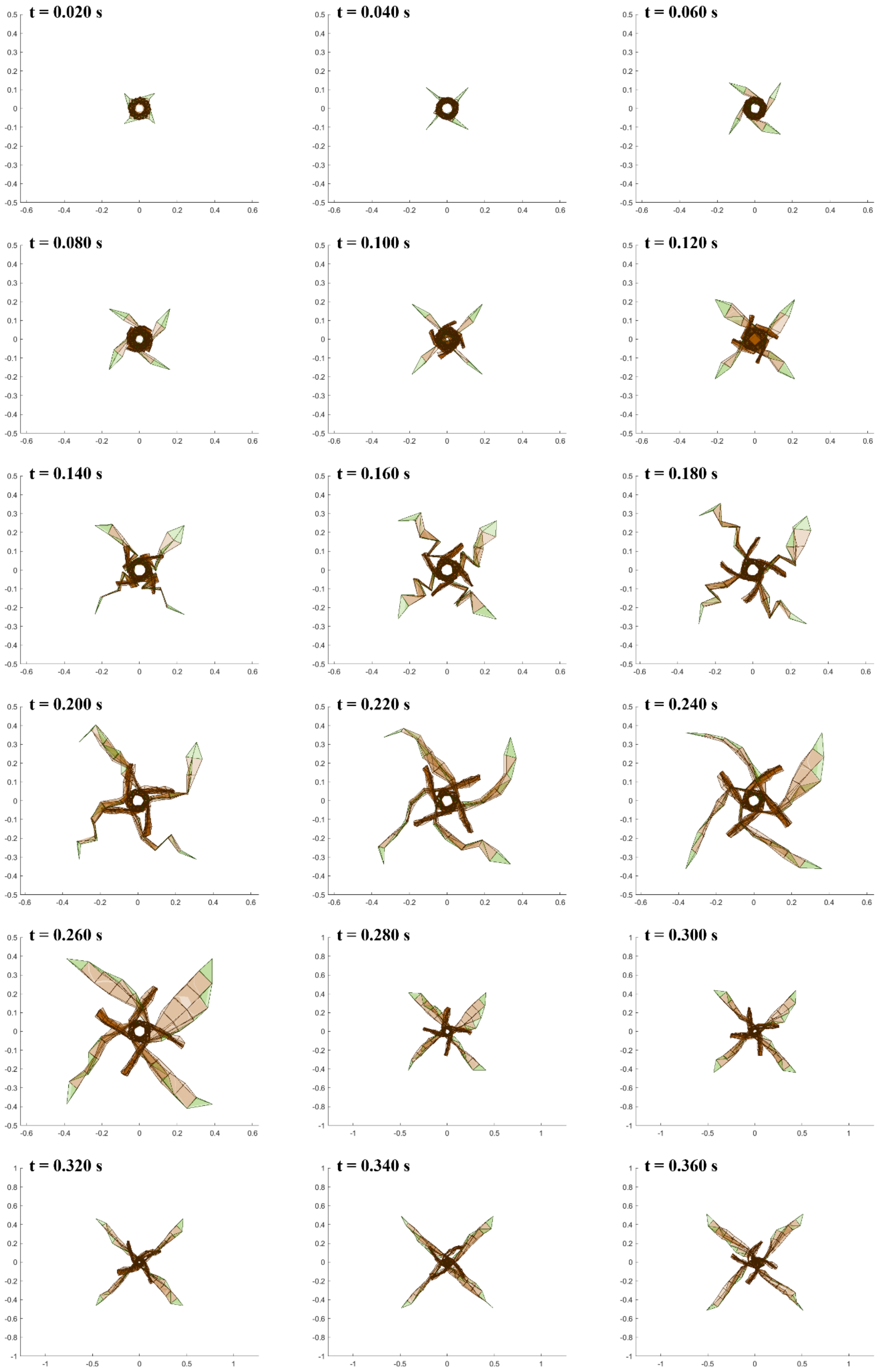
t = 0.020 s
t = 0.040 s
t = 0.060 s
t = 0.080 s
t = 0.100 s
t = 0.120 s
t = 0.140 s
t = 0.160 s
t = 0.180 s
t = 0.200 s
t = 0.220 s
t = 0.240 s
t = 0.260 s
t = 0.280 s
t = 0.300 s
t = 0.320 s
t = 0.340 s
t = 0.360 s
0.5
0.4
0.3
0.2
0.1
0
-0.1
-0.2
-0.3
-0.4
-0.5
-0.6
0.6
1
0.8
0.6
-0.6
-0.8
-1
-0.5
0.5

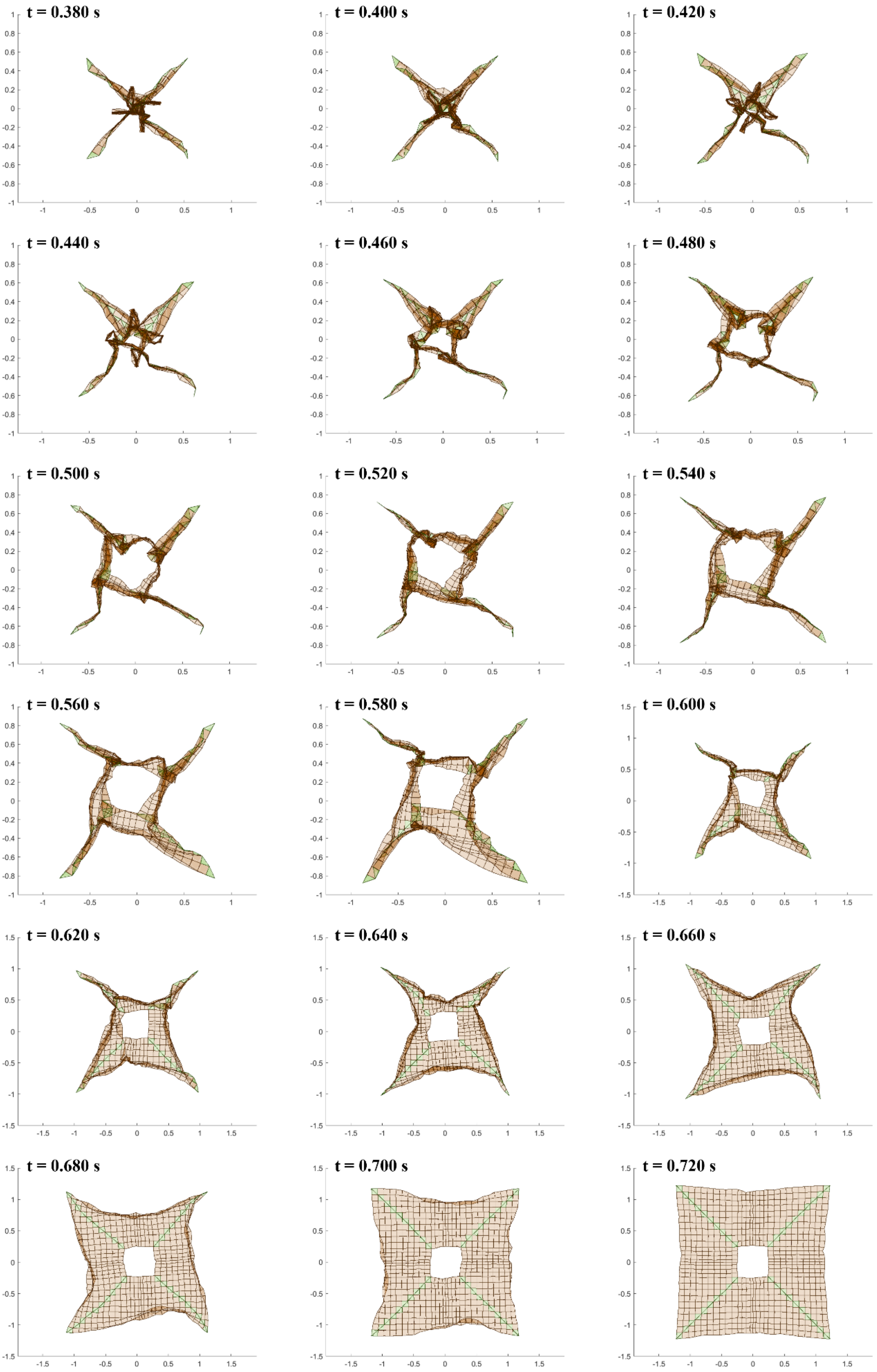

Figure 4.30: Simulation result of sail deployment for SDOM with the central hub model parameters as k = 25 and d = 0 and the compression stiffness ratio $R_{cs} = 10^{-3}$.

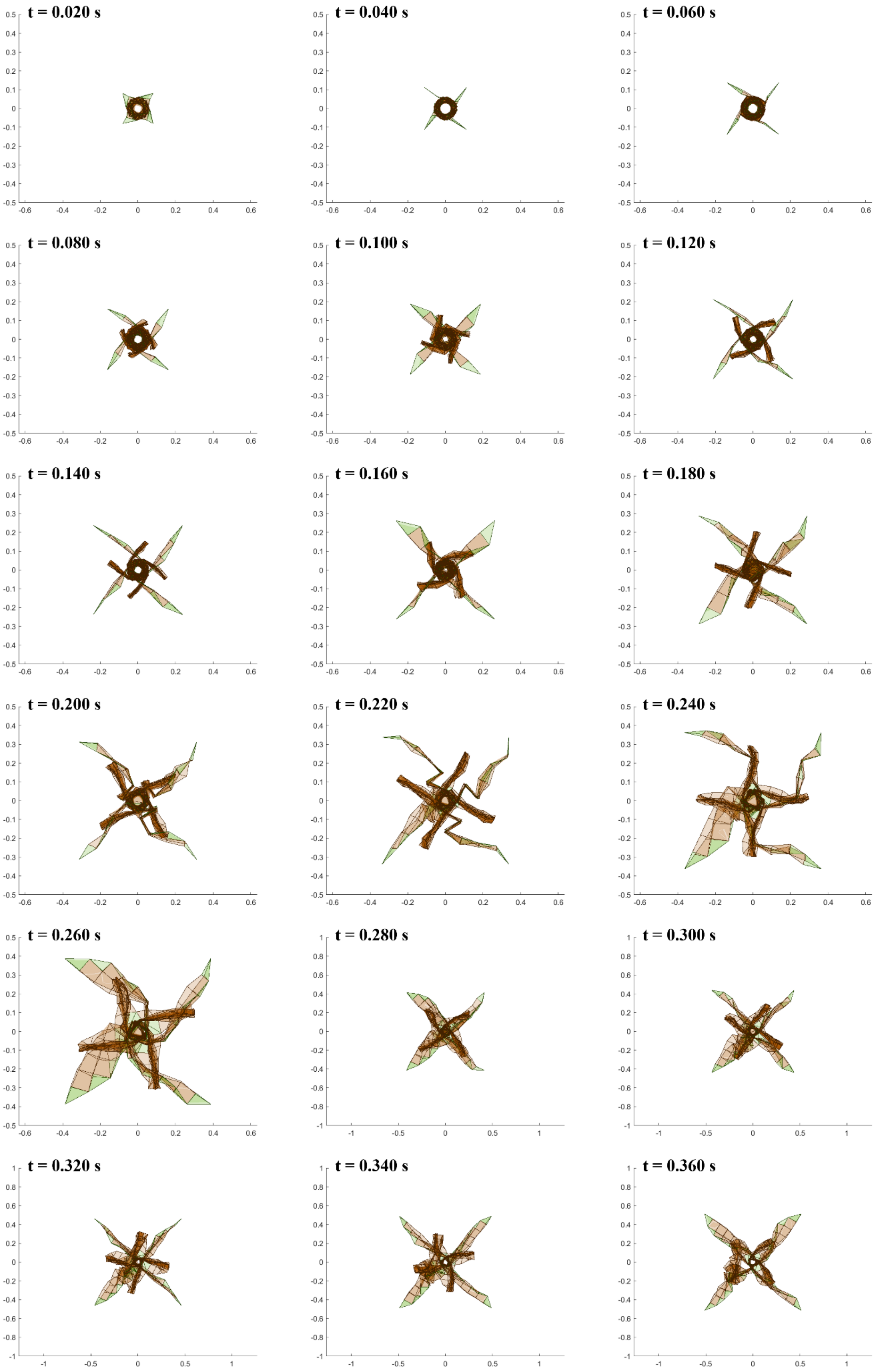
t = 0.020 s
t = 0.040 s
t = 0.060 s
t = 0.080 s
t = 0.100 s
t = 0.120 s
t = 0.140 s
t = 0.160 s
t = 0.180 s
t = 0.200 s
t = 0.220 s
t = 0.240 s
t = 0.260 s
t = 0.280 s
t = 0.300 s
t = 0.320 s
t = 0.340 s
t = 0.360 s

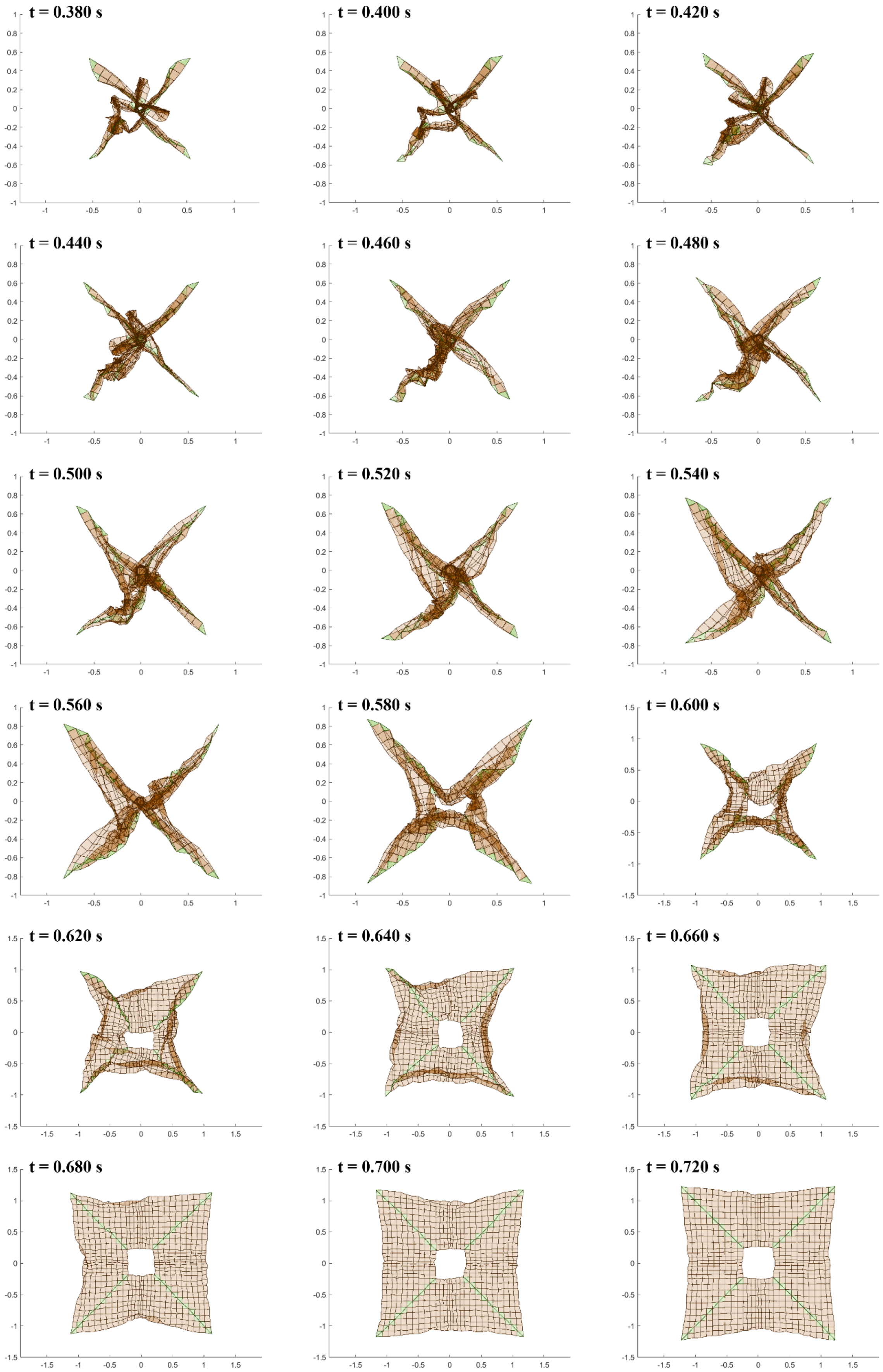

Figure 4.31: Simulation result of sail deployment for SDOM with the central hub model parameters as k = 50 and d = 0 and the compression stiffness ratio $R_{cs} = 10^{-3}$.

4.8.1. Strain Energy per Unit Convex Tape Length

The parameter that affects the extension times most critically is the strain energy stored in the coiled convex tapes. The strain energy calculated per unit convex tape length, is directly proportional to the extension force of the convex tapes. Although the friction between the guide roller and the convex tape is considered in the model, the friction that occurs between the coiled layers of the convex tape due to the outward radial force exerted by the convex tapes on the outer wall of the hub element that contains them is not considered.

When stored, coiled convex tapes radially expand to stay coiled at the largest radius possible within their container. With increased coiling radius, the strain energy stored is decreased and a lower energy state is achieved. This behavior will result in decreased extension force. In order to avoid this, the container for convex tapes in systems using convex tapes are designed to closely fit the required coiled size of the convex tape. This is also the case in DOM2500. However, the coiled tapes in storage configuration will still exert a radial expanding force to the out wall of the container. This force is larger than the extension force and existent at every layer of the convex tape as opposed to the extension force that occurs at the ploy region.

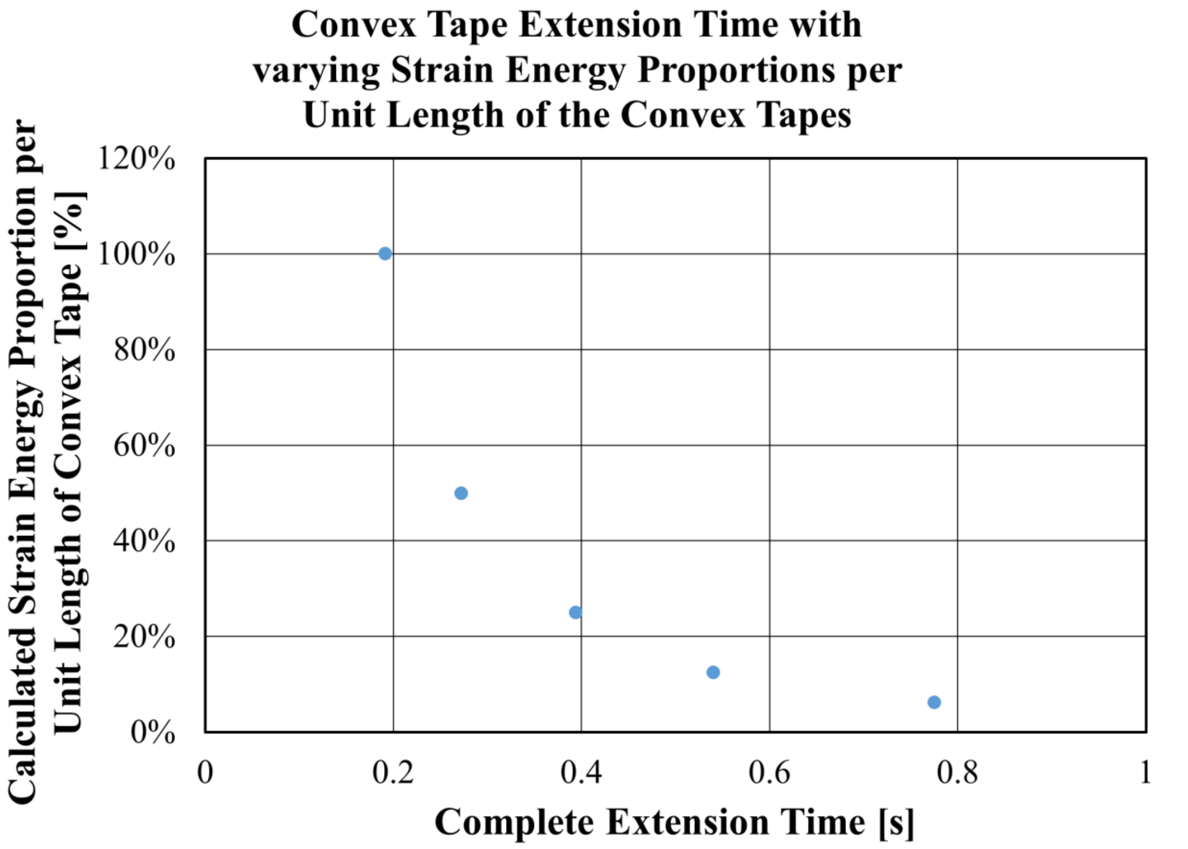

Figure 4.32: Convex tape extension completion time with varying strain energy proportions per unit length of the convex tapes.

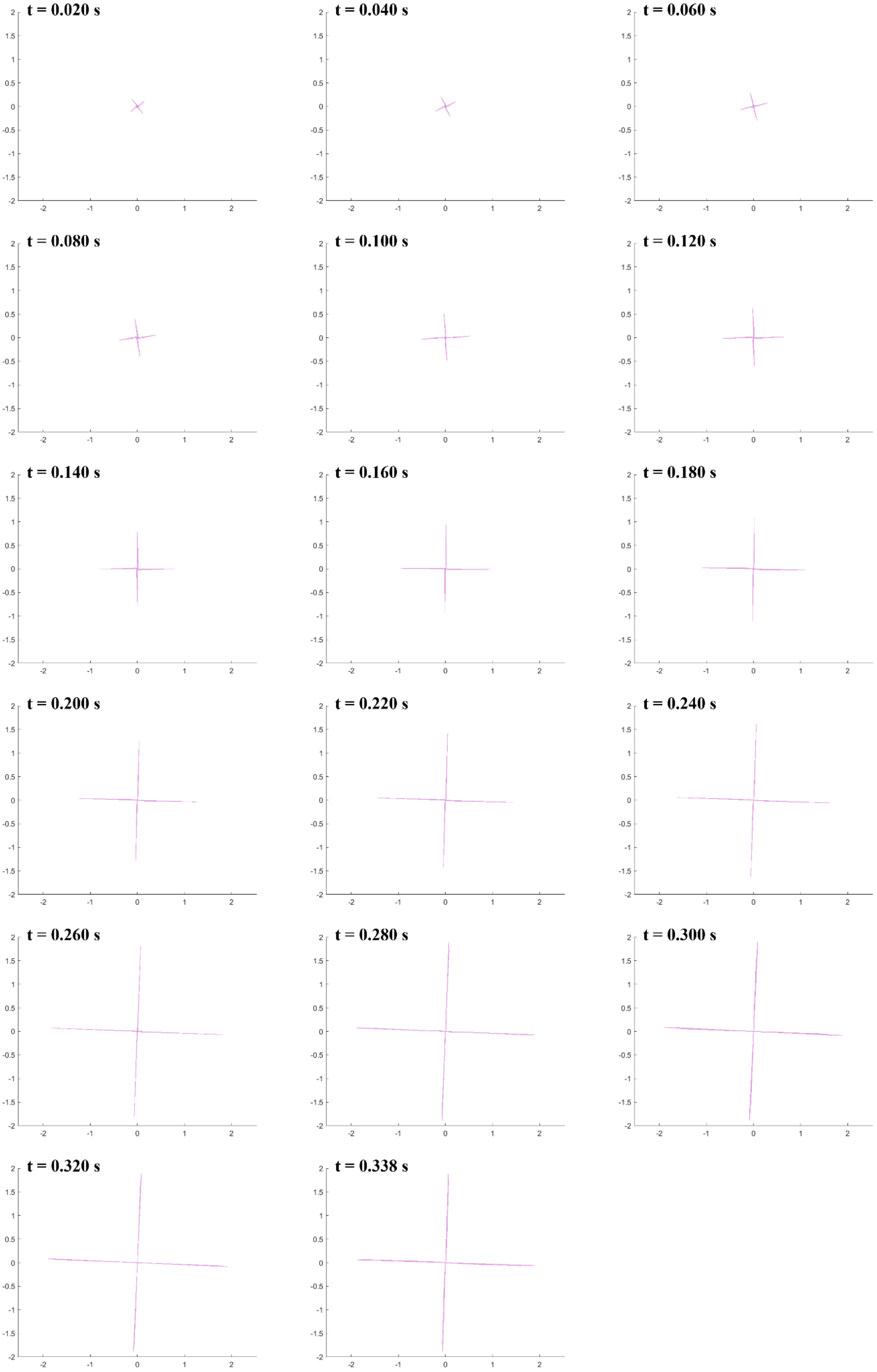

Figure 4.33: Simulation result of convex tape extension with strain energy Π_{total} decreased to 1/2 of the calculated value.

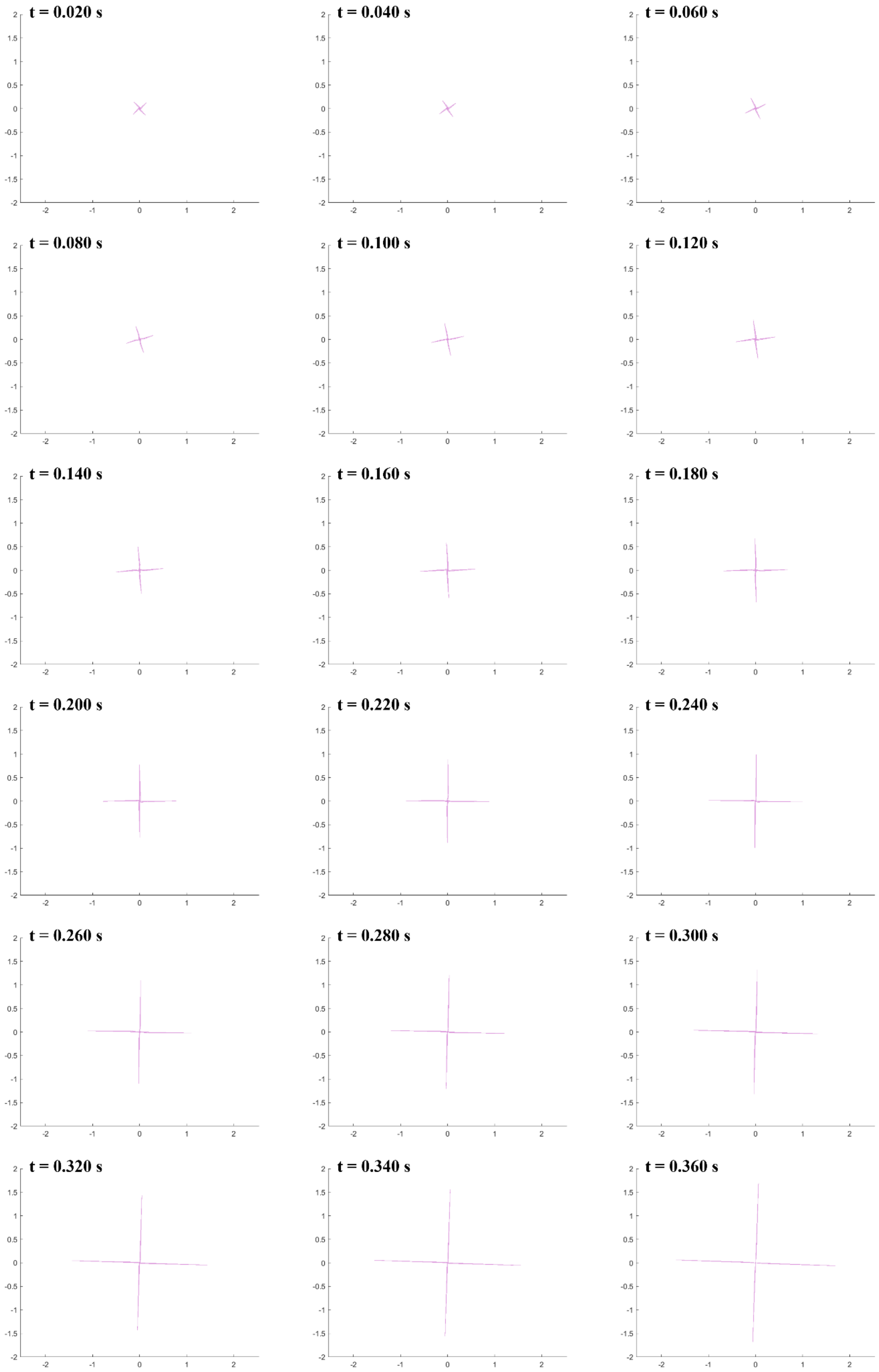
t = 0.020 s
t = 0.040 s
t = 0.060 s
t = 0.080 s
t = 0.100 s
t = 0.120 s
t = 0.140 s
t = 0.160 s
t = 0.180 s
t = 0.200 s
t = 0.220 s
t = 0.240 s
t = 0.260 s
t = 0.280 s
t = 0.300 s
t = 0.320 s
t = 0.340 s
t = 0.360 s
2
1.5
1
0.5
0
-0.5
-1
-1.5
-2
-2
-1
0
1
2

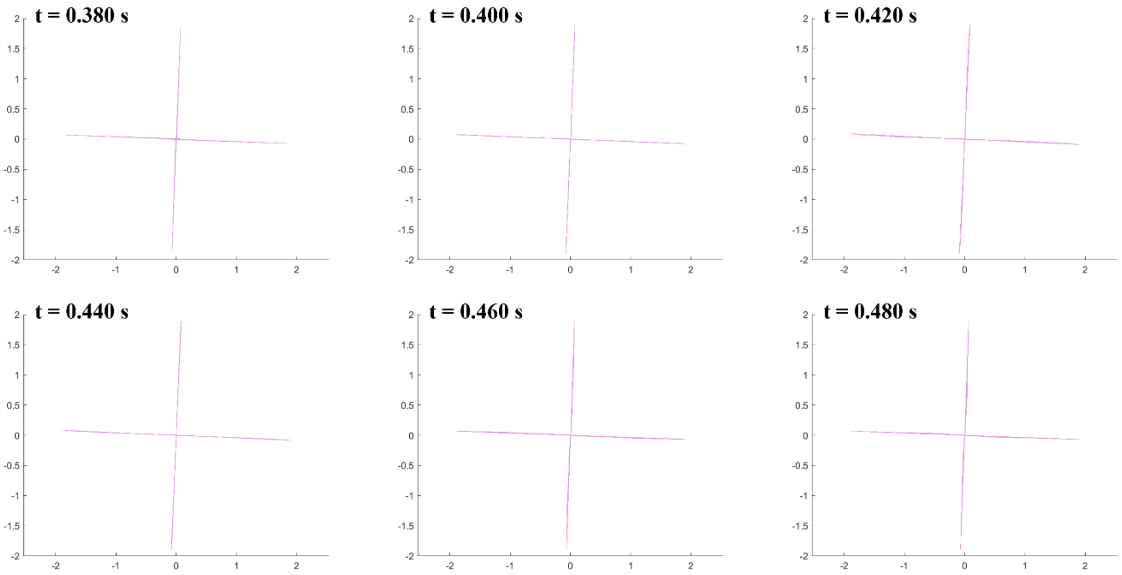

Figure 4.34: Simulation result of convex tape extension with strain energy Π_{total} decreased to 1/4 of the calculated value.

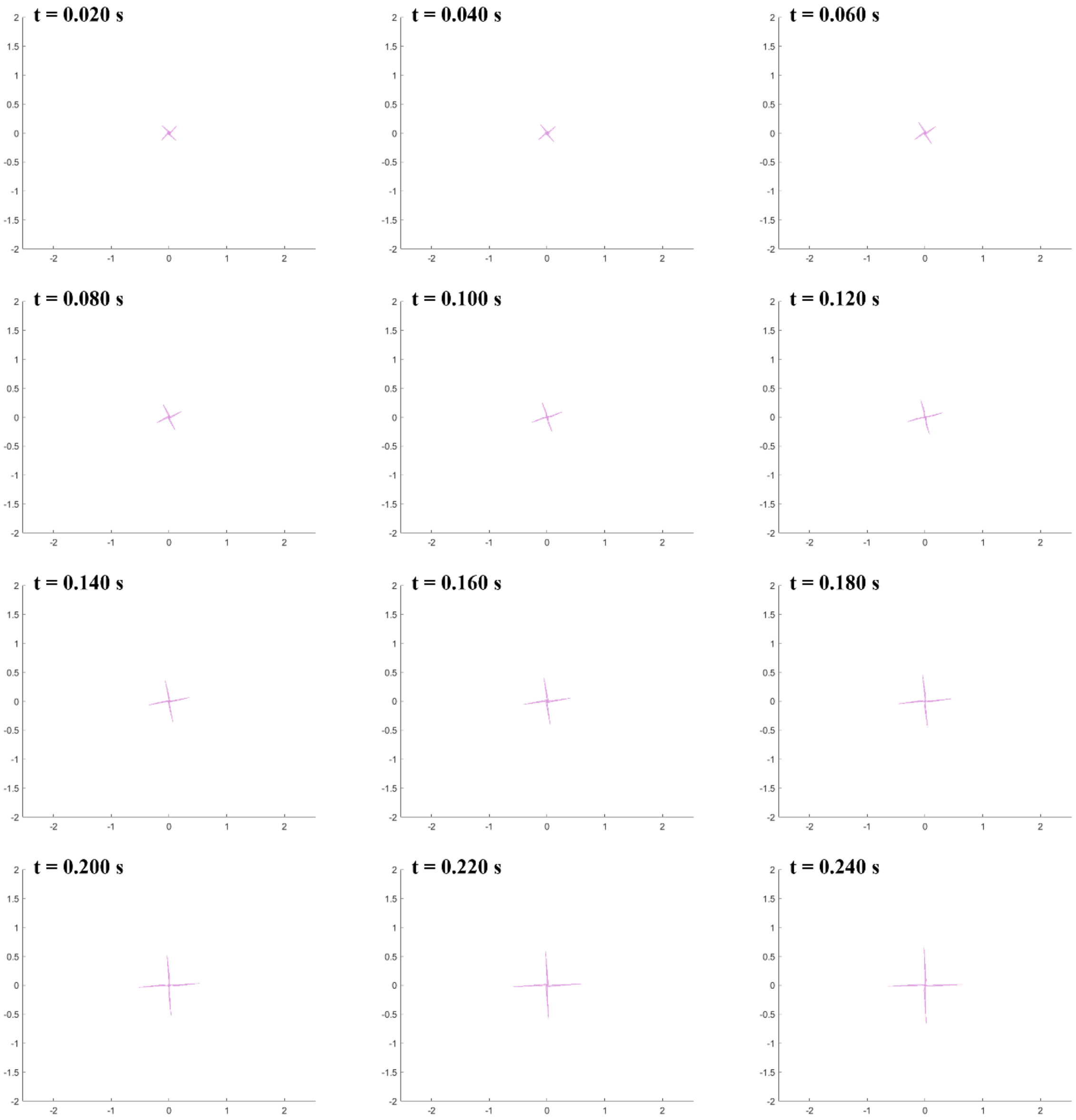

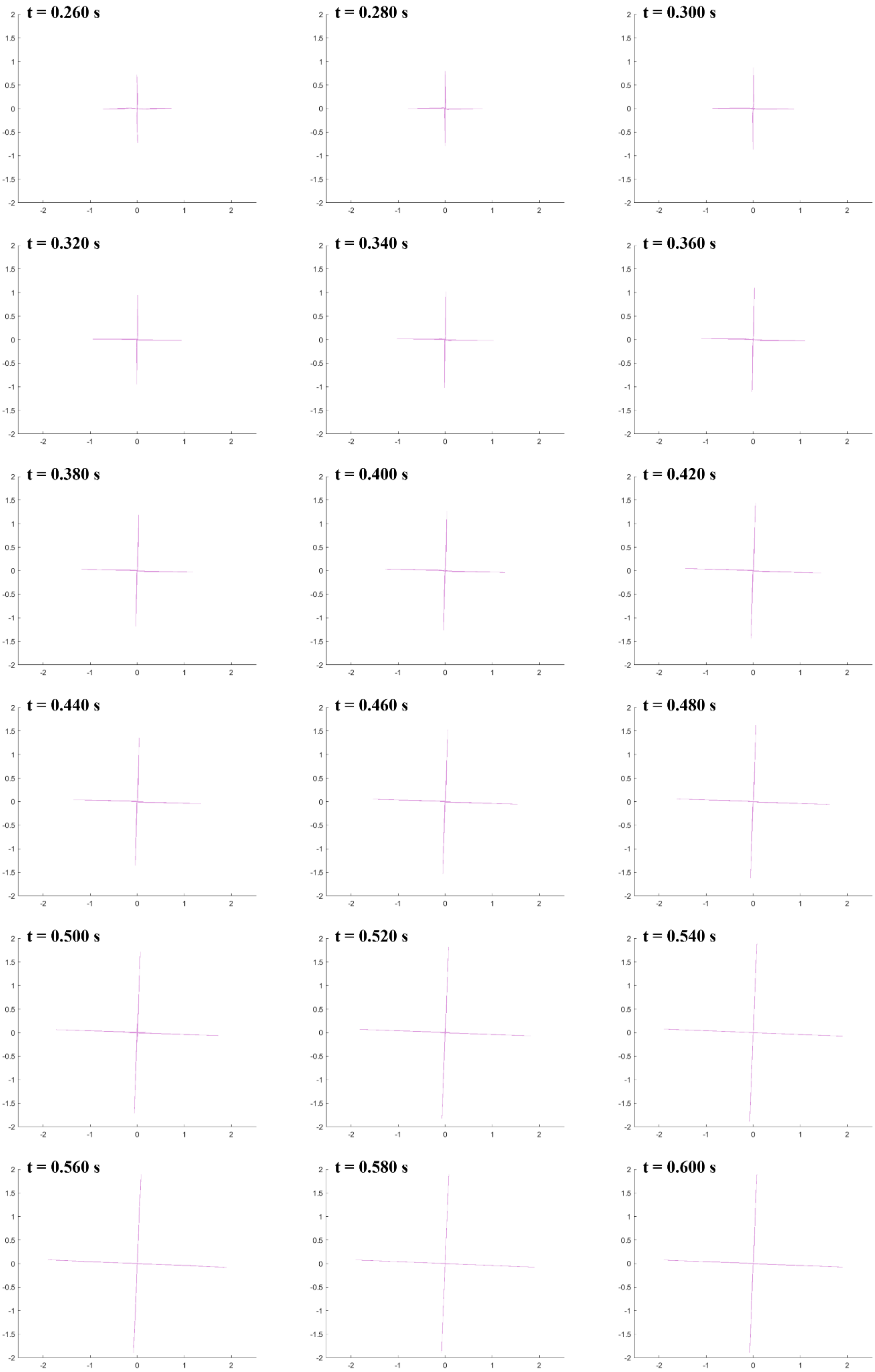

Figure 4.35: Simulation result of convex tape extension with strain energy Π_{total} decreased to 1/8 of the calculated value.

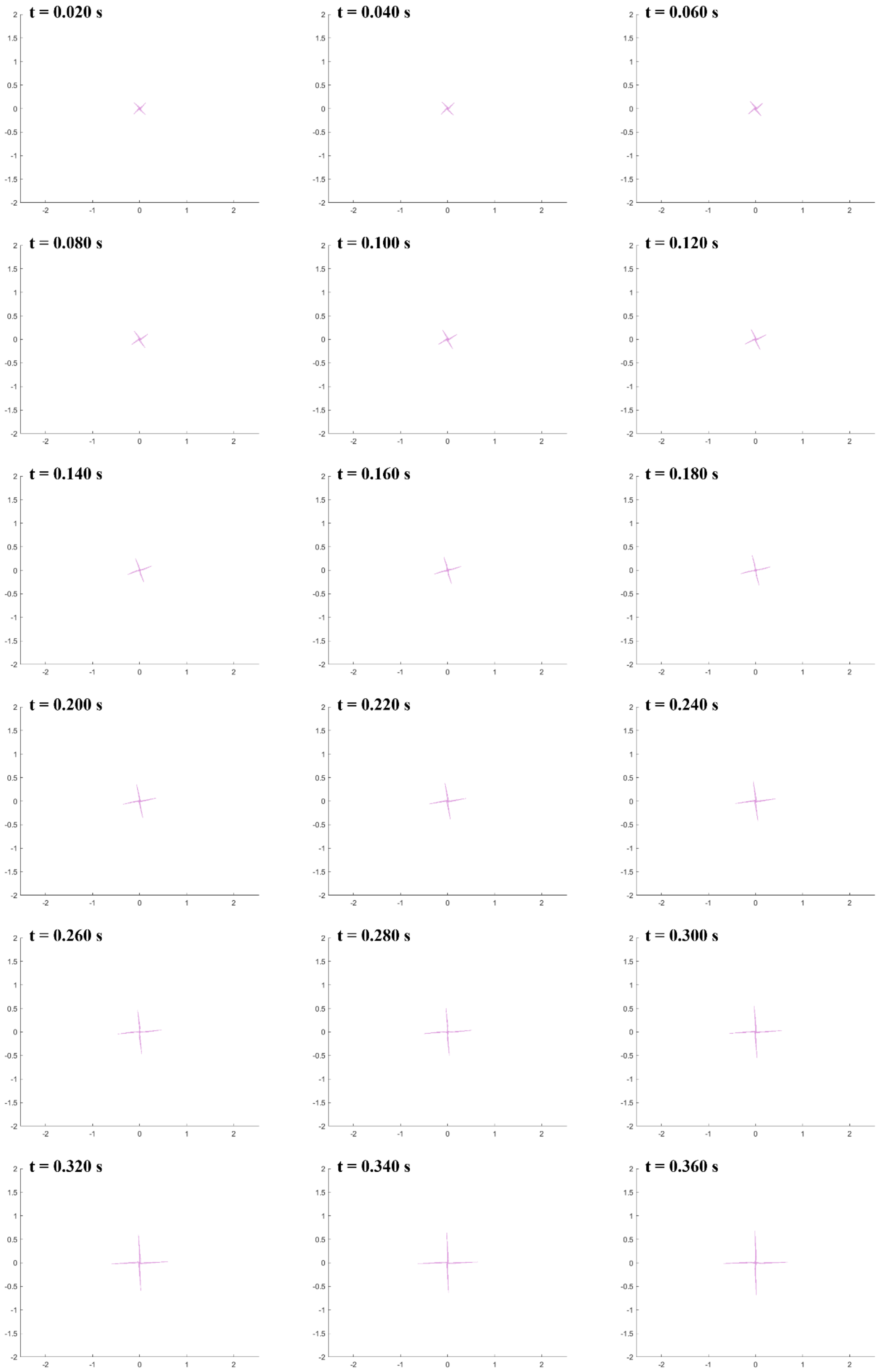
t = 0.020 s
t = 0.040 s
t = 0.060 s
t = 0.080 s
t = 0.100 s
t = 0.120 s
t = 0.140 s
t = 0.160 s
t = 0.180 s
t = 0.200 s
t = 0.220 s
t = 0.240 s
t = 0.260 s
t = 0.280 s
t = 0.300 s
t = 0.320 s
t = 0.340 s
t = 0.360 s
2
1.5
1
0.5
0
-0.5
-1
-1.5
-2
-2
-1
0
1
2

t = 0.380 s

t = 0.400 s

t = 0.420 s

t = 0.440 s

t = 0.460 s

t = 0.480 s

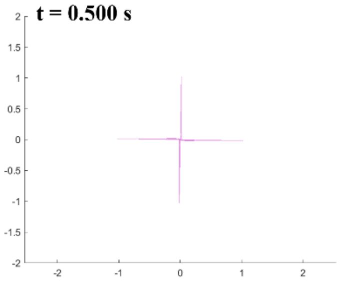

t = 0.500 s

t = 0.520 s

t = 0.540 s

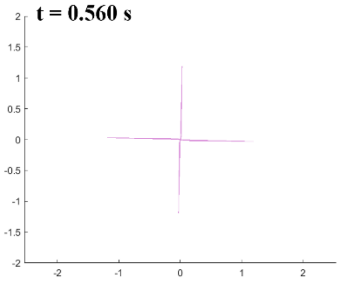

t = 0.560 s

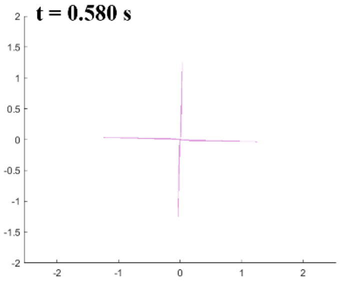

t = 0.580 s

t = 0.600 s

t = 0.620 s

t = 0.640 s

t = 0.660 s

t = 0.680 s

t = 0.700 s

t = 0.720 s

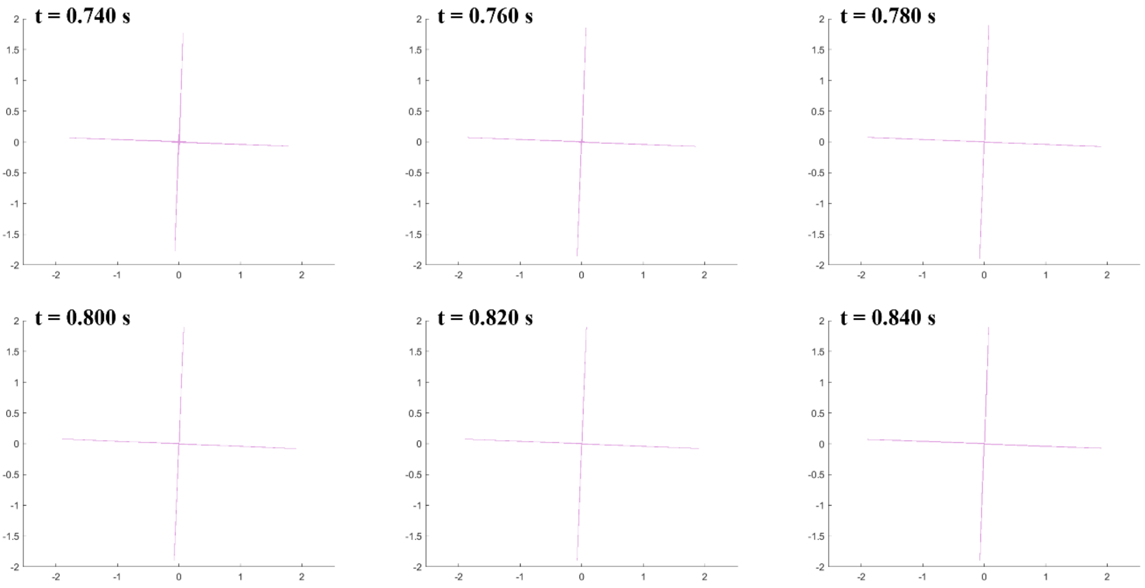

Figure 4.36: Simulation result of convex tape extension with strain energy Π_{total} decreased to 1/16 of the calculated value.

Due to the accumulated friction between the layers of the convex tapes, and between the outer wall of the container and the outmost layer of the convex tape, the resultant force that pulls the corners of the membrane is less than the calculated self-extending force of the convex tapes.

Since the calculated strain energy per unit length of the convex tapes directly correlates to the extension force that occurs, if this strain energy is decreased, the decrease of the resultant extension force due to friction can be simulated. In order to sample the extension times with the strain energy, simulations were run with varying strain energy Π_{total} proportions. Figure 4.32 show the extension completion time with different strain energy proportions and Figs. 4.33 to 4.36 show the variations [1/2, 1/4, 1/8, 1/16]. It is important to note that the reference value of 0.7 s is the fusion model and the addition of the membrane also increases the extension time of the convex tapes by a factor of 1.75 in the initial simulation results presented in chapter 2. Therefore, the target time for extension with only using the convex tapes is ~0.4 s.

In Figs. 4.33 to 4.36 with strain energy varied in proportions of calculated energy as [1/2, 1/4, 1/8, 1/16], complete extension is achieved at t = 0.28 s, t = 0.4 s, t = 0.54 and t = 0.76 s respectively. The most suitable result to be used on to the fusion model appears at 1/4th of the calculated strain energy as seen in Fig. 34. From this, it is concluded that in the case of DOM2500 the friction that occurs between the convex tape layers and the container outer wall is about 3/4th of the extension force that occurs. As mentioned before, in many cases, this friction can be larger than the extension force and not let the convex tapes extend at all. Usually, rollers are placed at the outer wall of the container to minimize this friction. This kind of design was adopted for DOM2500, and also for the mast extension of ALE-1 as discussed in chapter 3.

4.9. Results of the Fusion Model with updated Parameters

As a final step, the fusion model of the updated membrane model and the updated convex tape model is considered. Figure 4.37 shows the results of this simulation. The membrane shape along the deployment is consistent with the in-orbit results presented in chapter 3, the deployment time adjusted through the convex tape strain energy per unit length of the convex tape is also consistent with the in-orbit results. The formation of the inner hole and the star shape before unfolding of the layers is observed consistent to the in-orbit results. The timestamp of t = 0.52 s where this occurs is also consistent with the in-orbit results where it happens at t = 2.0 s which is 0.5 s after the initiation of deployment as can be seen from Fig. 3.45. Following the unwrapping behavior of the whole membrane into the star shape, the fold layers are observed to unfold starting from the inner most layers as is the case for the in-orbit results. Complete deployment is achieved between t = 0.72 s and t = 0.74 s which is also consistent with the in-orbit results presented in Fig 3.45 where complete deployment occurs between t = 2.2 s and t = 2.3 s, which are 0.7 s and 0.8 s after the initiation respectively. Additionally the rotational movement of the whole convex tape frame that occur in the in-orbit results can also be observed in the simulation of the fusion model. This rotation is in the counter-clockwise direction for the in-orbit results, and clockwise direction for the simulation. This is due to observer position being at the opposite sides of the membrane and the convex tape frame.

4.4. Discussion of the Parameters

Up to this point a total of 4 important parameters are adjusted to achieve the final results presented in the previous section. These parameters are, the spring constant k and the damping ratio d for the omnidirectional spring model of the hub, the compression stiffness ratio R_{cs} of the stiffness reduction model introduced in section 2.2.9 as ε_1 and ε_2, and the strain energy per unit length of the convex tape Π_{total} introduced in section 2.4.9. These parameters, theirs effects on the deployment of the membrane, along with the corresponding simulation instances to observe these results are summarized in Table 4.1.

The hub model parameters k and d are model specific to this case and are less important if the membrane elements can be modeled to not pass through each other. However, the addition of this constraint increases the computational cost of the model. A preliminary trial showed at best case, a single simulation would take about 2 months to solve. Currently, each simulation costs about 25 hours of computational time. Therefore, the model that was implemented is only between the hub and the membrane elements, instead of between the membrane and the

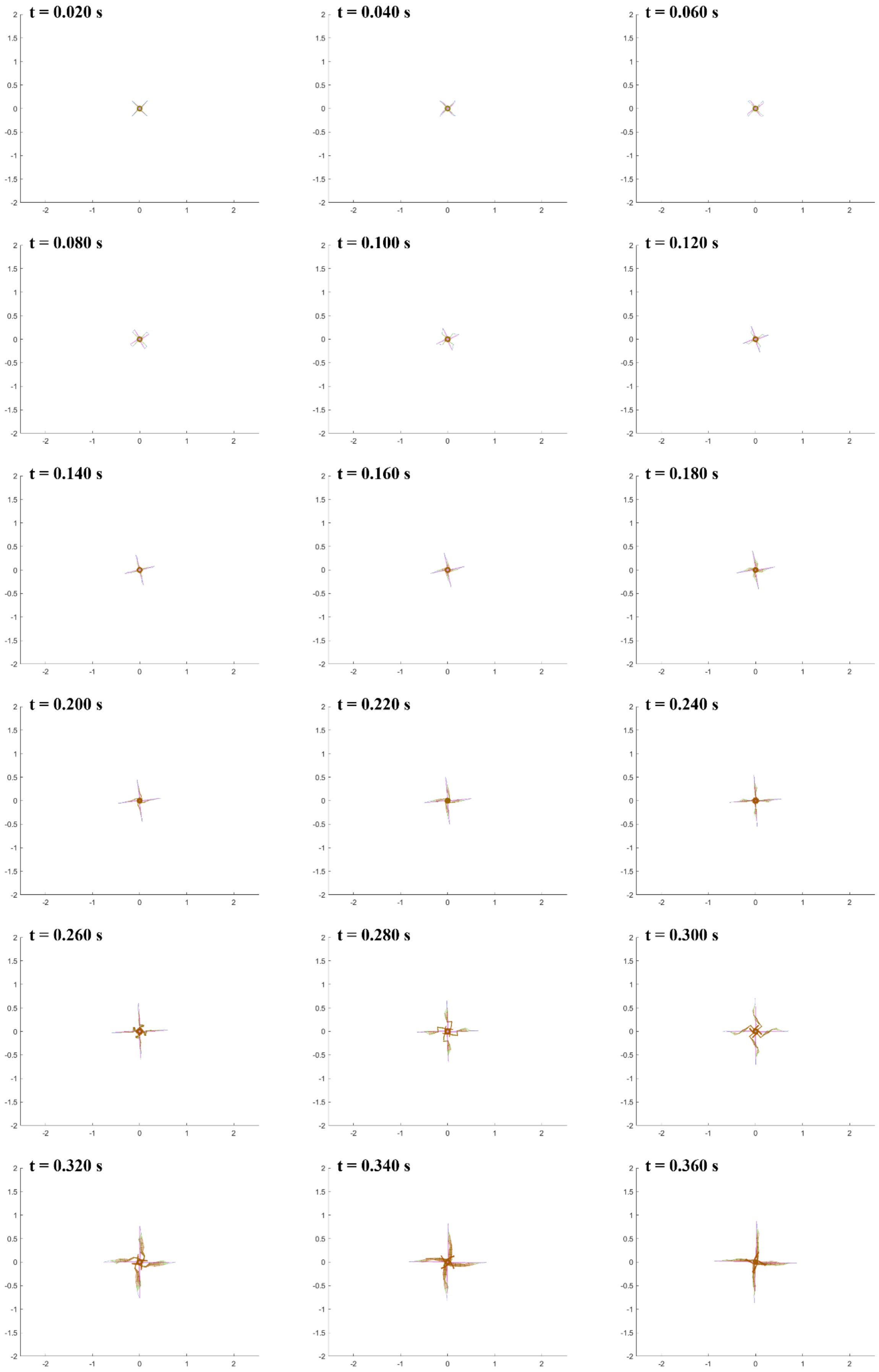
t = 0.020 s
t = 0.040 s
t = 0.060 s
t = 0.080 s
t = 0.100 s
t = 0.120 s
t = 0.140 s
t = 0.160 s
t = 0.180 s
t = 0.200 s
t = 0.220 s
t = 0.240 s
t = 0.260 s
t = 0.280 s
t = 0.300 s
t = 0.320 s
t = 0.340 s
t = 0.360 s
2
1.5
1
0.5
0
-0.5
-1
-1.5
-2
-2
-1
0
1
2

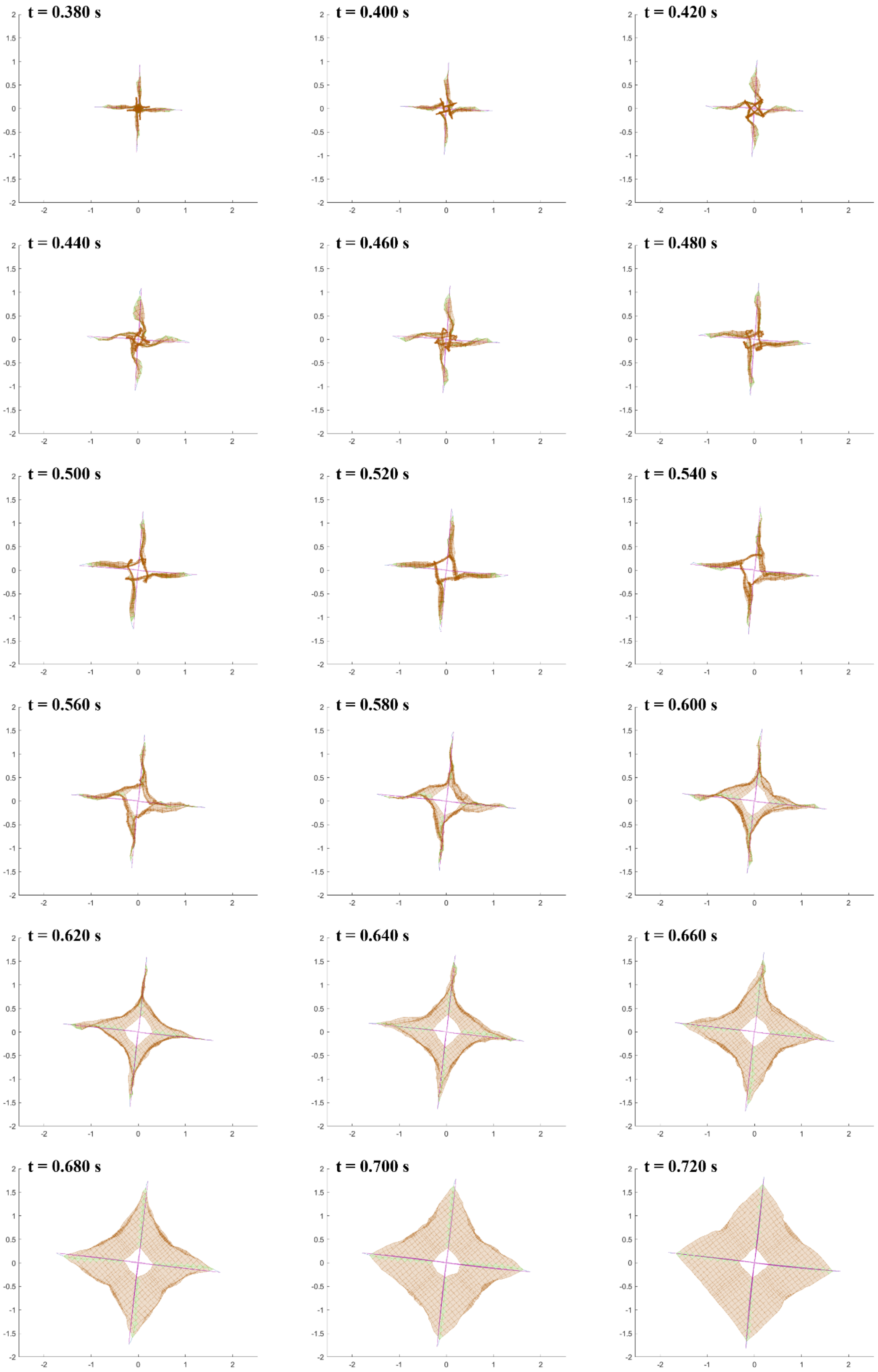
t = 0.380 s
t = 0.400 s
t = 0.420 s
t = 0.440 s
t = 0.460 s
t = 0.480 s
t = 0.500 s
t = 0.520 s
t = 0.540 s
t = 0.560 s
t = 0.580 s
t = 0.600 s
t = 0.620 s
t = 0.640 s
t = 0.660 s
t = 0.680 s
t = 0.700 s
t = 0.720 s
2
1.5
1
0.5
0
-0.5
-1
-1.5
-2
-2
-1
0
1
2

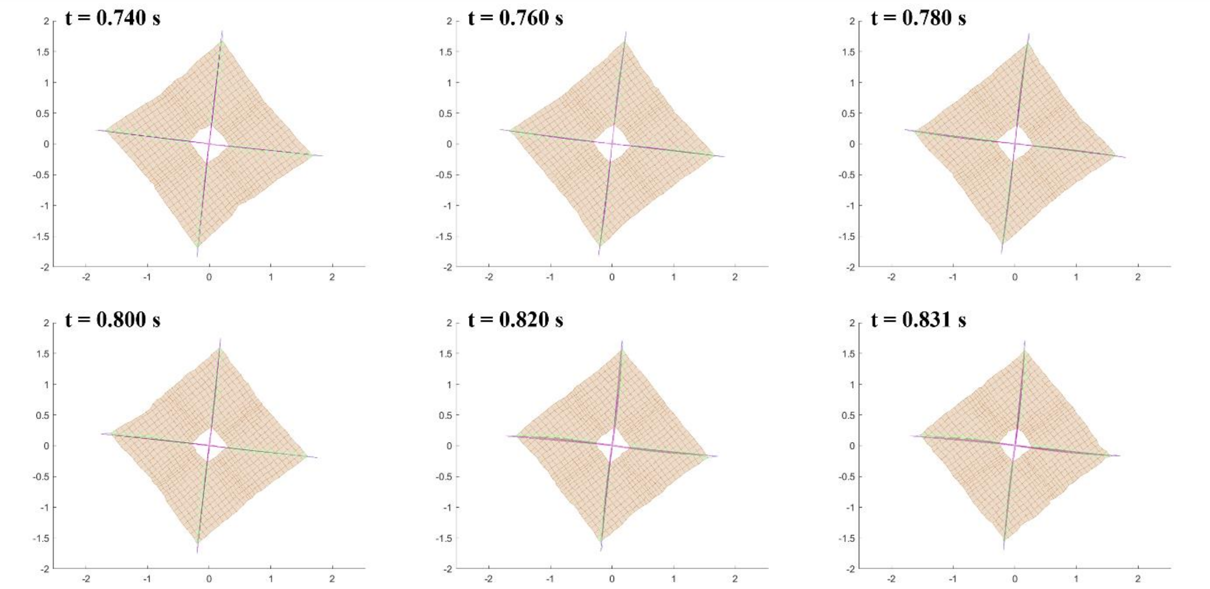

Figure 4.37: Deployment results for the fusion model of the parameter-tuned membrane model and the convex tape model.

membrane elements. The omnidirectional spring model at the hub, pushes the membrane elements that try to cross over the hub outwards. The linear pulling from the corners and the radial outward pushing from the hub spring induces a rotational movement to the membrane. This motion is realistic to the real membrane motion, where it is pulled from the corners and is rotated around the hub in order to continue unwrapping. Depending on the value of the spring constant, this rotation rate is increased or decreased. Normally, this would result in twisting stress to the membrane, but the membrane element are free to pass through each other, therefore this is not the case. It is important to adjust the speed of this rotation to acquire the star shaped folded membrane state before unfolding of the layers are initiated with the increased tension.

The compression stiffness ratio has effects on the unfolding of the membrane layers. When the compression modulus of the membrane is higher, the membrane elements are less likely to buckle under compressive stress and more likely to stay together in the folded state. The buckling between two consecutive fold lines is inducing premature unfolding of the membrane. If the compressive modulus is too high, some layers are never unfolded to the being too stiff. This parameter is designed to represent the small compressive stiffness present in the membrane as a fraction of its tensile modulus as discussed in Chapter 2. However, the magnitude of this smallness is iteratively decided with the comparison of the experimental results to the simulation results. With a low value, the membrane elements easily buckle and move towards outward to result in premature unfolding of the membrane folds before the membrane unwraps into the star shape state.

Table 4.1: Summary of the adjusted parameters.

Parameter	Corresponding effects on the membrane deployment	Corresponding Figures	Considered Values	Final Value
Spring constant k	Rotational unwrapping rate of the folded membrane around the hub.	First iteration: 4.10, 4.11 Second iteration: 4.30, 4.31	[10000, 1000, 50, 25, 20, 15, 10, 5, 0]	20
Damping ratio d	Insignificant results compared to its computational cost.	4.13	[0, 10^{-7}, 10^{-6}, 10^{-5}, 10^{-4}]	0
Compression stiffness ratio R_{cs}	The compressive modulus of the membrane elements to local buckling, consequently the ease of unfolding of layers of membrane.	4.18, 4.19	[10^{-8}, 10^{-7}, 10^{-5}, 10^{-4}, 10^{-3}, 10^{-2}]	10^{-3}
Strain energy per unit length of convex tape Π_{total}	The self-extending force of the convex tapes, and consequently the deployment time of the membrane.	4.32	[1, 1/2, 1/4, 1/8, 1/16]	1/4

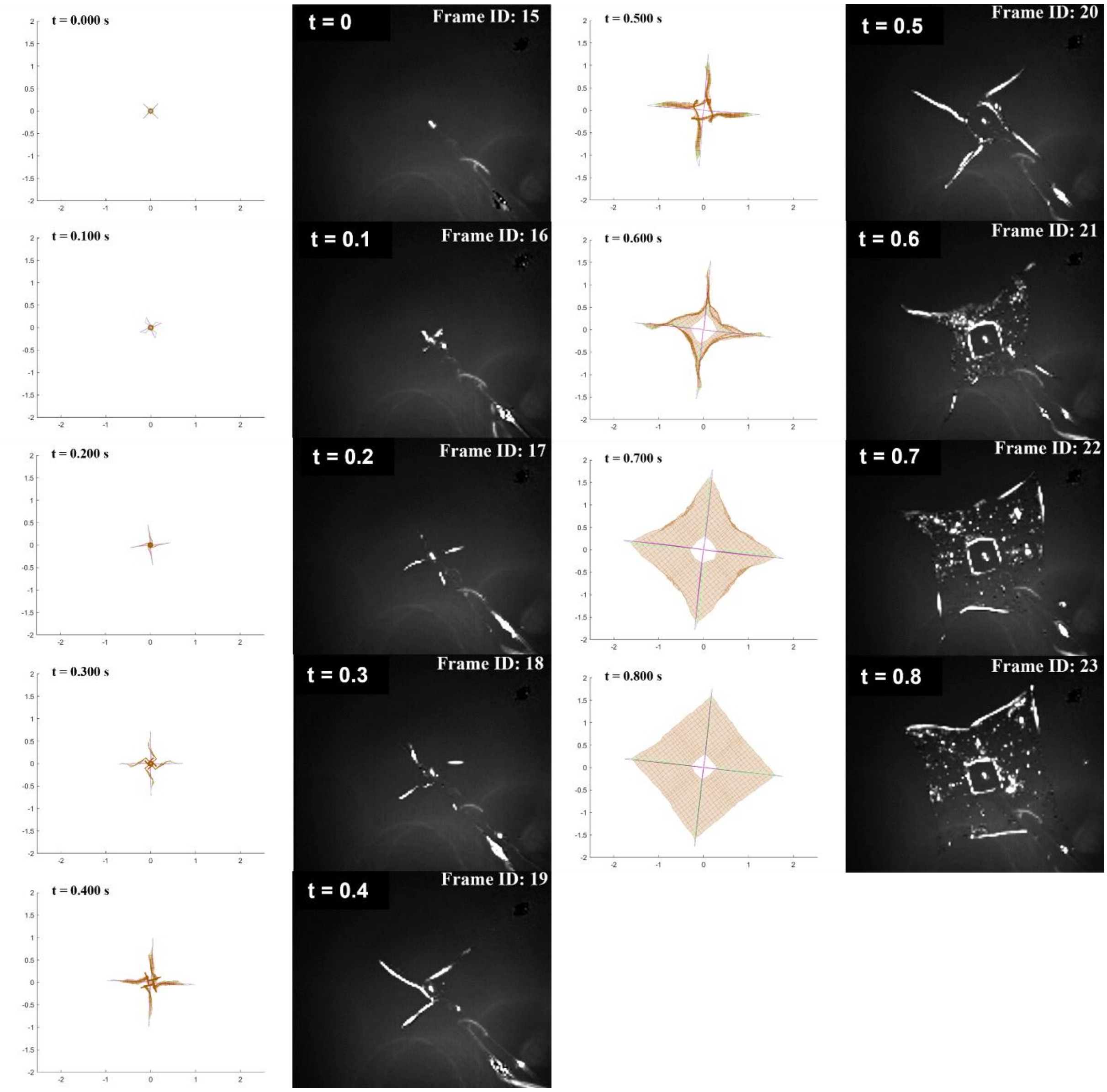

Figure 4.38: Side-by-side comparison of fusion simulation results and in-orbit results.

Finally, the strain energy calculated per unit length of the convex tape is adjusted. By normalizing the strain energy per unit length, the resulting parameter directly correlates to the self-extending force of the convex tapes. In this model, the friction between the convex tape layers, and the friction between the outmost convex tape layer to the hub wall is not represented. These frictions decrease the acting resultant force that is pulling the membrane from its corners. In order to include the effect of this energy loss through friction, the calculated strain energy per unit length was sampled as a fraction of itself. The extension completion time for each case was compared to the real extension completion time in space. As a results, the friction that acts on the convex tapes were concluded to be as high as 3/4th of their self-extending force. Additionally, the fusion simulation results, and the in-orbit deployment results are placed side-by-side for better confirmation of the similarities. Figure 4.38 show this comparison.

4.5. Future Work

The initial step in the future direction of this work is adjustment of the sail fold pattern. Up to this point, the sail is modeled using 10 cm folding width, whereas in reality the sail used in SDOM has 2 cm folding width. Although this was intended to be implemented, due to limitations in the computational load, it was not possible. Further improvements on the calculation algorithms and more cost-efficient assembly of the simulation environment including a hard-coded parallel computation function may enable this. Overcoming computational cost issue will also enable the addition of contact restriction between elements which will help facilitate this environment further.

Furthermore, with the modeled convex tapes, the mast extension of SDOM can be simulated, and the deployment can be initiated at the tip of the boom effectively giving insight to the torsional vibrations at the mast-side.

In conclusion, improvements are needed in convex tape modelling and computational cost efficiency for the future of this simulation environment. Afterwards, large scale hypothetical cases can be effectively simulated to gain insight on the possible outcomes of the systems before mission to improve possible failure points.

4.6. Summary

In chapter 4, various model parameters are investigated to achieve a realistic simulation result that is consistent with the in-orbit deployment result.

For the hub contact restriction model and the rotational movement around the hub, contact coefficient k and damping coefficient d introduced in section 2.5 are varied. As the noticeable difference was insignificant with respect to additional calculation cost it brought, the damping coefficient d is excluded from the simulation altogether and deemed unimportant for the scope of this analysis. The contact coefficient k is varied and the amount of rotation for the pseudo corners of the membrane are measured. The rotational value for the DOM2500 at the wrapping of the membrane around its inner hub is 1.25 revolutions by design. The value of k to most closely represent this was achieved at k = 20.

The compressive stiffness ratio R_{cs} introduced in section 2.2.9 was varied to avoid the premature unfolding of the membrane. The inclusion of this parameter not only increases numerical model accuracy for the wrinkle/slack analysis, but also compensates for the lack of spring back force modelling at the membrane folds. This side-effect of the compressive stiffness ratio allows for the alleviation of the modelling of spring elements between consecutive elements to represent the spring back force originating from the plastic deformation of the membrane at fold lines. The best value for R_{cs} was found to be 10^{-3} where the folds do not prematurely unfold, and also start unfolding immediately after the star shape formation of the membrane. This specific value of compressive stiffness ratio can be assumed a material property for the specific membrane used in this model in a computational analysis that does not account for the spring back force of the membrane to decrease computational cost.

As a last step, the strain energy per unit length of the convex tapes is varied as its own proportions. The strain energy is calculated per unit length, and this normalization makes it equivalent to the self-extending force of the convex tapes. This force then directly relates to the extension speed, and the extension completion time. Although the calculated value represents the strain energy, the model does not account for the friction occurring between layers of coiled convex tapes, and between the outer most convex tape layer and the outer wall of the DOM2500 due to the radial expansion force of the convex tapes. This friction is experimentally modeled in by decreasing the acting strain energy. The acting strain energy per unit length of the convex tapes are found to be 1/4th of the calculated strain energy per unit length of the convex tapes.

Finally, the membrane model and the convex tape model are fused together, and the results are compared to the in-orbit deployment results. The timestamps for the unwrapping and unfolding stages of the deployment are consistent in each case. The deployment completion times and the intermediary membrane shapes during deployment are also consistent. This end model can then be assumed realistic. As a result, it can be claimed that the numerical analysis model was successfully constructed.

5. Conclusions

5.1. Summary

This dissertation presents a novel idea to accomplish an orbital maneuver using a de-orbiting mechanism as its primary source of impulse. In order to achieve this in a successful manner, an existing de-orbiting device with space heritage is improved with additional functionalities. These functionalities include separability to stop the de-orbiting phase after desired altitude is reached for orbital longevity and extendibility to bring the sail away from the satellite before deployment for better operability of the satellite during the orbital maneuver.

The addition of these functionalities also gave opportunity for the observation of the aforementioned de-orbiting mechanism in a meaningful manner. The fully successful deployment of a drag sail from a vertical angle of view is recorded in a video with a Time of Flight range finder including three dimensional distance information. This kind of data acquisition is in fact first in the world and is an invaluable reference both for the successful design of future missions and for the elucidation of gossamer structure dynamics. Using this data, the established numerical analysis methods are verified and more accurate models are implemented with realistic parameter-tuning.

5.2. Conclusions

Chapter 1: Introduction

In chapter one, the need for de-orbiting devices in general and the space debris problem are introduced. A literature review was conducted on the matter to explore various de-orbiting devices, their advantages, and their disadvantages. The drag sail deployment mechanism (DOM2500) used for this research is introduced, and the general satellite project (ALE-1) that enabled the space demonstration of this research is explained. Additionally, the importance of the simulative approach on the matter is defined.

Chapter 2: Numerical Analysis Methods for Membrane Deployment Behavior

In chapter two, the necessary groundwork for the simulation of the membrane structures is laid out. A review of nonlinear finite element methods used for membrane deployment behavior is conducted. The wrinkle/slack theory behind accurate membrane dynamics is discussed, and stiffness reduction model is introduced. These ideas are then applied to nonlinear finite elements in conjunction with the energy-momentum method. Following this, the model used for the numerical analysis of the self-extending convex tapes are summarized. Finally, the initial simulation results with untouched parameters are given as a starting reference point.

Chapter 3: Development of Separable De-Orbit Mechanism (SDOM)

In chapter three, the needed improvements on the DOM2500 for the ALE-1 mission is thoroughly discussed. All the criteria that are necessary to be fulfilled are clearly explained. Then the details of the newly designed system and its improved mechanisms are introduced. For compliance with fast project development periods, many mechanisms that have proven their success are recycled in different configurations. The separability, extendibility and observability capabilities are incorporated into the newly designed Separable De-Orbit Mechanism (SDOM). The system is evaluated with a de-orbiting simulation and the orbital maneuver mission time is estimated to take around 650 days. The remaining orbit time without separation would be as short as 50 days if continued to de-orbit, however after separation of the de-orbiting device the remaining orbit time is estimated to be 550 days. This remaining mission time is sufficient for the main mission of ALE-1 which is demonstration of artificial shooting stars. The observation systems to acquire invaluable data are thoroughly explained. The main sensor used for sail observation is the Sentis-M120-Laser. It has some limitations on data acquisition in space, however these limitations are tried to overcome with design modifications. Following this, ground verification results of the SDOM functions are shared. Difficulties encountered during these stages can be listed as, pin misalignment and resistance for the lock system, non-existence of nano-scale zero force connectors, resistance of convex tape self-extension, loss of voltage at long distances for actuation All these issues are resolved at the engineering model and the flight model is manufactured overcoming every obstacle and successfully clearing a vibration test and a thermal vacuum test, without losing functionality. Next, in-orbit demonstration results for SDOM are discussed. The lid is opened with a short delay, and the boom is extended with a very long delay. These delays are theorized to be caused by long storage times in space environment. With the feedback from these unsatisfactory results, the existing mechanism designs are improved. The spring providing the unlocking movement of the pin needs to be able to provide more force. The convex tapes would benefit from an initial kick-starting the self-extension movement with help of springs. Additionally, the sail used in DOM2500 lost two of its corner connections quickly after deployment. The connection method of the sail needs to change to a sturdier option such as direct connection through metallic ring chains. Furthermore, the sail appeared to have deployed in space only to 75% of its potential area. The reasons behind this low percentage are thoroughly analyzed and found to be, partly due to appearing smaller in camera because the sail is situated further away from the camera than the design value, and partly due to the fact that the sail is not in a planar state but a parachute like semi-plumped state, oscillating between flat and curvy states immediately after deployment. Although data was very limited, it seemed to stabilize at a curvy attitude. All of these facts cause the effective drag area to be lower than the design. For a more efficient sail use, the sail needs to be tensioned more and reinforced against ripping. With a lower effective drag area, the de-orbiting estimations acquired were no longer relevant. In fact, at the current state of the sail, it was not possible to calculate a new effective drag are, with the drag flag state of the sail that is moving around constantly. Therefore, a value for the effective drag area was estimated using the real flight telemetry de-orbiting rate during the past two years as reference. From this, it is found that even at a drag flag state, the sail is as effective as 25% of its theoretical flat area. It is important to reiterate, that due to the folding lines of the sail, at a free relaxed state its projected area is in fact not its flat area. Therefore, it is possible that the 25% effectiveness of a drag flag state can be higher for a sheet that is rolled out instead of unfolded for deployment. On the other hand, it can also be lower depending on the effects of the creases themselves. In either case, it is proven that a drag flag is also an effective method of de-orbiting, albeit with less effectiveness. To quantify, it is a 1/4th as effective as an attitude controlled drag sail and ½ as effective as a tumbling satellite with a drag sail, and it is a new method to be considered for de-orbiting.

In addition to the main mission results, Sentis-M120-Laser was used in space for the first time. To the authors knowledge, Raspberry Pi 3B was also used in space for the first time, outside of very controlled environments such as the International Space Station. Both devices proved their durability to function in space for long periods. Although it is important to mention, both of them were booted only when needed, and not all the time. The fact that they were asleep most of the time is a big factor to consider, especially when considering radiation events. Additionally, although it was durable, unfortunately Sentis-M120-Laser could not acquire clear data against all precautions taken. For future missions, laser range finders are not recommended by the author of this dissertation for the simple fact of enormous background noise.

Chapter 4: Model Parameter Identification with In-Orbit Flight Demonstration

In chapter four, the simulation model established in chapter two is improved with the help of the in-orbit data acquired in chapter three. First, a contact restriction is established between the central hub element and the membrane to ensure the membrane cannot pass through the hub element so that a rotational unwrapping is induced in the membrane during deployment. This unwrapping rate is adjusted by varying the spring constant for the contact restriction of the hub element. Following this, the unfolding rate of the fold lines of the membrane is adjusted by varying the compression stiffness ratio. It is found that a compression stiffness ratio of the magnitude 10^{-3} is most accurate when modelling membrane structures when using the stiffness reduction model proposed by Miyazaki to accurately simulate the unwrapping and unfolding dynamics and their order in conjunction with the applied tension on the membrane. Next, the spring constant of the hub element was re-explored to acquire better results with the newly adjusted compression stiffness ratio. It is found that this spring constant is highly dependent on other parameters unlike the compression stiffness ratio which is mostly independent. Following this, the convex tape model is tuned to reflect better extension times. The strain energy stored per unit length of the convex tapes which is directly proportional to the extension force is sampled to estimate the amount of friction that occur in the designed convex tape system. Finally, the fine-tuned membrane model is fused with the fine-tuned convex tape model for the deployment mechanics instead of the use of a constant pulling force. The unwrapping of the membrane up to the star shape and the formation of the inner hole, as well as the following unfolding of the fold layers were found to be consistent with the in-orbit results. Additionally, the timestamps for these behaviors were also consistent with the in-orbit results. The existence of convex tapes` self-extending behavior induces a clockwise rotation in the whole membrane during deployment which is also consistent with the real in-orbit results, where a twisting force is induced on the mast from the angular momentum of the uncoiling convex tapes. The chapter is concluded with the proposal of improvements and future work for the model.

In conclusion, in-orbit demonstration of a membrane deployment was conducted and an analysis model that can express this behavior was constructed. The analysis model parameters are adjusted in accordance with the observation data of the in-orbit deployment. The gained knowledge is believed to contribute to the field, for design evaluation of future membrane structure development, and for the elucidation of the membrane dynamics in outer space.

Bibliography

[1] Klinkrad, H., 2006. Space debris: models and risk analysis. Springer Science & Business Media.

[2] Kessler, D.J., 1989. Orbital debris environment for spacecraft designed to operate in low Earth orbit (Vol. 100471). National Aeronautics and Space Administration.

[3] Kessler, D.J. and Cour‐Palais, B.G., 1978. Collision frequency of artificial satellites: The creation of a debris belt. Journal of Geophysical Research: Space Physics, 83(A6), pp.2637-2646.

[4] Kessler, D.J., Johnson, N.L., Liou, J.C. and Matney, M., 2010. The kessler syndrome: implications to future space operations. Advances in the Astronautical Sciences, 137(8), p.2010.

[5] "IADC space debris mitigation guidelines", UNCOPUOS 40-th session, Vienna, 17-28 February 2003, Space Debris, A/AC.105/C.1/L.260.

[6] Shan, M., Guo, J. and Gill, E., 2016. Review and comparison of active space debris capturing and removal methods. Progress in Aerospace Sciences, 80, pp.18-32.

[7] Biesbroek, R., Innocenti, L., Wolahan, A. and Serrano, S.M., 2017, April. e. Deorbit-ESA's active debris removal mission. In Proceedings of the 7th European Conference on Space Debris (Vol. 10). ESA Space Debris Office.

[8] Wiedemann, C., Krag, H., Bendisch, J. and Sdunnus, H., 2004. Analyzing costs of space debris mitigation methods. Advances in Space Research, 34(5), pp.1241-1245.

[9] Wormnes, K., Le Letty, R., Summerer, L., Schonenborg, R., Dubois-Matra, O., Luraschi, E., Cropp, A., Krag, H. and Delaval, J., 2013, April. ESA technologies for space debris remediation. In *6th European Conference on Space Debris* (Vol. 1, pp. 1-8). Noordwijk, The Netherlands: ESA Communications ESTEC.

[10] Janovsky, R., 2002. End-of-life de-orbiting strategies for satellites. In 54th International Astronautical Congress of the International Astronautical Federation, the International Academy of Astronautics, and the International Institute of Space Law (pp. IAA-5).

[11] Standard, N.S., 1995. Guidelines and assessment procedures for limiting orbital debris. NASA NSS, 1740, p.14.

[12] Burkhardt, H., Sippel, M., Krülle, G., Janovsky, R., Kassebom, M., Lübberstedt, H., Romberg, O. and Fritsche, B., 2002. Evaluation of propulsion systems for satellite end-of-life de-orbiting. In 38th AIAA/ASME/SAE/ASEE Joint Propulsion Conference & Exhibit (p. 4208).

[13] Sahara, H., Shimizu, M., Osa, K., Watanabe, K. and Nakamura, Y., SOLAR THERMAL PROPULSION FOR MICROSATELLITES END-OF-LIFE DE-ORBITING.

[14] Reissner, A., Seifert, B., Jelem, D. and Sypniewski, R., 2017. EFFICIENT DE-ORBITING OF MICRO-AND NANO SATELLITES USING THE IFM NANO THRUSTER. In Proceedings of 7th European Conference on Space Debris, European Space Agency, DE.

[15] Chandra, A. and Thangavelautham, J., 2018. De-orbiting Small Satellites Using Inflatables. arXiv preprint arXiv:1809.04459.

[16] Cohen, A.F., 1984. Cosmos 954 and the International Law of Satellite Accidents. Yale J. Int'l l., 10, p.78.

[17] Nock, K., Gates, K., Aaron, K. and McRonald, A., 2010, August. Gossamer Orbit Lowering Device (GOLD) for safe and efficient de-orbit. In AIAA/AAS Astrodynamics specialist conference (p. 7824).

[18] Iess, L., Bruno, C., Ulivieri, C., Ponzi, U., Parisse, M., Laneve, G., Vannaroni, G., Dobrowolny, M., De Venuto, F., Bertotti, B. and Anselmo, L., 2002. Satellite de-orbiting by means of electrodynamic tethers part I: General concepts and requirements. Acta Astronautica, 50(7), pp.399-406.

[19] Iess, L., Bruno, C., Ulivieri, C. and Vannaroni, G., 2002. Satellite de-orbiting by means of electrodynamic tethers part II: System configuration and performance. Acta Astronautica, 50(7), pp.407-416.

[20] Ohkawa, Y., Kawamoto, S., Okumura, T., Iki, K., Okamoto, H., Inoue, K., Uchiyama, T. and Tsujita, D., 2020. Review of KITE–Electrodynamic tether experiment on the H-II Transfer Vehicle. Acta Astronautica, 177, pp.750-758.

[21] Pardini, C., Hanada, T. and Krisko, P.H., 2009. Benefits and risks of using electrodynamic tethers to de-orbit spacecraft. Acta Astronautica, 64(5-6), pp.571-588.

[22] Vaughn, J., Curtis, L., Gilchrist, B., Bilen, S. and Lorenzini, E., 2004, July. Review of the proseds electrodynamic tether mission development. In 40th AIAA/ASME/SAE/ASEE Joint Propulsion Conference and Exhibit (p. 3501).

[23] Bruno, C., Anselmo, L., Bussolino, L., Iess, L., Licata, R., Schirone, L. and Somensi, L., 2001, October. EDOARD: an electrodynamic tether device for efficient spacecraft de-orbiting. In Space Debris (Vol. 473, pp. 707-712).

[24] Hoyt, R., 2009, September. Terminator Tape: A Cost-Effective De-Orbit Module for End-of-Life Disposal of LEO Satellites. In AIAA Space 2009 Conference & Exposition (p. 6733).

[25] Stankey, H.C. and Hoyt, R.P., 2021. In-Flight Performance of the Terminator Tape End-of-Life Deorbit Module.

[26] Kawamoto, S., Ohkawa, Y., Kitamura, S. and Nishida, S.I., 2009. Strategy for active debris removal using electrodynamic tether. Transactions of the Japan Society for Aeronautical and Space Sciences, Space Technology Japan, 7(ists26), pp.Pr_2_7-Pr_2_12.

[27] Standard, N.S., 2021. Process for Limiting Orbital Debris. NASA-STD-8719.14C

[28] Majid, A., Owais, M., Qureshi, M., 2018, July. Aerodynamic Drag Computation of Lower Earth Orbit(LEO) Satellites. In Journal of Space Technology (Vol. 8, No. 1)

[29] Nelson, R.C., 1998. *Flight stability and automatic control* (Vol. 2). New York: WCB/McGraw Hill.

[30] Garner, C. and Leipold, M., 2000. Developments and activities in solar sail propulsion. In 36th AIAA/ASME/SAE/ASEE Joint Propulsion Conference and Exhibit (p. 3858).

[31] Macdonald, M., McInnes, C. and Hughes, G., 2010. Technology requirements of exploration beyond Neptune by solar sail propulsion. Journal of Spacecraft and Rockets, 47(3), pp.472-483.

[32] Mori, O., Tsuda, Y., Sawada, H., Funase, R., Saiki, T., Yamamoto, T., Yonekura, K., Hoshino, H., Minamino, H., Endo, T. and Kawaguchi, J., 2012. IKAROS and extended solar power sail missions for outer planetary exploration. Transactions of the Japan Society for Aeronautical and Space Sciences, Aerospace Technology Japan, 10(ists28), pp.Po_4_13-Po_4_20.

[33] Mori, O., Sawada, H., Funase, R., Morimoto, M., Endo, T., Yamamoto, T., Tsuda, Y., Kawakatsu, Y., Kawaguchi, J.I., Miyazaki, Y. and Shirasawa, Y., 2010. First solar power sail demonstration by IKAROS. Transactions of the Japan Society for Aeronautical and Space Sciences, Aerospace Technology Japan, 8(ists27), pp.To_4_25-To_4_31.

[34] Tsuda, Y., Mori, O., Funase, R., Sawada, H., Yamamoto, T., Saiki, T., Endo, T. and Kawaguchi, J.I., 2011. Flight status of IKAROS deep space solar sail demonstrator. Acta astronautica, 69(9-10), pp.833-840.

[35] Vulpetti, G., Johnson, L. and Matloff, G.L., 2015. The NanoSAIL-D2 NASA Mission. In Solar Sails (pp. 173-178). Springer, New York, NY.

[36] Katan, C., 2012, August. NASA’s Next Solar Sail: Lessons from NanoSail–D2. In 26th Annual AIAA/USU Conference on Small Satellites: Enhancing Global Awareness through Small Satellites (pp. 1-9).

[37] Bonin, G., Hiemstra, J., Sears, T. and Zee, R., 2013. The CanX-7 drag sail demonstration mission: enabling environmental stewardship for nano-and microsatellites.

[38] Cotton, B., Bennett, I. and Zee, R., 2017. On-orbit results from the CanX-7 drag sail deorbit mission.

[39] Underwood, C., Viquerat, A., Taylor, B., Massimiani, C., Duke, R., Fellowes, S., Schenk, M., Stewart, B., Bridges, C.P., Masutti, D. and Denis, A., 2018. The InflateSail CubeSat Mission–The First European Demonstration of Drag-Sail De-Orbiting. AAS Advances in the Astronautical Sciences Series, 163.

[40] Taylor, B., Underwood, C., Viquerat, A., Schenk, M., Fellowes, S., Massimiani, C., Duke, R. and Stewart, B., 2018. Flight Results of the InflateSail Spacecraft and Future Applications of DragSails.

[41] Ikeya, K., Sakamoto, H., Nakanishi, H., Furuya, H., Tomura, T., Ide, R., Iijima, R., Iwasaki, Y., Ohno, K., Omoto, K. and Furuya, T., 2020. Significance of 3U CubeSat OrigamiSat-1 for space demonstration of multifunctional deployable membrane. Acta Astronautica, 173, pp.363-377.

[42] Sakamoto, H., Furuya, H., Nakanishi, H., Watanabe, A., Kawabata, N., Hori, T., Ito, H., Kuratomi, T., Shimoda, Y., Hidaka, N. and Watanabe, K., 2021. On-Orbit Demonstration of Innovative Multifunctional Membrane Structure for Ultra-Lightweight Solar Arrays and Array Antennas by 3U CubeSat OrigamiSat-1.

[43] MOGI, T., KUWAHARA, T. and UTO, H., 2016. Structural design of de-orbit mechanism demonstration CubeSat FREEDOM. TRANSACTIONS OF THE JAPAN SOCIETY FOR

AERONAUTICAL AND SPACE SCIENCES, AEROSPACE TECHNOLOGY JAPAN, 14(ists30), pp.Pf_61-Pf_68.

[44] Uto, H., Kuwahara, T. and Honda, T., 2019. Orbit verification results of the de-orbit mechanism demonstration CubeSat FREEDOM. TRANSACTIONS OF THE JAPAN SOCIETY FOR AERONAUTICAL AND SPACE SCIENCES, AEROSPACE TECHNOLOGY JAPAN, 17(3), pp.295-300.

[45] Kuwahara, T., Yoshida, K., Sakamoto, Y., Tomioka, Y., Fukuda, K., Fukuyama, M., Tanabe, Y. and Shibuya, Y., 2012, December. Qualification results of a sail deployment mechanism for active prevention and reduction of space debries. In 63rd International Astronautical Congress 2012, IAC 2012 (pp. 2565-2570).

[46] Sakamoto, Y., Tanabe, Y., Yagisawa, H., Sugimura, N., Yoshida, K., Nishio, M., Nakajo, T. and Akiyama, H., 2014. Operation Results of Cubesat RAIKO Released from International Space Station. Transactions of the Japan Society for Aeronautical And Space Sciences, Aerospace Technology Japan, 12(ists29), pp.Tf_7-Tf_12.

[47] Sakamoto, Y., Takahashi, Y., Yoshida, K., Fukuda, K., Nakano, T., Battazzo, S., Fukuhara, T. and Kurihara, J., 2010, December. Development of the microsatellite RISING-2 by Tohoku University and Hokkaido University. In 61st International Astronautical Congress 2010, IAC 2010 (pp. 469-473).

[48] Sakamoto, Y., Sugimura, N., Fukuda, K., Kuwahara, T., Yoshida, K., Kurihara, J., Fukuhara, T. and Takahashi, Y., 2016. Development and flight results of microsatellite bus system for RISING-2. Transactions Of The Japan Society For Aeronautical And Space Sciences, Aerospace Technology Japan, 14(ists30), pp.Pf_89-Pf_96.

[49] Grillmayer, G., Lengowski, M., Walz, S., Roeser, H.P., Huber, F., Schoenermark, M.V. and Wegmann, T., 2004. Flying Laptop-Micro Satellite of the University of Stuttgart for Earth Observation and Technology Demonstration. In 55th International Astronautical Congress of the International Astronautical Federation, the International Academy of Astronautics, and the International Institute of Space Law (pp. IAA-4).

[50] Kuwahara, T., Böhringer, F., Falke, A., Eickhoff, J., Huber, F. and Röser, H.P., 2009. FPGA-based operational concept and payload data processing for the Flying Laptop satellite. Acta Astronautica, 65(11-12), pp.1616-1627.

[51] Kuwahara, T., Yoshida, K., Sakamoto, Y., Takahashi, Y., Kurihara, J., Yamakawa, H. and Takada, A., 2011, December. A Japanese microsatellite bus system for international scientific missions. In 62nd International Astronautical Congress 2011, IAC 2011 (pp. 3699-3706).

[52] Kuwahara, T., Yoshida, K., Sakamoto, Y., Tomioka, Y., Fukuda, K., Fukuyama, M. and Shibuya, Y., 2012. International scientific micro-satellite RISESAT based on space plug and play avionics.

[53] Tangdhanakanond, P., Kuwahara, T., Shibuya, Y., Honda, T., Pala, A.A., Fujita, S., Sato, Y., Shibuya, T. and Kamachi, K., 2021. Structural Design and Verification of Aeronomy Study Satellite ALE-1. TRANSACTIONS OF THE JAPAN SOCIETY FOR AERONAUTICAL AND SPACE SCIENCES, AEROSPACE TECHNOLOGY JAPAN, 19(1), pp.42-51.

[54] Pala, A., Kuwahara, T., Honda, T., Uto, H., Kaneko, T., Potier, A., Tangdhanakanond, P., Fujita, S., Shibuya, Y., Sato, Y. and Shibuya, T., 2021. System Design, Development and

Ground Verification of a Separable De-Orbit Mechanism for the Orbital Manoeuvre of Micro-Satellite ALE-1. TRANSACTIONS OF THE JAPAN SOCIETY FOR AERONAUTICAL AND SPACE SCIENCES, AEROSPACE TECHNOLOGY JAPAN, 19(3), pp.360-367.

[55] Lemal, A., Abe, S., Kamachi, K. and Okajima, L., Man-made Shooting Stars Aerothermodynamics and Flight Data on-Demand.

[56] Kamachi, K., Shibuya, Y., Oikawa, Y., Yamada, S., Imura, S., Arisaka, I., Takao, T., Okajima, L., Kuwahara, T., Fujita, S. and Sato, Y., 2018, October. Mission Planning for Artificial Shooting Star and Risk Assessment. In Proc. 62nd Space Science and Technology Conference (pp. 24-26).

[57] Morita, Y., Imoto, T., Tokudome, S. and Ohtsuka, H., 2012. Epsilon rocket launcher and future solid rocket technologies. TRANSACTIONS OF THE JAPAN SOCIETY FOR AERONAUTICAL AND SPACE SCIENCES, AEROSPACE TECHNOLOGY JAPAN, 10(ists28), pp.Tg_19-Tg_24.

[58] Horikawa, M., Izumi, H., Ohagi, Y., Noguchi, Y., Yagi, K. and Imoto, T., 2019. The Successful Launch of the Fourth Epsilon Launch Vehicle and its Future Rideshare Plans.

[59] Hori, K., Katsumi, T., Sawai, S., Azuma, N., Hatai, K. and Nakatsuka, J., 2019. HAN‐Based Green Propellant, SHP163−Its R&D and Test in Space. Propellants, Explosives, Pyrotechnics, 44(9), pp.1080-1083.

[60] Hiramatsu, T., Shirasaka, S. and Nakasuka, S., 2016, October. MicroDragon: a Vietnamese Ocean-observation Microsatellite Based on Hodoyoshi Architecture. In 7th Nano-Satellite Symposium and the 4th UNISEC-Global Meeting.

[61] 山口清, 鈴木智大 and 宮崎康行, 2016. 次世代アマチュア衛星通信技術実証「NEXUS」. In スペース・エンジニアリング・コンファレンス講演論文集 2016.25 (p. 1B3). 一般社団法人 日本機械学会.

[62] Bui, T., Tran, Q., Lew, J., Selvadurai, S., Tan, B., Ling, A., Yang, L. and Seng, L., 2018. Design and Development of AOBA VELOX-IV nanosatellite for future Lunar Horizon Glow mission.

[63] Koumoto, Y., Tanimoto, K., Terakado, Y., Ueno, T., Suzuki, Y., Oka, N. and Umesato, M., 2021. Result of Space Particle Monitor (SPM) on-Orbit Demonstration.

[64] Koizumi, S., Kikuya, Y., Sasaki, K., Masuda, Y., Iwasaki, Y., Watanabe, K., Yatsu, Y. and Matsunaga, S., 2018. Development of Attitude Sensor using Deep Learning.

[65] Sato, Y., Fujita, S., Kuwahara, T., Honda, T., Sakamoto, Y., Shibuya, Y. and Kamachi, K., 2020. Establishment of the Ground Evaluation and Operational Training System of Artificial Meteor Micro-satellite ALE-1. TRANSACTIONS OF THE JAPAN SOCIETY FOR AERONAUTICAL AND SPACE SCIENCES, AEROSPACE TECHNOLOGY JAPAN, 18(3), pp.84-92.

[66] Fujita, S., Sato, Y., Kuwahara, T., Sakamoto, Y., Shibuya, Y. and Kamachi, K., 2021. Double Fail-Safe Attitude Control System for Artificial Meteor Microsatellite ALE-1.

TRANSACTIONS OF THE JAPAN SOCIETY FOR AERONAUTICAL AND SPACE SCIENCES, AEROSPACE TECHNOLOGY JAPAN, 19(1), pp.9-16.

[67] Reissner, E., 1938. On tension field theory. *Proc. of the 5th Int. Congr. for Applied Mechanics Harvard Univ. & MIT*, pp.88-92.

[68] Stein, M. and Hedgepeth, J.M., 1961. *Analysis of partly wrinkled membranes.* National Aeronautics and Space Administration.

[69] Ding, H. and Yang, B., 2003. The modeling and numerical analysis of wrinkled membranes. *International Journal for Numerical Methods in Engineering*, 58(12), pp.1785-1801.

[70] Pipkin, A.C., 1986. The relaxed energy density for isotropic elastic membranes. *IMA journal of applied mathematics*, *36*(1), pp.85-99.

[71] Roddeman, D.G., Drukker, J., Oomens, C.W.J. and Janssen, J.D., 1987. The wrinkling of thin membranes: Part I—theory, *Journal of Applied Mechanics*, 1998, 54, pp.884-887.

[72] Epstein, M. and Forcinito, M.A., 2001. Anisotropic membrane wrinkling: theory and analysis. *International Journal of Solids and Structures*, *38*(30-31), pp.5253-5272.

[73] Kang, S. and Im, S., 1999. Finite element analysis of dynamic response of wrinkling membranes. *Computer Methods in Applied Mechanics and Engineering*, *173*(1-2), pp.227-240.

[74] Iwasa, T., Natori, M.C. and Higuchi, K., 2003. Evaluation of tension field theory for wrinkling analysis with respect to the study of imperfect bifurcation. In *Proceedings of 2003 ASME International Mechanical Engineering Congress AND RD & Expo*.

[75] Miyazaki, Y., 1998. Dynamic analysis of deployable cable-membrane structures with slackening members. In *Proceedings of 21st International Symposium on Space Technology and Science, 1998*.

[76] Kang, S. and Im, S., 1997. Finite element analysis of wrinkling membranes. *Journal of Applied mechanics,* 1997, 64, pp.263-269.

[77] Lu, K., Accorsi, M. and Leonard, J., 2001. Finite element analysis of membrane wrinkling. *International Journal for numerical methods in engineering*, *50*(5), pp.1017-1038.

[78] Miyazaki, Y. and Uchiki, M., 2002, April. Deployment dynamics of inflatable tube. In *43rd AIAA/ASME/ASCE/AHS/ASC Structures, Structural Dynamics, and Materials Conference* (p. 1254).

[79] Miyazaki, Y., Inoue, S. and Tamura, A., 2015. Analytical solution of the bending of a bi-convex boom. *Mechanical Engineering Journal*, *2*(6), pp.15-00465.

[80] Barois, T., Tadrist, L., Quilliet, C. and Forterre, Y., 2014. How a curved elastic strip opens. *Physical review letters*, *113*(21), p.214301.

[81] Woo, K., Nandukar, K. and Jenkins, C.H., 2008. Effective modulus of creased thin membranes. *Journal of Spacecraft and Rockets*, *45*(1), pp.19-26.

[82] Mori, O., Sawada, H., Hanaoka, F., Kawaguchi, J., Shirasawa, Y., Sugita, M., Miyazaki, Y., Sakamoto, H. and Funase, R., 2009. Development of deployment system for small size solar sail mission. *Transactions of the Japan Society for Aeronautical and Space Sciences, Space Technology Japan*, *7*(ists26), pp.Pd_87-Pd_94.

[83] Standard, G.E.V., 2013. GSFC-STD-7000. NASA Goddard Space Flight Center: Greenbelt, MD, USA.

[84] JAXA: Epsilon launch Vehicle User's Manual, JAXA, 2018, http://global.jaxa.jp/projects/rockets/epsilon/pdf/EpsilonUsersMan ual_e.pdf (accessed April 4, 2019)

[85] Tada, N., Inoue, S., Miyazaki, Y. and Yamazaki, M., 2017. Membrane Deployment de-orbit System by convex tapes. In 4th AIAA Spacecraft Structures Conference (p. 0619).

[86] Walker, J., 2018. Flight System Architecture of the Sorato Lunar Rover. In 16th International Symposium on Artificial Intelligence, Robotics and Automation in Space (i-SAIRAS), Madrid, Spain.

[87] Walker, J., Britton, N., Yoshida, K., Shimizu, T., Burtz, L.J. and Pala, A., 2016. Update on the qualification of the hakuto micro-rover for the google lunar x-prize. In Field and Service Robotics (pp. 313-330). Springer, Cham.

[88] Uno, K., Burtz, L.J., Hulcelle, M. and Yoshida, K., 2018. Qualification of a Time-of-Flight Camera as a Hazard Detection and Avoidance Sensor for a Moon Exploration Microrover. Transactions of The Japan Society for Aeronautical and Space Sciences, Aerospace Technology Japan, 16(7), pp.619-627.

[89] Oikawa, T., Tanaka, T., Suebe, Y., Uno, K., Zuliani, H., Burtz, L.J. and Yoshida, K., 2018. Preliminary radiation test result for space-ready qualification of lunar micro rover. TRANSACTIONS OF THE JAPAN SOCIETY FOR AERONAUTICAL AND SPACE SCIENCES, AEROSPACE TECHNOLOGY JAPAN, 16(7), pp.613-618.

[90] Uno, K., Burtz, L.J., Endo, M., Nagaoka, K. and Yoshida, K., 2018. Quality Of The 3d Point Cloud Of A Time-of-Flight Camera Under Lunar Surface Illumination Conditions: Impact And Improvement Techniques. In International Symposium on Artificial Intelligence, Robotics and Automation in Space, Madrid, Spain.

[91] Koskinen, M., Kostamovaara, J.T. and Myllylae, R.A., 1992, March. Comparison of continuous-wave and pulsed time-of-flight laser range-finding techniques. In Optics, Illumination, and Image Sensing for Machine Vision VI (Vol. 1614, pp. 296-305). International Society for Optics and Photonics.

[92] Adrien Potier, 2019, Development and Evaluation of a Time-of-Flight Monitoring Camera System for the De-orbiting Drag Sail of the Microsatellite ALE-1, Master's Thesis, Tohoku University, Sendai, Japan

[93] Miyazaki, Y., 2006. Wrinkle/slack model and finite element dynamics of membrane. International Journal for Numerical Methods in Engineering, 66(7), pp.1179-1209.

[94] Potier, A., Kuwahara, T., Pala, A., Fujita, S., Sato, Y., Shibuya, Y., Tomio, H., Tanghanakanond, P., Honda, T., Shibuya, T. and Koh, K., 2021. Time-of-Flight Monitoring Camera System of the De-orbiting Drag Sail for Microsatellite ALE-1. TRANSACTIONS OF THE JAPAN SOCIETY FOR AERONAUTICAL AND SPACE SCIENCES, AEROSPACE TECHNOLOGY JAPAN, 19(5), pp.774-783.

[95] Pala, A., Kuwahara, T., Takeda, K., Shibuya, Y., Sato, Y., Fujita, S., Suzuki, D. and Kaneko, T., 2022, January. Orbital Maneuver Evaluation of Micro-satellite ALE-1 with a

Separable Drag Sail. In 2022 IEEE/SICE International Symposium on System Integration (SII) (pp. 877-881). IEEE.

Acknowledgements

First and foremost, I would like to express my utmost gratitude and appreciation to Professor Kazuya Yoshida, for mentoring, providing extra-ordinary opportunities and supporting me throughout my higher education. Without his enabling approach or his warm welcome, I would not have been able to find a place for myself in Sendai that I can call my second home.

I would like to extend my gratitude towards the rest of the thesis committee: Professor Tomonaga Okabe, Professor Kanjuro Makihara, Professor Yasuyuki Miyazaki and Associate Professor Toshinori Kuwahara. The feedback I got through my researching years from my academic advisor Associate Professor Kuwahara, and Professor Miyazaki is what kept me going. Thank you for believing in me when I was hesitant and pushing me further with kindness.

I thank Assistant Professor Shinya Fujita for his support, especially on the experimentation using the flight model hardware.

I thank Nakashimada Engineering Works Co. Ltd. for providing engineering solutions, funding, and the opportunity to realize this research, and ALE Co. Ltd. for funding and providing the satellite and the project that enabled this research.

I thank Assistant Professor Jose V. Salazar, for his unending support, mostly unrelated to this research but still very relevant mentally in the grand scheme of undergoing PhD level research. If it weren’t for his constant encouraging, this research would not be conclusive.

I thank Assistant Professor Kentaro Uno, for his support, related and unrelated to this research.

I thank Yoshihiko Shibuya for walking this path together with me and providing support throughout. Additionally I thank Takumi Saitou for his kind collaboration on this research.

I thank Roy Somech, Ozkan Gokcekaya, Carlos Rivero, Dwiky Rendra, Angaddeep Singh and Seiko Sasaki for their unconditional support and friendship, which helped me get through tough times.

I thank my friends, Kuniaki Hayami, Kyouhei Maruya, Kazumasa Sawada and Tatano Sou for their tutorship throughout the years I spent in Japan.

I thank Yuto Suebe and Honoka Hashimoto for their unparalleled kindness and help on making my life easier on all aspects with their extreme understanding and support.

Finally, I would like to thank my family: my parents Iskender and Hulya Pala, my sisters Hilye Banu Degerli and Elif Dilasa Kose and their respective spouses, in other words my brothers, Bilal Degerli and Emin Kose for their unconditional support and trust in me.

August 2022

Tohoku University

Sendai, Japan

Copyright Notice

This dissertation contains reprints from the author's original publications as follows:

1. Chapter 3 contains figures from [54]. Copyright ©2021 JSASS. Reprinted, with permission, from A. Pala, T. Kuwahara, T. Hponda, H. Uto, T. Kaneko, A. Potier, P. Tangdhanakanond, S. Fujita, Y. Shibuya, Y. Sato and T. Shibuya, "System Design, Development and Ground Verification of a Seperable De-Orbit mechanism for the Orbital Manoeuvre of Micro-Satellite ALE-1," 2021. Transactions of The Japan Society for Aeronautical and Space Sciences, Aerospace Technology Japan, 19(3), pp.360-367.
2. Chapter 3 contains figures from [94]. Copyright ©2021 JSASS. Reprinted, with permission, from A. Potier, T. Kuwahara, A. Pala, S. Fujita, Y. Sato, Y. Shibuya, H. Tomio, P. Tanghanakanond, T. Honda, T. Shibuya and K. Kamachi, "Time-of-Flight Monitoring Camera System of the De-orbiting Drag Sail for Microsatellite ALE-1," 2021. Transactions of The Japan Society for Aeronautical and Space Sciences, Aerospace Technology Japan, 19(5), pp.774-783.
3. Chapter 3 contains figures from [95]. Copyright ©2022 IEEE. Reprinted, with permission, from A. Pala, T. Kuwahara, K. Takeda, Y. Shibuya, Y. Sato, S. Fujita, D. Suzuki and T. Kaneko, "Orbital Meuver Evaluation of Micro-satellite ALE-1 with a Separable Drag Sail," In 2022 IEEE/SICE International Symposium on System Integration (SII) (pp. 877-881). IEEE.